A Compact and Transportable Ultracold Matter System and Progress Towards a Continuously Operating Neutral Rydberg Atom Quantum Computer

by

Kai M. Hudek

B.S., Colorado School of Mines, 2005

M.S., University of Colorado, 2011

A thesis submitted to the

Faculty of the Graduate School of the

University of Colorado in partial fulfillment

of the requirements for the degree of

Doctor of Philosophy

Department of Physics

2012

This thesis entitled:
A Compact and Transportable Ultracold Matter System and Progress Towards a Continuously Operating Neutral Rydberg Atom Quantum Computer
written by Kai M. Hudek
has been approved for the Department of Physics

Dana Z. Anderson

James K. Thompson

Date

The final copy of this thesis has been examined by the signatories, and we find that both the content and the form meet acceptable presentation standards of scholarly work in the above mentioned discipline.

Hudek, Kai M. (Ph.D., Physics)

A Compact and Transportable Ultracold Matter System and Progress Towards a Continuously Operating Neutral Rydberg Atom Quantum Computer

Thesis directed by Professor Dana Z. Anderson

The work in this thesis falls into two broad categories: creating Bose-Einstein condensates (BECs) in compact and portable systems, and manipulating neutral atoms in small systems to facilitate a continuously running neutral Rydberg atom quantum computer. Chapters 1 and 2 supply the overall motivation and theory behind these two subjects, while Chapter 3 lays the experimental foundation for the systems used in these two broad experiments.

Chapter 4 focuses on the miniaturization of ultracold matter systems. Ultracold matter has potential uses in many practical applications, such as atomic clocks, inertial sensors, and electric and magnetic field sensing. Much of the potential of atom chip based systems relies on the ability for the system to make its way out of the lab.

Chapter 5 focuses on the ongoing work in atom manipulation for neutral Rydberg atom quantum computing. Neutral Rydberg atom quantum computing has great potential and, by harnessing the tool kit developed working with cold atoms, has the potential of scalability and continuous operation.

Chapter 6 discusses the future of the quantum computing project. Appendix A goes into detail on the home-built electronics cicuitry, and appendix B goes into detailed calculations on the effect of finite atom chip trace widths.

Dedication

To my parents, Regina and Steve, who raised me well.

Acknowledgements

I have matured greatly in my graduate career, both as a scientist and a person, and the lion's share of responsibility for that falls on my advisor Dana Anderson. I am very grateful that I had him as a mentor these last several years.

I would like to thank the many people I have had the pleasure of working with here in the group. The graduate and undergraduate students, current and former: Seth Caliga, Evan Salim, Steve Segal, Farhad Majdetemouri, Matt Squires, Rick Chuang, Brad Dinardo, Carrie Weidner, Cameron Straasma, Dan Maser, Marika Meertens, Jon Pfeiffer, Justin Lanfranchi, Jake Pittine, Janet Duggan, Christina Jones, and Andy Holmgren. My "one and only" post-doc Dan Farkas, who taught me everything I know about electronics. Leslie Czaia is "one of a kind," and I have taken much pleasure over the years in learning from her both personally and professionally.

The instrument makers of JILA have been invaluable to my development as an experimentalist and have given me more tools (pun intended) than almost anyone. My thanks to Hans Green, Todd Asnicar, Tracy Keep, Blaine Horner, Kels Detra, Dave Alchenberger, Kim Hagen, Ariel Paul and Tom Foote. I would like to thank the electronics wizards Carl Sauer, James Fung-a-fat, Mike Whitmore, Terry Brown and Chris Ho.

Thanks to the many people I have collaborated with over the years. Sterling McBride and Joey Michalchuk of SRI International have been a pleasure to work with throughout my graduate career, as well as Alex Zozulya of Worcester Polytechnic Institute, Steve Hughes of ColdQuanta, Jeffry DeNatale and Robert Mihailiovich of Teledyne Scientific, Shegwang

Du, formerly of the University of Colorado and now at Hong Hong University of Science and Technology, Robert Gray and David VanWie of Boulder Labs, and of course Mark Saffman of the University of Wisconsin.

I would also like to thank those who helped me out before I came to the University of Colorado. At the Colorado School of Mines: my undergraduate advisor Chip Durfee who introduced me to lasers, James McNeil, Tim Ohno, Jeff Squier, and Todd Ruskell. At my summer research time in Stanford: Alberto Fasso and Heinz Vincke. At my summer research time in Berkley: Kevin Lesko, Alan Poon and Reyco Henning.

Last but not least, I would like to thank all of the wonderful people I've had the pleasure of meeting over the last several years. I am incredibly grateful for the love and support of my friends in this beautiful place we currently call home.

Contents

Chapter

Tables

Table

Figures

Figure

Chapter 1

Introduction and motivation

The work in this dissertation falls into two broad categories: creating Bose-Einstein condensates (BECs) in compact and portable systems, and manipulating neutral atoms in small systems to facilitate a continuously running neutral Rydberg atom quantum computer. This chapter will briefly delve into some background information on these two broad topics and provide the motivation for the work accomplished.

1.1 Making BEC on a chip and making it portable

BECs were originally made, and many still are, in large vacuum systems with magnetic traps made from coils outside the vacuum system [1,2]. Large vacuum systems are beneficial in creating the lowest vacuum pressures and thus the longest BEC lifetimes. However, one of the prices paid is that the coils too must be made larger and to achieve the necessary trapping gradients, hundreds of amperes of current must be run through them. This requires specialized thermal management, such as water cooling or superconducting coils. Additionally, this limits the feature size of the magnetic trap, which scales as the distance of the atoms from the coils. In general, these systems take up one (or more) optical tables and an entire rack full of electronics.

Since the earliest experimental demonstrations of BEC in a gas of neutral atoms, studies of BEC and related forms of ultracold matter have been largely motivated by purely scientific interests. However, it has become increasingly evident that ultracold matter can

play a utilitarian role in applications such as atomic clocks, inertial sensors, and electric and magnetic field sensing [3–8]. The complexity and size of the required apparatus necessitates that these experiments remain confined to research laboratories. Indeed, much of the work on ultracold atom chip technology is predicated on the need for compact systems that can find their way out of the laboratory and into the field.

The first demonstration of BEC on an atom chip really opened the door to addressing many of the practical issues surrounding ultra-cold atoms [9]. The magnetic trap used was generated on chip with only a few amperes of current, which greatly reduces the complexity and power consumption of the system. The entire BEC production took less than 10 s, which is an order of magnitude faster than previous systems. And, remarkably, they were able to transport their BEC several millimeters with their chip wires.

Utilizing atom chips, the systems developed in this lab have worked to further address functional BEC. BECs on atom chips have been used to demonstrate remarkable results with high repetition rates approaching something that might be useful in the field. However, system integration also plays an important role and compact, reliable instrumentation that addresses the stringent needs of cutting-edge atomic physics is necessary if cold atoms are to be made practical.

1.2 Quantum computing with neutral Rydberg atoms

Quantum computing takes advantage of the quantum properties of atoms to perform algorithms with the prospect that, eventually, certain calculations will be exponentially faster than a classical computer. There has been sustained progress in the experimental development of quantum computing since the first demonstration of a quantum gate using a trapped ion [10]. In current state-of-the-art quantum computing, a few quantum gate operations can be performed on a handful of qubits, most notably with trapped ions [11], but also with superconducting [12] and photonic [13] qubits. However, in order to reach the regime where one is exploring computationally interesting systems that exceed the capabilities of classical

computers, it is necessary to increase the number of qubits with which one has to work.

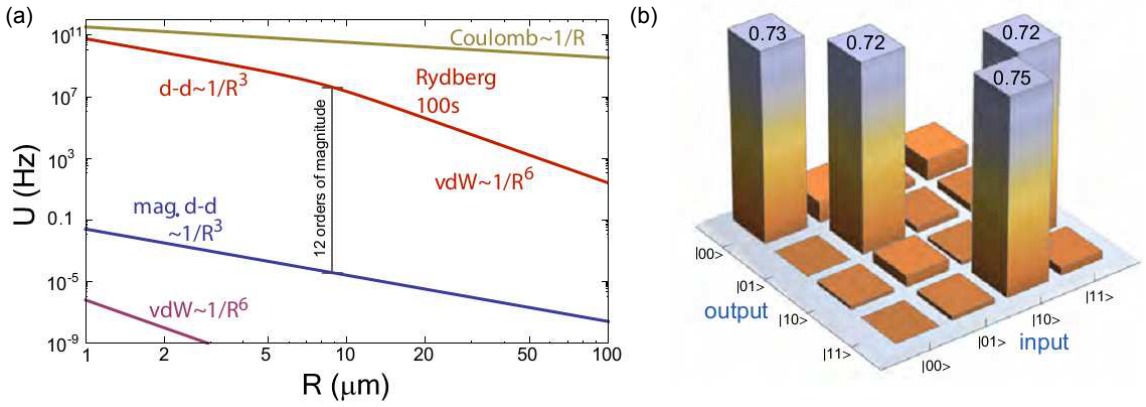

Figure 1.1: (a) Characteristic energy scale of the two-atom Coulomb, Rydberg, magnetic dipole-dipole and van der Waals interaction. Image credit [14]. (b) Two-qubit CNOT Rydberg interaction mediated gate truth table. Image credit [15].

Neutral atoms differ from ions because of their state-dependent interaction properties. Shown in Figure 1.1(a) is the two-particle interaction strength versus separation for singly charged ions, ground-state neutral atoms, and Rydberg atoms. Singly charged ions interact dominantly via the 1/R Coulomb force, which is both strongly interacting and long range, both of which are good characteristics for qubits. However, the "always" on character of the Coulomb interaction makes the task of establishing a many-qubit register appear quite difficult. The ground-state neutral atom interaction is dominated by $1/R^6$ van der Waals forces at very short range (off the graph to the left) and by $1/R^3$ magnetic dipole-dipole forces beyond about 30 nm. At a separation of 10 μm the interaction is very weak, about 10^{-5} Hz in frequency units. On the other hand, excitation of Rubidium atoms to the 100 s Rydberg level results in a very strong interaction that is $1/R^3$ electic dipole-dipole at short distances and $1/R^6$ van der Waals at long distances. At a separation of 10 μm the interaction is very strong, about 10^7 Hz. This implies that an array of neutral atom qubits in the ground state can be structurally stable and thus scalable, but that turning on the Rydberg interaction can selectively increase atom-atom interaction by 10^{12} [14]. The ability to turn the atom-atom interaction on and off by 12 orders of magnitude is a strong argument for

pursuing Rydberg-mediated quantum gates. The ability to control the interaction strength over such a wide range appears unique to the Rydberg system [14]. Shown in Figure 1.1(b) is a controlled-NOT (CNOT) gate truth table demonstrated via the Rydberg interaction between two rubidium atoms separated by $10\,\mu$m excited to the $n = 97$ Rydberg level [15].

1.3 Transporting atoms in small systems

Unlike, for example, superconducting qubits, which are physically stable, neutral atom qubits held in optical traps have finite lifetimes due to collisions with thermal background atoms in the vacuum chamber. One solution to the problem of finite lifetime is to have a "reservoir" of atoms ready and waiting to replenish atoms that have fallen out of the trap. Providing a pre-cooled source of atoms to an atom reservoir has been proposed and demonstrated [16–19]. However, a common theme is that these achievements occur in large vacuum systems, where stray-field isolation and optical isolation are more easily achievable than in smaller systems, and can arise naturally from the spatial separation of the atom reservoir and collection regions. This facilitates the use of standard atom-cooling and -trapping techniques, such as sub-Doppler cooling and magnetic trapping and transport.

In general, the interactions between the Rydberg atoms are sensitive to external magnetic and electric fields. The large dipole matrix-element of Rydberg states makes them extremely sensitive to small low-frequency (DC) electric fields. The electric stability requirement for a qubit array where atoms are excited to the $n = 100$ Rydberg level is on the order of 10^{-4} V/cm [14]. Modest magnetic fields can also strongly affect the Rydberg-Rydberg interactions by breaking the Zeeman degeneracy [20]. In smaller systems, where for instance the separation of the collection region from the qubit array is only a few centimeters, there are much more stringent requirements on stray-field changes. Additionally, high optical isolation must be achieved through clever choice of geometry rather than, say, in vacuo shuttering [18], as any stray resonant light hitting the qubit array will destroy its coherence. Thus, transporting atoms from the collection region to the science chamber

presents a unique set of challenges if we are to shrink the system's footprint.

1.4 Dissertation outline

The rest of the dissertation is organized as follows: Chapter 2 introduces the basic concepts, mathematics, and theory necessary to understand the work in this dissertation. Chapter 3 goes into detail about the many vacuum systems that form the heart of the work in this dissertation, and presents current state-of-the-art cells. Chapter 4 details the portable BEC system, which is the first major area of research in this dissertation. Chapter 5 details the ongoing quantum computing effort, which is the second major area of research. Chapter 6 looks ahead at the next generation of work, especially in the quantum computing work that is in progress. Appendicies A and B go into greater detail on the BEC cart electronics and forced-evaporation modeling and are for the more in-depth reader.

Chapter 2

Theory

This chapter will go over concepts and terms that will form the basis for understanding the rest of the work contained in this dissertation. We'll start with the basics of trapping neutral atoms in a magnetic field, then go into the more complicated geometries that can be achieved with atom chips. We will then switch gears and talk about the physics behind a moving molasses MOT. Finally, we will talk about the trapping of atoms in an optical field. This is a brief introduction meant to give the reader the ability to understand the salient parts of this dissertation. For more in-depth discussion there are many good dissertations and review articles, some of which are described in [21–27].

2.1 Magnetically trapping atoms

Atoms with non-zero magnetic dipole moments can be thought of as tiny bar magnets, and in a magnetic field have a potential energy based on their orientation. The potential U_{mag} from the Zeeman effect for atoms in a magnetic field B is given by Equation 2.1.

$$U_{\text{mag}} = -\vec{\mu} \cdot \vec{B} = g_F \mu_B m_f B, \tag{2.1}$$

where $\vec{\mu}$ is the magnetic moment g_F is the Landé-g factor, μ_B is the Bohr magneton, and m_F is the z-component of the atomic angular momentum. The force an atom experiences is simply the gradient of the magnetic field, given by Equation 2.2.

$$\vec{F} = -\nabla U = -g_F \mu_B m_f \nabla B, \tag{2.2}$$

which is a conservative force.

As a consequence of Gauss's law, individual components of a magnetic field vector cannot have a local minimum or maximum in free space. Additionally, it is impossible to produce a local maximum in the magnitude of the magnetic field in free space; however the magnitude of the magnetic field can produce a minimum in free space. Thus, only atoms in weak-field-seeking states $g_F\, m_F > 0$ can be trapped ($U_{\text{mag}} < 0$). Strong-field-seeking states $g_F\, m_F < 0$ are anti-trapped and forced away from the trap. To hold atoms, the trap must be tight enough to overcome gravity. In a quadrupole trap, the gradient is used to describe the trap's confinement. In a harmonic trap the gradient term is not the dominant effect. Instead, the second derivative, the trap frequency ω, is used to describe the trap's confinement. In this case it is useful to calculate the "sag" that the atoms will experience, i.e., where the atoms will sit in the trap under the influence of gravity. Naturally, this needs to be a small fraction of the size of the trap, or the atoms will move too far from the center (harmonic) portion of the trap or simply fall out. These conditions are given by

$$\text{Quadrupole:} \qquad g_F \mu_B m_f \nabla B > mg, \tag{2.3}$$

$$\text{Harmonic:} \qquad \Delta z = \frac{2g}{\omega}. \tag{2.4}$$

In quadrupole traps, $|\vec{B}|$ goes to zero at the trap center, thus atoms are unable to adiabatically follow the magnetic field. Atom spin-flips into untrapped states are lost, and are referred to as Majorana losses. The adiabaticity condition is given as

$$\frac{\mathrm{d}\theta}{\mathrm{d}t} < \frac{g_F \mu_B m_f |\vec{B}|}{\hbar F} = \omega_L, \tag{2.5}$$

where θ is the instantaneous alignment of the atom's magnetic moment with the magnetic field, F is the hyperfine quantum number, and ω_L is the Larmor frequency. Majorana losses generally occur as the atomic cloud gets colder and spends more of its time near the center of the trap, i.e., a larger fraction of atoms sample the low-field region of the trap. Quadrupole traps are still useful as low loss magnetic traps for atoms at Doppler, and even sub-Doppler,

temperatures. In order to avoid Majorana losses, a Ioffe-Pritchard (IP) trap can be used, which is harmonic in the center and has a non-zero minimum. The minimum magnetic field necessary to prevent Majorana losses in an IP trap is typically a few Gauss, but the actual value depends on the temperature, and thus velocity, of the atom cloud in the trap.

2.2 Atom chip traps

Traditional BEC systems employ coils external to the vacuum system to create their magnetic field traps. However, this usually requires physically large coils, hundreds of amperes of current, and water cooling in order to generate large enough fields. Atom chips overcome many of these limitations and in our systems are key to making BEC in a fast, efficient, and compact manner.

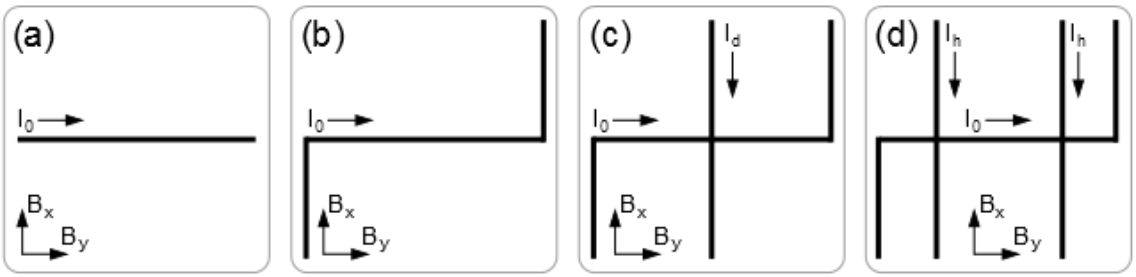

Figure 2.1: The chip is in the x-y plane at z=0. Four basic chip trap wire geometries: (a) Side guide trap. (b) Z-wire trap. (c) Dimple-wire trap. (d) H-wire trap.

Shown in Figure 2.1 are four basic chip trap wire geometries, which we will be discussing. The chip wires are patterned in the x-y plane and sit at z=0. The side guide trap is a good conceptual starting point for the more complicated traps.

2.2.1 Side guide trap

The simplest situation arises when you have an infinitely long wire carrying current I_0 as shown in Figure 2.1(a) and Figure 2.2(a). This produces a magnetic field and gradient of

$$B_0 = \frac{\mu_0 I_0}{2\pi r}, \tag{2.6}$$

$$B_0' = -\frac{\mu_0 I_0}{\pi r^2}. \tag{2.7}$$

From this simple picture it's clear that, because of the $1/r^2$ falloff of the magnetic field gradient, large gradients can be achieved much faster by moving the atoms closer to the current source than by increasing the current. If a bias field B_y is applied perpendicular to the wire, then a zero of magnetic field will be located a distance z_0 above the wire, where

$$z_0 = \frac{\mu_0}{2\pi}\frac{I_0}{B_y}, \tag{2.8}$$

as shown in Figure 2.2(b) and (c). In Figure 2.2(b) and (c) a current of $I_0 = 1\,\mathrm{A}$ and a bias field of $B_y = -4\,\mathrm{G}$ were used for the calculation. Figure 2.2(b) is a contour plot of the magnitude of the magnetic field in the y-z plane. The current-carrying wire at the origin is running in-and-out of the page, and the contours go from 0 G (dark region) to 6 G (white is >6 G) in increments of 0.3 G. Figure 2.2(c) is the magnitude of the magnetic field along the z-axis direction, labelled "z-slice" in Figure 2.2(b). The dashed line is the magnetic field at infinity which is equal to B_y, and in this trapping geometry is equal to the the trap depth.

The gradient of the field at the trap center z_0 can be expressed as

$$\begin{aligned} B_y'|_{z_0} &= \frac{\mu_0}{2\pi}\frac{I_0}{z^2}|_{z_0}, \\ &= \frac{B_y}{z_0}. \end{aligned} \tag{2.9}$$

The side guide trap is a starting point for atom chip traps but it has two shortfalls: it is a waveguide and thus only confines atoms radially, and it is a quadrupole trap, which has a zero of magnetic field at its minimum as shown in Figure 2.2(c), which allows Majorana spin flips to occur.

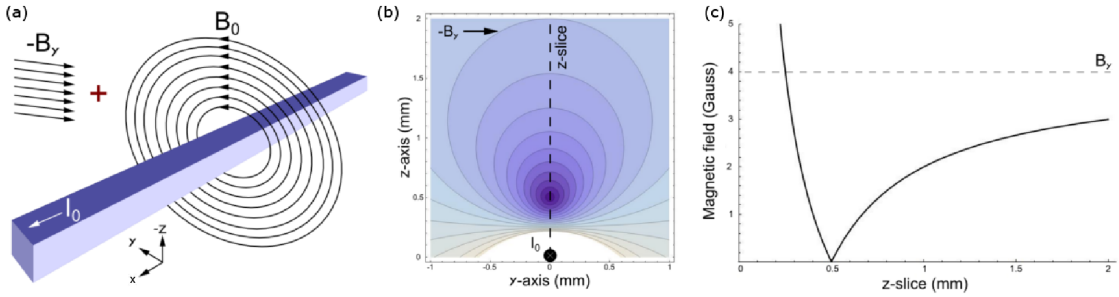

Figure 2.2: (Color) (a) Trapping fields for the chip side guide with 1 A of current and bias fields of $(B_x, B_y, B_z) = (1, -4, 0)$ G. (b) A contour plot of the magnitude of the magnetic field in the x-z plane. The current-carrying wire runs in and out of the page at the origin. (c) The magnitude of the magnetic field as a function of z along the "z-slice". The chip surface is at z=0.

2.2.2 Z-wire trap

The Z-wire geometry, shown in Figure 2.1(b), is a simple extension of the side guide, and turns the side guide from a quadrupole waveguide into an IP trap with an approximate axisymmetric geometry, i.e., it has radial symmetry with tight confinement and an axis with loose confinement. Plots of a Z-wire trap are shown in Figure 2.3, where the legs of the Z-wire running vertically along the y-axis are 10 mm in length, and the main part of the Z-wire running horizontally along the x-axis is 20 mm in length. The plots were made running a current of $I_0 = 1\,\mathrm{A}$ and a field of $(B_x, B_y, B_z) = (1, -4, 0)\,\mathrm{G}$.

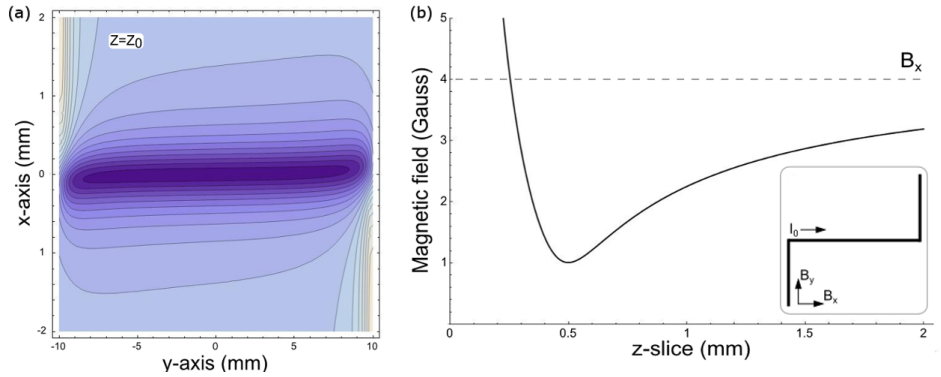

Figure 2.3: (Color) Trapping fields for the chip Z-wire with 1 A of current and bias fields of $(B_x, B_y, B_z) = (1, -4, 0)\,\mathrm{G}$. (a) A contour plot of the trap in the x-y plane at the trap minimum z_0. (b) The magnitude of the magnetic field as a function of z. The chip surface is at z=0.

Here the trap depth is determined by the difference between the field at infinity corresponding to the bias fields, and the field at the trap center $B_{\min}$. A detailed discussion of the approximate analytic solutions to $B_{\min}$ can be found in [28]. The calculations here were done using the analytic Biot-Savart method discussed in more detail in Appendix B.

2.2.3 Dimple-wire trap

The dimple-wire trap is created by running a trace through the center of a Z-wire trap along the x-axis direction, as shown in Figure 2.1(c). The dimple-wire trap is also

an approximately axisymmetric trap, but with the advantage of having much tighter axial confinement than the Z-wire trap. During RF evaporation, rethermalization rates are proportional to the geometrically averaged trap frequency $\bar{\omega} = (\omega_i \omega_j \omega_k)^{1/3}$, where $\omega_{i,j,k}$ are the three eigenfrequencies of the trap. Thus, tighter axial confinement increases $\bar{\omega}$, which allows for faster RF evaporation.

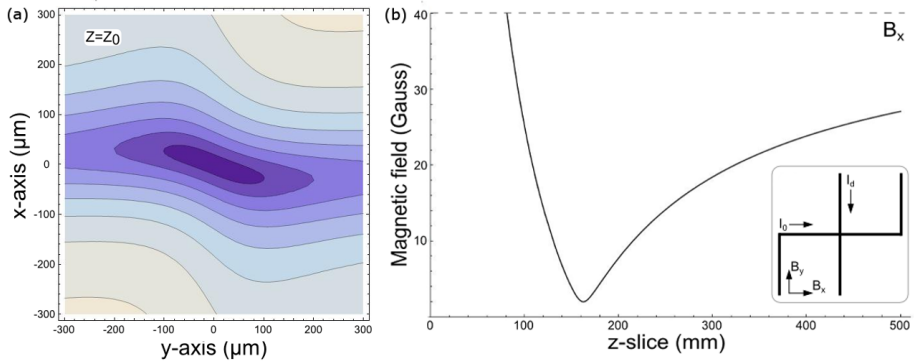

Figure 2.4: (Color) Trapping fields for the chip dimple-wire trap with 3.25 A of current in the Z-wire, 1.25 A in the dimple wire and bias fields of $(B_x, B_y, B_z) = (16, -40, 0)$ G. (a) The field as a function of z. The chip surface is at z=0. (b) A contour plot of the trap in the x-y plane at the trap minimum z_0.

Because of the faster rethermalization, the dimple-wire trap was used to create BEC in Chapter 4. The approximate experimental parameters from Section 4.10.3.1 are shown in Figure 2.4. The main z-wire carries current of $I_0 = 3.25$ A and the dimple-wire carries a current $I_d = 1.25$ A. The bias fields generating the trap are $(B_x, B_y, B_z) = (16, -40, 0)$ G. The tighter axial confinement can clearly be seen as the extent of the plot in Figure 2.4(a) spans ± 0.5 mm horizontally, whereas Figure 2.3(a) spans ± 10 mm. The in-plane tilt of the trap axis is approximately given by

$$\theta_{\text{dimple}} = \tan^{-1} \frac{I_0}{I_d}. \tag{2.10}$$

The exact eigenaxes and eigenfrequencies can be determined by the method discussed in Appendix B.

2.2.4 H-wire trap

The H-wire geometry, shown in Figure 2.1(d), is a symmetric extension of the Z-wire trap. Plots of an H-wire trap are shown in Figure 2.5, with a current of 1 A for both I_0 and I_h and bias fields of $(B_x, B_y, B_z) = (-1, -4, 0)$ G. The legs of the H-wire are 10 mm long separated by 10 mm, and the main Z-wire is still 20 mm in length.

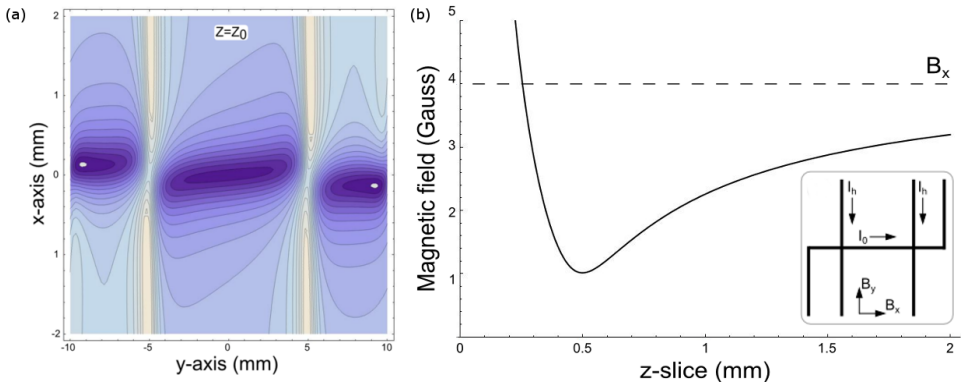

Figure 2.5: (Color) Trapping fields for the chip h-wire with 1 A of current and bias fields of $(-4, -1, 0)$ G. (a) A contour plot of the trap in the x-y plane at the trap minimum z_0. (b) The field as a function of z. The chip surface is at z=0.

The main advantage of the H-wire trap is that it decouples the H-legs of the trap from the Z-legs, and the current I_0 from I_h. As shown in Figure 2.5(a), the axial trap frequency can be determined, and modulated, by physical placement of the H-wire legs and the current I_h. Additionally, one could imagine adiabatically increasing the axial trap frequency by running current through a series of H-wires with physically smaller separation when performing RF evaporation, and then reversing the process to increase BEC lifetime after evaporating to degeneracy. These chip-wire models are useful in visualizing atom chip traps and what designs are possible. Atom chips are discussed in detail in Section 3.1.3.

2.3 Moving molasses magneto-optical trap

The starting point for a majority of cold atom experiments, and all of the work in this dissertation, is the magneto-optical trap (MOT), which takes atoms from room temperature

and cools them down to a few hundred microkelvin. A MOT geometry that is novel to this lab is the moving molasses (MM) MOT [29–33] whose geometry is shown in Figure 2.6. There are several methods for producing a high-flux, slow source of atoms, including a 2D MOT, an "atom funnel," or an LVIS [34, 35]. These sources produce beams with fluxes from 10^6 to 10^{10} atoms/s, and average velocities from 1 m/s to 50 m/s. However, the velocity dispersion tends to be rather broad, with $\Delta v \sim \bar{v}$ [31]. The MM MOT, by contrast, produces a beam that is cold both longitudinally and transversely ($\Delta v \ll v$), with a precisely controllable velocity down to less than 1 m/s.

A 2D magnetic field identical to that of a 2D MOT [28, 36] is generated by coils or permanent magnets with the zero of the magnetic field running vertically along the center. The field gradient is given by

$$\vec{B}' = (-B'x, B'y, 0). \tag{2.11}$$

Four independent counter-propagating beams with with opposite circular polarization $\sigma^{\pm}$ enter the cell at an angle of $\alpha = 45°$ in the x-z plane, i.e., along the $|x| = |z|$ lines. A retro-reflected beam enters the cell along the y-axis direction to provide a confining force along the third dimension of the trap. The center laser frequency ω is red detuned by an amount Δ from atomic resonance, with values similar to a standard MOT. For $\alpha = 0°$, the standard 2D MOT configuration is realized. For $\alpha = 45°$, efficient cooling and trapping in a MOT is obtained in the radial direction and efficient slowing of the atomic motion in an optical molasses is obtained along the vertical direction.

In an optical molasses, the average force an atom experiences against its motion is just the momentum carried by a photon times the average rate of absorbing and scattering photons [37], given by

$$\vec{F} = \hbar\vec{k}R_{\mathrm{SC}} = \hbar\vec{k}\frac{\Gamma}{2}\frac{\Omega^2/2}{\Delta^2 + \Omega^2/2 + \Gamma/4}, \tag{2.12}$$

where $\hbar k = h/\lambda$ is the photon momentum, Γ is the linewidth of the atomic transition, Ω is the Rabi frequency, and $\Delta = \omega_l - (\omega_0 \pm \vec{k}\cdot\vec{v})$ is the detuning from resonance, where $\vec{v}$ is the

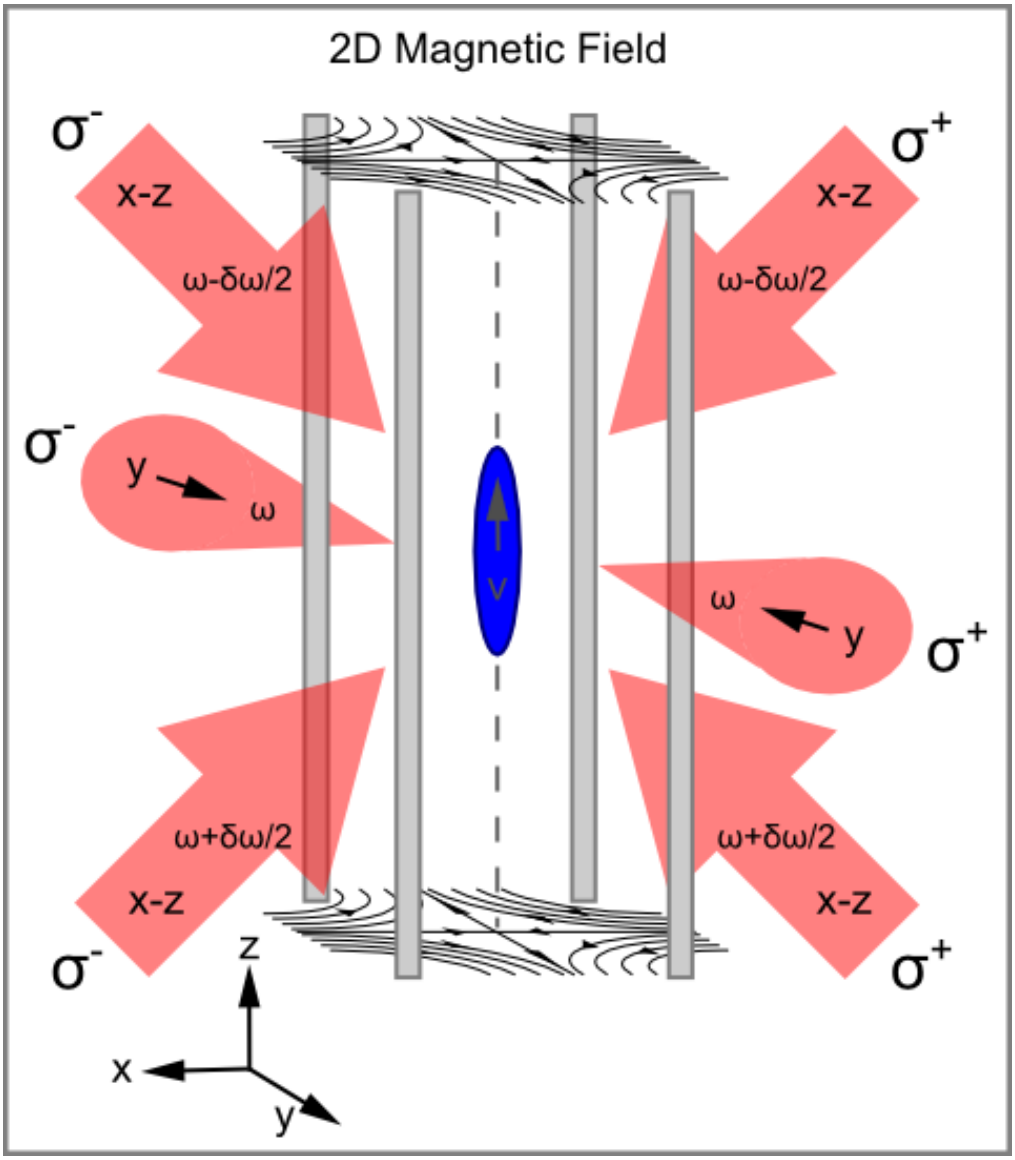

Figure 2.6: (Color) Moving molasses magneto-optical trap diagram. Four independent counter-propagating beams enter the cell at an angle of 45° in the x-z plane and are shifted by $\pm\delta\omega$ from the center frequency ω to create a net velocity for the atoms upward. A retro-reflected beam enters the cell along the y-axis direction to provide a confining force along the third dimension of the trap.

velocity of the atom and $\vec{k} \cdot \vec{v}$ is the associated Doppler shift. For two counter-propagating beams the force on the atom is just $F_+ + F_-$ or

$$\vec{F} = \vec{F}[\omega_l - (\omega_0 - \vec{k} \cdot \vec{v})] + \vec{F}[\omega_l - (\omega_0 + \vec{k} \cdot \vec{v})], \tag{2.13}$$

from which it is clear that the forces tend to balance as $v \to 0$. A plot of the individual forces (thin black dashed lines) along with the net force generated by two counter-propagating beams (thick black dashed line) is shown in Figure 2.7.

In order to generate a moving optical molasses, i.e., an optical molasses with a non-zero net velocity in the laboratory reference frame, an additional detuning $\delta\omega$ can be applied symmetrically to the optical molasses beams, which changes the detuning to

$$\Delta' = \omega_l - (\omega_0 \pm \vec{k} \cdot \vec{v} \mp \delta\omega) \tag{2.14}$$

and modifies Equation 2.13 to be

$$\vec{F} = \vec{F}[\omega_l - (\omega_0 - \vec{k} \cdot \vec{v} + \delta\omega)] + \vec{F}[\omega_l - (\omega_0 + \vec{k} \cdot \vec{v} - \delta\omega)], \tag{2.15}$$

where $\vec{k} \cdot \vec{v} = kv\cos(\theta)$, with θ the angle between the velocity and light propagation directions. From Equation2.15 it is clear that the forces tend to balance as $v \to \delta\omega/k\cos(\theta)$. The individual forces are shown in Figure 2.7 by the thin solid red lines. The sum of these two forces is shown in Figure 2.7 by the thick solid red line, where the relative detuning is such that the laboratory-frame velocity is $kv/\Gamma = 4$. This can be thought of intuitively where, because all of the beams are red detuned to begin with, by shifting the frequency up (down), the laser is tuned closer (further) from resonance and thus exerts a larger (smaller) force on the atoms. The atoms then move to a reference frame in which the Doppler effect has brought both pairs of beams back to the same detuning. To the moving atoms this again appears as a stationary optical molasses. Writing the average cloud velocity $\bar{v}$ as a function of the detuning for the beam geometry in Figure 2.6 gives

$$\bar{v} = \sqrt{2}\,\delta\nu\,\lambda, \tag{2.16}$$

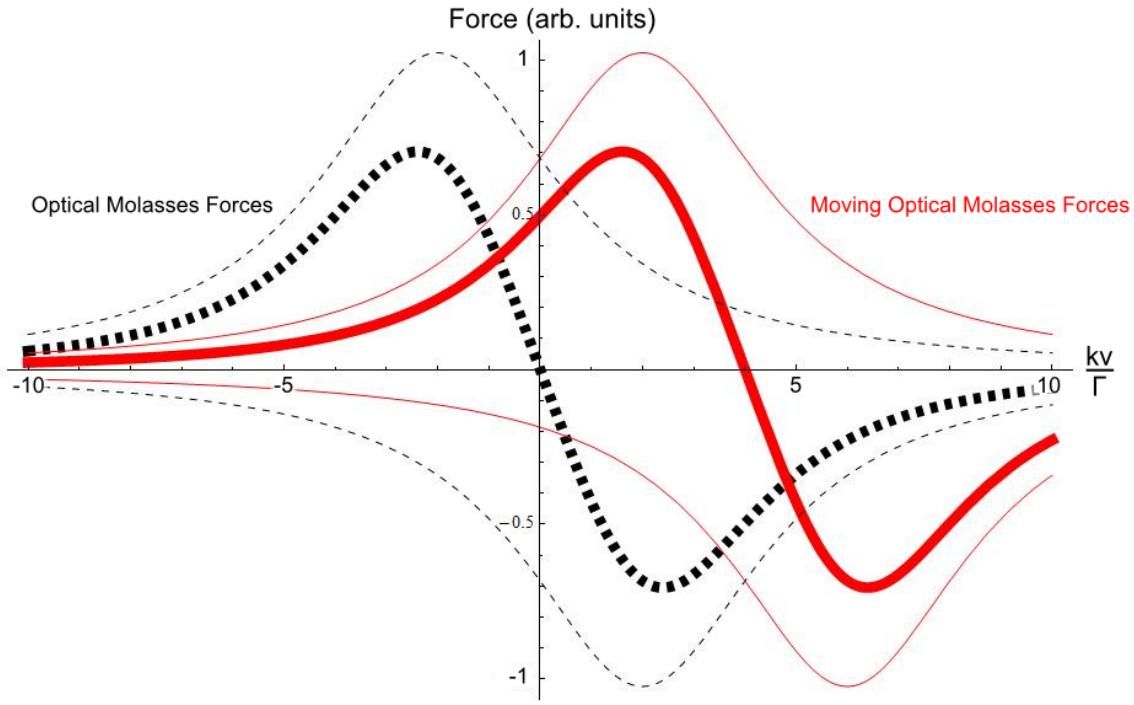

Figure 2.7: (Color) Optical molasses forces as a function of the scaled unitless velocity kv/Γ. The thin black dashed lines are the forces from the individual counter-propagating optical molasses beams with zero relative detuning. The thick black dashed line is the net force felt by the atom with zero relative detuning. The forces tend to balance at a velocity of $kv/\Gamma = 0$. The thin red solid lines are the forces from the individual counter-propagating optical molasses beams with non-zero relative detuning. The thick red solid line is the net force felt by the atom with non-zero relative detuning. The forces tend to balance at a velocity of $kv/\Gamma = 4$.

where we have replaced $\delta\omega = 2\pi\,\delta\nu$ and $\cos(\theta) = \cos(\pi/4) = 1/\sqrt{2}$. This is the upward velocity $\bar{v}$ shown in Figure 2.6, where the upper pair of beams in the x-z plane have their frequency shifted by $\omega - \delta\omega$ and the lower beams have their frequency shifted by $\omega + \delta\omega$. Extracting atoms from the MM MOT cloud can be implemented in two ways. In a pulsed extraction scheme, the MM MOT is loaded at $\delta\omega = 0$. Usually some form of sub-Doppler cooling is performed and then the relative detuning $\delta\omega$ is ramped over a few milliseconds to accelerate the cloud to $\bar{v}$. After the moving molasses the beams are shuttered and ball of atoms is sent upward in the dark [30, 38, 39]. In a continuous extraction scheme, the MM MOT is loaded from a separate source such as a 2D MOT. The loading of the MM MOT is done at a fixed non-zero relative detuning $\delta\omega \neq 0$, which allows a constant flux of atoms to be extracted [31, 40].

2.4 Optically trapping atoms

Optical dipole traps rely on the electric dipole interaction with far detuned light. The optical scattering and heating rate can be very low when the detuning is large, and the dipole force becomes approximately conservative. Under certain conditions, optical dipole traps are independent of the particular sub-level of the electronic ground state of the atoms. Thus, a richer set of dynamics can be exploited for experiments than in a magnetic trap, which are limited to $g_F\, m_F > 0$ ground states, as explained in Section 2.1. The dipole force can be both attractive and repulsive. Additionally, complicated three-dimensional geometries away from surfaces (e.g. an atom chip) and multi-well lattices in one-, two-, or three-dimensions can be generated [41].

2.4.1 Optical dipole potential

A light field is really just an electric field $\vec{E}(\vec{r},t)$ oscillating at frequency ω_l which can be written as

$$\vec{E}(\vec{r},t) = \frac{1}{2}\hat{e}E(\vec{r})exp(-i\omega_l t) + \text{c.c.}, \tag{2.17}$$

where $\hat{e}$ is the unit polarization, $E(\vec{r})$ is the electric field amplitude, and c.c. denotes the complex conjugate. This induces an atomic dipole moment $\vec{p}(\vec{r},t)$ that also oscillates at ω_l and whose amplitude $p(\vec{r})$ is proportional to the electric field amplitude $E(\vec{r})$ by

$$p(\vec{r}) = \alpha E(\vec{r}), \tag{2.18}$$

where α is the complex polarizability and is dependent on the driving laser frequency. The induced dipole potential arises from the dispersive interaction of $\vec{p}$ with the light field. Because the oscillating frequency ω_l of the light field is on time scales much, much faster than all other time scales, U_{dip} is given by the time average of the interaction potential between the driving field $\vec{E}$ and the induced dipole moment $\vec{p}$

$$U_{\text{dip}} = -\frac{1}{2} < \vec{p}\vec{E} > = -\frac{1}{2\epsilon_0 c}\Re(\alpha)I(\vec{r}), \tag{2.19}$$

where ϵ_0 is the permittivity of free space, $\Re(\alpha)$ denotes the real part of the complex polarizability, and $I = 2c\epsilon_0|E|^2$ is the light field intensity. The dipole force $\vec{F}_{\text{dip}}$ arises from a gradient in the potential written as

$$\vec{F}_{\text{dip}} = -\nabla U_{\text{dip}} = \frac{1}{2\epsilon_0 c}\Re(\alpha)\nabla I(\vec{r}), \tag{2.20}$$

The absorptive part of the complex polarizability gives rise to some photon scattering from the light field. The scattering rate $\Gamma_{sc}(\vec{r})$ is given by

$$\Gamma_{\text{sc}}(\vec{r}) = \frac{< \dot{\vec{p}}\vec{E} >}{\hbar\omega} = \frac{1}{\hbar\epsilon_0 c}\Im(\alpha)I(\vec{r}), \tag{2.21}$$

where $\Im(\alpha)$ denotes the imaginary part of the complex polarizability. Equation 2.21 is essentially the power absorbed and re-emitted by the atoms divided by the energy per photon.

Intuitively, the power absorbed by the atoms is proportional to $\Im(\alpha)$, which can be thought of as the out-of-phase component of the atom oscillation [24].

Using two key approximations allow Equation 2.19 to be written in a more useful form. First, the complex polarizability can be rewritten in terms of physical constants using the semiclassical approach, which is described in textbooks [42]. Second, for a laser detuned from atomic resonance, ω_0, where the detuning $|\Delta| \ll \omega_0$, the well known rotating-wave approximation simplifies the dipole potential [43], which can be written as

$$U_{\text{dip}}(\vec{r}) = \frac{3\pi c^2}{2\omega_0^3}\frac{\Gamma}{\Delta}I(\vec{r}) = U_0 I(\vec{r}), \tag{2.22}$$

and the scattering rate to

$$\Gamma_{\text{sc}}(\vec{r}) = \frac{3\pi c^2}{2\hbar\omega_0^3}\left(\frac{\Gamma}{\Delta}\right)^2 I(\vec{r}), \tag{2.23}$$

where Γ is the natural linewidth of the atomic transition. The scattering rate has a simple relationship to the dipole potential, which is given by

$$\hbar\Gamma_{\text{sc}} = \frac{\Gamma}{\Delta}U_{\text{dip}}. \tag{2.24}$$

One can use perturbative methods to calculate the light shifts or ac Stark shifts that a two-level atom sees, which in the ground state exactly corresponds to the dipole potential in Equation 2.22. The interesting result is that the ground state of the atoms is shifted in an equal and opposite way from the excited state. A spatially varying intensity $I(\vec{r})$, e.g., a Gaussian beam, will cause the atoms to feel a force towards (or away) from areas of high intensity for red detuned (blue detuned) light. A red detuned trap is shown in Figure 2.8. The left-hand side shows the unshifted and shifted energy-level diagram for the ground and first-excited state. The right-hand side shows the 1D radial trapping potential of a red detuned Gaussian beam where atoms (orange) would be attracted to the center of the beam.

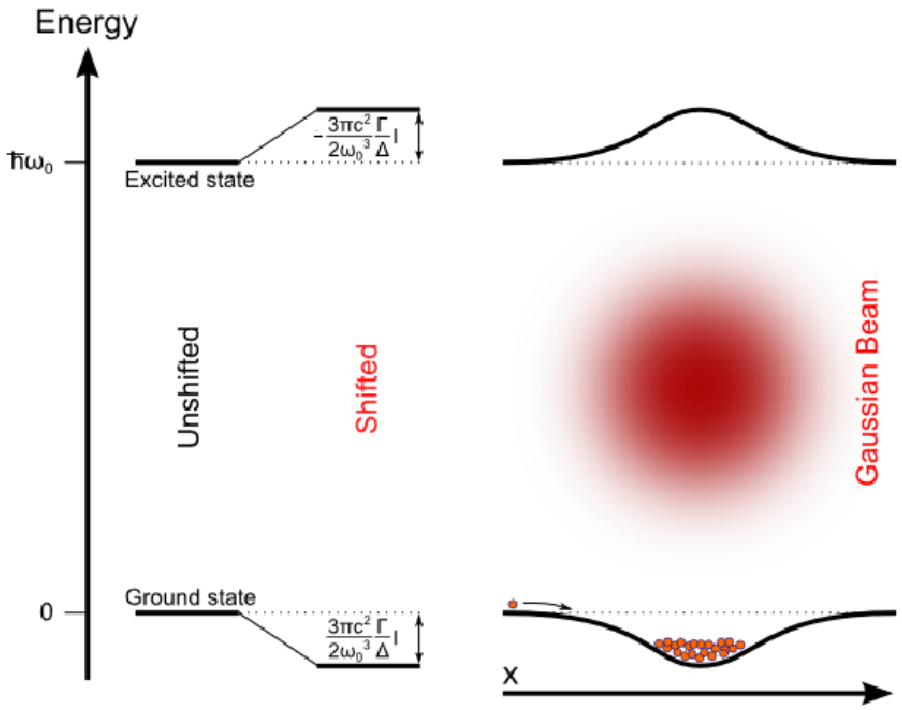

Figure 2.8: (Color) Dipole trapping potential and light shifts for a two-level atom for red detuned light. The left-hand side shows the symmetric shift away from the the resonant frequency $\hbar\omega_0$. The right-hand side shows the shift a spatially varying field would produce, and the trapping potential felt by the atoms.

2.4.2 Red detuned traps for alkali atoms

The main red detuned dipole trap of interest is created with a focused Gaussian beam that is far detuned. By far detuned, we mean that the laser detuning is much greater than the hyperfine splitting in the alkali atom (e.g. the splitting of the D_2 line of ^{87}Rb shown on the right-hand side in Figure 4.5) but is comparable to the fine structure splitting between the D_1 and D_2 lines. For example, in cesium the D_1 and D_2 lines have relative wavelengths of 894.6 nm and 852.3 nm, with a fine structure detuning of $\Delta_{\mathrm{FS}} = 10^2$ THz. A 1064 nm wavelength dipole laser has a detuning of $\Delta_{\mathrm{D_1}} = 3.4 \times 10^2$ THz and $\Delta_{\mathrm{D_2}} = 4.4 \times 10^2$ THz with respect to the D_1 and D_2 lines. In this regime, the dipole trapping laser interacts with both fine structure lines of the alkali atom, and Equation 2.22 is modified to

$$U_{\mathrm{dip}}(\vec{r}) = U_0 \left(\frac{2 + P g_F m_F}{\Delta_{\mathrm{D_2}}} + \frac{1 - P g_F m_F}{\Delta_{\mathrm{D_1}}} \right) I(\vec{r}), \tag{2.25}$$

where $P = 0, \pm 1$ characterizes the laser polarization as linear, $\sigma^{\pm}$ circular. Because we are only going to be dealing with linearly polarized dipole trapping light, we can redefine the detuning Δ with an effective detuning expressed as

$$\Delta = \frac{3}{\Delta_{\mathrm{D_1}}^{-1} + 2\Delta_{\mathrm{D_2}}^{-1}}. \tag{2.26}$$

A focused Gaussian beam creates an axisymmetric trap with a loose (tight) trap along (perpendicular to) the propagation direction of the beam. The trapping potential given in Equation 2.22 can be explicitly written by replacing $I(\vec{r})$ with the well-known Gaussian propagation function as

$$U_G(\rho, z) \;=\; U_0 \frac{2P}{\pi w(z)^2} \exp\left[-\frac{2\rho^2}{w(z)^2}, \right] \tag{2.27}$$

where $w(z) = w_0\sqrt{1 + (z/z_R)^2}$, w_0 is the beam waist at the focus, $z_R = \pi w_0^2/\lambda_l$, and λ_l is the laser wavelength. The trap frequencies as a function of beam waist and power can be found evaluating the second spatial derivative of the potential $U_G(\rho, z)$ at the center of the

beam focus ($z = \rho = 0$), and are given by

$$\Omega_z(w_0, P) = 2\sqrt{\frac{|U_0|P}{\pi m w_0^2 z_R^2}}, \tag{2.28}$$

$$\Omega_\rho(w_0, P) = 4\sqrt{\frac{|U_0|P}{\pi m w_0^4}}. \tag{2.29}$$

In order to create a dipole trap that is tight in both directions, a crossed dipole trap can be formed at the intersection of two orthogonal, focused Gaussian beams.

2.4.3 Blue detuned traps

A blue detuned trap is harder to make than a red detuned trap because one cannot simply focus a beam but instead must create a void of intensity surrounded by regions of high intensity. One way to achieve this is with a spiral phase plate (SPP). An SPP generates a "vortex" (or "doughnut") beam in its far field diffraction pattern, which is simply a Laguerre-Gaussian (LG) mode and a stable solution to Maxwell's equations in free space. An SPP is a dispersive device and spatially modulates the optical phase of the incident laser beam. A single order (or charge) SPP, whose phase profile is shown in Figure 2.9(a), delays the optical phase from 0 to 2π (blue to red) as a function of angle ϕ, with a discontinuity in the center. Higher charge SPPs modulate the phase in multiples of 2π and create higher order LG modes [44], given by

$$\begin{aligned} \mathrm{LG}_p^l(R, \phi, z) \quad &\propto \quad \frac{1}{\sqrt{1 + z^2/z_R^2}} \left(\frac{\sqrt{2}r}{w(z)}\right) L_p^l \left(\frac{2r^2}{w(z)^2}\right) \\ &\times \quad \exp\left(\frac{-ikr^2}{2R(z)}\right) \exp\left(\frac{-r^2}{w(z)^2}\right) \exp(-il\phi) \\ &\times \quad \exp\left[i(2p + l + 1)\tan^{-1}\left(\frac{z}{z_R}\right)\right], \end{aligned} \tag{2.30}$$

where $R(z) = z + z_R^2/z$ is the radius of curvature of the phase front. This simplifies greatly when considering only the first order, the TEM_{01} doughnut mode, which is given by

$$U(\vec{r}) = \frac{\hbar \Omega_0^2(z)}{4\Delta} \frac{\rho^2}{w(z)^2} \exp\left(-2\frac{\rho^2}{w(z)^2}\right), \tag{2.31}$$

where $\Omega_0(z)$ is the maximum Rabi frequency obtained at the radial position $\rho = w(z)/\sqrt{2}$ where the intensity is greatest [45].

The output of the RPC Photonics VPP-1c vortex phase plate is shown in Figure 2.9(b), in which the diffraction pattern was imaged into the far field via a Fourier transform lens. The zero intensity in the center can be understood intuitively. In a physical vortex (e.g., in a BEC), the velocity in the center is undefined because of the discontinuity, and therefore the density has to go to zero. Here, the vortex beam has an undefined phase in the center because of the discontinuity, so the intensity has to go to zero in the far field. Unlike a single focused

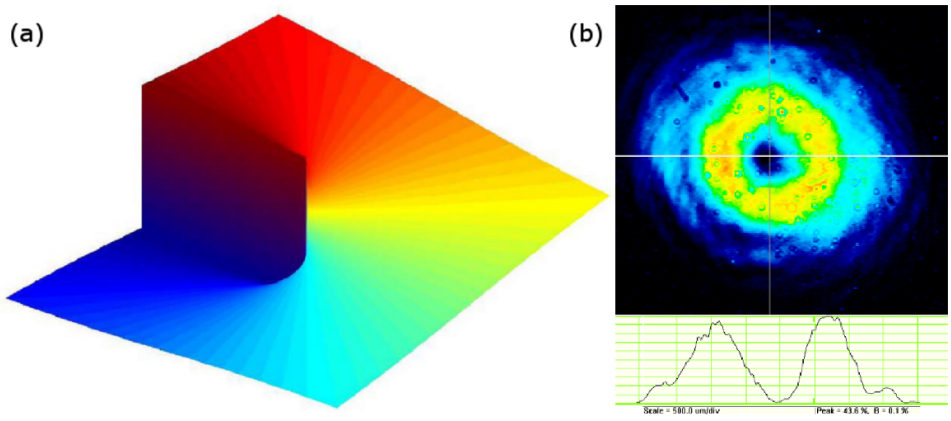

Figure 2.9: (Color) (a) A picture of the spiral phase plate phase profile. (b) Output of the spiral phase plate.

red detuned Gaussian beam which creates an axisymmetric trap, a single vortex beam can create a waveguide but cannot create a three dimensional trap [45]. Crossed vortex beams can create a 3D potential for trapping atoms as in [46], or creating a high density MOT, as in [47]. Interference of Gaussian or Laguerre-Gaussian modes can also be used to create a three dimensional trap [48, 49]

2.4.4 Moving-standing wave trap

A 1D optical lattice can be formed from the interference pattern of two counter-propagating Gaussian beams. This can be easily accomplished by retroreflecting a beam back

on itself. However, it gets a little more interesting if two independent counter-propagating beams are used, as shown in Figure 2.10.

Deriving the beams from the same laser ensures that the beams are both phase and frequency stable with respect to one another if the beam path lengths are equal to within the coherence length of the laser. The coherence length L is given by

$$L = \frac{c}{n\Delta f}, \tag{2.32}$$

where Δf is the laser linewidth. A typical diode laser linewidth of 1 MHz has a coherence length of 300 m. A fiber laser with a linewidth of 50 kHz has a coherence length of around 6 km. A fiber laser with a spectral linewidth of 2 nm and a center wavelength of 1064 nm has a frequency linewidth of $\Delta f = 0.53$ THz and a coherence length of 5.7 mm.

Each beam is sent through a double-pass AOM in the cat's eye configuration [50], which shifts the frequencies of both beams in the same direction. The double-pass geometry allows for frequency changes around the central AOM frequency without change in beam pointing. The AOMs are driven with two independent RF drivers (here with an Agilent 33250A and HP 8642A) that are frequency locked via the RF drivers' internal 10 MHz clocks. This ensures that the standing wave created is spatially stable. Jumps in phase cause jumps in the intensity pattern, which lead to heating and atom loss. If the two AOMs are at the same frequency, a standing wave is produced similar to the retroreflecting case. If, however, a difference in frequency is applied to the legs, a "moving-standing wave" potential U_{msw} is generated given by

$$U_{\mathrm{msw}}(\rho, z, t) = U_G(\rho, z) \cos^2\left(\frac{\Delta\omega}{2}t - kz\right). \tag{2.33}$$

The velocity of the standing wave is given by

$$v_{\mathrm{msw}} = \frac{\lambda_l \Delta\omega}{4\pi}. \tag{2.34}$$

The trap frequency in the radial direction is the same as in Equation 2.29. The trap frequency along the axial direction changes because now it is not dependent on the Rayleigh range of

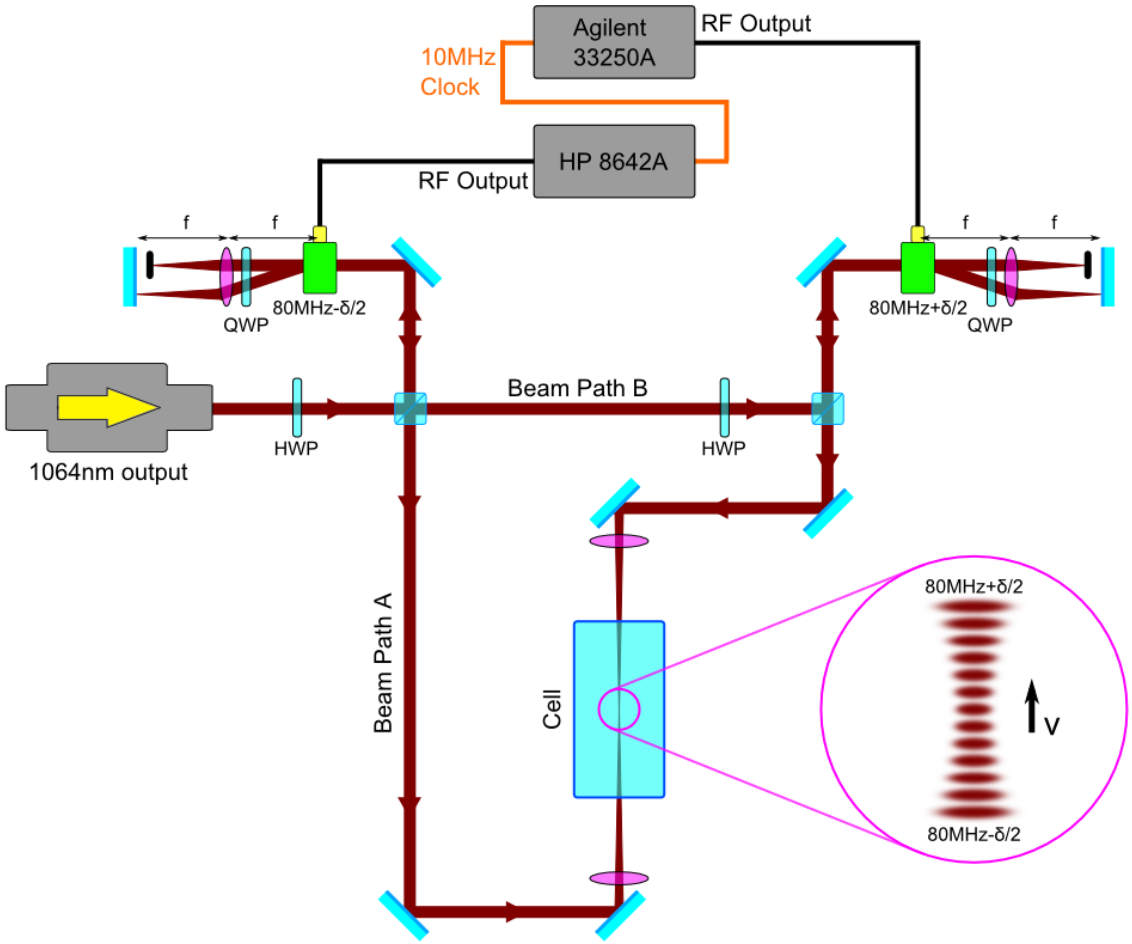

Figure 2.10: (Color) Moving-standing wave optical setup diagram. A 1064 nm laser is split into two beam paths labelled A and B. Each beam is sent through a double-pass AOM in the cat's eye configuration to minimize beam walk-off during frequency shifting [50]. The beams are then sent into the cell in a counter-propagating configuration and focused with parallel polarizations. Path lengths are matched as well as possible to ensure high-fringe visibility from the laser's coherence length.

the beam z_R, but on the interference pattern formed, which is given by

$$\Omega_z = 4\sqrt{\frac{2\pi U_0 P}{m w_0^2 \lambda_l^2}}. \tag{2.35}$$

A moving-standing wave has been demonstrated, with remarkable control over atoms, via deterministic movement of single atoms over a finite distance using a red detuned optical lattice [51]. We are planning on utilizing this technique in the quantum computing project described in Chapter 5 to enable deterministic single atom reloading of the qubit array. It is also possible that this technique will be appliccable to atom transport as well, but its limitations are described in Section 5.4.1.2.

2.4.5 Dipole trap heating

An important factor in optical dipole traps is the heating rate of the atom cloud. Unlike magnetic potentials, as shown in Equation 2.23, optical potentials are not completely conservative. Occasionally an atom in the cloud will scatter a photon and increase its temperature by T_{rec} which is given by

$$T_{\text{rec}} = \frac{\hbar^2 k^2}{m k_B}, \tag{2.36}$$

where k is the momentum and m is the mass of the atom. The power absorbed by the atoms $\dot{\bar{E}}_{\text{heat}}$ then, is just the thermal energy gained per photon times the rate photons are scattered, which is given by

$$\dot{\bar{E}}_{\text{heat}} = k_B T_{\text{rec}} \bar{\Gamma}_{\text{sc}}. \tag{2.37}$$

Because the intensity is spatially varying, the average scattering $\bar{\Gamma}_{\text{sc}}$ depends on how much the cloud interacts with the light, i.e., the relationship between the extent of the atom cloud with the size and shape of the potential. We can define the ratio of the potential energy to the kinetic energy as $\bar{E}_{\text{pot}}/\bar{E}_{\text{kin}} \equiv \kappa$ and write the mean total energy of the cloud in a 3D trap in thermal equilibrium as

$$\bar{E} = \frac{3}{2}(1+\kappa) k_B T. \tag{2.38}$$

The variable κ is a function of the trapping potential geometry and describes how much the atoms "see" the trapping light. In general, a three dimensional trap $U(x, y, z)$ is separable and can be written

$$U(x, y, z) = U_0 + a_1 x^{n_1} + a_2 y^{n_2} + a_3 z^{n_3}, \tag{2.39}$$

where U_0 is the offset at the trap center. According to the virial theorem then, κ is given by

$$\kappa = \frac{2}{3}\left(\frac{1}{n_1} + \frac{1}{n_2} + \frac{1}{n_3}\right). \tag{2.40}$$

Rearranging Equation 2.37, the mean heating rate $\dot{T}_{\text{heat}}$ is given by

$$\dot{T}_{\text{heat}} = \frac{2/3}{1+\kappa} T_{\text{rec}} \bar{\Gamma}_{\text{sc}}. \tag{2.41}$$

The mean scattering rate $\bar{\Gamma}_{\text{sc}}$ can also be calculated. The dipole potential in Equation 2.39 can be rewritten as

$$\bar{U}_{\text{dip}} = U_0 + \bar{E}_{\text{pot}} = U_0 + \kappa \bar{E}_{\text{kin}} = U_0 + \frac{3\kappa}{2} T. \tag{2.42}$$

The relationship between the mean dipole potential and the scattering rate can be found from Equations 2.22 and 2.23. It can be expressed as

$$\frac{\Gamma}{\Delta} \bar{U}_{\text{dip}} = \hbar \bar{\Gamma}_{\text{sc}}, \tag{2.43}$$

which yields

$$\bar{\Gamma}_{\text{sc}} = \frac{\Gamma}{\hbar \Delta}\left(U_0 + \frac{3\kappa}{2} k_B T\right). \tag{2.44}$$

Two situations arise when considering dipole trapping. A red detuned dipole trap where $\Delta < 0$ traps atoms in regions of high intensity. A blue detuned dipole trap where $\Delta > 0$ repels atoms from regions of high intensity and atoms can be trapped in regions of low intensity. A diagram of these two situations is shown in Figure 2.11. The red detuned trap is generated with a focused Gaussian beam with a waist of $100\,\mu$m and 1 W of power.

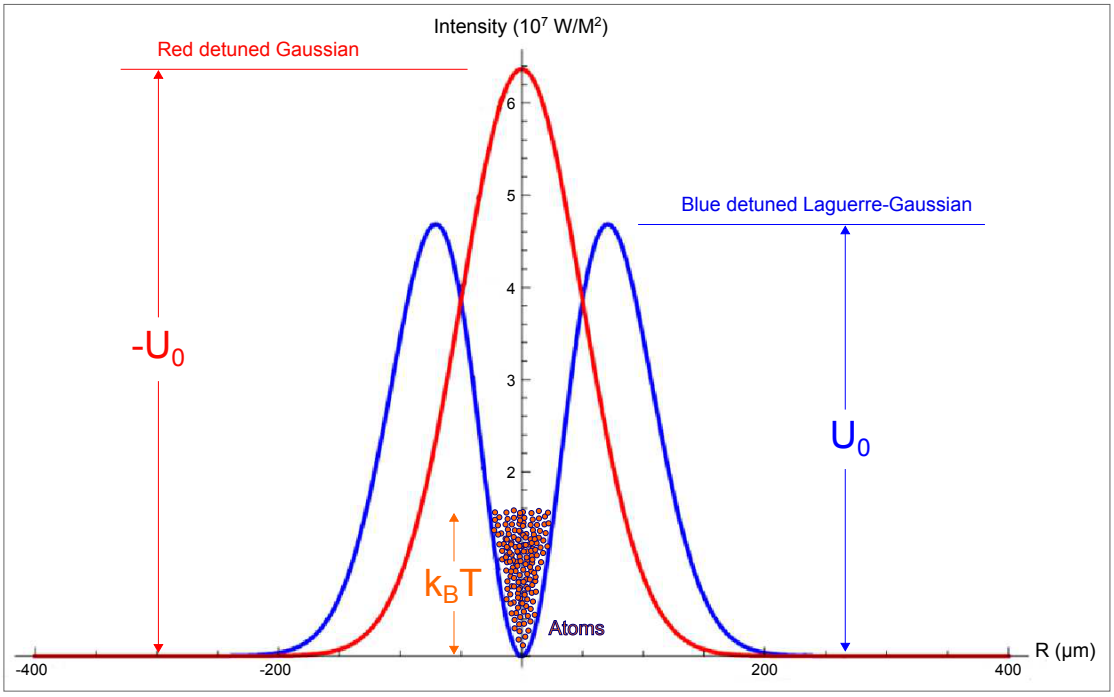

Figure 2.11: (Color) A plot of the potential of a red and blue detuned trap. The red detuned trap is a focused Gaussian beam with a waist of 100 μm. The blue detuned trap is a focused Laguerre-Gaussian TEM_{01} mode with a 100 μm waist and the same power as in the red detuned trap. In both cases atoms would be trapped in the center.

Similarly, the blue detuned trap is generated with a focused Laguerre-Gaussian TEM_{01} mode with a 100 μm waist and the same power as in the red trap. The plot shows the intensity I of the beam versus radial position ρ. In both cases atoms would be trapped in the center. In the limit of a very deep trap where $|U_0| \gg k_B T$, combining Equations 2.41 and 2.44, gives the heating rates for red and blue detuned traps as

$$\dot{T}_{\text{red}} = \frac{2/3}{1+\kappa} T_{\text{rec}} \frac{\Gamma}{\hbar|\Delta|} |U_0|, \tag{2.45}$$

$$\dot{T}_{\text{blue}} = \frac{\kappa}{1+\kappa} T_{\text{rec}} \frac{\Gamma}{\hbar\Delta} k_B T. \tag{2.46}$$

The ratio of the red and blue detuned heating rates is then given by

$$\frac{\dot{T}_{\text{red}}}{\dot{T}_{\text{blue}}} = \frac{3\kappa}{2} \frac{k_B T}{|U_0|}. \tag{2.47}$$

As shown in Equation 2.47, a blue detuned trap offers substantial advantages to reduce the heating effects of the trapping light in two situations: when the trap wall height is much greater than the temperature of the atoms, $|U_0| \gg k_B T$, or when the potential is box-like with hard, steep walls, $\kappa \ll 1$.

Chapter 3

UHV cells for atomic physics

All cold atom experiments are done under high vacuum. In BEC experiments especially, the need for the highest quality vacuum ($< 10^{-9}$ torr) is paramount. In many cases the lifetime of trapped atoms is proportional to the background pressure. Better vacuum equates to a longer scientifically useful atomic sample. The theory behind miniaturizing vacuum systems and the challenges that arise are discussed in detail in [52]. The motivation for miniaturization was presented in Section 1.1. This section will go in depth on the ultra-high vacuum (UHV) cells utilized and developed in the work in this dissertation. How the cells are actually used will be discussed in Chapters 4 and 5.

3.1 Double chambered cell

The main vacuum chamber utilized by the group over the last several years is the double chambered cell shown in Figure 3.1. This cell is discussed in detail, and is well characterized in previous Ph.D. dissertations [28, 52, 53]. However, because an appreciable amount of work in this dissertation was performed in this cell, and because it forms the basis of understanding for the more exotic cells described in this chapter, several of the features of the double chambered cell will be discussed explicitly.

The double chambered cell is processed on a larger pumpout station, which uses roughing, turbo, titanium sublimation, and large ion pumps to take the system from ambient down to $<10^{-11}$ torr. After the cell is processed, it is pinched off via the copper nipple. During

pinch off, a hydraulic jaws compress the nipple along a line normal to its axis. Because the inner walls of the nipple are extremely clean copper, as the walls are pressed together, they form a hermetically sealing cold-weld, which seals both ends, and breaks off at the joint. After pinch off, the double chambered cell is completely self-contained, and UHV is maintained with only a 2 l/s ion pump and two non-evaporable getters (NEGs, ST-172): one in the $2D^+$ MOT chamber and one in the 3D MOT chamber. The role of the NEGs is largely to pump hydrogen, which is the main contaminant to our vacuum system. Unfortunately, we must intentionally introduce hydrogen into the double chambered cell. In addition to the wanted alkali metal vapor, hydrogen is the other major output gas of the alkali metal dispenser. The ion pump serves to pump everything else in the system.

Current can be passed through the 3D NEG via a two-pin ConFlat feedthrough, which also serves as its *in vacuo* mount. Current is passed into the $2D^+$ MOT chamber via silicon feedthroughs at the bottom of the chamber, which are connected to the 2D NEG and the alkali metal dispenser. The silicon feedthrough design maintains 1 cm of optical access through the bottom face of the $2D^+$ MOT chamber, with a stack-up height of only a few millimeters. Current is run through the alkali metal dispenser to maintain an equilibrium pressure in the range of 10^{-7} torr under normal operation. A 1 mm thick machined silicon square with a 750 μm pinhole maintains a differential pumping of two orders of magnitude between the $2D^+$ MOT chamber and the rest of the system. The silicon square is anodically bonded to both the $2D^+$ MOT chamber and a glass-to-metal (G2M) transition.

A rectangular cell is glass blown onto a G2M and forms the 3D MOT chamber, which is maintained in the range of 10^{-9} torr and forms our science chamber. Both the $2D^+$ MOT and 3D MOT chambers are 2 cm inner diameter (ID) square cross section Pyrex fluorometry cells. At the top of the 3D MOT chamber is an anodically bonded atom chip, which, unlike most atom chip experiments [54–57], is used to maintain UHV in the system. This has the significant advantage of allowing BECs to be made physically very close to ambient conditions. This enables various applications, such as high-NA imaging and projection of

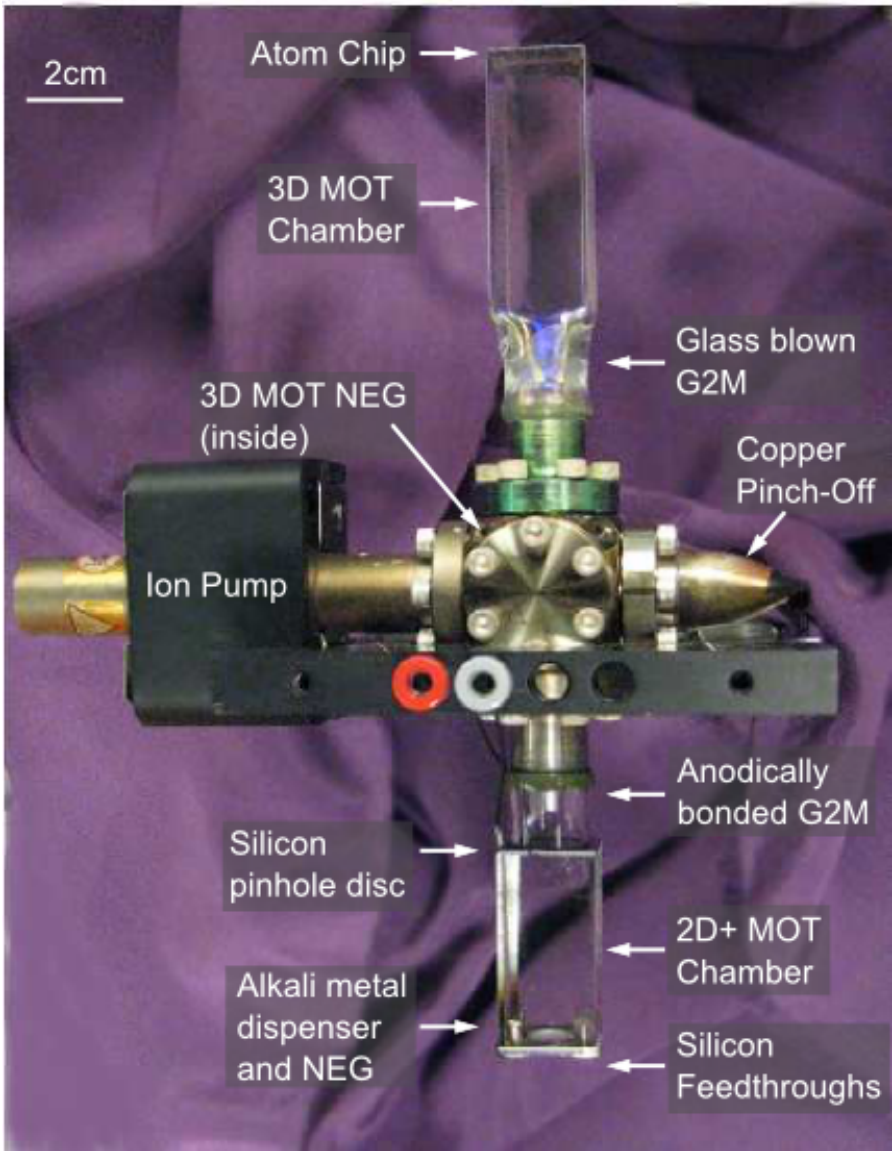

Figure 3.1: (Color) A photo of the standard double chamber cell for BEC production. The distance from the bottom of the $2D^+$ MOT chamber to the top of the atom chip is 27 cm.

light fields for manipulating and probing BECs [58], or using BECs to probe ambient electric and magnetic fields [4].

3.1.1 Source feedthroughs

There has been a significant amount of development work to create continuous high-current and high-power UHV compatible and anodic bonding compatible feedthroughs. Three generations of source feedthroughs are shown in Figure 3.2 with the current design, developed under this dissertation work, on the right.

The original source tube design, shown in Figure 3.2(a), used tungsten pins glass blown onto a Pyrex cylinder. Tungsten wets to the Pyrex and creates a UHV compatible electrical feedthrough. Nickel rod was welded onto the UHV side of the tungsten, to which the dispenser and NEG were spot welded. The ambient side of the tungsten has nickel braid welded on for flexibility and ease of handling when connecting to the source tube. The Pyrex cylinder and components create the "source tube," which was glass blown onto the side of a 1 cm square cross section $2D^+$ MOT cell. This assembly was anodically bonded to a silicon pinhole disc similar to that described in Section 3.1.

There were a few main issues with this design. The source tube added a large protrusion onto the $2D^+$ MOT cell, which caused it to be delicate. This was necessary to keep the dispenser and NEG far enough away from the glass blowing torch, thus the source tube resisted miniaturization. The glass blowing onto the $2D^+$ MOT cell obscured some of the optical access, and caused warping of the cell face. Additionally, because of the geometry (e.g., conductance) and added volume, the source tube needed a heating element to efficiently transfer the alkali vapor into the $2D^+$ MOT chamber.

The next generation of source tube, which was partially developed under this dissertation, shown in Figure 3.2(b), used the same tungsten pins as in the previous source tube design, but eliminated the bulk. A cylindrical Pyrex tube was glass blown onto a smaller diameter G2M, which created a cylindrical recess between the outer diameter (OD) of the

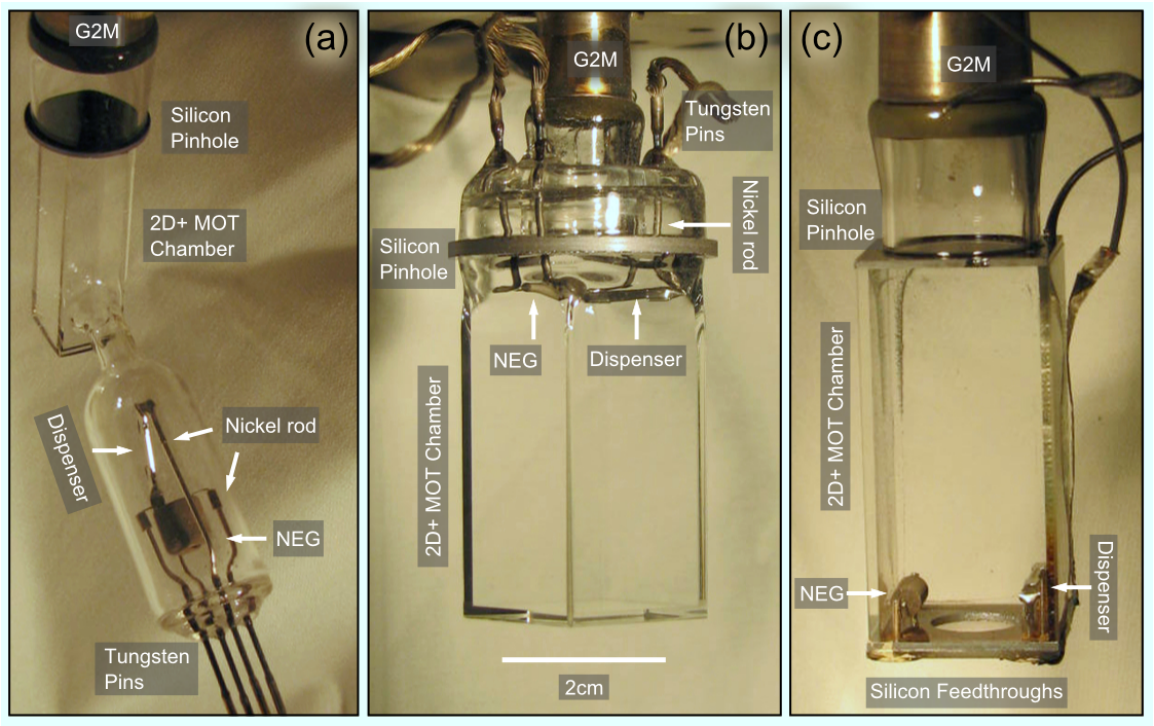

Figure 3.2: (Color) Three generations of source feedthroughs. (a) The feedthroughs are tungsten pins glass blown onto a Pyrex cylinder and welded to nickel leads on the UHV side. The dispenser and getter are spot welded to the nickel leads. The source tube is then glass blown onto the side of a 1 cm $2D^+$ MOT cell. (b) The feedthroughs are the same design as in (a) but come in from the G2M side. The silicon pinhole has a surrounding silicon doughnut, and the feedthroughs pass into the $2D^+$ MOT chamber through the recess between them. (c) The current generation of source tubes uses metalized, highly conductive silicon as the electrical feedthrough. UHV connection is made through nickel pins held in place with spring washers. Optical access is maintained through a 1 cm window in the bottom of the cell.

G2M and the ID of the Pyrex tube. The tungsten pins were glass blown through the joint where these two meet near the G2M. This recess allowed the nickel leads to be bent below the surface of where the pinhole is to be located, which allowed the Pyrex to be polished. After polishing, the nickel leads were bent to extend above the surface, the silicon pinhole and doughnut were anodically bonded to the Pyrex, and the dispenser and NEG were spot welded to the nickel. The 1 cm $2D^+$ MOT chamber was replaced with a 2 cm cell that had a small section near the top glass blown into a circle so that it matched the OD of the silicon doughnut. This increased surface area and relieved stress for anodic bonding. After polishing, circularly symmetric surfaces generally have a superior flatness profile compared to a square cross section, e.g., a cell end. The major flaw in this design was in the processing. The tungsten feedthroughs, while robust to the temperature cycling required for glass blowing, anodic bonding, and bakeout, were weak to the physical stresses of bending the nickel leads. The failure mechanism of these source tubes was generally due to cracking and micro-fissures in the Pyrex. Additionally, we wanted to move away from glass blowing and towards anodic bonding because of its precision and maintenance of optical quality surfaces.

The current generation of source tubes was fully developed under this dissertation and is shown in Figure 3.2(c), with the individual parts arrayed in Figure 3.3. It replaced the tungsten pins glass blown into Pyrex with highly conductive ($<0.01\,\Omega$-cm) silicon pads. Four 6 mm diameter conductive silicon pads were anodically bonded to a 23 mm $\times$ 23 mm, 1 mm thick machined Pyrex square in a single step, shown in Figure 3.3(a). The silicon discs were centered on 1/8 in. cored holes in the Pyrex, spaced 17 mm apart, shown in Figure 3.3(b). The silicon was then chemically etched *in situ* with hydrofluoric (HF) acid or Piranha solution to remove the naturally occurring SiO_2 layer. SiO_2 is an insulating layer that prevented the silicon from acting as an effective conductor. The Pyrex was masked off with either photoresist or metal shielding for metallization; 20 nm of titanium and 200 nm of silver were deposited on both the ambient and vacuum side of the silicon via a thermal evaporator. The titanium acted as an adhering layer between the silver and the silicon. Silver

was chosen because of the conductivity of its oxide layer [59], which allowed it to be processed at elevated temperatures without special consideration, such as an inert atmosphere.

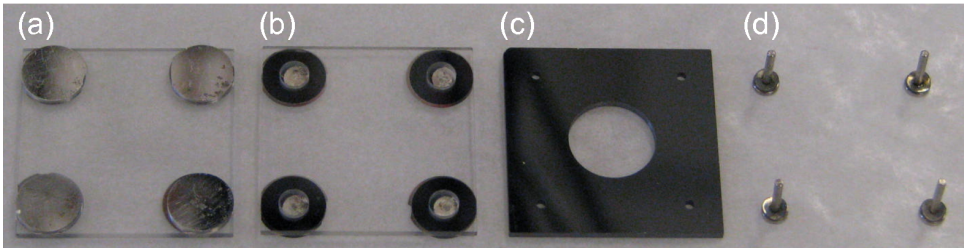

Figure 3.3: (Color) Source tube feedthrough parts. (a) Ambient side of an anodically bonded Pyrex square with metalized conductive silicon discs. (b) Vacuum side of the Pyrex square showing the 1/8 in. cores in the Pyrex square and metalized silicon. (c) The high resistivity silicon square with four 1/16 in. holes for the pins and a 1 cm centered hole for the $2D^+$ MOT push beam. (d) Nickel pins with Inconel spring washers for making electrical connections on the UHV side of the feedthrough.

Electrical connection to the silicon pads on the UHV side was made with nickel nail-head style pins, shown in Figure 3.3(d). The pin was approximately 1.2 mm in diameter and 5 mm to 7 mm long, with an 1/8 in. undersized head diameter that is 500 μm thick. A high resistivity (>2000 Ω-cm), 1 mm thick, 23 mm $\times$ 23 mm machined silicon square with four, 1/16 in. holes, 17 mm apart, held the pins in place. Inconel alloy spring washers were placed in between the head of the pin and the silicon such that the overall stacked height of the pin head and spring is >1 mm, i.e., the thickness of the Pyrex square. The Pyrex square with the metalized conductive silicon pads was aligned to the high-resistivity silicon with the pins and spring washers *in situ*. Mating the two pieces with $\geq$5 lb of force compressed the Inconel springs, providing robust electrical contact to the silicon pads on the UHV side. The two pieces were then anodically bonded, which provided a permanent hermetic seal to the feedthroughs. A 1 cm centered core in the high resistivity silicon provided optical access for the $2D^+$ MOT push beam. Next, the dispenser and NEG were spot welded to the nickel pins. This source feedthrough was then bonded to the end of the $2D^+$ MOT chamber in a nitrogen atmosphere to limit activation of the NEG. The end result was a robust, high

temperature, UHV compatible, high current ($\geq$10 A) feedthrough that required no glass blowing and preserved optical quality and access of the cell.

3.1.2 Silicon part recovery

Source tubes, and some of the UHV cells discussed below, could have several anodic bonds. Each additional anodic bond added complexity, introduced stresses, and increased chance for failure. A bond failure at the very end of a complicated structure's construction could be costly in both time and effort. Thus, a technique for recovering parts from failed and cracked anodic bonds was developed. Shown in Figure 3.4 is the G2M side of a silicon pinhole square with a $2D^+$ MOT cell and source feedthrough anodically bonded to the side not shown (Figure 3.2(c)).

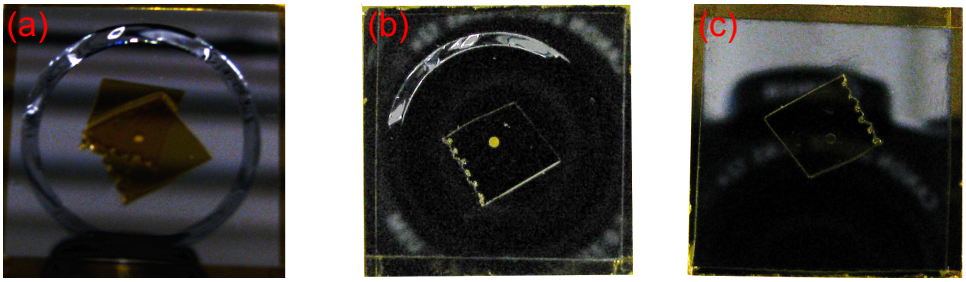

Figure 3.4: (Color) Sequence of silicon pinhole recovery via HF removal of glass. The pinhole, $2D^+$ MOT chamber optical faces, and $2D^+$ MOT chamber anodic bond with the silicon have been protectively masked with Kapton tape. (a) Silicon after anodic bonding with a clearly visible ring of Pyrex and no HF etching. (b) Silicon with some HF etching showing the removal of the lower portion of the ring. (c) Silicon after successful HF etching.

This piece was taken from a $2D^+$ MOT chamber that had sheared off of its G2M transition, leaving the ring of Pyrex shown in Figure 3.4(a). The pinhole, $2D^+$ MOT chamber optical faces, and $2D^+$ MOT chamber anodic bond with the silicon were protectively masked with Kapton tape. Even in a well-ventilated hood, the HF fumes were enough to damage the optical quality of the $2D^+$ MOT chamber Pyrex surfaces. High concentration (48%) HF was placed on the exposed silicon and allowed to sit from 5 min to 30 min before being removed and refreshed with new HF. The HF slowly etched away the Pyrex but left the silicon of

the pinhole square unaffected. Because of the different thicknesses of Pyrex left over from the broken bond, the lower part of the ring was dissolved first (Figure 3.4(b)). The upper portion remaining began as several 10s of microns. A pristine surface was achieved, shown in Figure 3.4(c), and successfully anodically bonded to another G2M.

3.1.3 Atom chips

The magnetic trapping and manipulation of BECs was done entirely on an atom chip, such as the one shown in Figure 3.1. The atom chips currently used in our group are based on 420 μm thick conductive silicon substrates that were manufactured with coplanar glass regions. The coplanar glass acts as an electrical insulator, which allows UHV compatible through-chip electrical vias. It can also act as optical access for through-chip imaging or on-chip optics [58, 60]. An excellent review on the more general topic of atom chips can be found in [61]. Because all of the science in the double chambered cell was done on the atom chip, it serves as a platform analogous to a vacuum tube with the same plug-and-play capabilities. There have been several atom chip designs [52, 53], of which the three relating to work in this dissertation are discussed below.

3.1.3.1 Standard atom chip

The vacuum side of the "standard" atom chip is shown in Figure 3.5. Figure 3.5(a) shows an older version of the standard atom chip, which was used in Chapter 4. Sixty UHV compatible electrical vias, shown as bright rectangles, surround the atom chip wire region. There is a single Z-wire trace that runs from the bottom left to the top right of the chip, indicated by the yellow arrows and the current I_0. Thirteen dimple-wires run perpendicular to the main leg of the Z-wire at a separation of 1 mm. The center of the chip is at the junction between the main Z-wire and the dimple wire, indicated by the white arrows and the current I_d. Each via can handle up to 2.5 A steady state, which is the limiting factor in the current run by each wire. The main Z-wire generally needs to run up to 5 A, thus

multiple vias connect to the main Z-wire on each end.

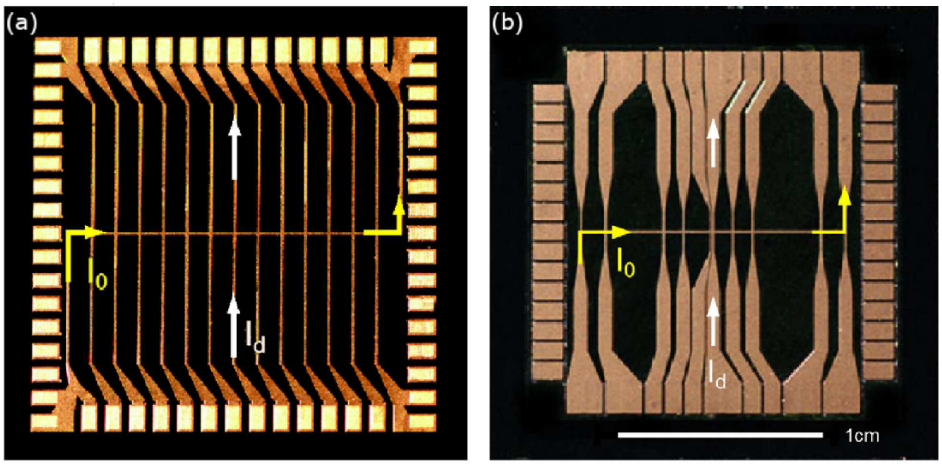

Figure 3.5: (Color) (a) A photo of the vacuum side of the "standard" atom chip used for BEC production. The main Z-wire is indicated by yellow arrows. Multiple redundant dimple wires run vertically. The dimple wire that runs through the center of the chip is indicated by white arrows. (b) An updated version of the standard BEC chip using conductive silicon vias and coplanar glass.

Figure 3.5(b) shows the current generation of the standard atom chip. The main Z-wire remains, but with added flexibility. The main Z-wire can now be run from the bottom left to the top right, and its mirror image. Additionally, the number of outer dimple-wires is reduced so that multiple vias can connect to a single dimple-wire. This allows for higher currents, which are necessary for an H-wire trap. A dimple wire now runs within 100 μm of the center dimple wire to allow for finer scale manipulation of the atoms, if required. The tapers in the wires were modeled to minimize resistance of the traces while maintaining the trapping fields of straight, thin wires [52].

3.1.3.2 Channel cell atom chip

An atom chip designed for use with the channel cell geometry, in order to maximize the space in the BEC chamber (Figure 3.9), is shown in Figure 3.6. A window is etched into the chip, with edges running parallel to the main wire traces 100 μm away. A Pyrex window is

anodically bonded to the ambient side of the chip to seal vacuum. In the double chambered cell, imaging was done after ballistic expansion (described in Section 4.8), which was possible because the chip is bonded perpendicularly to the optical interface of the 3D MOT chamber. In the channel cell shown in Figure 3.9, the region below the chip is obscured by the silicon manifold. With the proper orientation of the channel cell atom chip with respect to gravity, the chip window allows for ballistic expansion imaging, as shown in Figure 4.21. This chip window is the precursor to the transistor atom chip in [60].

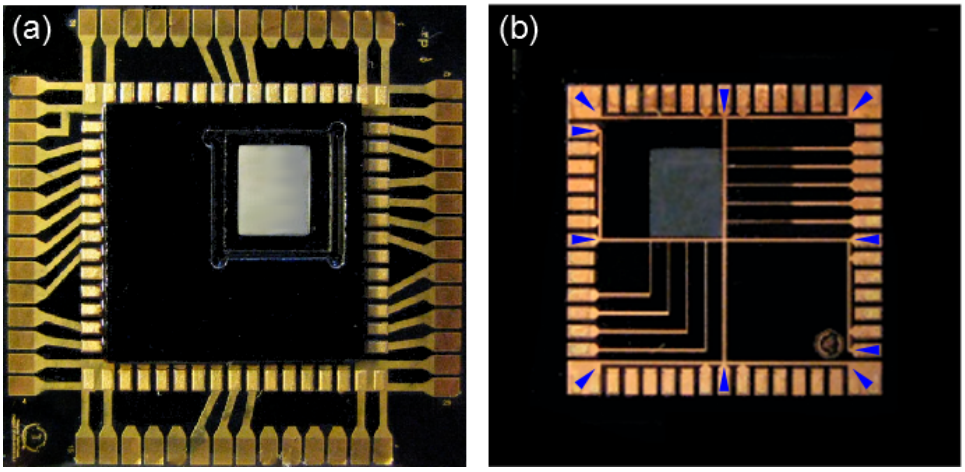

Figure 3.6: (Color) A photo of the atom chip used in the V2 channel cell.(a) The ambient side of the atom chip. A window is etched into the chip inside the electrical connection pads and feedthrough via metallization. A Pyrex window is anodically bonded to this side to seal vacuum. (b) The main wires, indicated with arrows at the vias, form a cross in the center of the chip. They were designed to use redundant vias and allow for a dimple trap in either orientation. The thinner wires can be used to form a T-trap in several locations.

The main wires are shown in Figure 3.6(b), with the feedthrough vias indicated by blue arrows. The vias were chosen such that a Z-wire trap and a dimple-wire trap could be generated in several orientations. The tapered thinner wires intersect the main wires away from the center of the chip. They can be used to form a T-trap [53], or T-traps, at the junction(s) of the thinner wire and the main wire. They add redundancy as well as flexibility in imaging anywhere along the edge of the window.

3.1.3.3 Direct evaporation atom chip

An atom chip designed for direct evaporation of an atomic cloud, discussed in depth in Section 4.11.2, is shown in Figure 3.7. The main Z-wire of this chip is the same as that in the standard atom chip. However, the dimple-wire is thinner, reduced from 100 μm thick in the standard atom chip to 20 μm thick. Additionally, there is a Z-wire on each side of the main Z-wire, which runs parallel to it, that is 20 μm thick. The main Z-wire is able to handle the high currents necessary to generate deep chip magnetic traps. This facilitates efficient transfer of atoms from an external coil magnetic trap to a chip magnetic trap, and confines the atoms during the initial stages of RF evaporation. The dimple-wire and parallel Z-wires do not dissipate as much power, and thus are able to be much thinner.

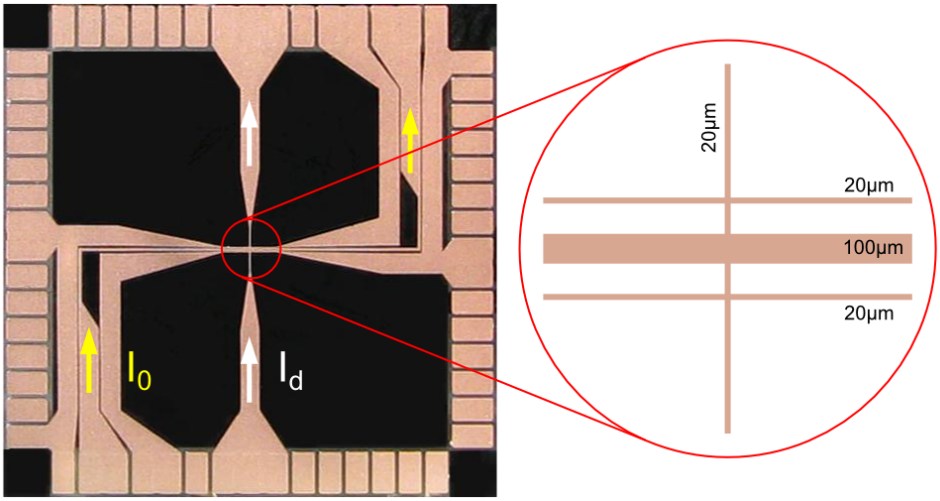

Figure 3.7: (Color) A photo of the atom chip designed for direct evaporation. There are three main traces, one with a 100 μm width and two that run parallel to it with a 20 μm width. There is one dimple trace that runs down the middle of the chip, which tapers to a 20 μm width at the center of the chip where it crosses the main wires.

Typically, during RF evaporation, the main Z-wire current was held constant as the RF field was swept. This was done to maintain the trapping frequencies and rethermalization rate of the magnetic potential. However, once the atoms are cold, a deep trap is unnecessary. In an initial chip trap, the atoms were a few hundred microkelvin (Section 4.10.2.2), but near

the BEC critical temperature, they were typically only a few microkelvin (Section 4.10.3.1). A trap for atoms near the BEC critical temperature requires much lower current. Once the atoms are cooled, they can be transferred adiabatically to a trap centered over the thin Z-wire. This will transfer the center of the atoms over a wire junction that is 20 μm on a side, as opposed to the standard 100 μm junction, providing tighter fields at shorter distances above the chip. Additional theory behind the design and implementation of this chip is discussed in Section 4.11.2.

3.2 Quadruple chambered cell

An extension of the double chambered cell is the quadruple chambered cell shown in Figure 3.8. The main body of the cell (everything up to the 3D MOT chamber) is identical to the double chambered cell. Here, the atom chip was replaced with a tertiary chamber bonded to the top of the 3D MOT chamber with a stress relieving machined silicon piece. A high optical quality window caps the right side of the third chamber. The third chamber has optical access from all sides, including the side bonded to the 3D MOT chamber (through the silicon pinhole). The goal of this cell was to act as a proxy for the cell described in Section 3.5, in which the third chamber takes the place of the Hex cell. The object of the third chamber is to create an atom reservoir in a crossed dipole beam trap, described in Section 2.4.2. The horizontal chamber was attached to the third chamber with an anodically bonded silicon-Pyrex-silicon stress relieving piece. This chamber will facilitate future horizontal atom transport experiments. A high optical quality window caps the left side of the horizontal chamber.

3.3 Flat channel cells

By moving away from ConFlat components, the size of the cell can be reduced dramatically, and the complexity is no longer constrained to right angles separated by several centimeters. This could have important applications in, for example, an atom laser,

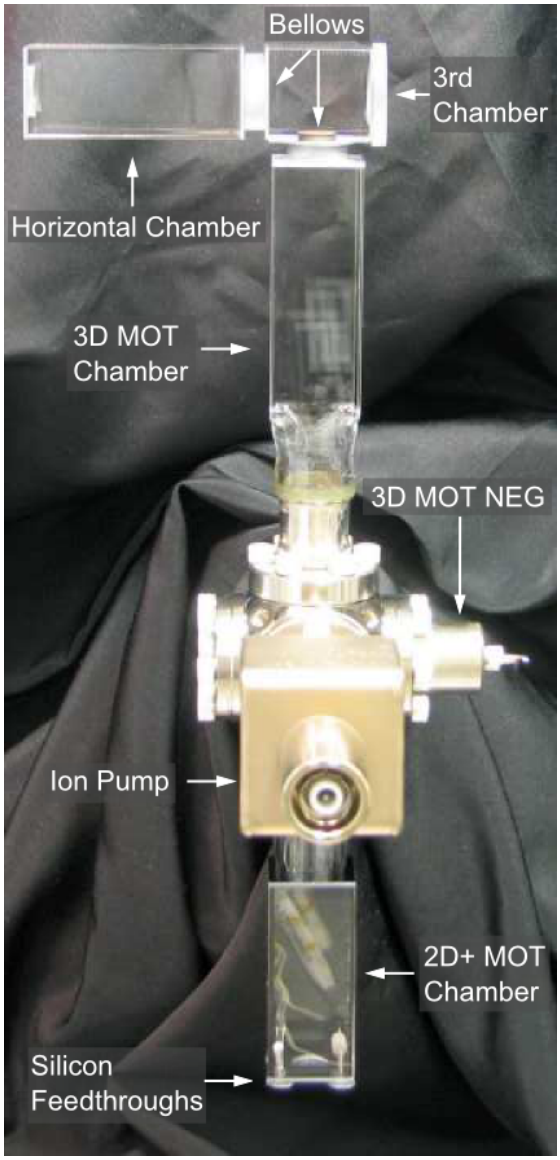

Figure 3.8: (Color) Quadruple chambered cell. The lower portion of the cell, up to the 3D MOT chamber, is the same as the double cell, shown in Figure 3.1. A tertiary chamber takes the place of the atom chip, bonded to the 3D MOT chamber with a silicon strain relieving piece. A fourth chamber is attached to the third chamber with a silicon-Pyrex-silicon strain relieving piece.

by providing *in vacuo* optically isolating geometries and a continuous source of pre-cooled atoms [17, 18, 62, 63]. Some examples of how this can be achieved are discussed in [52].

The V2 channel cell is shown in Figure 3.9. The concept of the channel cell started with a monolithic block of silicon where channels were machined partially through the depth and on alternating sides. Anodically sealing both sides with Pyrex allowed an interconnection of multiple channels and chambers, described in detail in [52].

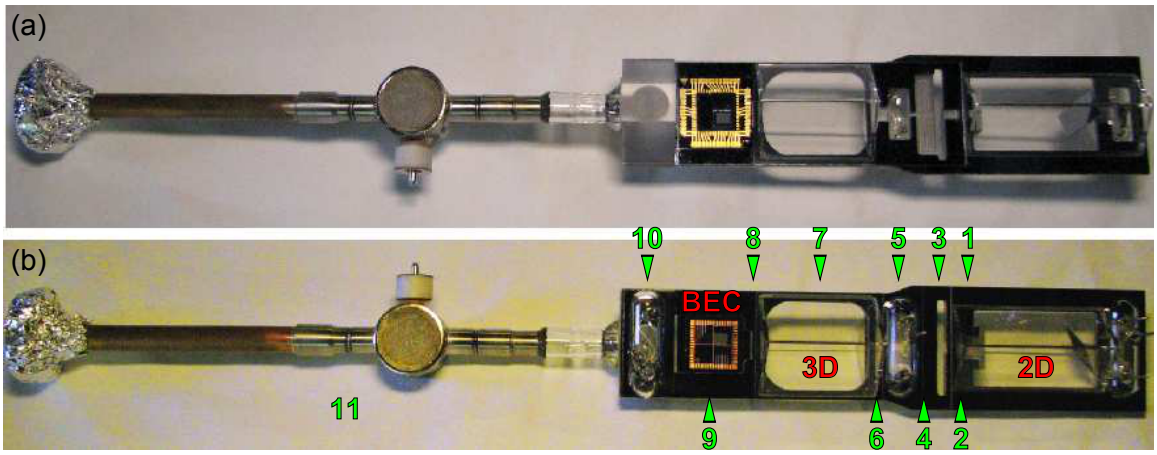

Figure 3.9: (Color) (a) A view of the bottom of the channel cell showing the nichrome wire and the vacuum and temperature isolation channels. (b) A view of the top of the channel cell showing the tungsten pin presses in a polished glass dome and the gold wrapped nichrome wire for making an evaporation getter. The 2D MOT, 3D MOT and BEC chambers are labeled in red, and the conductance channel paths are labeled in green.

There are several major changes from the V1 channel cell in [52] to the V2 channel cell described here. Rather than just having a Pyrex-silicon-Pyrex layer structure, additional layers of Pyrex and silicon were added to create five- and seven-layer structures, shown in Figure 3.10. This increased optical access, conductance, and vacuum properties by allowing structures such as in-line feedthroughs (5-layers) and rectangular chambers (7-layers). The rectangular chambers allowed increased optical access and volume over the flat chambers in [52], which should increase atomic cooling and trapping efficiency and fluxes [64, 65], achieving better vacuum properties from reduced dispenser power.

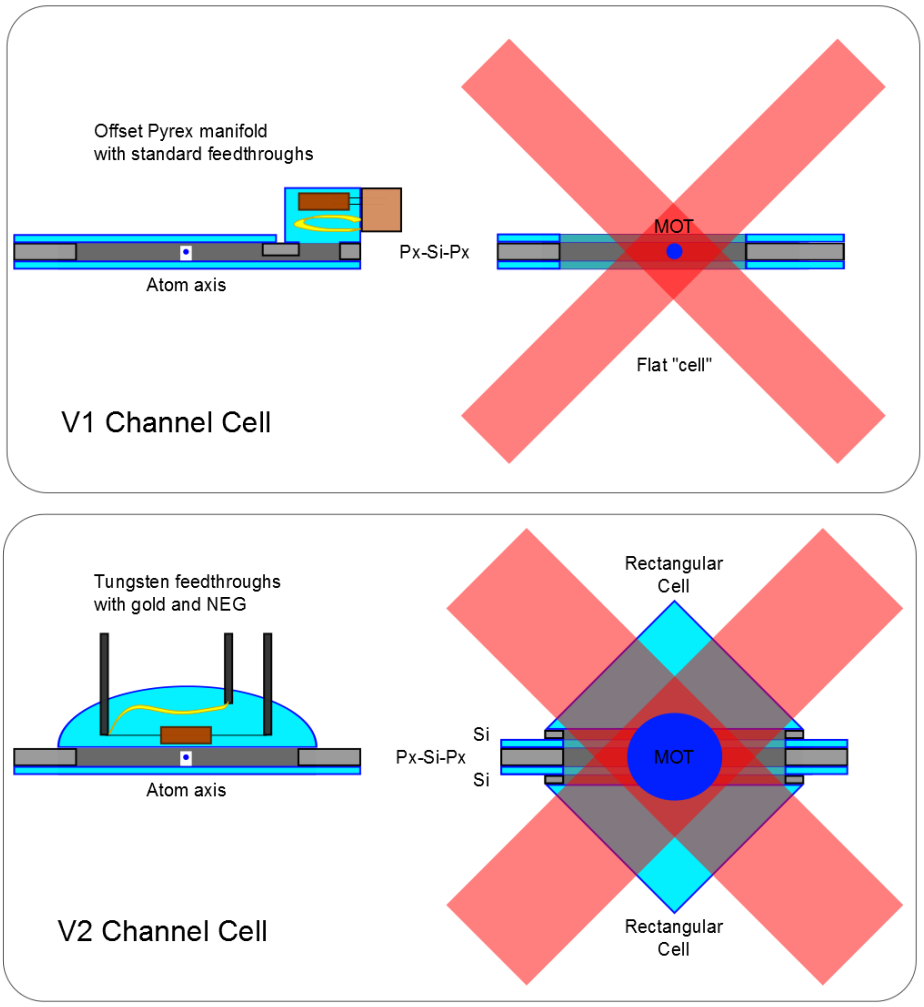

Figure 3.10: (Color) Cross sectional view of the V2 channel cell compared to the V1 channel cell. The tungsten pin presses increase the volume of the cell so that the gold evaporators and NEGs can be in-line with the cold atom axis, increasing its pumping speed. The rectangular chambers increase the trapping volume and optical access, increasing atom flux and therefore cell efficiency.

3.3.1 *In vacuo* optics

Incorporating optics inside small vacuum systems via anodic bonding was utilized by the group for the first time in the V2 channel cell. The *in vacuo* $2D^+$ MOT push beam optics are shown in Figure 3.11. A square silicon mirror was bonded to a polished Pyrex support at a compound angle, which allows the push beam to enter the cell normal to its face and travel on axis with the $2D^+$ MOT and channel cell. The $2D^+$ MOT conductance limiting pinhole, from Section 3.1, was also an anodically bonded silicon square with a rectangular Pyrex support, which was bonded to the silicon channel cell body.

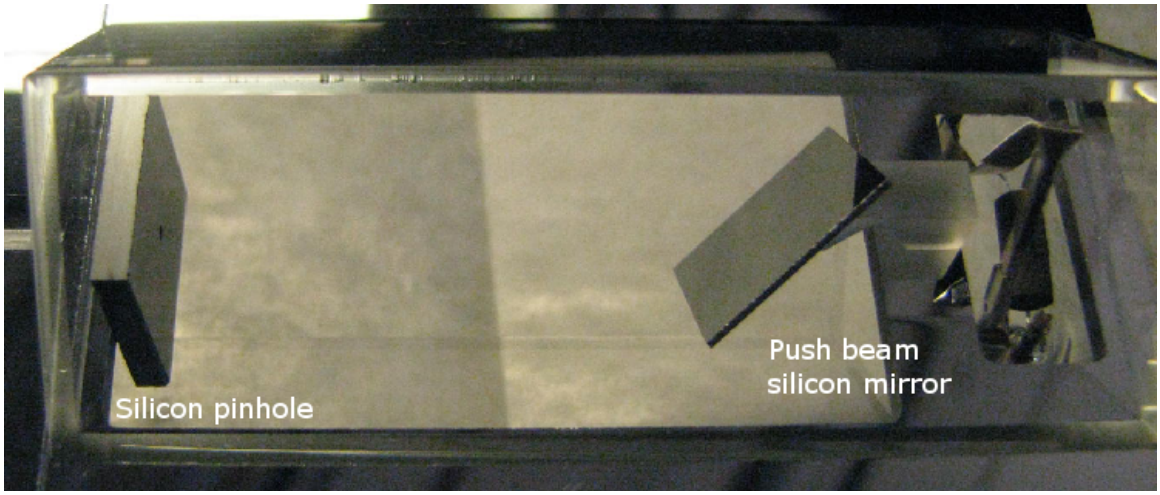

Figure 3.11: (Color) A photo of *in vacuo* anodically bonded $2D^+$ MOT optics. On the right is the input mirror. On the left is the retroreflecting mirror with pinhole. Both mirrors are bare polished silicon.

Further improvements could be made to these *in vacuo* optics. Mirror metallization or dielectric coating could increase the silicon reflectivity from its approximately 35% at 780 nm. However, equal powers in the push and retroreflected beam are not necessarily ideal [36]. Strain relieving geometries and post-cutting polishing could increase flatness from a few wavelengths to sub-wavelength, which would reduce wavefront distortion.

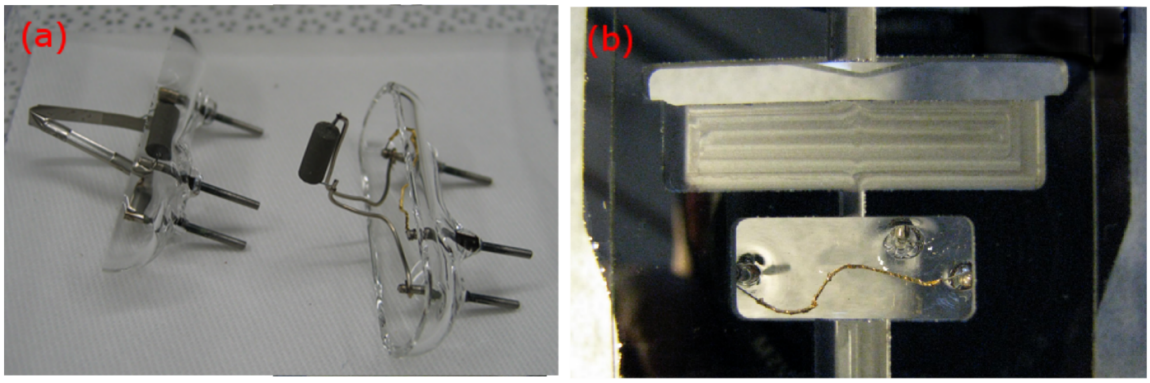

Figure 3.12: (Color) (a) A view of the tungsten pin presses in polished glass domes. On the left is the source feedthough, with a Rubidium dispenser and NEG. On the right is the gold wrapped nichrome wire for making an evaporation getter and an NEG, which is bent to be out of line of sight. (b) The opposite view of (a) showing the nichrome wire and the vacuum and temperature isolation channels.

3.3.2 Pin press feedthoughs, gold evaporation getters, and channels

Miniaturized Pyrex electrical feedthroughs that are compatible with anodic bonding were developed, and are shown in Figure 3.12(a). Tungsten pins were glass blown into a half-cylindrical dome shape, which was then polished for anodic bonding. Bonding these to a silicon frame allowed bonding to the Pyrex-silicon-Pyrex manifold. This was a significant size reduction from the feedthroughs in the V1 channel cell, and the ConFlat feedthroughs in Section 3.1. Additionally, this geometry allowed the feedthroughs to be in-line with the atomic flux. Incorporating gold evaporation getters and NEGs in-line with the atomic flux maximized their pumping speed. The pin presses could be further improved by incorporating the silicon feedthrough technology (Figure 3.3(c)) and machined glass to remove the glass blowing and tungsten pins.

The gold evaporation getters, shown in Figure 3.12(a) and (b), were developed to help pump background alkali gas that is introduced to the system, e.g., Rubidium or Cesium. Ion pumps are poor pumps of alkali metals. Gold, however, is easy to clean (i.e., make UHV compatible), and is known to make an alloy with Rubidium [66], which in certain cases can be detrimental to cold atom experiments [28], but here is used to improve the vacuum quality. The gold evaporator getter can be periodically activated to coat the line-of-sight walls with gold, which will pump the alkali metal vapor until its sorption capacity is reached.

Shown in Figure 3.12(b) is a channel that was cut fully through the silicon manifold, capped on both ends by Pyrex, and spans most of the width of the manifold. This limits the thermal conductance of the manifold, and takes advantage of the formed temperature gradients in two ways: the pressure in the volume of a vacuum system depends on temperature, and the alkali metal vapor pressure is strongly dependent on temperature. By heating the $2D^+$ MOT chamber, the pressure (and thus efficiency) of the vapor loaded $2D^+$ MOT is increased. By cooling the 3D MOT and BEC chamber, the trap lifetimes are increased. By strongly cooling the region in between the 2D chamber and the 3D chamber, the alkali gas

that contacts the walls, i.e., thermal background atoms that exit through the pinhole but are not cooled and directional from the $2D^+$ MOT, can condense and become trapped on the walls with a very low vapor pressure.

3.3.3 Channel cell vacuum properties

The channel cell has a significantly more complicated geometry than the double chambered cell of Section 3.1, and thus deserves a more in-depth calculation of its vacuum properties. There are three chambers in which the pressure is important: the 2D MOT, 3D MOT and BEC chip chambers. The 2D MOT chamber is separated from the 3D MOT chamber by a small aperture and a series of rectangular channels that limit the conductance. The 3D MOT chamber is separated from the BEC chip chamber by a rectangular aperture. The pumping station is separated from the BEC chip chamber by a long tube, ion pump, and Pyrex manifold.

Matrix analysis was used to calculate the pressure in the three chambers [67]. The conductances for individual aperture geometries can be found in [68]. All the conductances are in series, indicated by the labelled numbers in Figure 3.9(b), with the 2D MOT chamber having the lowest conductance (farthest from the pump), and the BEC chamber having the highest. The individual apertures and conductances are listed in Table 3.1, with the overall conductances to the pumpout station listed at the bottom.

The gas throughput Q in a system is given by

$$Q = (P_1 - P_2)\, C, \tag{3.1}$$

where C is the conductance, P_1 and P_2 are pressures at two different points in the system, and Q has units of torr·liters/sec. Here, Q is the throughput of gas out of the system as pumped by the turbo-pump, C is the conductance from the point of interest in the channel cell to the ion gauge (which is assumed to be close enough to the turbo-pump that the conductance between the two is very large), P_1 is the pressure at the point of interest in the

#	**Aperture**	**Dimensions (mm)**	**C (l/s)**
1	Cylnd. 2D Pinhole	$0.375\,\phi \times 2$	0.031
2	Rect. Channel 1	$4 \times 1.5 \times 10$	0.175
3	Rect. Channel 2	$30 \times 1.5 \times 10.5$	1.64
4	Rect. Channel 3	$2 \times 1.5 \times 2$	0.344
5	Pin Press Channel	$4 \times 1.5 \times 10$	12.57
6	Rect. Channel 4	$6 \times 1.5 \times 8$	0.361
7	3D MOT Chamber	$20 \times 20 \times 37$	28.9
8	Rect. Channel 5	$10 \times 2 \times 7$	1.27
9	BEC Chamber	$20 \times 2 \times 38$	0.512
10	Cylnd. Manifold	$8\,\phi \times 6$	15.75
11	Cylnd. Pinch Off	$4.13\,\phi \times 220$	0.269
	BEC to Station	Apertures 10-11	0.264
	3D Chamber to Station	Apertures 8-11	0.153
	2D Chamber to Station	Apertures 1-11	0.022

Table 3.1: Conductance calculations of the V2 channel cell as shown in Figure 3.9.

channel cell, and P_2 is the pressure at the ion gauge (thus at the turbo-pump inlet). Solving for P_1 gives

$$\begin{aligned} P_1 &= \frac{Q}{C} + P_2, \\ P_1 &= P_2 \left(\frac{S_P}{C} + 1 \right), \end{aligned} \tag{3.2}$$

where $S_P = Q/P_2$ is the pumping speed. The specified pumping speed of the Varian V-70 turbo pump gives the pumping rates for standard gasses at pressures $<10^{-4}$ torr as: H_2 - 45 liters/sec, He - 60 liters/sec, and N_2 - 70 liters/sec. Hydrogen is the most persistent gas in our systems. Estimating a $Q = 50$ liters/sec and an inlet pressure of $P_{\text{inlet}} = 4.3 \times 10^{-8}$ torr, then the calculated pressure in the three chambers of the channel cell are given by

$$\begin{aligned} P_{\text{2D}} &= 4.0 \times 10^{-5} \text{ torr}, \\ P_{\text{3D}} &= 1.1 \times 10^{-5} \text{ torr}, \\ P_{\text{BEC}} &= 9.5 \times 10^{-6} \text{ torr}. \end{aligned}$$

As a comparison, applying the same numbers and assumptions, the pressure for the double chambered cell of Section 3.1 can be estimated. The conductance from the pumping station to the 2D chamber and to the BEC chamber is 0.077 liters/sec and 2.8 liters/sec respectively, which gives pressures of

$$\begin{aligned} P_{\text{2D}} &= 2.8 \times 10^{-5} \text{ torr}, \\ P_{\text{BEC}} &= 8.1 \times 10^{-7} \text{ torr}. \end{aligned}$$

With the V2 design, the critical pressure, which is at the atom chip, is over an order of magnitude worse than the double chambered cell. This is a concern because BEC lifetime from single body loss is directly proportional to background pressure. As a design consideration it must be addressed, for instance, by utilizing a different form factor, as in Section 3.5.

3.4 Anodically bonded ion pump cell

The 0.4 l/s ion pump shown in Figure 3.9 is the largest single component of the channel cell, which makes it an appropriate target for miniaturization. Its steel exterior places limits on how it can be incorporated into a channel cell type geometry, and decreases its conductance. An anodically bonded ion pump was developed under this dissertation and is shown in Figure 3.13. An exploded view of the ion pump is shown in Figure 3.14. The body of the ion pump is a machined Pyrex block. The anode is a titanium cylinder with a welded-on rod. The rod was attached *in vacuo* to the Pyrex body with a nut and spring. Electrical connection was made with a steel spring to a metalized, conductive silicon piece, shown at the bottom of Figure 3.13, which served as the anode feedthrough. The top and bottom of the ion pump body were capped by metalized, conductive silicon, which served as the cathode feedthrough. The conductive silicon electrodes are similar to the conductive silicon source tube in Section 3.1.1. Anodically bonded to each cathode was a Pyrex ring with a partial slot cut out of the bonding side, forming a lip. A titanium plate, which was given a slight radius of curvature so that it has a spring constant, was slid under the Pyrex lip. The spring force of the titanium plate against the Pyrex ring maintained electrical connectivity with the cathode feedthrough. This assembly was then bonded to the UHV cell manifold. A detailed discussion of the physics behind ion pumps can be found in [69] and [70].

The UHV cell made to test the anodically bonded ion pump cell is shown in Figure 3.13. On the right is the $2D^+$ MOT chamber with a source feedthrough similar to that in Figure 3.2(c). The $2D^+$ MOT chamber was bonded to a silicon pinhole square and to the machined Pyrex manifold. The manifold was polished on four sides and has a cross machined through the interior. The ion pump was bonded to the manifold with a silicon washer, of identical ID, perpendicular to the $2D^+$ MOT chamber. Opposite the ion pump was bonded a 0.75 in. OD G2M transition. The G2M was cut and polished with 3 in. of Pyrex left after the actual transition. Half-way between the transition and the polished end, the OD was

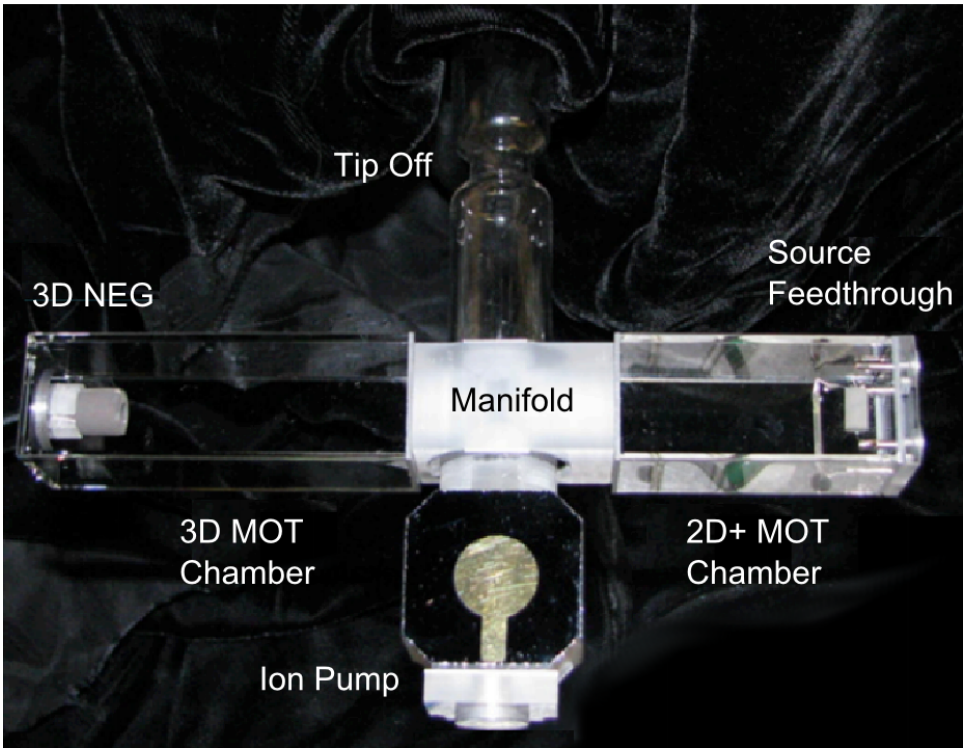

Figure 3.13: (Color) A photo of the fully silicon and glass anodically bonded double MOT ion pump test cell.

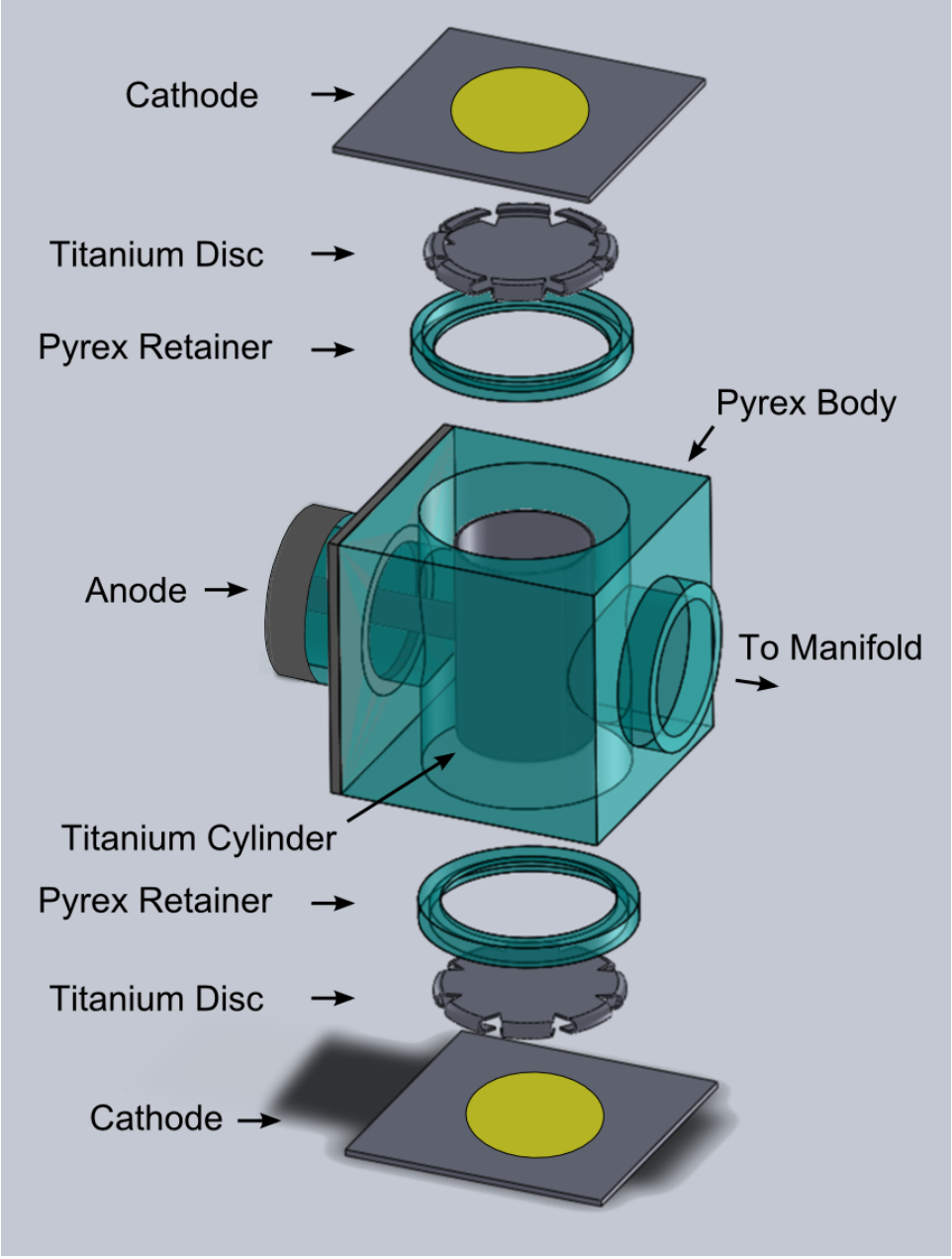

Figure 3.14: (Color) An exploded view of the anodically bonded ion pump. The machined Pyrex body is capped on the top and bottom by metallized, conductive silicon, which forms the cathode. A machined Pyrex ring is anodically bonded to the cathode to retain a titanium disc, which is electrically connected to the cathode. The anode is a titanium cylinder and rod that is attached *in vacuo* to the Pyrex body with a nut and spring. Electrical connection is made with a steel spring to a metalized, conductive silicon piece

necked down to 0.5 in. OD. The cell was to be removed from the pumping station, once processing was complete, via a glass-tip-off, in which a torch is used to soften the glass and the pressure difference between the vacuum and ambient sides of the G2M would pull the tube inward and fuse together to form a UHV seal. The necked down portion of the G2M to facilitate this process by minimizing the draw down and heat required.

Opposite the $2D^+$ MOT, on the left side of Figure 3.13, is the 3D MOT chamber. The 3D NEG, which is the same NEG as in the double chamber cell from Section 3.1, was mounted to a quartz pedestal. The quartz pedestal provided thermal isolation for the 3D NEG, and has a softening temperature around 1600 °C, which is well above the activation temperatures of the 3D NEG. The quartz pedestal was mounted to the end of the 3D chamber opposite the manifold with a silicon retaining ring. The 3D NEG was mounted in this way to avoid adding extra electrical feedthroughs to the cell. Because the 3D NEG was not connected to electrical feedthroughs, the 3D NEG was processed using RF inductive heating, discussed in Section 3.4.1.

The functional geometry of the ion pump test cell mimics that of the double chamber cell. In order to measure the absolute pressure of the cell, and the efficacy of the ion pump, the lifetime of the 3D MOT provides the most sensitive test. The measurement of the lifetime of a 3D MOT versus absolute pressure was done in a double chambered cell, which is shown in Figure 3.15.

In order to modulate the pressure, the dispenser current was varied between 3.75 A and 6 A. The pressure was monitored with the ion pump controller (Varian MicroVac), which is sensitive down to 4×10^{-10} torr. The Varian MicroVac operates at a voltage of 3.3 kV. The $1/e$ lifetime of the 3D MOT was measured by blocking the $2D^+$ MOT and watching the fluorescence signal decay on a photodetector. Plotted in Figure 3.15 is the inverse of the $1/e$ lifetime versus pressure. The inverse of the 3D MOT lifetime was plotted to show the linear relationship, i.e., $1/t_d \propto P/P_0 + P_m$, where P_0 and P_m scale the pressure and set the minimum pressure, respectively. The linear fit obtained for the pressure and MOT lifetime

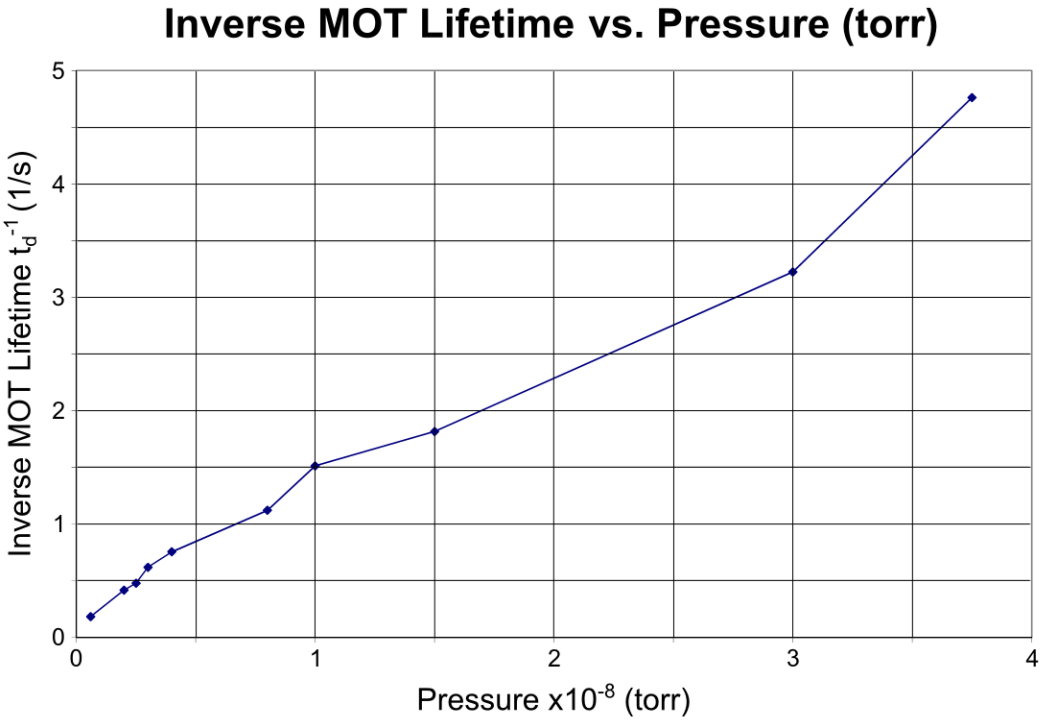

Figure 3.15: (Color) The inverse of 3D MOT lifetime versus absolute pressure in a double chamber cell. The x-axis is the pressure measured with the ion pump current. The y-axis is the inverse of the MOT lifetime. A linear relationship between the pressure and the inverse MOT lifetime is evident.

from Figure 3.15 was

$$P = \frac{P_0(1 - P_m t_d)}{t_d}, \tag{3.3}$$

$$t_d = \frac{P_0}{P + P_m P_0}, \tag{3.4}$$

where $P_0 = 8.8 \times 10^{-9}$, $P_m = 2.14 \times 10^{-1}$, P has units of torr, and t_d has units of seconds.

A double MOT was made in the ion pump test cell using the laser system described in Section 4.2. Figure 3.16 shows the MOT lifetime and atom number as a function of dispenser current. MOT atom number increased with dispenser current, as expected, because the $2D^+$ MOT flux is proportional to the alkali metal background pressure in the source chamber. The MOT lifetime, however, stayed flat, around 140 ms to 160 ms, as dispenser current increased. The alkali metal dispenser, when operating, emits both the alkali metal vapor and background gasses, mainly hydrogen. When the ion pump and NEGs are operating normally, the background pressure is proportional to the dispenser current, thus the lifetime of the MOT is inversely proportional to the dispenser current, with typical MOT lifetimes on the order of 15 s [52].

We believe that the lifetime in Figure 3.16 was limited by a background of hydrogen gas. During bonding of the cell, it is likely that the NEGs were partially activated and exposed to atmosphere, which would greatly reduce both their sorption rate and capacity. Ion pumps are, in general, bad at pumping hydrogen. If the background pressure was dominated by hydrogen, then that would be the limiting factor in the lifetime. Running a larger dispenser current would increase the partial pressure of cesium, which increases the MOT number. This would also increase the hydrogen gas background, but in general pumping efficiency goes up with pressure, so an equilibrium was reached. From this, the estimated background pressure in the ion pump test cell, independent of dispenser current, was around 6×10^{-8} torr, two orders of magnitude higher than in the double chamber cell.

Keeping a constant dispenser current of 3.5 A, the MOT atom number was measured as a function of time after turning off the high voltage to the ion pump, shown in Figure 3.17.

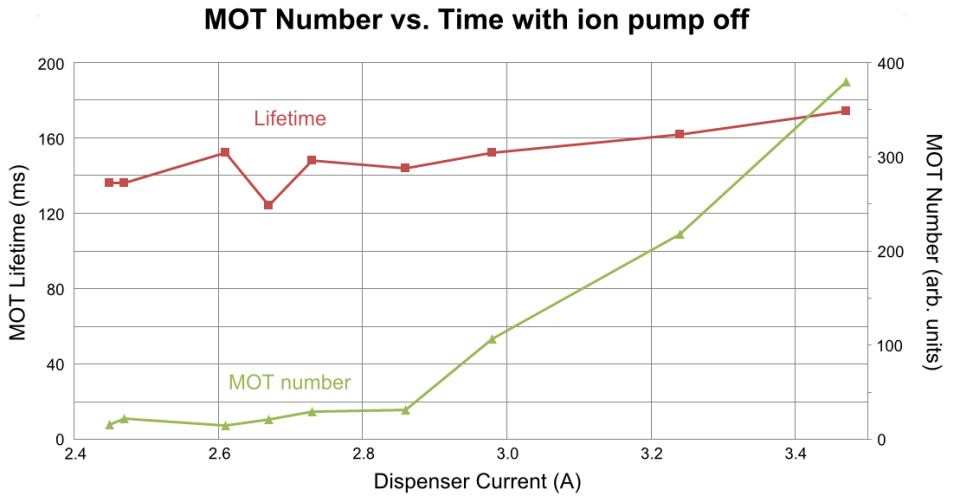

Figure 3.16: (Color) Plot of the MOT number and lifetime vs. dispenser current. MOT atom number, shown in green, increases with dispenser current. The MOT lifetime, shown in red, stays flat, around 140 ms to 150 ms, as dispenser current increases.

The MOT atom number decayed by 17% over 24 min. Assuming that MOT number is linear with background pressure from Equation 3.3, the background pressure increased from 6×10^{-8} torr to 7.2×10^{-8} torr in that time.

Although the ion pump tests in this cell were inconclusive, a double chambered cell was made in which the blanked off ConFlat port was replaced with the anodically bonded ion pump bonded to a G2M. A double MOT was generated, and its lifetime was compared when the system was being pumped on by the standard 2 l/s ion pump versus the anodically bonded ion pump, which should mimic a 0.4 l/s ion pump. This cell showed that the MOT lifetime was proportional to the pumping speed.

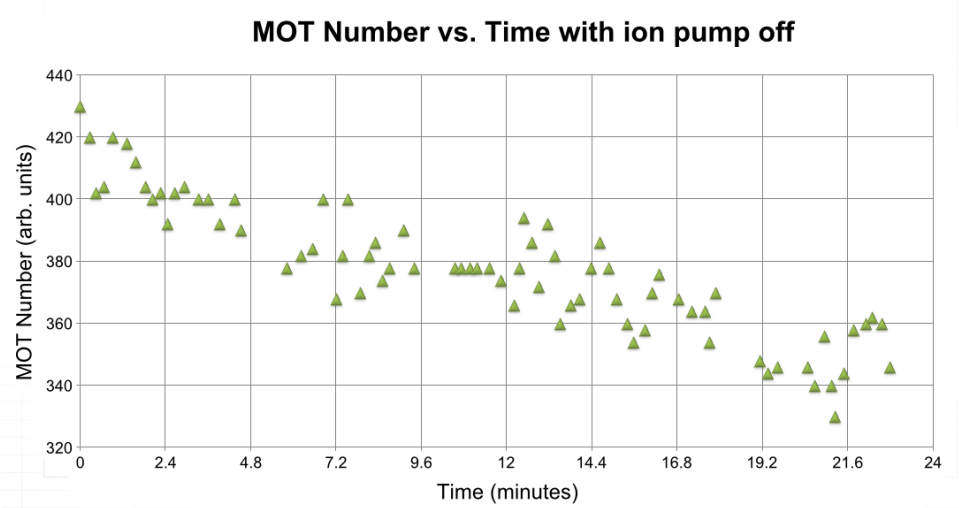

Figure 3.17: (Color) Plot of the MOT number vs. time without operating the ion pump. The MOT atom number decays by 17% over 24 min.

3.4.1 RF inductive activation

During vacuum processing, NEGs must be "activated." An NEG is a sintered porous structure, which allows gases to diffuse into the bulk of its mass. When the NEG is manufactured, a thin passivating layer is formed on the surface, which prevents any sorption of gasses. Activation under vacuum, by heating the NEG, removes this layer by allowing it to diffuse into the bulk mass, leaving the surface ready for gas sorption. Generally, the NEG has

a heater wire that runs through its structure. Running a current of a few amperes (depending on the NEG) through the heater wire is enough to activate the NEG. However, passing current into UHV provides more avenues for possible leaks, limits the available geometries, and in the case of a channel cell, for instance, increases complexity.

An alternative way to activate NEGs is through RF inductive heating. An RF coil radiates power, which is picked up by the NEG, which is conductive, through mutual induction. This induces a current in the NEG, causing resistive heating. The setup used to activate the NEG in the ion pump test cell is shown in Figure 3.18. The RF coil, shown on the left, has an ID that is large enough to fit over the end of the 3D MOT chamber. Because the RF coil will tend to heat anything that is conductive, with the heating efficiency based on geometry, the 3D NEG was placed on the far end of the 3D MOT chamber to minimize pickup of the titanium and steel in the ion pump. The RF coil was driven by a power supply that operates in a frequency range of 100 kHz to 200 kHz, and can supply up to 600 A. The RF coil was water cooled to dissipate the heat generated by the power supply. However, the water cooling was sufficient to dissipate the heat of the bakeout oven (300 °C), thus allowing the RF activation to take place while the cell is hot. The coil was slid over the end of the cell where it was aligned so that the geometric centers of the coil and the NEG overlap.

Because the coupling efficiency, and thus heating as a function of RF power, depends on the geometry of the coil and NEG, a separate test setup with an NEG attached to standard feedthrough leads was put under vacuum. Known activation currents were run through the test setup's NEG. During RF activation, the NEG gets hot enough to glow in the visible spectrum. A straight forward approximation to the temperature of the RF inductively heated NEG was to match its color to the test NEG of known temperature.

3.5 AQuA cell

The current generation of channel cell style vacuum systems is the Atomic Qubit Array (AQuA) cell, shown in Figure 3.19. The source feedthrough was bonded to a 2 cm cell, which

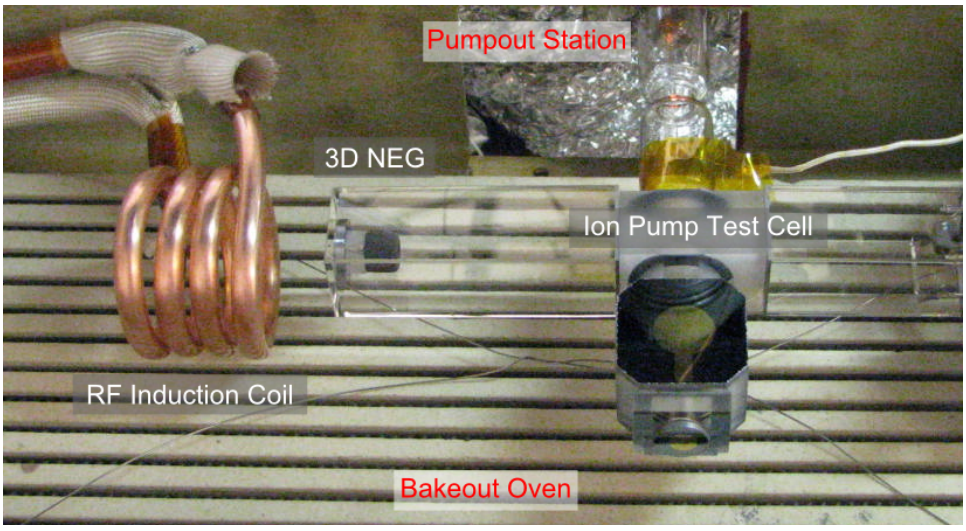

Figure 3.18: (Color) Photo of the RF inductive heater, ion pump test cell, and bakeout setup. The RF coil bore is large enough that it can slide over the ion pump test cell and was centered over the 3D NEG.

was bonded to a 2 cm silicon square with a 1 cm hole cored at the center. This comprises the source tube, which was bonded to a 1 cm × 4.5 cm cell, which comprises the $2D^+$ MOT chamber. The $2D^+$ MOT pinhole was bonded to a Pyrex cylinder, which acts as a spacer between the $2D^+$ MOT and MM MOT chambers. In future generations, this cylinder will also contain a getter for improved vacuum quality, which will require RF inductive activation. The MM MOT chamber is also a 1 cm × 4.5 cm cell. The MM MOT chamber was bonded to an oversized silicon and Pyrex ring, which was then bonded to the manifold. In general, anodic bonds are high stress regions because of the slight material coefficient of thermal expansion (CTE) mismatch, and differences in surface flatness (e.g., from polishing). As bonds stack up in series, as in the source tube through MM MOT bonds, the stress adds up down the line. The silicon and Pyrex ring is allowed to bend and flex, and provides a stress relieving geometry.

The support structure consists of two Pyrex cylinders that were glued into precisely cored holes in the manifold using a ceramic epoxy that can both withstand the 300+ °C for bakeout and anodic bonding, and is matched in its CTE to silicon and Pyrex. A machined Pyrex block with an anodically bonded Pyrex arm spans the two cylinders. The flexible but rigid Pyrex arm was anodically bonded to the bottom silicon of the source tube and then glued to the Pyrex cylinders with the same ceramic epoxy. The support structure essentially provides an extension of the manifold, which acts as the mechanical ground, to the top of the "atom collection" region, increasing rigidity and decreasing the moment.

The manifold is an approximately 1 cm thick piece of machined Pyrex polished on the top and bottom faces. Channels were machined into the Pyrex to connect the various components of the AQuA cell, shown in Figure 3.21. A pinhole centered on the cold atom axis isolates vacuum between the atom collection region and hex cell, which is the "science" cell. The hex cell was made via optical contacting and anodic bonding, and is shown close up in Figure 3.20.

There are two ion pumps in order to pump separately on the atom collection region

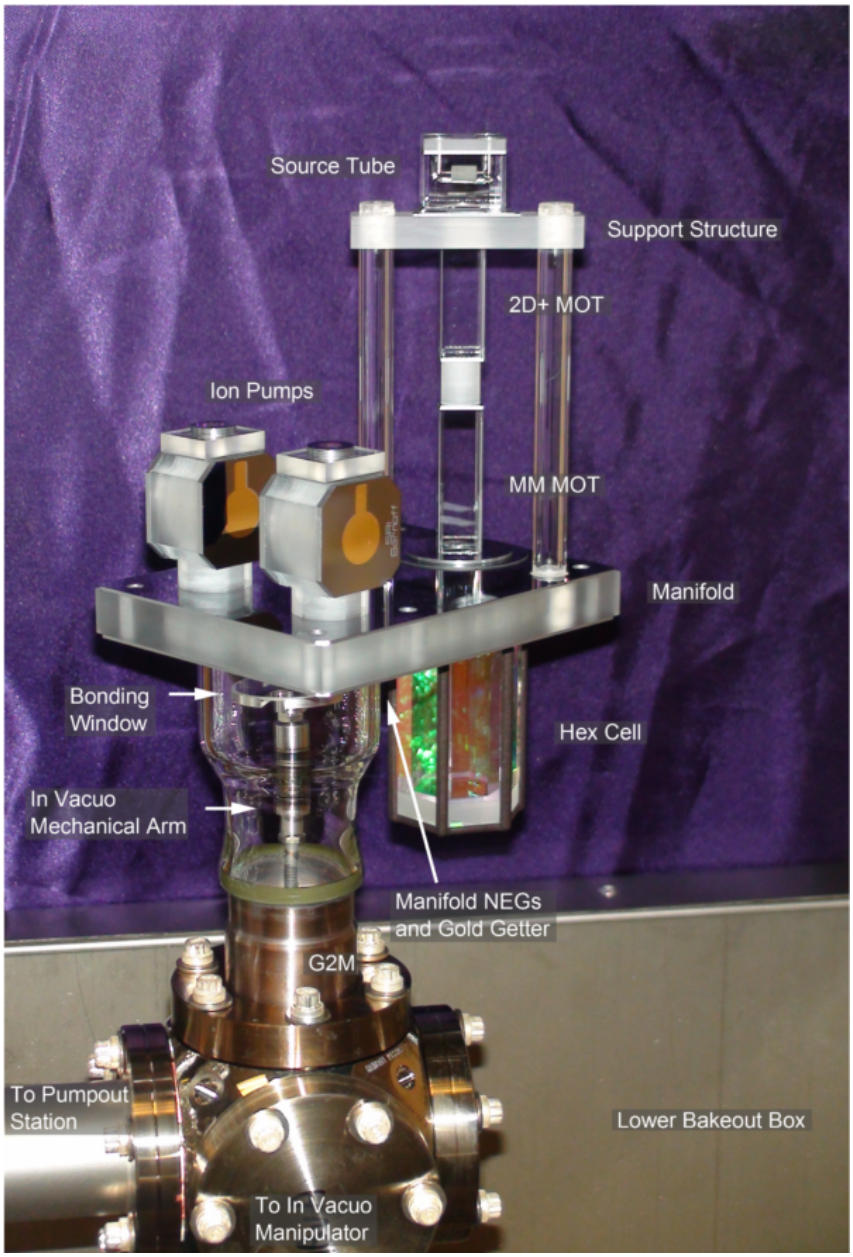

Figure 3.19: (Color) Photo of the finished AQuA cell. The source tube, $2D^+$ MOT chamber, and MM MOT chamber form the cold atom axis, and are bonded to the manifold with a stress relieving geometry. Support rods were mated to the manifold with high temperature ceramic epoxy, and to a bridging piece that was anodically bonded to the source tube to provide mechanical stability and reduced vibrations. The two ion pumps were bonded to the manifold. The hex cell and hex cell pinhole are centered over the cold atom axis. NEGs were bonded into the manifold with silicon feedthroughs to improve hydrogen gettering. *In vacuo* bonding ports were sealed after bakeout. The G2M attaches to a 2-3/4 in. ConFlat.

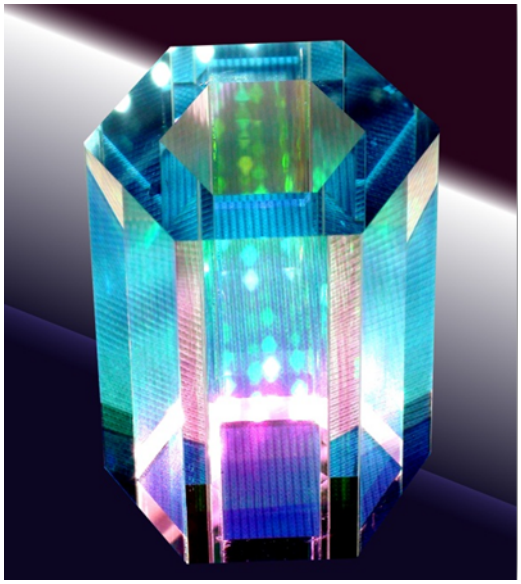

Figure 3.20: (Color) Photo of the AQuA cell hexagonal cell after polishing and AR coating.

and the hex cell. Two channels were machined down the length of the Pyrex to connect the atom collection region and hex cell to their respective, independent ion pumps. The channels also connect to the shared pumpout port. Two 1 mm thick machined silicon plates cap the top and bottom to isolate vacuum. Bonded to the manifold were two silicon feedthroughs, similar to that in Figure 3.3. A 2-contact feedthrough attaches to an NEG, and bonded inside the channel that connects to the atom collection region. A 4-contact feedthrough attaches to an NEG and a gold evaporative getter, and was bonded inside the channel that connects to the hex cell. After processing, the shared vacuum pumpout port was sealed with an *in vacuo* anodically bonded window, which hermetically sealed UHV and isolated the two sides of the AQuA cell. The anodic bond was done via an *in vacuo* mechanical manipulator arm, which brought the Pyrex and silicon faces into contact, and acted as the cathode. The silicon anode was connected to *ex vacuo* with colloidal silver and steel wire. Heat for the anodic bond was provided by the bakeout oven. After removal from the bakeout station, the G2M was removed with a wet saw.

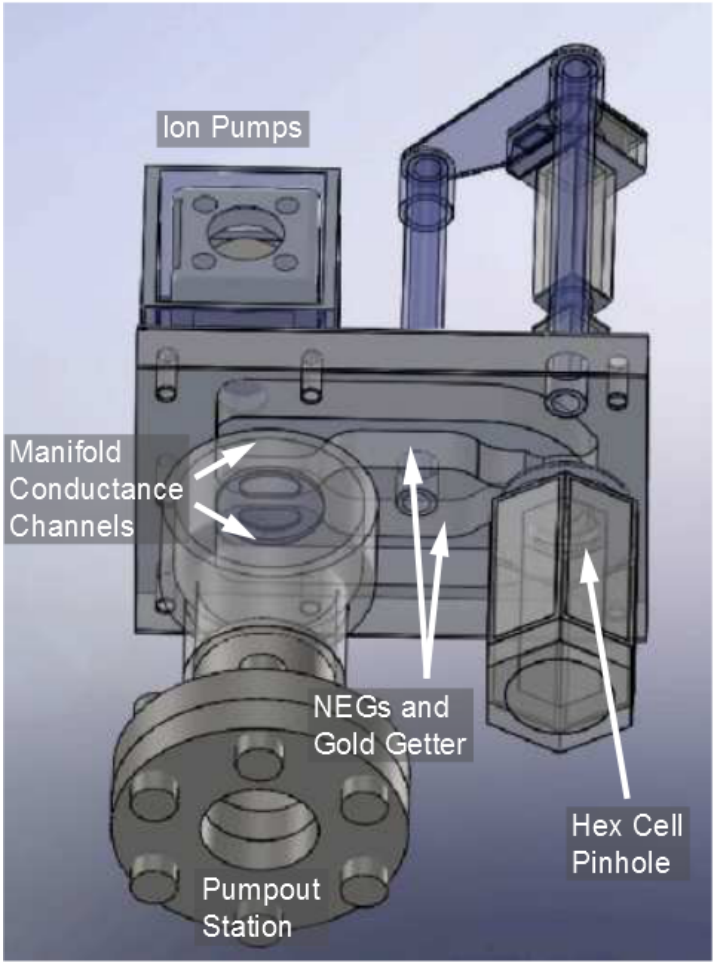

Figure 3.21: (Color) A SolidWorks rendering of the AQuA cell showing the layout of the manifold. The hex cell is isolated from the atom source and resonant light region via a pinhole offset from the atom axis. Separate high conductance channels through the manifold connect the hex cell and atom source to an individual ion pump and to the pumpout station. NEGs and a gold evaporation getter are in line with the conductance channels to improve vacuum quality.

Chapter 4

Portable BEC system

This chapter will go into detail on the portable BEC system (or "BEC cart") that, at the time, was the world's smallest complete system for making BECs. This compact, movable, atom chip-based BEC production system is shown in Figure 4.1 [71]. The BEC cart occupies a volume of $0.4\,\mathrm{m}^3$, operates at a repetition rate as high as $0.3\,\mathrm{Hz}$, consumes an average power of $525\,\mathrm{W}$, and produces BECs containing around 2×10^4 atoms in the $|F = 2, m_F = 2\rangle$ ground state of ^{87}Rb. The system contains all of the components needed to produce and image BECs, including the UHV system shown in Figure 3.1, lasers, data acquisition hardware, electronics, and imaging equipment, which are described in the following sections. The system can be easily reconfigured for different applications simply by changing the atom chip wire patterns, such as those in Chapter 3. As such, the hope is that it can serve as a standardized platform for a variety of portable experiments that utilize ultracold matter.

4.1 UHV cell for BEC production

The heart of the portable BEC cart is the UHV cell, described in Section 3.1. The atom chip used here to make BEC is the standard atom chip described in Section 3.1.3.1. A significant practical challenge in using the atom chips, described in Chapter 3, is making robust electrical connections to the ambient side of the atom chip. The atom chip is a $420\,\mu$m thick square of silicon, in a high-stress geometry from anodic bonding, and during operation

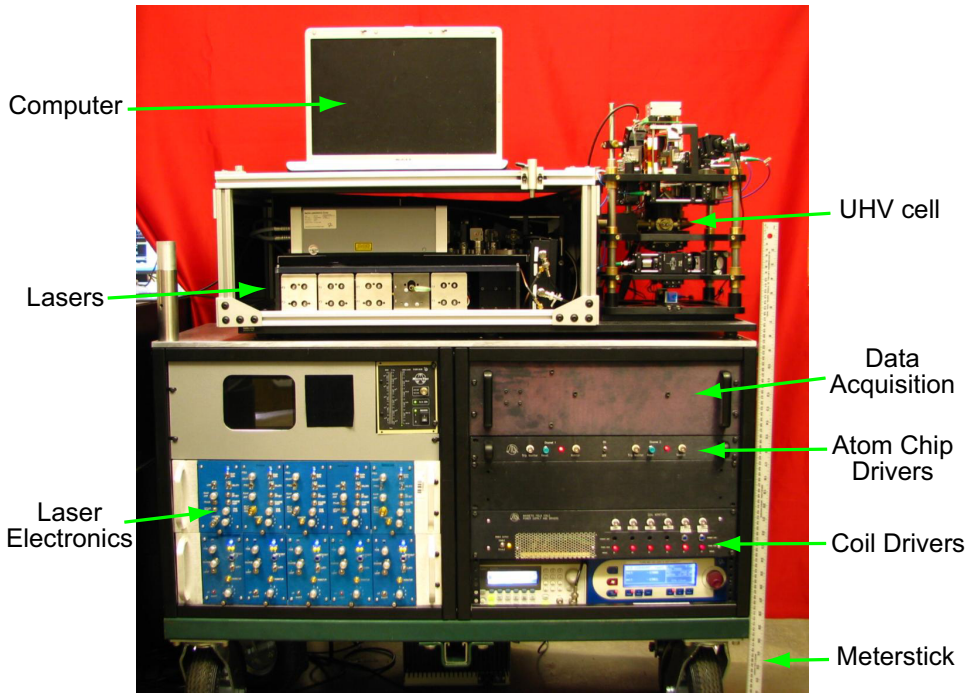

Figure 4.1: (Color) Photo of the complete portable system for BEC generation. Shown are the lasers and laser electronics, UHV cell and surrounding optomechanics package, coil and atom chip drivers, DAQ system, and a meter stick on the right for scale. Not shown is the RF system and switching power supplies mounted internally.

can get over 150 °C. This means that any connectorization scheme must have low insertion force, not add additional stress to the atom chip, and be robust at high temperature.

4.1.1 Chip connectors

The chip connectors developed for use with the standard atom chip are shown in Figure 4.2. The old style chip, shown in Figure 4.2(a), has a single row of vias, but a double row of connecting pads. The pads and vias have a 50 mil (50 thousandth of an inch) pitch. The pads are 100 mil wide, which gives a larger area to connect to, but requires that they be staggered. The connectors in Figure 4.2(a) are Mill-Max P/N 830-10-050-20-001000 ultra-low insertion force, single row, right angle interconnects. The Mill-Max connectors were cut with a jeweler's saw to 7, and 8, pins in length. They are epoxied together lengthwise with 5-minute epoxy, and centered, which forms double row staggered connectors that match the pad pitch.

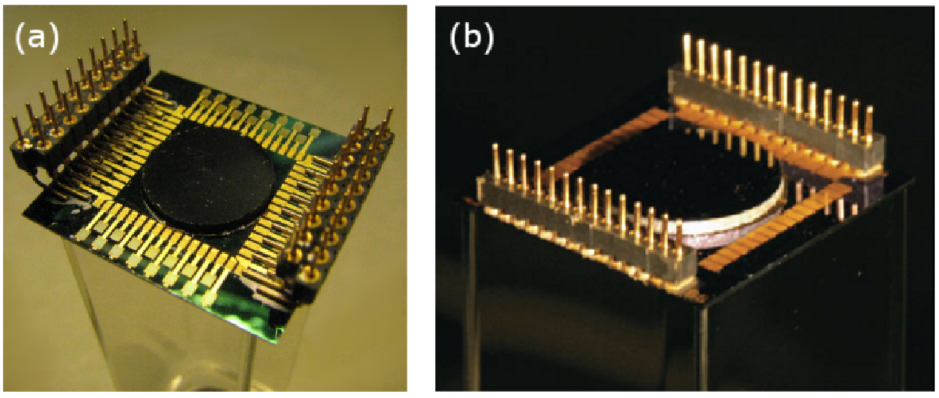

Figure 4.2: (Color) (a) Photo of the chip connectors for the older style, standard BEC chip. (b) Photo of the chip connectors for the newer style, standard BEC chip. Image credit [60].

The custom, double-row connector was then potted to the chip with Epo-Tek OD1001, a single component, flexible, and low shrinkage epoxy. Electrical connection was made with a combination of spring force from the connectors, where the right angle bend contacting the pads is compressed during the potting process, and colloidal silver, which, when applied,

meniscuses between the pad and the pin. The colloidal silver can be cured either with a heat lamp at $\geq$150 °C, or during operation when current is passed through the contact joint. After the colloidal silver cures, it provides an extremely low resistivity and robust connection. Epo-Tek E2101 electrically conductive epoxy was used initially in this connector geometry to provide the robust contact between the pins and pads. However, layer thickness of more than a few 10's of microns tended to give higher resistances than expected, and often failed altogether. The colloidal silver did not seem to have such a restriction.

The new style chip, shown in Figure 4.2(b) (image credit [52]), has vias at a 39 mil (1 mm) pitch, and a single row of connecting pads with a 50 mil pitch. A single row of connectors was realized by reducing the number of connecting pads. Where it was planned to run more current through certain wires, one connecting pad was electrically connected to two vias. These included the main Z-wire, H-wires, and the central dimple wire. The connectors shown in Figure 4.2(b) are Mill-Max P/N 399-10-002-00-310000 low-insertion-force interconnects with block style feet for surface mounting. Electrical connection is made with Epo-Tek E2101 silver conductive epoxy, and the Mill-Max are potted with Epo-Tek OD2002, an updated epoxy from the OD1001. The new connectors decreased the gap between mating surfaces, which allowed the E2101 epoxy to be used, with moderate success. However, because of the differences in flatness between the atom chip and these connectors, poor and open connections were fixed with colloidal silver filling or bridging gaps.

The on-chip connectors were mated with their appropriate headers. The headers were soldered to ultra-flexible wire (Cooner Wire P/N 26-6544), which was used to bring the electrical connections up to a break-out board, shown in Figure 4.3. The chip currents come in through a 2-pair, shielded twisted pair cable, which is attached to a screw terminal soldered onto the break-out board, shown at the top of the figure. The dimple-wire current flows through the green and white wires, and the Z-wire current flows through the red and black wires. The big-Z coil current comes in through the red and black banana connectors, and the compression coil current comes in through the blue and green banana connectors.

The RF coil connection is not shown.

4.2 Laser system

A block diagram of the laser system is shown in Figure 4.4. Five distributed feedback (DFB) laser diodes are collimated, sent through a pair of optical isolators, and fiber coupled without mirrors using a 5-axis FiberPort coupler with an incorporated lens. The laser light is then split and combined in evanescent wave couplers (EWCs) with fixed ratios. The cooling master is first split, with 50% of the light coupled into a compact saturated absorption spectroscopy (SAS) module for locking to the ^{87}Rb $|F = 2\rangle \rightarrow |F' = 2\rangle/|F' = 3\rangle$ crossover peak. The other 50% is split equally into four beams: 12.5% is combined with the pump/probe laser, 12.5% is combined with the cooling slave laser, and the other 25% is used for diagnostic purposes. The repump master is split, with 90% sent into the SAS module and locked to the ^{87}Rb $|F = 1\rangle \rightarrow |F' = 2\rangle$ transition, and 10% combined with the repump slave for frequency offset locking. The pump/probe is split, with 10% combined with the cooling master for frequency offset locking, and 90% going into the pump/probe fast-shuttering box. The cooling slave is similarly split, with 10% combined with the cooling master, and 90% combined with the repump slave. The combined light in the pump/probe, repump slave, and cooling slave fibers are sent to separate fast photodiodes (PDs) via 50/50 combiners, which create the beat note used for frequency offset locking. Voltage-controlled oscillators set the offset frequency with the laser beat note using an RF heterodyne technique.

A combined 7 mW of light from the cooling slave and repump slave fiber seeds the tapered amplifier (TA). The 7 mW seeding the TA is 82%/18% cooling slave/repump slave. The downside of EWCs is that the 82%/18% repump slave/cooling slave light that exits the other port is lost. A diode protection circuit was integrated into the current driver of the five DFBs to avoid damage from electrical spikes. Three signal diodes (1N4148) are put in series in the forward biased direction to prevent the laser diode driving voltage from exceeding 2.1 V. A single signal diode in the opposite direction prevents reverse voltage of over 0.7 V.

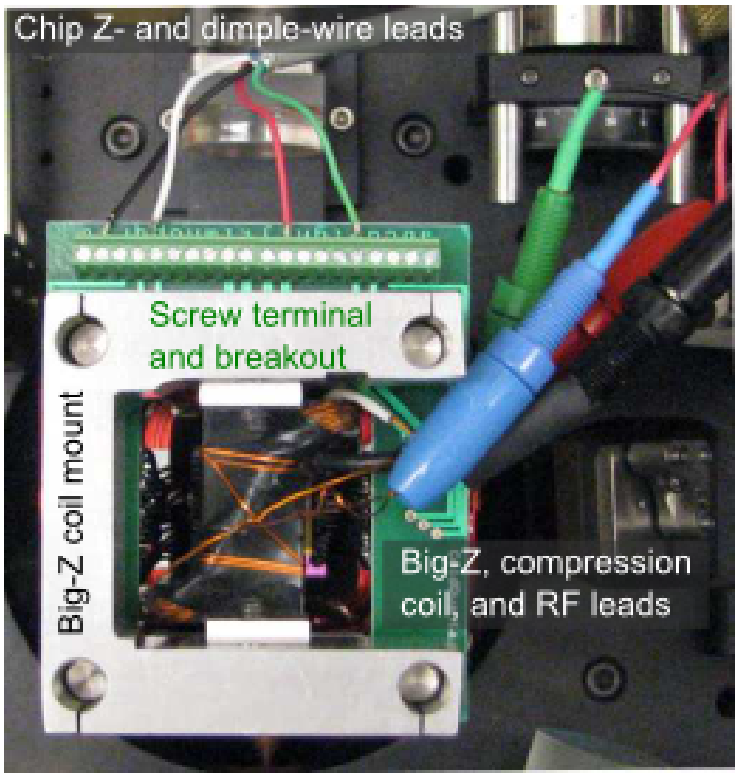

Figure 4.3: (Color) Photo of the chip connector breakout board (green PCB). Chip wire connections come in from the top. Also shown are the compression wire (blue/green banana) and big-Z (red/black banana) connections, and the RF coil connection (SMA).

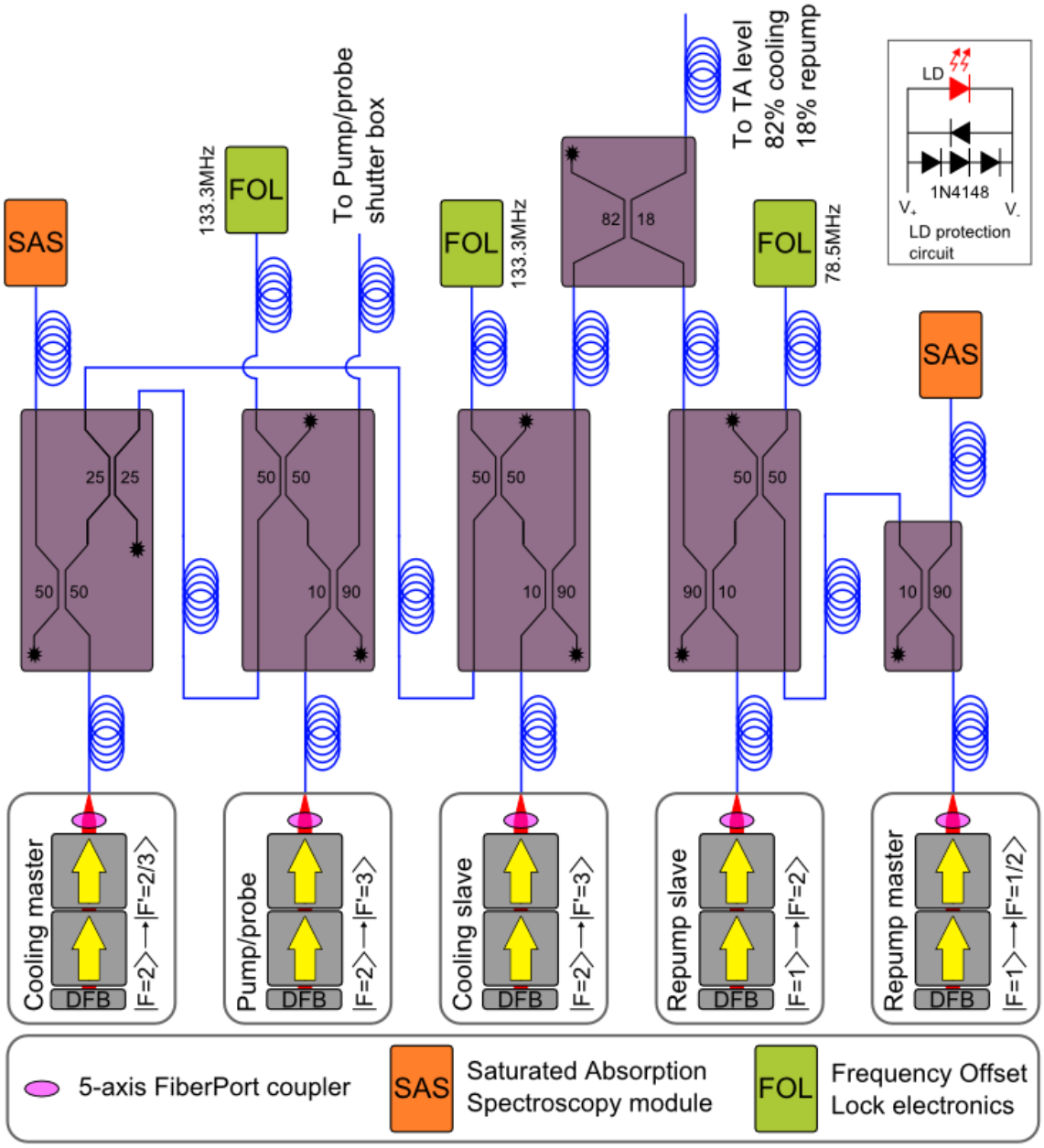

Figure 4.4: (Color) Block diagram of the cart laser system. Five DFB lasers are collimated, isolated, and fiber coupled, shown at the bottom. The laser light is then split and combined using EWCs, shown in purple. The SASs are used to lock the laser to the absolute ^{87}Rb transition, and the FOL were used to offset lock the slaves to the SAS locked lasers. The TA is seeded with the light from the top fiber.

The laser frequencies generated by this laser system are summarized in Figure 4.5.

The laser system is split into two levels, with everything in Figure 4.4 on the bottom level. The second level consisted of the TA, and the TA input and output coupling optics. A photo of the bottom level of the laser system is shown in Figure 4.6(a). The TA level of the laser system is shown in Figure 4.6(b). The seed light, from the cooling slave and repump slave, comes in from the yellow fiber, where it is collimated with a lens that mode matches to the TA chip. Because TA chips put out a significant ($\geq$1 mW) amount of amplified spontaneous emission from the rear facet, an additional optical isolator is put after the input collimation lens. Two coupling mirrors, a half waveplate to match the polarization of the input beam to the TA chip, and an input coupling aspheric lens inside the TA housing, are used to couple into the TA chip. The output of the TA chip is collimated with an output coupling aspheric lens inside the TA housing. The TA output is split, with power controlled via a half waveplate and a polarizing beam splitter (PBS), into the 2D MOT and 3D MOT beams. The 2D MOT has a mechanical shutter before the fiber coupling. The 3D MOT beam is sent through a 1:1 focused telescope before being fiber coupled. The mechanical shutter is placed at the focus of the telescope in order to decrease the rise and fall times of the shutter. Pump and probe shuttering is discussed in detail in Section 4.3. In the end, four fibers enter the system: 2D MOT, 3D MOT, optical pump, and probe.

4.3 Optical shuttering

Cold atom experiments require high optical isolation, which usually means mechanical shutters. For MOTs, the shuttering can generally be slow, with rise and fall times on the order of 100 μs to 1 ms. The 2D and 3D MOT shutters are shown in Figure 4.6(b). The shutters are EOPC SH-10 interlock shutters, which are solenoids that activate to swing an anodized aluminum blade into, and out of, the beam. The rise and fall time of a mechanical shutter is the beam diameter divided by the shutter velocity. The 3D MOT passes through a 1:1 telescope and is shuttered at the focus, i.e., the minimum beam waist, to decrease

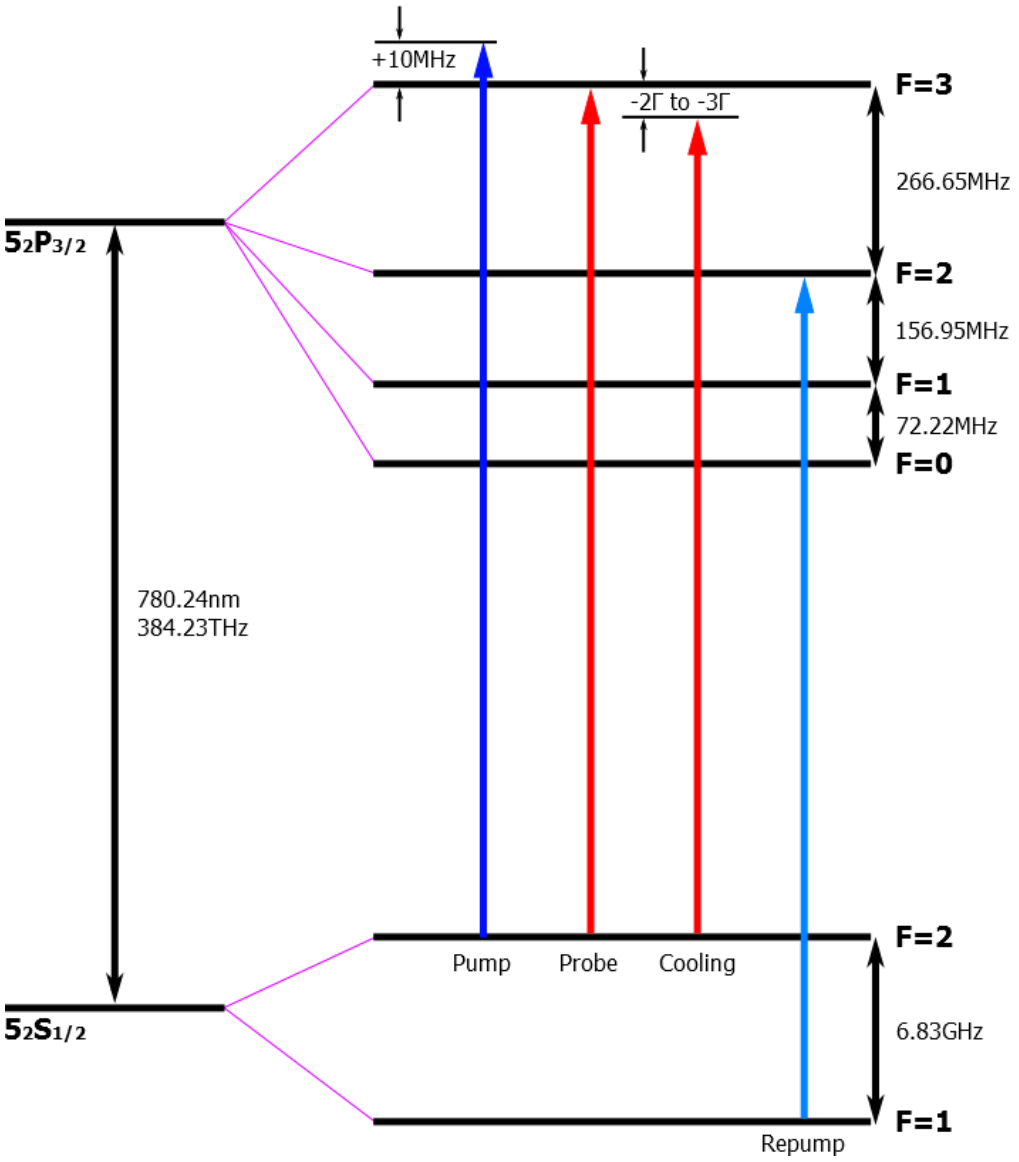

Figure 4.5: (Color) The ^{87}Rb D2 spectral lines and experimental laser frequencies.

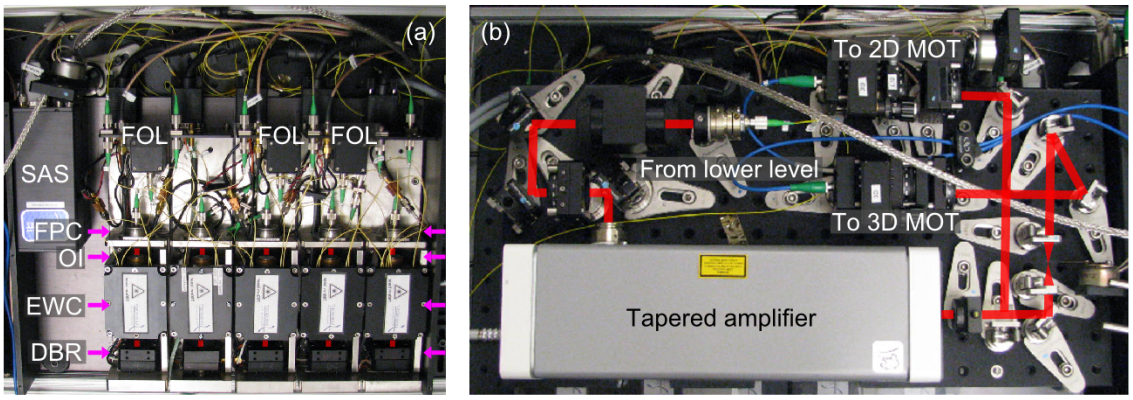

Figure 4.6: (Color) (a) Photo of the five DFB lasers that make up the cart laser system. (b) Photo of the TA input/output level of the cart laser system that sits on top of the DFB laser level.

rise/fall time of the shutter to $\leq 100\,\mu$s.

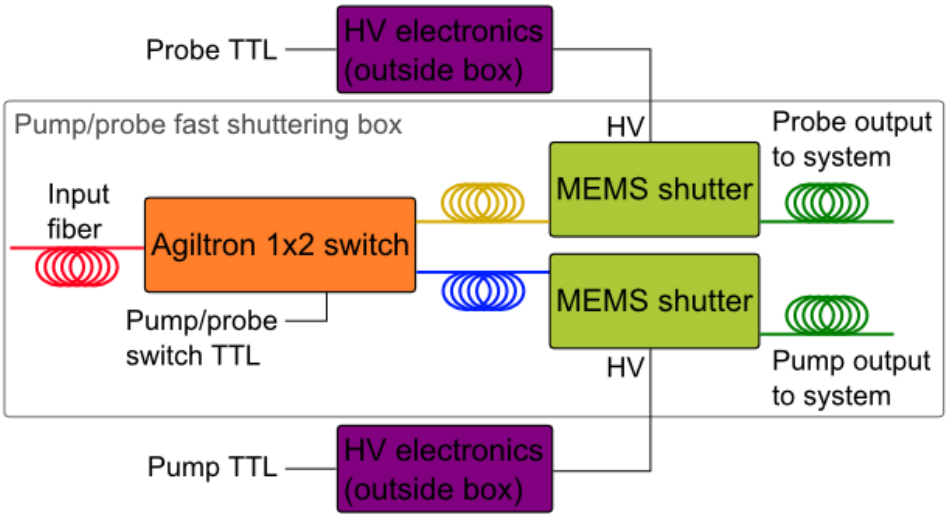

Figure 4.7: (Color) Block diagram of the pump/probe fast shuttering system. The pump/probe input is switched between two output fibers via the Agiltron fiber-optics switch. Each output has a MEMS mechanical shutter for high optical isolation, before being coupled out of the box.

Large mechanical shutters have two limitations: the slow rise/fall times, and large delays between responses to activation pulses, i.e., the minimum response time of the shutter between an open pulse and a close pulse is at least several milliseconds. To increase the effective speed of the shuttering, mechanical shutters can be placed in series with acousto-optics modulators (AOMs), which provide very fast shuttering (10 ns to 10 μs), but poor isolation (approximately 30 dB) [28,52,53]. AOMs, however, require a fairly large footprint to operate. A sufficient path length must be implemented after the AOM to allow the diffracted and non-diffracted beams to spatially separate. Additionally, the driving RF electronics consume a fair amount of power (> 2 W), and require heatsinking. To get around this the BEC cart utilized a combination of a fiber-optics switch and a custom MEMS mechanical shutter. The BEC cart's fast pump/probe shuttering system is shown diagrammatically in Figure 4.7.

Fast shuttering is achieved with an Agiltron NS 1x2 fiber-optic switch, which provides

$\geq$25 dB of isolation between the output ports, and a rise/fall time on the order of nanoseconds. Mechanical shuttering is provided by two MEMS shutters, developed by Teledyne Scientific, which overcomes the minimum time-between-pulses problem mentioned above and decreases size. The MEMS shutter is a fiber-in/fiber-out device, with a free space shutter, driven with a high voltage (HV) signal (approximately 100 V). It is mounted in a telecom-style butterfly package. The MEMS shutters are shown in Figure 4.8.

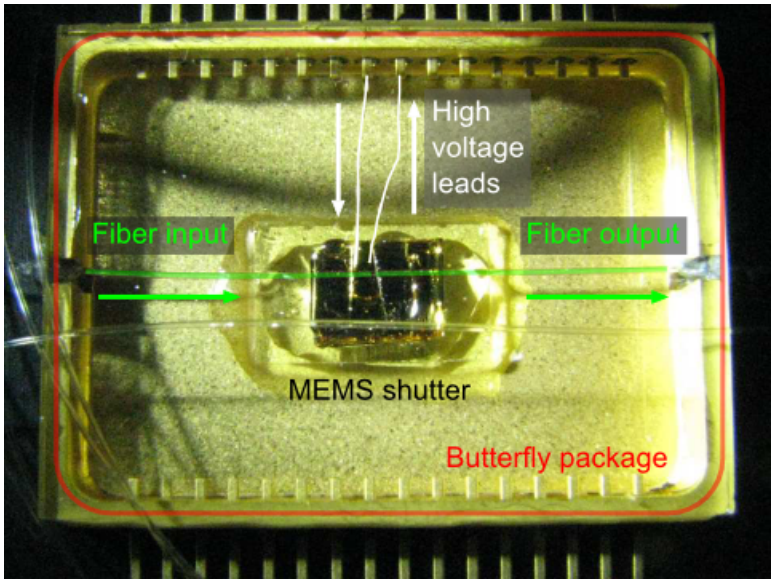

Figure 4.8: (Color) Photo of the fast MEMS mechanical shutter in its butterfly package. The two high voltage wire bonds can be seen coming in from the top. The input fiber can be see on the left and the output fiber is on the right. The MEMS shutter is in the center.

The complete, fiber-in/fiber-out, fast shuttering package was fit into a 5 in. $\times$12 in. box that is 1 in. thick, shown in Figure 4.9. The HV circuitry is outside the box and accepts a TTL signal. The HV to drive the MEMS switches comes into the box through the BNC connectors shown on the left. The TTL signal to drive the fiber-optic switch comes into the box through the SMA connectors shown on the left. The pump/probe fiber, with the red jacket, is coupled into the box on the right, and is the input to the fiber-optic switch. The two outputs of the fiber-optic switch, the blue fiber and yellow fiber, are coupled into the MEMS shutters. The output of the MEMS shutters are coupled out of the box and sent into

the system.

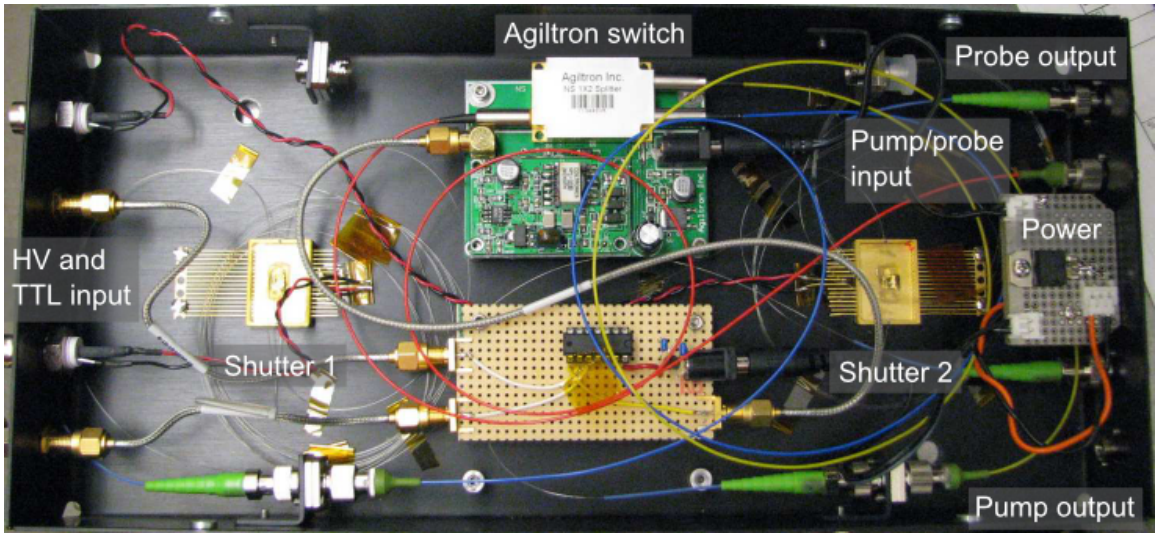

Figure 4.9: (Color) Photo of the complete pump/probe fast shuttering system. The HV and TTL come into the box from the left. The pump/probe fiber (red) comes in from the right and is sent into the fiber-optic switch. The two fiber outputs of the fiber-optic switch (blue and yellow) are coupled into the MEMS shutters, then coupled out of the box.

4.4 Computer control system

The computer control system, which is used to control the timing of experimental hardware, via analog and digital outputs, is shown in Figure 4.10. The system is based around the National Instruments (NI) compact reconfigurable input/output (cRIO) field programmable gate array (FPGA) platform. The cRIO is a real time (RT) computer and chassis, with an embedded FPGA chip, that accepts modules with various input and output channels. The modules provide various inputs to the cRIO RT, and output to hardware from the cRIO, and can be swapped in and out, thus the reconfigurability. The FPGA is a reprogrammable microchip that is customizable based on the chosen modules and required outputs and timing.

A block diagram of the computer control setup is shown in Figure 4.11. High level code is written in LabVIEW and run on a Windows PC host computer, shown in yellow. The

Figure 4.10: (Color) Photo of the cart computer control system. The left half of the box contains the NI cRIO. The right half of the box contains the NI CVS.

timing tree generated by the high level code is downloaded to the cRIO RT, shown in red, before each experimental run. The cRIO RT interprets the timing tree for the FPGA, and FPGA executes the timing tree, with hardware-determined timing, off of the internal 40 MHz clock. Four 4-channel DACs provide the analog output signals, which drive the hardware, shown in orange. The digital output modules are also shown in orange. The limiting factor in the timing is the update rate of the DAC, which, for the NI-9263 module, is 100 kS/s (kilosamples/second), or 10 μs. Hardware directly driven by the cRIO modules is shown in teal. The magnetic field coils, atom chip wires, and the RF coil used for RF evaporation, are shown in green.

Image capture and processing was done with a secondary embedded RT and FPGA system, the NI compact vision system (CVS). The CVS accepts a TTL trigger from the cRIO to start the imaging sequence. Either the CVS or the cRIO can trigger the camera, shown in Figure 4.11 in pink. The camera output is IEEE 1394 (Firewire), which is input into the CVS RT. The CVS RT uploads to the host computer for high-level LabVIEW, processing as well as off-line analysis. The computer control system was put into a box for shielding, shown in Figure 4.10.

4.5 Coils

The magnetic field coils used for cooling and trapping are shown in Figure 4.12(a). A pair of square anti-Helmholtz coils, for producing the quadrupole field necessary for creating a MOT, is centered approximately 1.8 cm below the atom chip. The chip quadrupole coil has the same dimensions as the MOT quadrupole coil, and sits above the MOT coil, where the pair is centered on the atom chip. The ladder quadrupole coil is rectangular, with an approximately 2:1 aspect ratio, and sits on the outside of the MOT and chip quadrupole coils. The ladder coil profile matches the outer diameter of the sum of the stacked MOT and chip quadrupole coils. Three orthogonal pairs of Helmholtz coils sit outside the quadrupole coils, and produce bias and shim fields along the x-, y-, and z-axes.

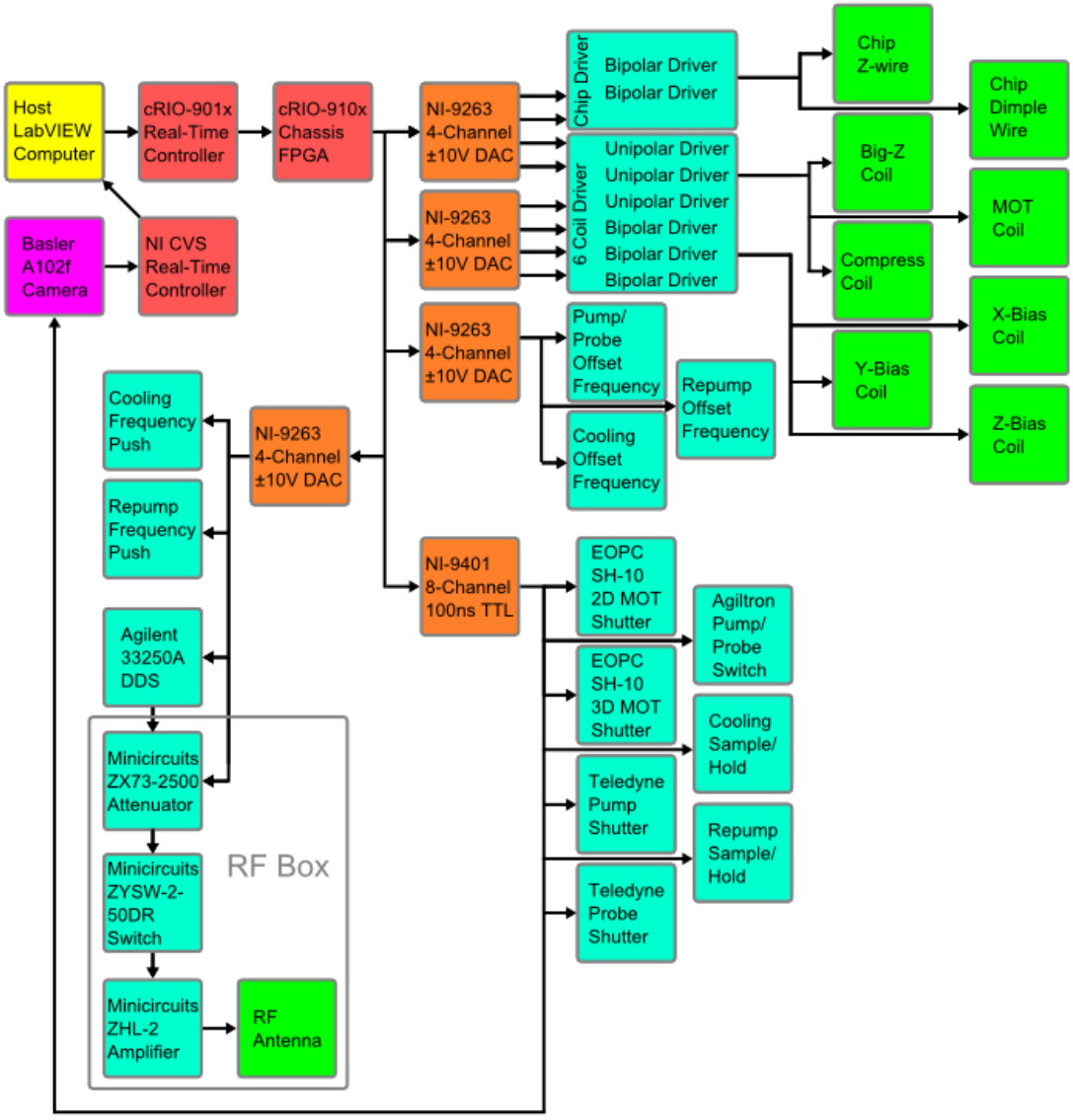

Figure 4.11: (Color) Block diagram of the cart control system. High level code is written on the host computer shown in yellow. The timing file generated is downloaded to the cRIO RT, shown in red, which interprets the timing tree for the FPGA. The digital and DAC output modules are shown in orange. Hardware directly driven by the cRIO modules is shown in teal. The magnetic field coils, atom chip wires, and the RF coil used for RF evaporation, are shown in green.

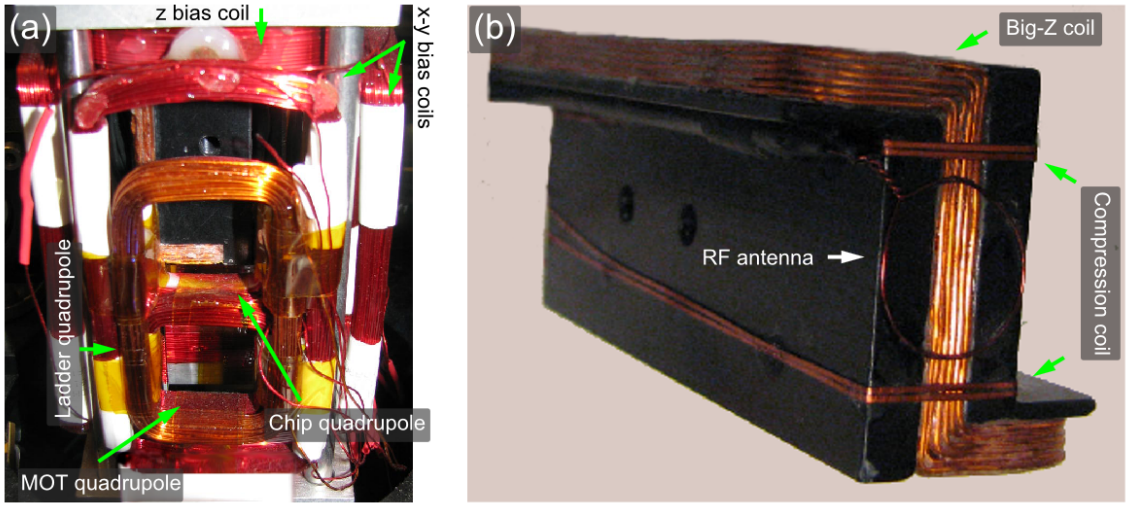

Figure 4.12: (Color) (a) Picture of the quadrupole and bias field external coils for the cart. (b) Picture of the big-Z coil used in magnetic transport for the cart. The near side of the big-Z (in the photo), where the RF coil sits, is centered approximately 1.2 mm from the back of the atom chip. The "compression" wires can be seen n either side of the RF coil.

The "big-Z" coil, in its mount, is shown in Figure 4.12(b). The big-Z is used for magnetic transport of the atomic cloud from the MOT level to the atom chip level. The big-Z coil face that is pointed out of the page of Figure 4.12(b) is placed approximately 1.2 mm from the ambient side of the atom chip. The compression coil is mounted to the big-Z coil. It consists of four turns of flattened magnet coil wire, so that its profile proud of the big-Z coil is minimized. The RF coil is mounted to the atom chip side of the big-Z coil. Electrical connections come in from the opposite side of the big-Z coil (not shown).

4.6 Coil and chip drivers

Typical power supplies used to drive magnetic field coils are large and bulky linear supplies, such as the Kepco BOP 20-20 [28]. In an effort to miniaturize the coil drivers, custom op-amp drivers, powered by high-efficiency switching mode power supplies (SMPS), were developed. The six channel, two layer, 2U rackmount coil driver box is shown in Figure 4.13. The bottom layer of the coil drive box is shown in Figure 4.13(a). The SMPS is an Excelsys XQB, shown on the left, which runs off of 120 V AC. The SMPS output is filtered in two stages (described in detail in Appendix A), shown in the middle. The filtered output passes up to the second level, shown on the right. An internal metal plate provides shielding between the two levels, to prevent radiative pickup. The top layer of the coil driver box has a screw terminal breakout for the output of the SMPS, where it is used to power the six coil drivers, shown in Figure 4.13(b). The top of the box has been replaced with a heatsink, to which the high power elements of the coil drivers have been directly bolted.

The three unipolar supplies, shown in Figure 4.13(b), are single op-amp supplies that drive high power MOSFETs, which servo the current through the quadrupole coils. The high power MOSFETs are bolted directly to the heatsink top. The current is monitored by an additional op-amp circuit. The three bipolar supplies, shown in Figure 4.13(b), are based on the Apex Microchip high power MP108 and MP111 op-amps. The visible green PCBs are the home-built driver circuits. Underneath are the Apex op-amps, which have a similar

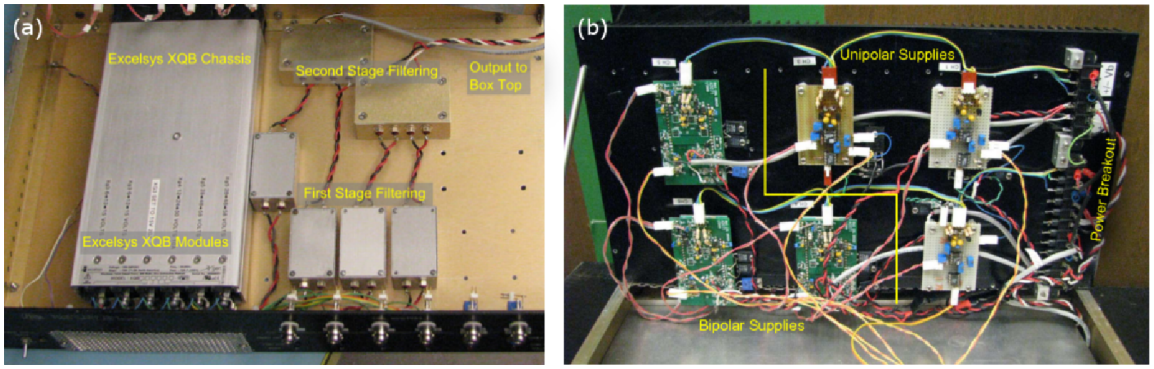

Figure 4.13: (Color) (a) Photo of the bottom layer of the coil driver box. The SMPS is an Excelsys XQB, shown on the left. The two stages of filtering are shown in the middle. The filtered output goes up to the second level, shown on the right. (b) Photo of the top layer of the coil driver box. The SMPS breakout comes in from the lower level to the screw terminals, shown on the right. The high power elements of the six coil drivers are bolted directly to the heatsink (black), which acts as the box's top. There are three unipolar coil drivers and three bipolar coil drivers. The inner plate (silver), shown on the bottom, provides shielding between the two levels.

footprint, and are bolted directly to the heatsink top. The Apex op-amps are connected via two, parallel, single-row (SIP) connectors. The current sensing resistors of all six coil drivers are also bolted to the heatsink top. The feedback network of both the unipolar and bipolar supplies incorporates phase compensation to stabilize the circuit because of the high inductances of the coils. The detailed circuit for the coil driver box is shown in Appendix A.

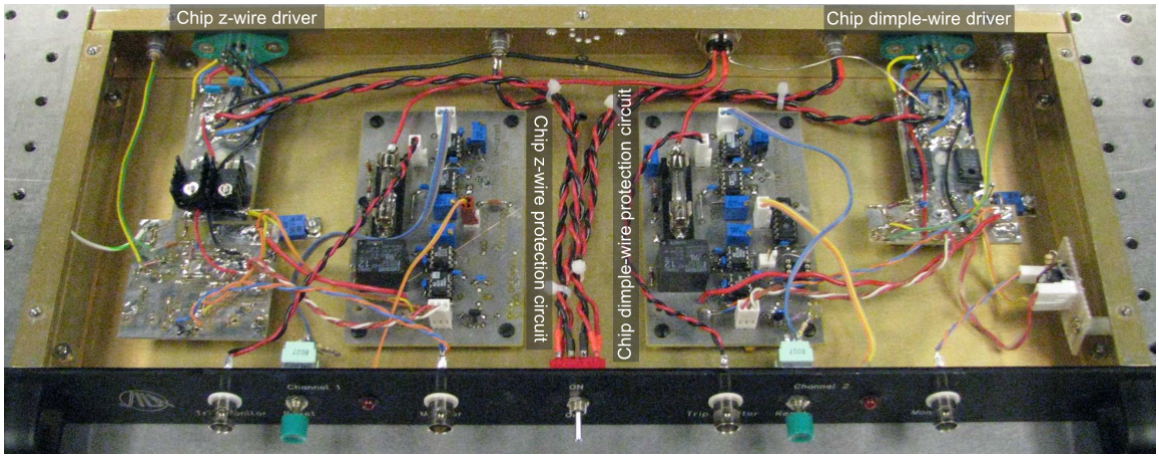

Figure 4.14: (Color) The chip driver and protection box. The outer two circuits are the two (main Z and dimple) chip driver circuits with the power op-amp mounted on the rear of the box for passive cooling and heat sinking. The inner two circuits are the two protection circuits. Both circuits are described in detail in Appendix A.

The circuit used to drive the atom chip wires is shown in Figure 4.14. The chip wires require much lower powers, and are effectively resistive loads. Unlike the coil drivers, where high power and stability driving an inductive load were paramount, the chip drivers require low noise and low drift. Additionally, novel protection circuits were designed to minimize the risk of destroying a chip wire, and overall thermal stress to the UHV cell. The outer two circuits shown in Figure 4.14 are the two chip driver circuits for the main Z-wire and dimple-wire on the atom chip. The power op-amp, which supplies the current to the chip wires, is mounted on the outside of the rear of the box, for passive cooling and heat sinking. The inner two circuits shown in Figure 4.14 are the two chip protection circuits. The chip driver and protection circuits are enclosed in a half-depth, 1U rackmount enclosure. The

detailed chip driver and protection circuitry is shown in Appendix A.

4.6.1 Switching mode power supplies

Because cold atoms and BECs are very sensitive to stray magnetic and electric field changes, low noise power sources, such as a battery, are generally used to power the driver circuits for atom chip magnetic traps. In order to miniaturize the system, an SMPS was used to power the driver circuits. Power supply noise affects the atoms most strongly in two regimes: at the magnetic trap frequency, where noise induces parametric heating [72], and at the RF spin-flip frequency of the atoms. Generally, trap frequencies are between 10 Hz and 10 kHz. RF spin-flips occur above 1 MHz, depending on the magnetic trap. The noise from an SMPS, which is significantly higher than a linear supply, comes from the switching frequency and its harmonics. Modern SMPS switching frequencies fall into the region between these two frequency ranges, with typical switching frequencies in the low 100's of kilohertz. Thus, if the higher harmonics are sufficiently filtered, then the SMPS switching frequency noise is unseen by the atoms. The SMPS used in the BEC cart is the Excelsys XQB, which is a 900W chassis, with reconfigurable modules that allow for customization of the output voltages and currents, and a switching frequency of 200 kHz. The reconfigurable modules are useful when attempting to impedance match the load to the power supply. A separate XQB was used to power the chip and coil drivers, as well as other electronic components in the cart, such as the cRIO. A detailed hookup and filtering diagram for the SMPS is shown in Appendix A.

4.7 RF evaporation system

The RF evaporation system is driven by an Agilent 33250A 80 MHz arbitrary waveform generator, which can output over 10 dBm. The frequency sweep is controlled via a cRIO DAC channel through the Agilent. The RF is fed into a DAC-controlled variable attenuator (Minicircuits ZX73-2500) and TTL-controlled switch (Minicircuits ZYSW-2-50DR). The signal is then fed into a 2 W fixed gain amplifier (Minicircuits ZHL-2), which runs to an

RF loop held just above the chip shown in Figure 4.12(b). A shielded, inline 50 Ω resistor crudely impedance matches the coil, which has negligible impedance at the frequencies used, to the 50 Ω output of the amplifier. A photo of the RF box is shown in Figure 4.15.

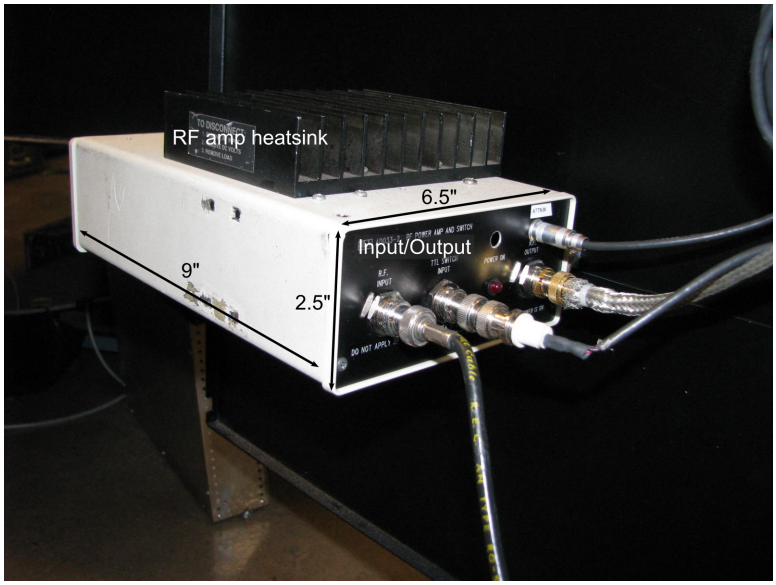

Figure 4.15: (Color) Photo of the RF system mounted in the cart.

4.8 Imaging system

The method used for imaging the cloud optical depth (OD) is absorption imaging of the atoms after being released from the trap and a time-of-flight (TOF) ballistic expansion. In absorption imaging, a resonant probe beam is absorbed by the atoms and the "shadow" is imaged onto a CCD, shown in Figure 4.16.

In practice, a second image is taken under the same conditions as the absorption image, but without atoms in the frame. This background image is then used to normalize the first image, and remove the spatial effects of the probe beam. Because the two shots are of the same duration there is no need to take "dark" shots to account for different levels of integrated stray light, as described in [73]. In this case, the optical density of the atoms is

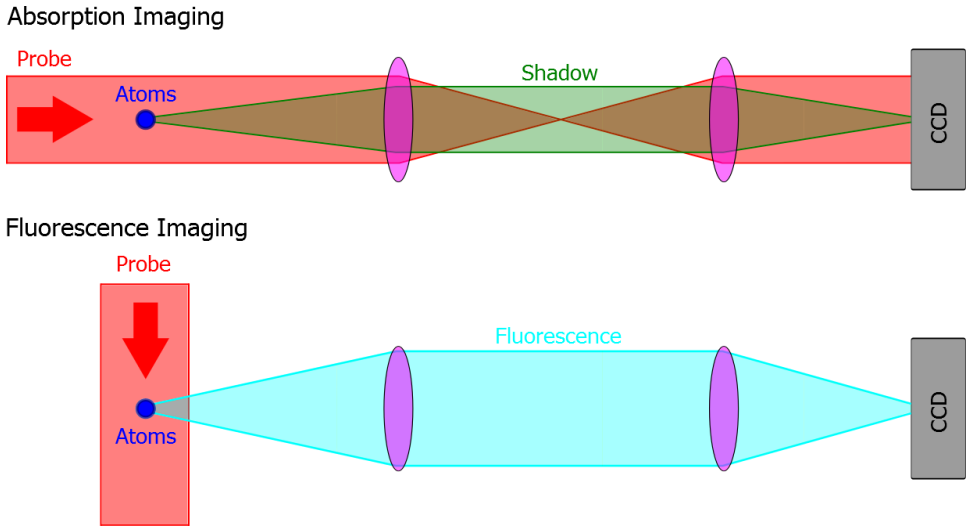

Figure 4.16: (Color) Diagram of absorption and fluorescence imaging. Top: In absorption imaging, the atoms cast a shadow, which is imaged onto the CCD camera, along with a bright background, which is the probe beam. Bottom: In fluorescence imaging, the atoms are illuminated, and their fluorescence is imaged onto the CCD, with the background now consisting only of scattered light.

simply

$$\mathrm{OD} = \ln\left(\frac{I_{\mathrm{background}}}{I_{\mathrm{absorption}}}\right). \tag{4.1}$$

The camera used to image the BEC cloud is a Basler A102f. The lens is an Infinity Photo-optical Infinimini, with the IF-2 objective and a DL doubling tube. This lens combination has a working distance of 100 mm, gives a magnification of 1x, and has a measured resolution of 4.5 μm per pixel. The probe beam is aligned to be normal to the UHV cell and intersect the atom chip. The camera and lens are aligned to the probe beam. The rough working distance is set by hand. Fine tuning of the focus is set with the focusing ring on the lens. The lens/camera combination is mounted on a pair of vertical steel rails, orthogonal to the atom chip. This allows the system to be easily raised and lowered for quick imaging at the MOT level or the atom chip level, as shown in Figure 4.17.

The probe timing sequence for absorption imaging is shown in Figure 4.18. The main advantage of the Basler, over other makes of camera, is that it allows a second picture to be taken while the first picture is being read out. The camera is triggered before the TOF, and begins exposing for a time t_{EXP}, which is greater than the readout time of the camera. The readout time varies based on the amount of the camera's sensor being utilized. A full frame readout for the Basler A102f is 90 ms. By exposing for longer than the readout time, this ensures that the second image will not finish exposing before the first image is done being read out, which would cause conflicts in the camera hardware. During the integration, before the TOF to be measured, there is no resonant light in the system.

Because the MEMS shutter is mechanical, there is a delay between the triggering TTL and the actual shutter opening, t_{TO}. Similarly, there is a delay between the triggering TTL and the actual shutter closing, t_{CD}. These set the minimum time the shutter must be open, and are taken into account when triggering. The MEMS shutter is held open for the span of the absorption and background pulses. A typical rise time of the MEMS shutter is t_{rise}=50 μs, and is triggered such that it is fully open at TOF (i.e., it is triggered t_{TO}+t_{rise}

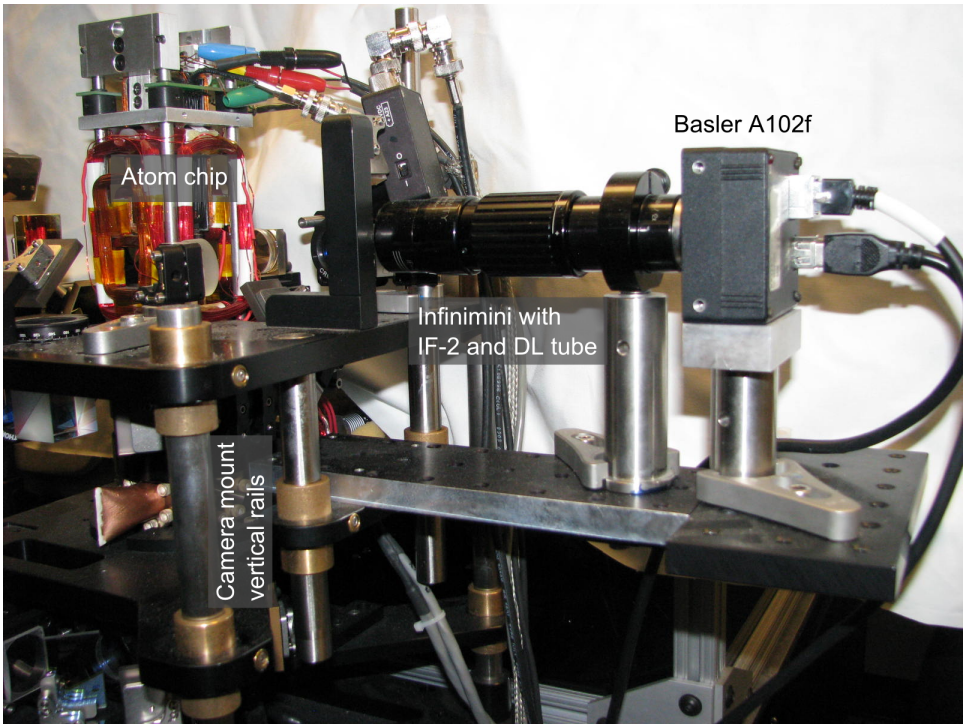

Figure 4.17: (Color) Photo of the camera mounting system in the cart optomechanics package. The probe beam is aligned to be normal to the UHV cell and intersect the atom chip. The camera and lens are aligned to the probe beam. The rough working distance is set by hand. Fine tuning of the focus is set with the focusing ring on the lens. The camera mount allows vertical translation that is orthogonal to the atom chip and UHV cell.

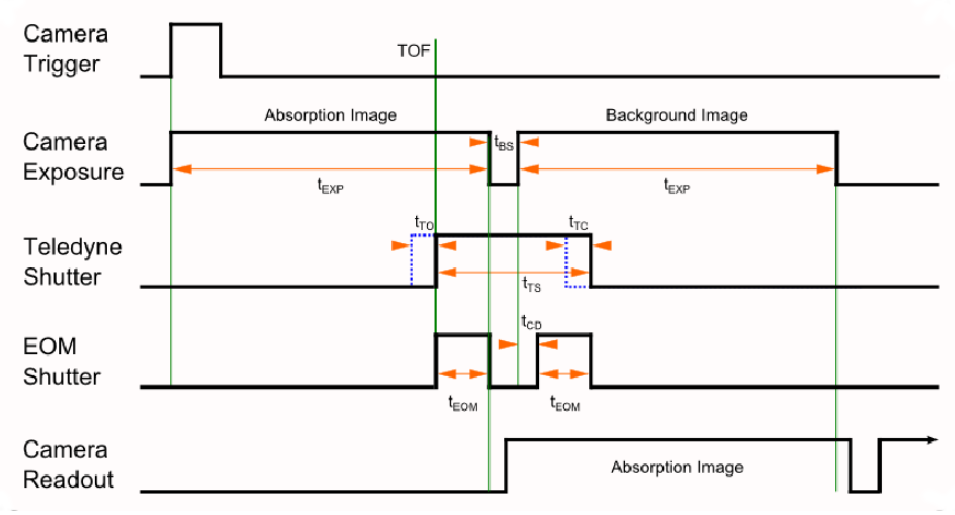

Figure 4.18: (Color) Diagram of the absorption imaging timing sequence in overlap mode. The camera is triggered before the TOF to be measured and begins exposing for a time t_{EXP} which is greater than the readout time of the camera. The absorption image is then taken so the falling edge of the probe pulse and camera coincide. Time t_{CD}, accounts for the delay the camera has from being triggered to the beginning of integration. An identical pulse to the first gives the background probe pulse, which is not resonant. The MEMS shutter closes shortly after the second pulse ends.

before TOF). The fiber-optic switch pulses the probe beam for t_{EOM}, which is typically 20 μs to 100 μs. The fiber-optic switch is used to fully control the temporal pulse shaping of the probe beam because its rise times are at the nanosecond level, and its repeatability is far superior to that of a mechanical shutter. The poor isolation of 25 dB the few milliseconds the MEMS shutter is open, but the fiber-optic switch is closed, does not effect the system.

Once the first fiber-optic switch pulse has finished, the absorption image camera exposure ends, and the CCD array is dumped to the readout pixels in one step. A small time between shots, t_{BS}, accounts for the pixel dump time. Between shots the probe is unlocked and pushed off of resonance. The camera is then triggered for its background exposure. A small delay, t_{CD}, accounts for the delay the camera has from being triggered to the beginning of integration. An identical fiber-optic switch pulse to the first gives the background probe pulse, which is now not resonant with any atoms that may still be in frame. The MEMS shutter closes shortly after the second switch pulse ends, and the camera continues to integrate in the dark until the absorption image has finished being read out, after which the background image can be read out.

This overlapping images technique allows as little as a 200 μs delay between probe pulses. Because AR coated cells are not currently utilized, the main source of imaging noise comes from intensity variations between the absorption and background images. This variation is mainly due to etaloning of the faces and diffraction from dust, which vary with thermal changes and vibrations. By reducing the time between shots, the structure in the background noise is reduced to near the camera noise threshold. Overlapping images only work when the stray resonant light (e.g., MOT light) has been extinguished for at least t_{EXP}. Imaging before this time relies on the more general technique where the fiber-optic switch pulse comes at the beginning of both the absorption image and background image (i.e., both timings are identical to that of the background image in Figure 4.18, where TOF is now the left-most green line). As documented in [52], this greatly increases our noise. However, when imaging at times just after the resonant light stages, the ODs and atom numbers being

measured are very large. In practice we do not need to overlap our shots until imaging clouds of 10^5 atoms or less, or ODs of 0.3 or less.

4.9 Optomechanics package

A custom optomechanics package was designed for tighter integration of the bulk optics and the UHV cell. It is shown in Figure 4.19. This replaces the optics table implementation, similar to that in [28], with a footprint less than a quarter of the size.

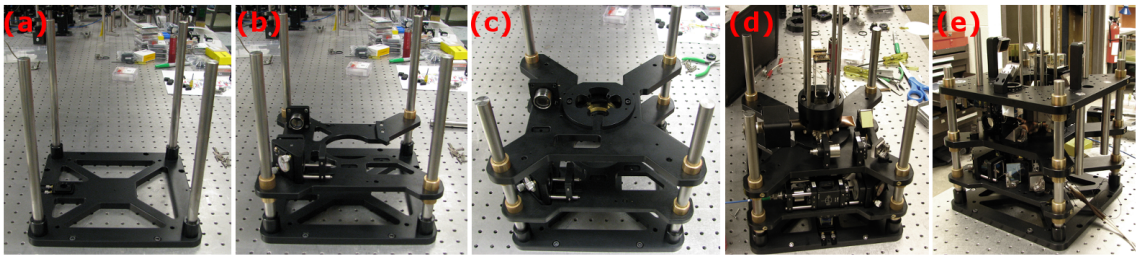

Figure 4.19: (Color) Cart optomechanics breakdown. (a) Baseplate with push beam optics. (b) $2D^+$ MOT optics stage. (c) Cell mounting stage. (d) Cell mounting stage with cell and some of the 3D MOT optics. (e) Full assembly with 3D MOT optics stage, but without coils and chip connectors [52].

The optomechanics package is designed with adjustable levels to accommodate variations in UHV cell production. The levels are made of anodized aluminum, and are press fitted with oil-impregnated brass bushings to act as the bearing surface against 5/8 in.-ground steel rod stock. The 5/8 in.-ground steel rod stock is press fit vertically into the bottom most level, which also has the push beam optics mounted on it. Clamps integrated into the bushing allow the levels to be locked into place. The $2D^+$ MOT level, 3D MOT level and cell mounting level are independent. The $2D^+$ MOT and 3D MOT optics can be aligned offline, and the UHV cell can be quickly and easily integrated into the system. The magnetic field coils are on rails to accommodate height variations. The optomechanics package is described in detail in [52].

4.10 Experimental sequence

This section will describe the experimental sequence for making BEC on the cart, followed by a couple of experiments on the cart that went beyond "standard" BEC production.

4.10.1 MOT, CMOT, PGC, OP

In the lower glass chamber, shown in Figure 3.1, a 2D MOT is generated with around 70 mW of cooling light detuned -2.5Γ from the $|F = 1\rangle \rightarrow |F' = 2\rangle$ cycling transition. Approximately 10 mW of repump light is used in the $2D^+$ MOT. Permanent magnets of 30 G/cm create a 2D quadrupole field with the axis of zero magnetic field aligned vertically. 5% of the cooling light is picked off and sent vertically through the cell where it retroreflects off the polished silicon pinhole. This "push" beam provides molasses cooling from the retroreflection, and momentum transfer to the atoms via the dark spot from the pinhole, which adds the "+" to $2D^+$ MOT. The $2D^+$ MOT increases the flux within the capture range of the 3D MOT by a factor of 3-10 over a 2D MOT. Fluxes as high as 1×10^9 atoms/s have been achieved.

The 3D MOT is generated by three retroreflected cooling beams with the same detuning as the $2D^+$ MOT. The 3D MOT is generated with around 50 mW of cooling power and 6 mW of repump power. The 3D MOT coils shown in Figure 4.12 provide a gradient of 10 G/cm to 15 G/cm during the 3D MOT loading stage. The 3D MOT is loaded to approximately 1×10^9 atoms in 1 s. At 25 ms before the end of the 3D MOT loading stage, the $2D^+$ MOT light is shuttered. After the 3D MOT loading stage is the compressed MOT (CMOT) stage. In the CMOT, the 3D MOT coil gradients are ramped to 2-3 times the MOT gradient, the cooling detuning is increased to -3Γ to -5Γ, and the repump is blue detuned around 30 Γ. The CMOT stage is typically 10-40 ms. This short stage causes a marked increase in density of the cloud by squeezing the atoms with the higher gradients, and further cooling the atoms by increasing the detuning of the cooling light. Blue detuning the repump effectively decreases

its interaction with the atoms. Typically, repump power is reduced to achieve this effect. However, this laser system does not have that ability. By decreasing the repump interaction, more atoms are pumped into the dark ground state, thus greatly reducing photon recoil pressure and increasing density [74].

After the CMOT stage, the 3D MOT quadrupole coil is switched off, and the repump detuning is jumped to zero, for sub-Doppler polarization gradient cooling (PGC). During PGC, or Sisyphus cooling [75], stray magnetic fields are carefully shimmed out to milligauss levels with the bias magnetic field coils, and the cooling light is further detuned to -8Γ to -12Γ. This stage lasts from 3-10 ms, and is the final laser cooling stage. Measured PGC temperatures for the BEC cart are as low as 8-10 μK, with typical temperatures of around 20 μK.

After PGC, all cooling light is shuttered, but the 3D repump light is left on for optical pumping (OP) [76]. A bias field provides Zeeman splitting of a few MHz, and a quantization axis for the atoms along the field. An OP beam hits the atoms at an angle of 5°-10° with respect to the quantization axis. The OP beam is circularly polarized, and blue detuned of resonance by 10 MHz, to couple the two Zeeman sublevels of $|m_F = i\rangle \rightarrow |m_F = i + 1\rangle$, as illustrated in [77]. OP changes the ground state sublevel of a large fraction the atoms, which are distributed among the $|F = 2\rangle$ Zeeman sublevels, to the $|F = 2, m_F = 2\rangle$ Zeeman sublevel. This increases our magnetic trap capture efficiency by a factor of 3. The OP stage typically lasts 0.5-1 ms, after which all laser light is extinguished.

4.10.2 Magnetic trapping and transport

After all of the resonant light is extinguished, the atoms are trapped magnetically, which is described in Chapter 2.1. The 3D MOT, CMOT, PGC, and OP stages occur in the same spatial location 15-20 mm below the atom chip. In order to load the atom chip magnetic trap, the two magnetic traps described in the next sections were designed to both trap and transport the atoms.

4.10.2.1 Ladder coil transport

Before the BEC cart was complete, 3D MOT and MT work was performed on an optical table, with the cell oriented horizontally. The horizontal orientation was necessary for implementing the ladder coil quadrupole transport geometry, because the strong axis of the magnetic trap it produced was required to hold against gravity, as shown in Equation 2.3. Quadrupole transfer is possible vertically, while maintaining the necessary optical access, as shown in [52], but the coil size (and thus power consumption) would need to be increased. In the ladder coil magnetic trap and transport scheme, 3D MOT atoms are captured in a quadrupole trap with the 3D MOT quadrupole coil. In transport, the 3D MOT quadrupole coil is linearly ramped down as the ladder coil quadrupole trap is ramped up. This adiabatically moves the atoms from the center of 3D MOT quadrupole coil to the center of the ladder coil. The procedure is repeated to transfer the atoms from the ladder coil to the chip quadrupole coil. In the geometry shown in Figure 4.20, the 3D MOT was loaded to approximately 1 billion atoms. After OP, approximately 80% of the 3D MOT atoms remain. The 3D MOT coils are snapped on after OP to 30-40 G/cm, which creates a tight and deep MT to hold against gravity. They are linearly ramped to zero over 200 ms to 300 ms. During that same time, the ladder coil is ramped to full field, with the same radial magnetic field gradient as the 3D MOT coil, but half the axial gradient because of its geometry. The axial gradient is orthogonal to gravity so the atoms remain trapped. The ladder coil is ramped down over 200 ms to 300 ms, and the chip coils are ramped up in the same way. The efficiency of the magnetic transport is approximately 50%.

As the atom cloud extent nears the chip, the chip Z-wire and the chip dimple-wire are ramped up to 3.25 A and 1.25 A, respectively, in order to create a magnetic trap with a vector magnetic field that adds to the chip-coil quadrupole field, so that the traps can be merged. Additionally, the chip wires create a strong repulsive barrier between the magnetic trap and the chip, which stops atom loss into the chip as the chip coil quadrupole trap is brought

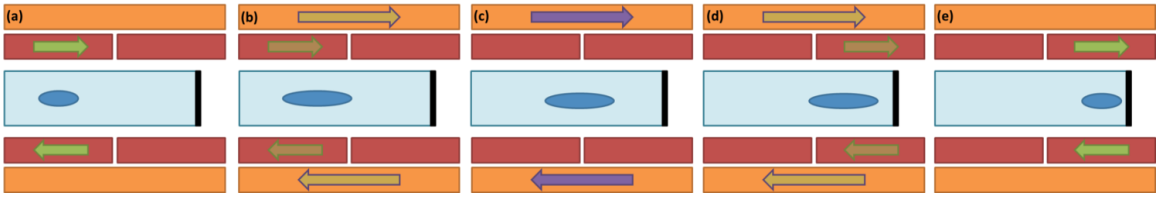

Figure 4.20: (Color) Quadrupole coil diagram for ladder transport showing the current ramping sequence. A magnetic trap is formed at the 3D MOT level in (a). The current in the 3D MOT quadrupole coils is ramped down as the ladder coil is ramped up in (b) and (c), moving the atoms towards the chip (black). The sequence is repeated in (d) and (e) to transfer the atoms to the chip quadrupole coils.

toward the chip, to overlap the chip wire magnetic trap. To mode match the macroscopic quadrupole trap to the chip dimple-wire trap, the chip coils were ramped adiabatically to approximately 120 G/cm, which spatially compresses the atoms. Adiabatic compression heats the atom cloud [78], but the chip trap is deep enough to hold them, and better efficiencies were achieved, of up to 30-40%, when the two traps were optimized for spatial mode matching. The cloud of atoms loaded into the dimple-wire trap was 120 million, a factor of 3-4 better than with the big-Z transport described in Section 4.10.2.2.

After loading atoms onto the vertically oriented atom chip and attempting RF evaporation, it was TOF imaging that proved to be a major obstacle. As stated earlier, the cell must be held horizontally in order to have the strong axis of the ladder coil MT holding against gravity. Because the atom chip is vertical, and the chip trap is only a few hundered microns from the chip (at most), the atoms cannot be simply dropped. The cloud is too close to the surface of the chip to image with a standard absorption beam, and the cloud would expand into the atom chip in under a millisecond. Instead, the atoms must be pushed away from the chip for TOF measurements, which distorts the Gaussian profile of the atom cloud, and makes temperature measurements difficult. In the end, it was decided that a vertical orientation for the cell was prudent. One solution to implementing the cell in a horizontal orientation would be with a 45° bonding surface polished into the 3D MOT cell, with a windowed atom chip similar to that in Section 3.1.3.2, so that the atom chip has the

orientation shown in Figure 4.21.

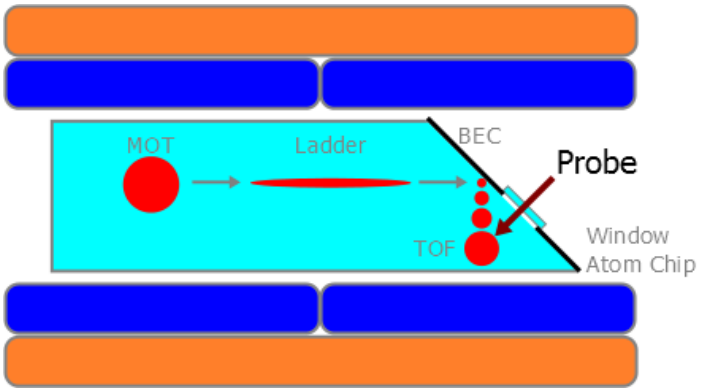

Figure 4.21: (Color) Diagram of a 45° chip mounted to a horizontally oriented cell. Ladder transport is utilized to load atoms onto the windowed atom chip. Because the atom chip is at 45°, conventional TOF absorption image can be taken through the window.

4.10.2.2 Big-Z transport

With the cell oriented vertically, the big-Z coil, shown in Figure 4.12(b), is used to transport atoms from the 3D MOT level to the atom chip. After PCG, the big-Z coil is snapped on from 0 A to 20 A, along with a bias field of $(B_x, B_y, B_z) = (14, 45, 0)$ G, which creates an IP trap at the 3D MOT level that is approximately $(\omega_x, \omega_y, \omega_z) = (0.44, 5.0, 5.0)$ Hz and 43 G deep. The big-Z current is linearly ramped down, along with the bias fields, over 700 ms, which moves the trap towards the atom chip. When the extent of the atom cloud is very near the chip, the chip Z-wire is ramped over 50 ms from 0 A to 5 A, which creates both a chip trap that adds to the big-Z potential, and also a barrier that prevents atom loss into the chip, as described in Section 4.10.2.1. The big-Z coil's main leg is approximately 32 mm in length. The chip Z-wire's main leg is 20 mm in length. The compression wires, shown in Figure 4.12(b), are oriented above the chip Z-wire legs. The compression wires are ramped to 10 A over 50 ms to increase the axial trap frequency of the big-Z magnetic trap, better mode matching it to the chip-Z, which increases the chip loading efficiency by 10% or more. This method of MT transport, from the 3D MOT level to the atom chip level was

used to create BEC, and is described in the next sections. The temperature of the atoms after the big-Z transport and loading into the initial chip trap was measured to be a few hundred microkelvin.

4.10.3 Chip trap, evaporation, and BEC

At the moment when the big-Z has been ramped to 0 A, the chip-Z has been ramped to 5 A, at which point the atoms have been transferred to the atom chip Z-wire trap. The atom chip vias (and wires) cannot sustain 5 A, but the higher current makes a spatially larger and deeper trap, which is centered up to $z_0 = 500\,\mu$m from the chip. This trap is necessary for efficient transfer from the big-Z magnetic trap to the chip Z-wire trap. Thus, the chip-Z is only at 5 A for 1 ms (at the peak of the ramp), and then is immediately ramped down to its value where we start RF evaporation, 3.25 A, over 300 ms. At the same time the chip-Z is ramping down, the dimple wire is ramping up from 0 A to 1.25 A. The ramp from chip-Z trap to chip dimple trap (Z-wire plus dimple wire) is an adiabatic process in a conservative magnetic trap potential. However, due to collisions, we see an increase in density in the center of the cloud. Approximately 30 million atoms are transferred from the big-Z MT to the chip Z-wire MT, with 10 million in the dimple trap. The initial RF evaporation potential is shown in Figure 4.22. The calculated trap is a distance $z_0 = 115\,\mu$m below the chip surface, with trap frequencies $(\omega_x, \omega_y, \omega_z)$ =(610 Hz,6.7 kHz,6.7 kHz). The dimple trap had a measured lifetime of 6.5 s.

4.10.3.1 RF evaporation sequence and BEC

Atoms are initially in both the dimple and chip-Z trap, as shown in Figure 4.22. The field for RF evaporation is produced by the RF coil shown in Figure 4.12(b). The RF is turned on well above the atoms in the chip Z-wire trap, and is ramped down to just above the atoms in the chip Z-wire trap in several milliseconds, where RF evaporation begins. The full RF evaporation is divided into five stages, all of equal duration, 300 ms. All RF ramps

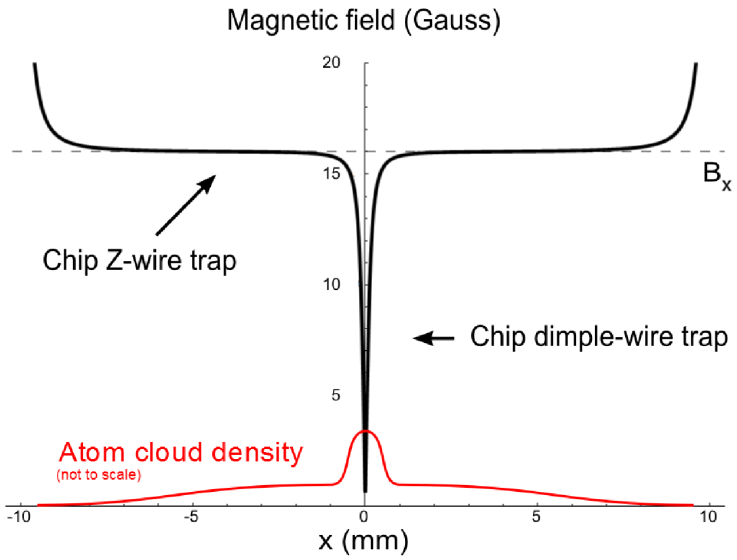

Figure 4.22: (Color) Plot of the RF evaporation chip dimple magnetic trap. The chip Z-wire trap is the plateau that extends from -10 mm to 10 mm along the x-direction, with a trap bottom of $B_x = 16\,\mathrm{G}$ and trap top of $B_x = 40\,\mathrm{G}$. The dimple trap can be seen in the middle, with a trap bottom of 2 G and an effective trap top of $B_x = 16\,\mathrm{G}$. A representation of the atom cloud distribution is shown in red.

are linear and the starting frequency of each subsequent stage is the ending frequency of the previous stage. The power was kept nearly constant at around 1 dBm through the first four stages. Evaporation stage A cuts from just above the atoms in the chip Z-wire trap to the top of the dimple trap, kicking out the higher potential energy atoms sitting in the chip-Z trap, but still providing cooling to the atoms in the dimple through efficient evaporation. After stage A the dimple trap is adiabatically loosened to avoid excessive three-body loss. By reducing the bias fields, the calculated trap frequencies of evaporation stages B, C, and D are $(\omega_x, \omega_y, \omega_z)$ =(340 Hz,2.3 kHz,2.3 kHz). The next three evaporation stages, B, C, and D, each cut approximately half of the remaining trap depth. For the trap shown in Figure 4.22, the depth of the dimple trap is 14 G. Stage B cuts from 16 G to 9 G, stage C cuts from 9 G to 5.5 G, and stage D cuts from 5.5 G to 3.75 G. In evaporation stage E, the RF power was lowered to around -4 dBm to reduce power broadening of the knife [79], and the RF sweeps down to the onset of degeneracy.

After evaporation stage E, the trap is again loosened adiabatically for imaging. The imaging trap has calculated trap frequencies of $(\omega_x, \omega_y, \omega_z)$ =(200 Hz,1.2 kHz,1.2 kHz). Figure 4.23 shows the OD distribution of the onset of condensation after evaporation stage E. In Figure 4.23(a), the RF sweep is 90 kHz above the trap bottom, which produces a cloud of 6.9×10^4 non-condensed atoms at a temperature of 1.92(6) μK. In Figure 4.23(b), the RF sweep is 60 kHz above the trap bottom, which results in a partially condensed cloud of 5×10^4 atoms at a temperature of 1.58(8) μK. In Figure 4.23(c), the RF sweep is 30 kHz above the trap bottom, which results in a nearly pure condensate of 1.9×10^4 atoms. The calculated transition temperature in the dimple trap is 1.1 μK. Images were taken after 5 ms of free expansion. The total time for production, from the beginning of the 3D MOT loading stage to BEC, was around 3 s, which was on par with other fast, atom chip based BEC production [80].

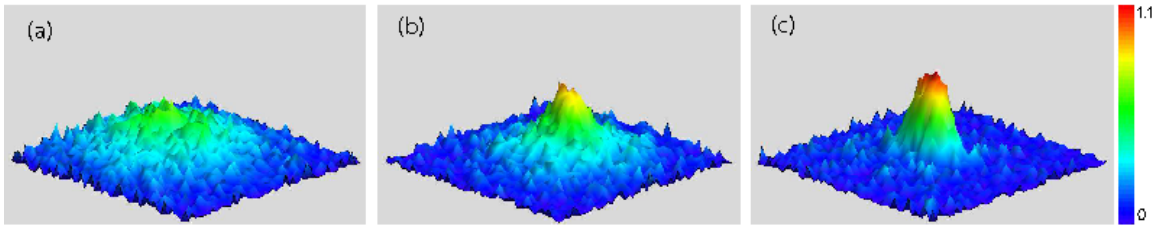

Figure 4.23: (Color) The measured OD distributions showing the onset of condensation using RF evaporation: (a) a cloud of 6.9×10^4 non-condensed atoms at a temperature of $1.92(6)\,\mu$K; (b) a partially condensed cloud of 5×10^4 atoms at $1.58(8)\,\mu$K; (c) a nearly pure condensate of 1.9×10^4 atoms. Images were taken after 5 ms of free expansion.

4.11 Experiments beyond BEC

After the initial demonstration of BEC, two additional experiments were performed using the BEC cart platform.

4.11.1 Double BEC

As a test of the versatility of the standard BEC chip, two dimple traps were generated with a single Z-wire trap using the current configuration shown in Figure 4.24. Dimple trap A was created by running current along the dimple wire represented by the blue arrow. The white arrow made dimple trap B and is the center dimple, which was used in the previous experiments.

Equal current was run in each dimple. The Z-wire trap loading was optimized so that both dimple traps had approximately the same starting atom number, 3 million atoms in trap A and 3.3 million in trap B. After an optimized RF evaporation sequence similar to the sequence above, two partially condensed BECs of 30k atoms and 60k atoms in trap A and B, respectively, were created, with equal peak ODs of 1.4.

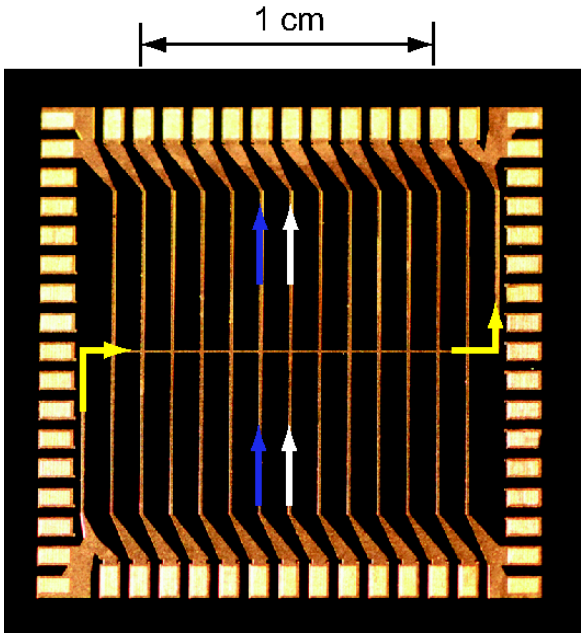

Figure 4.24: (Color) Photo of the atom chip used to create two simultaneous BECs. A second dimple wire (blue) was used in addition to the center dimple (white) to create two dimple traps 1 mm apart.

4.11.2 Direct evaporation sequence

In general, the system for RF evaporation adds to the size, complexity, and power consumption necessary for producing a BEC. Du and Oh proposed a novel way of performing forced evaporative cooling without inducing spin-flips, but rather by directly lowering the magnetic field trapping potential, shown in Figure 4.25, utilizing a chip H-wire trap [81]. In almost all configurations that make magnetic traps with traditional external coils, as the trapping potential is lowered, the trap frequency is also lowered. This lowering of the trap frequencies reduces the rethermalization rates, and does not lead to efficient RF evaporative cooling of the atoms. However, the problem of inefficient, direct-forced evaporative cooling in external coil magnetic traps can be overcome with a suitable choice of atom chip trap [82]. The atom chip used in this experiment is described in Section 3.1.3, and the direct evaporation was performed in a dimple trap, described in Section 2.2.3. In general, a 3D harmonic trap can be described by eight parameters: the center of the trap, which is given by three spatial coordinates, the trap's three eigenfrequencies, the trap depth U_d, and trap minimum B_m at the trap center.

With the dimple trap geometry things get a bit simpler. The trap is always centered above the junction of the dimple- and Z-wires, namely $x_0 = y_0 = 0$. Additionally, we assume that the trap has an axisymmetric shape, i.e., that there are only two eigenfrequencies, the loose axial eigenfrequency $B''_{\parallel}$ and the tight radial eigenfrequency $B''_{\perp}$. This constrains three parameters and leaves the trap described by only the remaining five. Experimentally, there are four independent knobs to turn in which to control the trap parameters: the Z-wire current I_0, dimple-wire current I_d, x-bias field B_{0x}, and y-bias field B_{0y}. For infinitely thin wires, the trap height z_0 does not affect the direct evaporation sequence, and so it does not need to be controlled. This leaves us with four parameters and four knobs. In theory, there is the control necessary to lower the trap depth while keeping the trap frequencies constant, and the trap bottom high enough to avoid Majorana spin-flip losses.

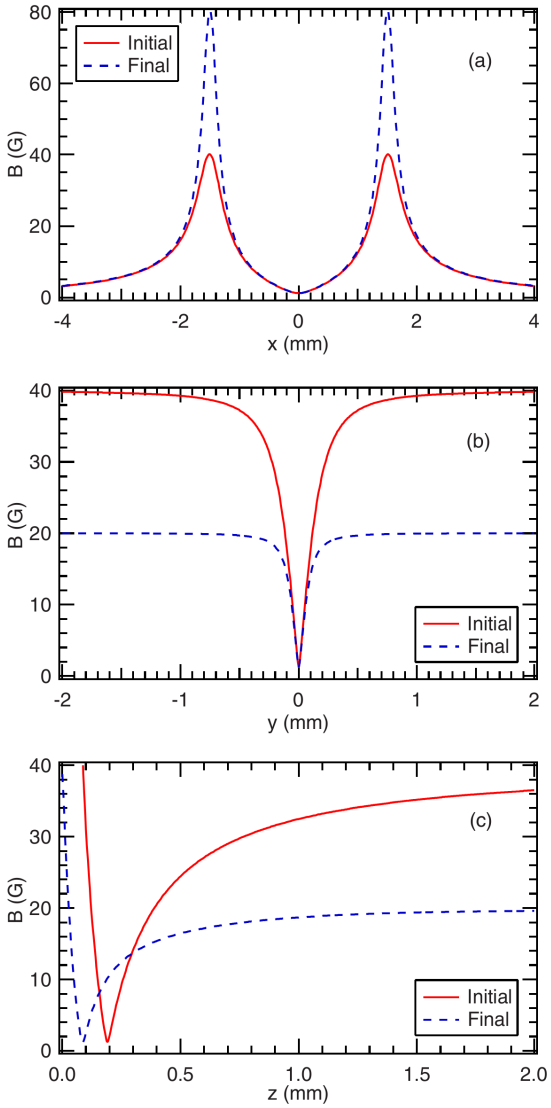

Figure 4.25: (Color) Plots of a chip H-wire scheme for forced direct evaporation in a magnetic trap. The magnetic field in the x-, y-, and z-dimensions are shown in (a), (b), and (c), respectively. The solid red line indicates the initial trap with parameters $I_0 = I_h = 4\,\mathrm{A}$, $B_{0x} = 0\,\mathrm{G}$, and $B_{0y} = 40\,\mathrm{G}$. The dashed blue line indicates the final trap with parameters $I_0 = 1\,\mathrm{A}$, $I_h = 4\,\mathrm{A}$, $B_{0x} = 0.64\,\mathrm{G}$, and $B_{0y} = 20\,\mathrm{G}$. Image credit [81].

However, atom chip traces are not infinitely thin. By solving the system of equations for the infinitely thin trace model, lowering the trap depth, while maintaining trap frequencies and minimum, causes the trap position z_0 to move closer to the atom chip. A more realistic model, accounting for the 100 μm width of the main trace and 20 μm width of the dimple trace (detailed in Appendix B), was used to estimate trap parameters as the atoms moved closer to the chip, to within 100 μm (the Z-wire trace width) of the chip. When the magnetic trap center z_0 moves to within the trace width of the atom chip, the trace can no longer be thought of as infinitely thin. The trace begins to look like a sheet of current, which flattens out the trap bottom and decreases the trapping frequencies.

Stage	I_z (A)	I_d (A)	B_{0x} (G)	B_{0y} (G)	U_d (G)	$\bar{\omega}$ (Hz)	B_m (G)	z_0 (μm)	t (ms)
Initial	3.25	1.25	25.2	42.3	41.6	983	7.7	137	N/A
A	2.2	1.25	14.4	19.8	21.9	536	2.5	204	400
B	1.1	0.55	8.1	8.1	7.9	216	3.6	222	400
C	0.58	0.3	4.7	4.1	3.9	144	2.3	219	700
D	0.23	0.06	3.8	3	1.9	171	2.7	119	400
Compress	3.25	1.25	14.8	36	38	1652	0.5	175	400
Final RF	3.25	1.25	20.8	36	35	785	6.1	165	800

Table 4.1: Trap parameters used for direct evaporative cooling. I_z, I_d, B_{0x} and B_{0y} are the experimentally controlled parameters. U_d, $\bar{\omega}$, B_m and z_0 were calculated using LiveAtom finite element analysis. Direct evaporation is performed during stages A through D. The "Compress" stage was used to make a BEC with a 2.9MHz RF sweep. The "Final RF" stage was used to make a BEC with a single frequency RF knife.

In order to account for the loosening of the trap as the trap position z_0 decreased, a partial constraint of keeping z_0 greater than 100 μm was imposed. This meant some loosening of the trap must be tolerated. The parameters of the direct evaporation sequence are shown in Table 4.1. After the initial chip trap, the direct evaporation sequence was divided into four stages, labeled A through D. The final values for the experimental parameters each stage were optimized for maximum phase space density (PSD), which are shown in Table 4.2. The full direct evaporation sequence lowered the trap depth by a factor of 20. The full direct evaporation sequence reduced the trap frequency by less than a factor of 6, which proved to

be a favorable enough ratio for efficient evaporation. The initial and final traps are shown in Figure 4.26.

Absorption images of the initial chip trap and the direct evaporation stages are shown in Figure 4.27 after 3 ms of free expansion. The absorption image of the initial trap of 3.7×10^7 atoms, shown in Figure 4.27(a), is zoomed in to show the increased atom density in the dimple trap, which is off-center to the right. The cloud extends past the border of the image, with similar profile to that shown in Figure 4.22. Shown in Figure 4.27(b), after evaporation stage A, most of the atoms in the initial trap not in the dimple trap have been evaporated away, which is similar to the RF evaporation stage A in Section 4.10.3.1. After evaporation stage A, 1.8×10^7 atoms are in the dimple trap. Even through the trap frequency was reduced in evaporation stage A, the OD has visibly increased, which is a clear sign of efficient evaporation and an increase in PSD. After evaporation stage B, shown in Figure 4.27(c), 5.6×10^6 atoms remain, and the OD has increased further. In evaporation stages C and D, shown in Figure 4.27(d) and (e), the OD remains unchanged, even though the number of atoms was roughly halved during each of these stages, to 2.6×10^6 atoms and 1.0×10^6 atoms, respectively. The peak OD in these images is 1.5.

After stages B, C, and D, the atoms were dropped and allowed to freely expand between 2 ms and 10 ms. Each TOF image was fit to a two-dimensional Gaussian function, and the fitted widths were used to extract the in-trap size and temperature of the cloud, shown in Table 4.2. The in-trap temperature gives the thermal de Broglie wavelength

$$\lambda_{dB} = \sqrt{\frac{2\pi\hbar^2}{mk_BT}}. \tag{4.2}$$

The peak density in the trap, assuming it's axisymmetric, is given by

$$n_{pk} = \frac{\mu m}{4\pi\hbar^2 a}, \tag{4.3}$$

where

$$\mu = \frac{1}{2}m\omega_i^2 x_i^2, \tag{4.4}$$

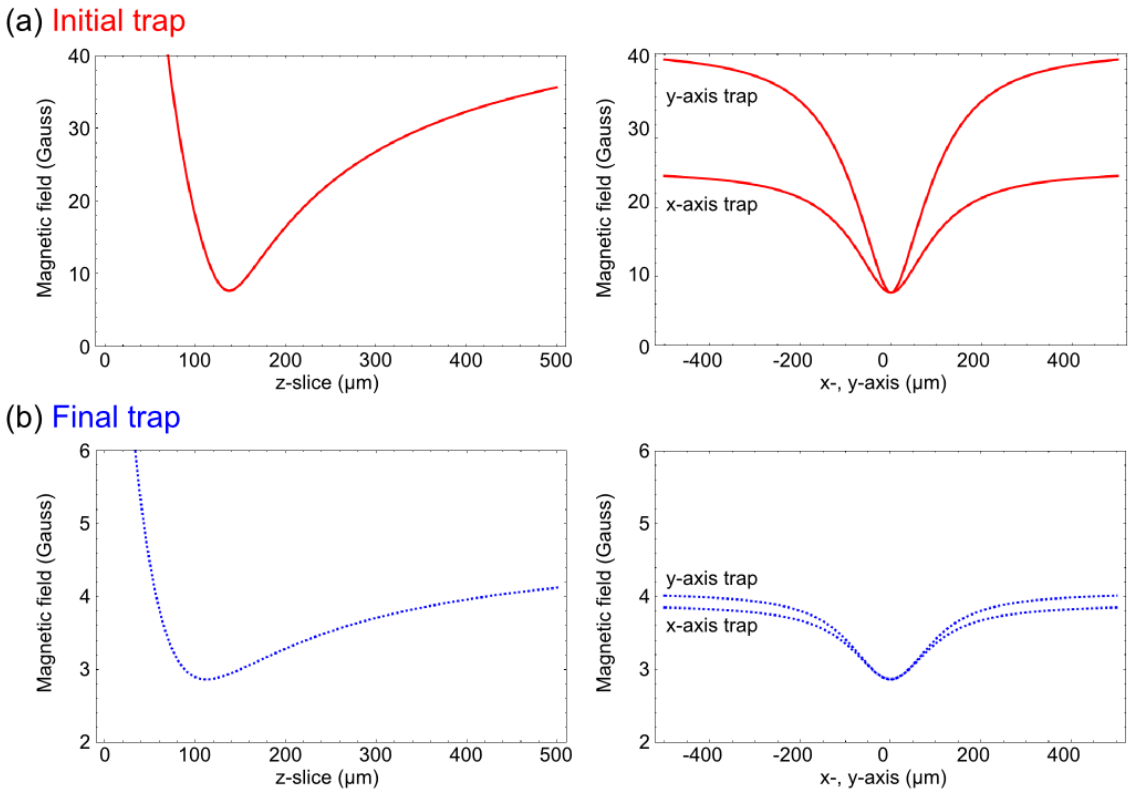

Figure 4.26: (Color) Plots of the initial and final traps for direct evaporation. (a) The solid red lines indicate the initial magnetic trapping fields. The magnetic field axis is from 0 G to 40 G. (b) The dashed blue lines indicate the final magnetic trapping fields. The magnetic field axis is from 2 G to 6 G. Left: Magnetic field along z-axis direction for the initial and final trap. Right: Magnetic field vs. x-, y-directions, at $z = z_0$, for the initial and final trap.

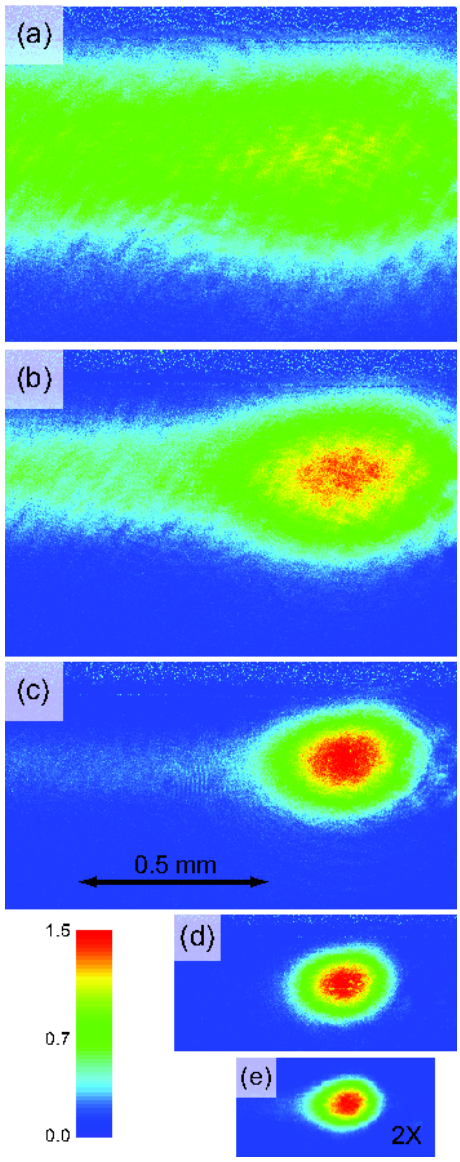

Figure 4.27: (Color) Absorption images showing OD after 3 ms of free expansion. (a) 3.6×10^7 atoms in the initial chip trap; (b) 1.8×10^7 atoms after direct evaporation stage A; (c) 5.6×10^6 atoms after stage B; (d) 2.6×10^6 atoms after stage C; and (e) 1.0×10^6 atoms after stage D.

and the PSD shown in Table 4.2 is given by

$$\text{PSD} = n_{pk}\lambda_{dB}^3. \tag{4.5}$$

In the initial trap, and after stage A, the atom cloud was too hot to get a reliable TOF measurement, as released atoms would collide with the chip and be lost. However, assuming evaporation efficiency in these stages to be similar to those in Table 4.2, then it is expected that the PSD of the initial cloud was increased by four orders of magnitude. At this point the experiment was limited by the width of the traces, and further attempted cooling of the atoms only led to atom loss.

Stage	T_x (μK)	T_y (μK)	σ_x (μm)	σ_y (μm)	PSD
B	94(1)	50.6(3)	254(7)	143(3)	$6.0(5) \times 10^{-7}$
C	28.5(2)	21.8(1)	160(2)	86(2)	$6.7(4) \times 10^{-6}$
D	14.0(1)	10.6(1)	122(1)	38(2)	$5.2(9) \times 10^{-5}$

Table 4.2: Temperatures T_x and T_y, in-trap cloud sizes σ_x and σ_y, and phase space densities PSD at the end of direct evaporation stages B, C, and D.

To take the final step and evaporate the atoms to degeneracy, two methods were used: a standard RF sweep and a fixed frequency RF knife. After stage D of the direct evaporation sequence, the atoms were adiabatically compressed into a deep, tight trap to allow for efficient rethermalization, and a BEC was produced with a 2.9 MHz sweep, significantly smaller than the 40 MHz sweep from [71]. The fixed frequency RF knife was held at 5 MHz, which was just above where the hottest trapped atoms are sitting. The trap bottom was then raised by increasing B_{0x}, pushing hotter atoms into the RF knife. Figure 4.28 shows the OD image and cross-section of a partially condensed BEC produced with the fixed frequency RF knife method, after 4 ms TOF expansion with approximately 2.2×10^4 atoms. The cloud was left partially condensed to highlight the bimodal distribution the condensed atoms form with the thermal background. The blue line is a bimodal fit, which is the sum of a Gaussian distribution for the thermal atoms, and an inverted paraboloid for the Thomas-

Fermi distribution in the center [73].

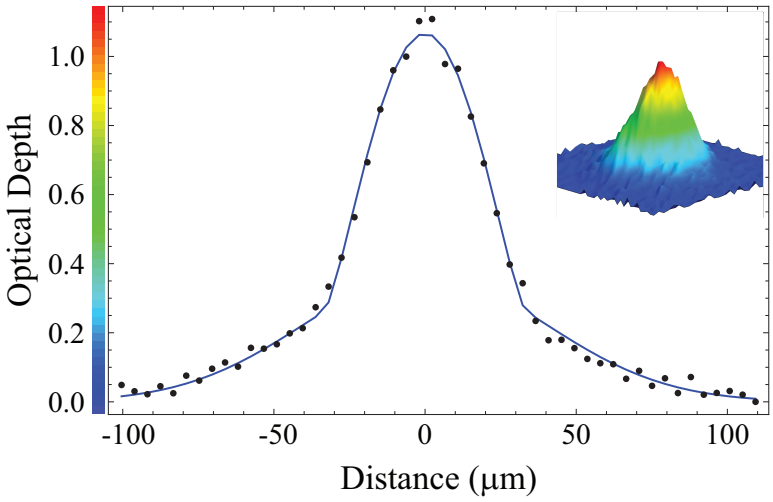

Figure 4.28: (Color) The measured OD of a BEC produced using a combination of direct evaporation and single-frequency RF evaporation. The image was taken after a free expansion of 4 ms. The black data points are an average of the three rows of pixels that pass through the center of the cloud. The blue line represents the best-fit to the sum of a Gaussian thermal component and paraboloid condensate core. The clear presence of a "kink" in the wings indicates partial condensation.

Because of the limitation imposed on direct evaporation by the trace width, the sequence could be further extended by making the chip traces narrower. Unfortunately, this limits the maximum current handling of the chip. The approach shown in Figure 3.7, but not implemented here, is to have a thinner trace run parallel to the main trace. The trap center can be adiabatically transferred to be over the thinner trace after the initial direct evaporation, where the atoms can be further cooled. This would theoretically allow the trap position z_0 to be five times smaller before the trace appears as a sheet of current rather than approximated by an infinitely thin line. Additionally, at very close range, Johnson noise will affect lifetime [83], but can be mitigated with the thinner traces [84].

4.11.3 Demonstration of portability

The ultimate goal of the BEC cart was, as stated at the beginning of this chapter, to demonstrate a portable BEC system. In the spring of 2010, the BEC cart was loaded into a

moving truck, and driven over 1200 miles from Boulder, CO to Portland, OR for the annual APS March Meeting. After about a day of unpacking and setup in the exhibition hall, and realignment and optimization, the system was able to produce BEC. This was made all the more remarkable since it was in an uncontrolled, non-laboratory environment. A bimodal distribution is clearly visible in Figure 4.29 (if you squint hard enough). Other groups have demonstrated portability [85], but to our knowledge, at the time this was the first ever public demonstration of BEC.

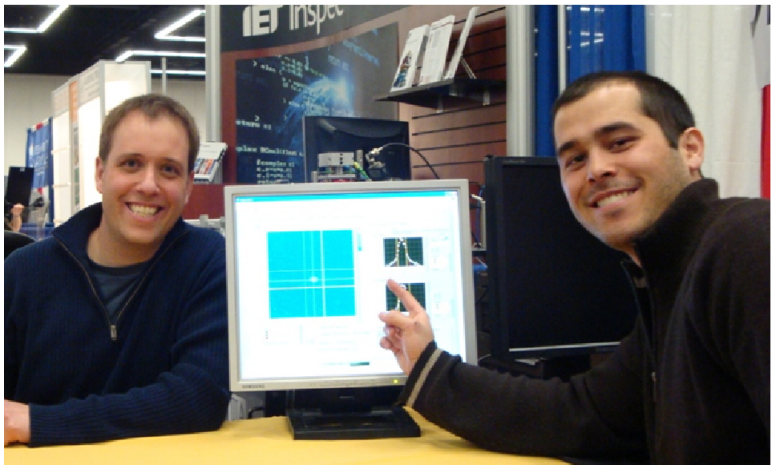

Figure 4.29: (Color) Photo of the BEC cart at the 2010 APS March Meeting.

Chapter 5

The AQuA Program—neutral Rydberg atom quantum computing

The ambitious goal of the Atomic Qubit Array (AQuA) program is to develop and demonstrate a continuously operating 64-element atomic qubit array. The final goal is to demonstrate, for the first time in a neutral atom system, all necessary control, readout, and initialization capabilities in a site selective fashion that fulfills the DiVincenzo criteria [86]. The quantum information in the qubit is stored in the atomic ground states of cesium. Two-qubit gates are based on exciting atoms to Rydberg states, which turns on a strong long-range interaction, as discussed in Section 1.2. The goal of the Cold Atom Technology (CAT) group, under which the work in this dissertation falls, is to implement site selective, on-demand atom reloading, and thereby demonstrate the principle scalability of neutral atom qubits to arbitrarily long quantum computations.

Neutral atom qubits held in optical traps have finite lifetimes due to collisions with thermal background atoms in the vacuum chamber. For the sake of discussion, imagine an extreme high vacuum of 10^{-4} nanotorr. Such conditions are feasible with cryogenic systems, or other specialized approaches [87], but are exceedingly difficult to achieve in a small footprint, compact system. Even if that vacuum level were reached, there would still exist a finite trap lifetime of only about one day. Because the goal is eventually to develop a quantum computer that can run arbitrarily long algorithms, atom loss is still an issue.

Our approach to solving this problem is shown in Figure 5.1. The AQuA cell device, which was developed in collaboration with ColdQuanta, Inc., and the Sarnoff Corporation,

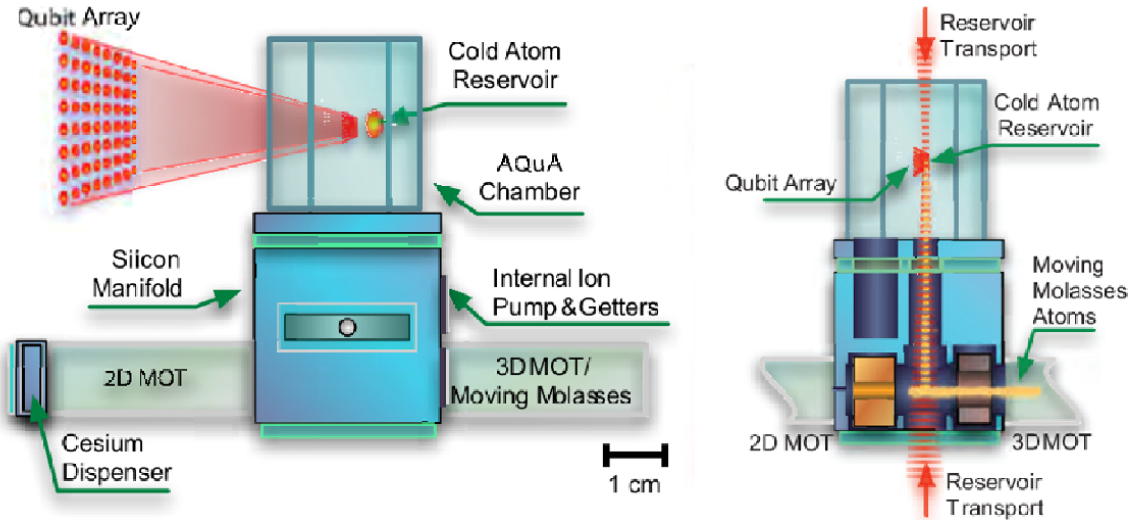

Figure 5.1: (Color) Concept for continuous reloading of the Rydberg atom array. The lower section is the atom collection region, where laser cooling and trapping collects and pre-cools atoms. The lower section is optically isolated from the AQuA chamber. A beam of pre-cooled atoms is non-resonantly optically transported to the AQuA chamber, where it is captured in a reservoir. The cold atom reservoir supplies pre-cooled atoms for single site reloading of the qubit array.

is discussed in detail in Section 3.5. The AQuA cell is a small footprint system that will provide a source of pre-cooled atoms, with the goal of maintaining excellent vacuum in the range of 0.1 nanotorr, which translates into a 100 s atom lifetime in the qubit array. This lifetime was chosen because it is long enough that the array can be continuously monitored for atom loss, and atoms at individual sites can be reloaded in the array as needed.

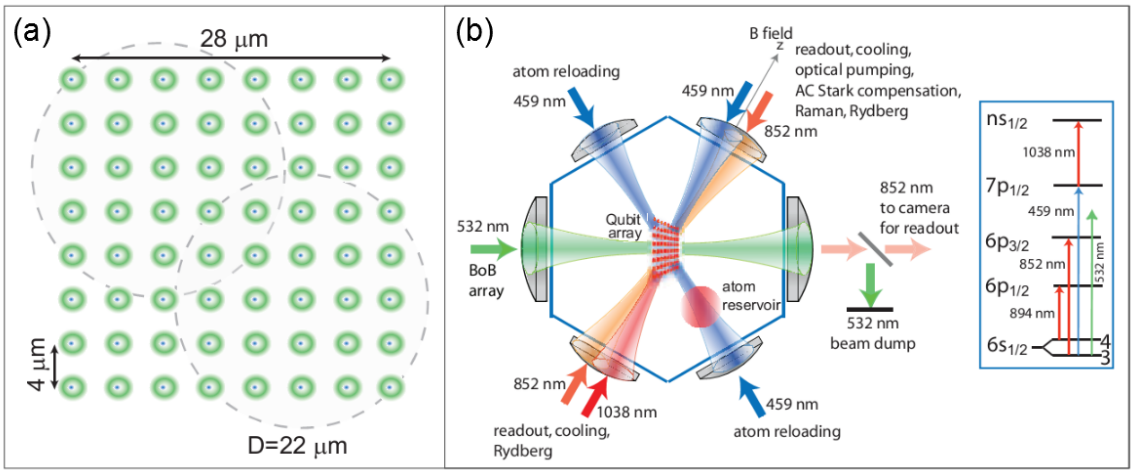

Figure 5.2: (Color) Qubit array and laser beam layout in the Hex cell. (a) Diagram of the 64 qubit array. Individual qubits are held in blue detuned traps 4 μm apart. Total array size is 28 μm $\times$ 28 μm. The blue dashed line of diameter D=20 μm represents the range of the Rydberg interaction, which can interconnect any two qubits with a single intermediate operation. (b) Top view of the Hex cell optical setup. Five laser frequencies enter the cell from the six sides via optics placed outside vacuum.

A diagram of the qubit array is shown in Figure 5.2(a). The total array size is 28 μm $\times$ 28 μm. The blue dashed line of diameter D = 20 μm represents the range of the Rydberg interaction, which can interconnect any two qubits with a single intermediate operation. The array itself will be 64 individual blue detuned traps with a separation of 4 μm [46, 48]. Because the atoms sit at a minimum of the trapping light intensity, coherence times are improved by reducing undesired trap-induced AC-Stark shifts and scattering of trapping light photons. The blue detuned traps will also trap the atoms when they are in the Rydberg state, which is an improvement over previous attempts [88]. The AQuA cell isolates the atom production region from the qubits, which will be held in an array in the

hexagonal (Hex) cell, shown in Figure 5.2(b). A hexagonal cell geometry was chosen for optical access. Five laser frequencies enter the cell from the six sides via optics placed entirely outside vacuum, which improves the ultimate vacuum quality. *Ex vacuo* optics allow the use of commercially available microscope objectives, and allow separate optimization of vacuum and optical alignment systems.

5.1 Laser system

The resonant laser system, at a wavelength of 852 nm, was designed around three Vescent D2-100-DBR-852 distributed Bragg reflector (DBR) diode laser systems and a New Focus VAMP TA-7616 tapered amplifier (TA). In addition to the resonant lasers, an IPG YLR-30-1064-LP-SF, which is a 30 W, linearly polarized, single frequency, 1064 nm fiber laser, was used for red detuned dipole trapping. A block diagram of the laser system is shown in Figure 5.3.

DBR laser diodes are very sensitive to back-reflected light. For all three DBRs, the output was collimated, sent through an optical isolator (OI), which provides 30 dB to 35 dB, and then through an anamorphic prism pair for beam shaping. In general, one OI is sufficient. However, because of the precise nature of single-mode fiber coupling, the overlap of the back-reflection with the output beam path is near perfect, and enough light can reach the diode to provide unwanted feedback. Therefore, all three beams were sent through an additional OI, for a total isolation of 60 dB to 70 dB.

The middle DBR in Figure 5.3 provided the cooling light. After the second OI, 5-10 mW of the cooling laser was picked off from the main beam line for locking to an SAS module. The locking beam was shifted 145 MHz to the blue via the second diffracted order of an 80 MHz center-frequency AOM, which was driven at 72.5 MHz. The blue-shifted light was locked to the $|F = 4\rangle \rightarrow |F' = 5\rangle$ cycling transition. With the laser locked, the light in the main beam line is red shifted from the cycling transition by 145 MHz. Around 10 mW of the main beam line was picked off and shifted into resonance with the cycling transition via

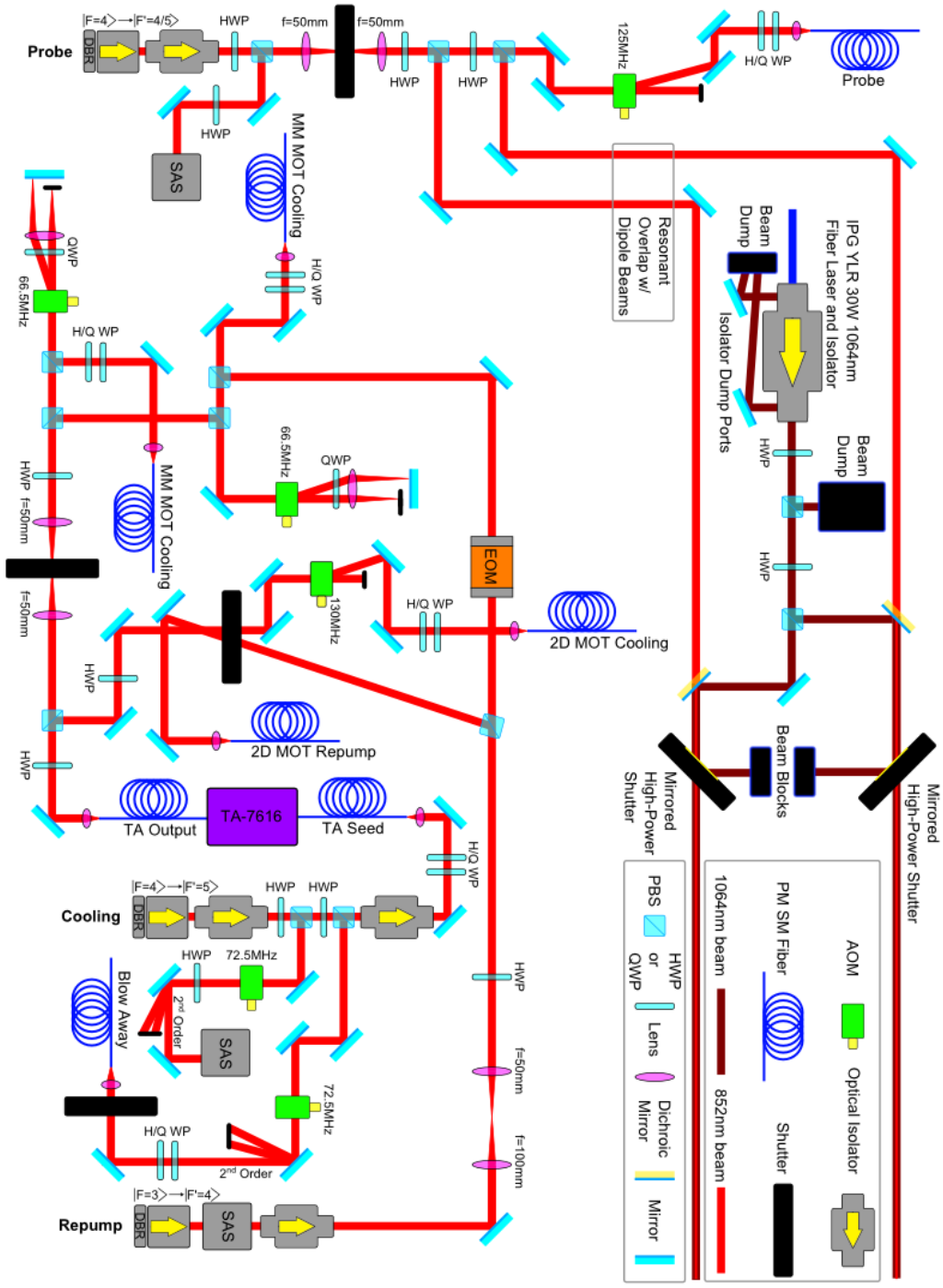

Figure 5.3: (Color) Block diagram of the quantum computing laser system. Three DBR lasers provide resonant light at 852 nm for cooling, repumping and probing of cesium. All three DBR lasers are locked to separate SAS modules. A TA provides the high power cooling light. The resonant light is fiber coupled before being sent into the system. A high power 1064 nm fiber laser provides red detuned dipole trapping light. The 1064 nm light is sent into the system in free space. Two resonant beams are spatially overlapped with the 1064 nm light via a dichroic mirror for alignment purposes.

the second diffracted order of another 80 MHz center-frequency AOM, which was driven at 72.5 MHz, and was fiber coupled. This "blow away" beam was pulsed between absorption imaging shots to push the atoms out of the imaging region, allowing for a shortened time between images. The remaining power in the main beam line was sent through an additional OI, because of the ASE produced by the TA, and 15 mW of fiber coupled light was used to seed the TA.

The output of the TA was split into two beams: the 2D cooling and the moving molasses (MM) cooling. The 2D cooling was blue shifted by a 120 MHz center frequency AOM, which was driven at 130 MHz, to have a detuning of -2.9 Γ from the cycling transition, where the linewidth of Cesium is $\Gamma = 2\pi \cdot 5.2\,\text{MHz}$. The 2D cooling was sent through a mechanical shutter before the fiber coupling. The fiber coupled output power of the 2D cooling is around 50 mW. The MM cooling was focused in a 1:1 telescope through a mechanical shutter to decrease the shuttering rise and fall times. It was then split into two beams. Each MM beam was sent through an 80 MHz center frequency AOM in the "cat's eye" double-pass configuration [50]. The cat's eye configuration greatly increases the range of frequency sweep on the AOM that can be achieved without affecting beam pointing at the output. Decoupling the frequency shift in the MM MOT beams from the fiber-coupled output power of the beams is critical, because the MM MOT relies on relative frequency shifts to accelerate the atoms. If this is coupled to beam power balancing, then precise control is lost. Each AOM was driven independently, at a center frequency of 66.5 MHz, to achieve a detuning of -2.3 Γ from the cycling transition. Independent drivers allow a computer controlled voltage to shift the center frequency up or down by an amount δ, which, when applied symmetrically, creates a relative detuning of $2\,\delta$ and the MM velocity in Equation 2.16.

The bottom DBR in Figure 5.3 provided the repump light. The repump laser was locked directly to the $|F = 3\rangle \rightarrow |F' = 4\rangle$ transition via an SAS module, which was placed in-line with the main beam line before the second OI. The repump light pumps atoms that fall into the $|F = 3\rangle$ ground state from the cycling transition back to the $|F = 4\rangle$ ground

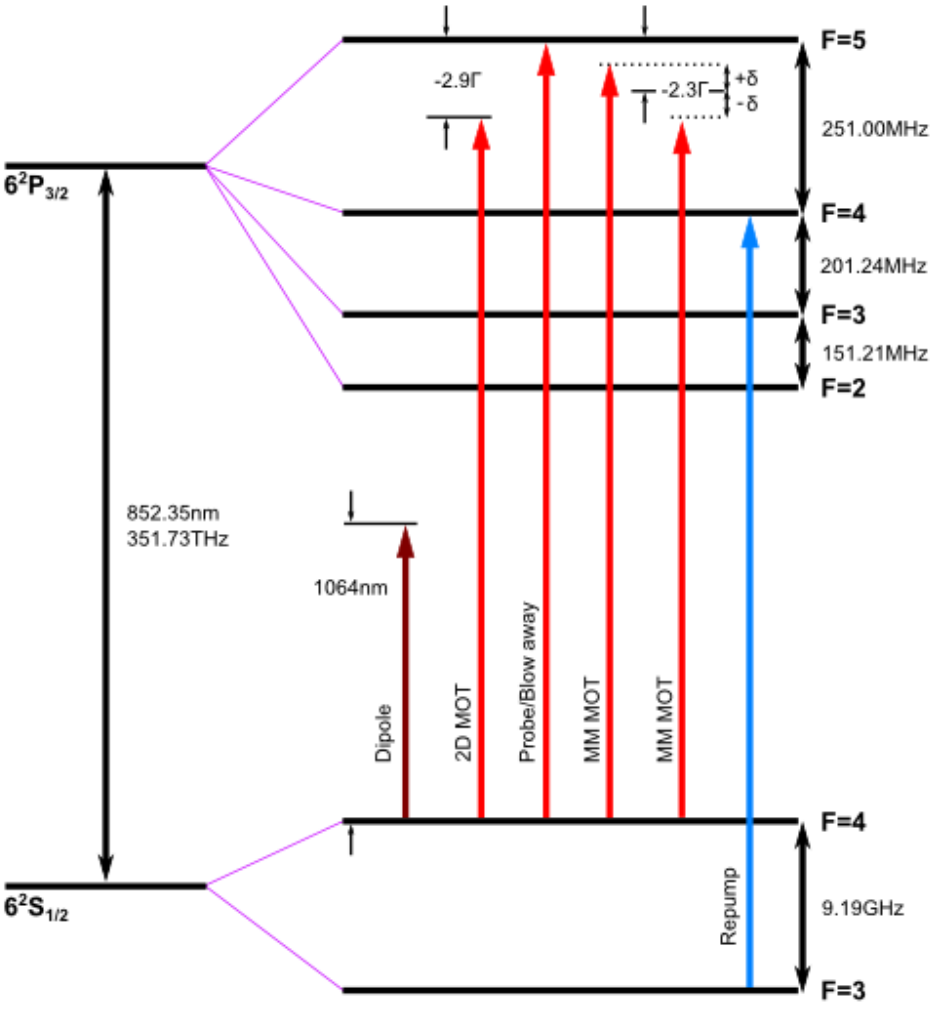

Figure 5.4: (Color) The Cesium D2 spectral lines and experimental laser frequencies. The repump light is locked to the $|F = 3\rangle \rightarrow |F' = 4\rangle$ transition. The $2D^+$ MOT cooling light is locked -2.9 Γ from the $|F = 4\rangle \rightarrow |F' = 5\rangle$ cycling transition. The MM MOT beams are locked -2.3 Γ center frequency from the $|F = 4\rangle \rightarrow |F' = 5\rangle$ cycling transition. The MM frequency is shifted symmetrically by $\pm\delta$ from the center frequency. The red detuned dipole trapping laser is at 1064 nm.

state, where they can continue to be cooled. In the design of the DBR, beam quality and beam collimation are coupled. The repump laser output optimization proved to be more difficult than the two other DBR lasers; thus, the repump was adjusted to have an optimal beam shape while allowing some divergence of the beam. After the first turning mirror, the beam was sent through Gaussian relay optics, which was simply a 2:1 shrinking telescope that is slightly focusing. The Gaussian relay optics effectively collimated the repump beam at the same beam size as the other two DBR laser outputs. The repump was then split into 2D repump, with around 10 mW of fiber coupled light, and MM repump, with around 5 mW of fiber coupled light. The 2D repump was sent through the same mechanical shutter as the 2D cooling, which simplifies the timing. The MM repump was sent through an electro-optic modulator (EOM), which, in combination with a PBS on the input and output of the EOM, provided power attenuation control; the EOM acts as a polarization rotator between the PBSs, which act as crossed polarizers. The MM repump was then spatially overlapped with the MM cooling via a PBS and fiber coupled into the same fiber, but along the perpendicular PM stress axis.

The top DBR in Figure 5.3 provided the probing light. The probe laser was locked to the $|F = 4\rangle \rightarrow |F' = 3\rangle/|F' = 5\rangle$ crossover transition via an SAS module. The probe laser was also focused in a 1:1 telescope through a mechanical shutter to decrease the shuttering rise and fall times. Two beam lines were picked off from the main beam line, which were then overlapped with the dipole beams. Having a resonant beam overlapped with the dipole beam is useful for alignment purposes, because only a small amount of power is necessary to see an effect on the atoms. The last beam of the probe laser was blue shifted by a 120 MHz center frequency AOM, which was driven at 125.5 MHz, to be resonant with the cycling transition. This beam was used as the probe beam in absorption and fluorescence imaging.

The output of the 1064 nm fiber laser is an optical isolator followed by collimation optics, which are integrated into the fiber's termination. Immediately after the integrated output optics is a half waveplate, a PBS, and a beam dump (Thorlabs BT600). This is an

important feature. When the laser is turned on, but not being driven at a current sufficient for the fiber to lase, a reasonable amount of ASE light ($\leq$1 W) is emitted, and can be worked with to align the beam. However, the beam pointing of this light is different than the lasing light. A minimum amount of power out of the laser ($\geq$3 W) is necessary to ensure that it is lasing properly, and that the emitted light is spatially stable. This is an impractical and dangerous amount of light to work with when aligning optics. Thus, the dump port allows one to both operate the laser in a power regime where it is lasing, and work with reasonable amounts of power for alignment. Including a slight angle to the optics closest to the output is also important, as they are the most likely to contribute to back reflections into the laser, which can be damaging to the device.

After the beam dump, the dipole laser was split into two beams, where they were overlapped with the resonant beams via dichroic mirrors. The two beams were shuttered mechanically with $AlMgF_2$ coated blades (Vincent VS14S1ZM0), which is a mirror-like finish. The mirror like finish on the blades allowed fast shuttering action by keeping the blades thin, while being able to handle high powers by dumping the dipole trapping power into beam blocks, rather than absorbing it. The two dipole beams were then sent to the UHV cell via free space.

5.2 Imaging system

The imaging system is based around two different cameras. The Basler A631f, which is similar to the Basler A102f described in Section 4.8, was used in this system for absorption imaging when the main source of imaging noise was from fluctuations and vibrations, as described in Section 4.8 and in [52]. The more sensitive Andor iXon 887 camera was utilized to implement fluorescence imaging. The iXon is a TEC cooled, electron multiplying CCD (EMCCD) camera with single photon sensitivity. In a CCD there are two main sources of noise: dark current, which arises from thermal energy within the silicon lattice comprising the CCD, creates electrons over time that are independent of the light falling on the detector.

These electrons are captured by the CCD's potential wells, which are then counted as signal. Dark current can be subtracted out from the signal with a "dark frame" [73]. However, the noise follows Poisson statistics, which goes as the square root of the mean dark current. By using a TEC to cool the CCD to -85 °C, the dark current in the iXon is reduced to 10^{-3} electrons/pixel/s, which is zero for all practical integration times.

The second noise source comes from the pixel readout. A pixel signal is read out of the CCD as a very tiny voltage, on the order of microvolts/electron. The signal is then passed to an analog-to-digital converter and an amplifier, both of which introduce electronic noise to the signal that can limit the detectable signal. With an EMCCD, an additional on-chip gain register is introduced between the CCD and the readout electronics. EM gain itself will add some noise to the measured signal due to the statistical nature of the multiplication process. However, the added noise is shot limited, which adds to the shot noise of the signal itself, bringing the total noise of the amplified signal to two times the shot noise, $\sqrt{2N}$. The readout noise on the iXon is the equivalent of around 50 electrons. Thus, by introducing an EM gain of $\geq$50, i.e., amplifying the pixel signal by 50, the readout noise is effectively reduced by a factor of 1/50, to $\leq$1 electron/pixel. By further increasing the EM gain, higher sensitivities can be achieved, but at the cost of dynamic range.

5.3 Computer control system

The computer control system is based around the NI PXI-1036 chassis, which houses the PXI-8102 embedded controller, and the PXI-7813R FPGA. The architecture is similar to that in Section 4.4. The PXI-8102 runs the RT LabVIEW code, which talks to the host computer and the PXI-7813R. The PXI-7813R is a 160 channel digital I/O FPGA, with four 40 output sections. One output section of the PXI-7813R is connected to the NI SCB-68 breakout box, via the NI SHC68-68-RDIO cable, which provides 40 digital outputs to the system. A second output section is connected to the NI 9151 expansion chassis, which supports C-series modules, which are similar to those in Section 4.4. The NI 9151 is

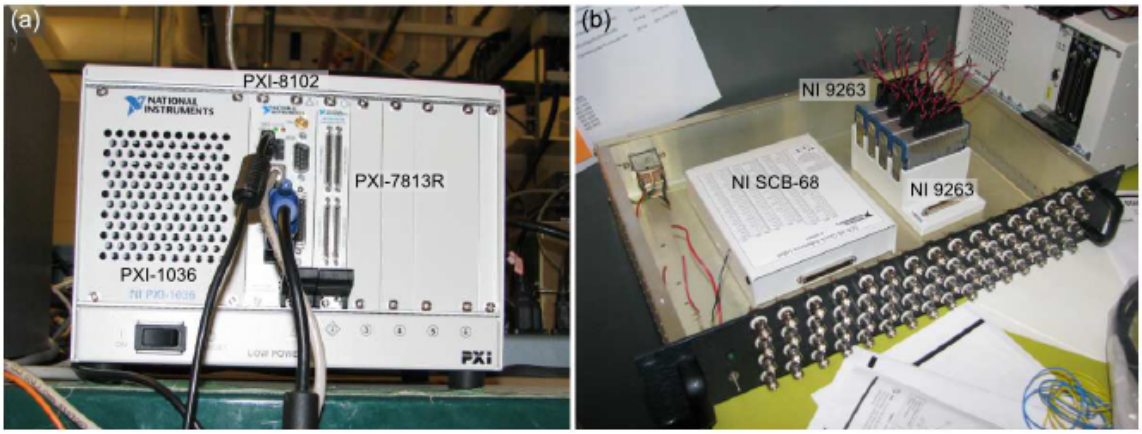

Figure 5.5: (Color) PXI FPGA chassis and analog/digital modules. (a) The PXI-1036 chassis, which houses the PXI-8102 embedded controller, and the PXI-7813R FPGA. (b) The NI SCB-68 breakout box for digital outputs, and the NI 9151 configured with four NI 9263 modules.

configured with four NI 9263 modules to provide sixteen 16-bit, 100 kS/s analog outputs to the system. The NI SCB-68 and NI 9151 are housed in a shielded box and connectorized with BNC outputs. The computer control system is shown in Figure 5.5.

5.4 Experimental sequence

Two main experimental setups were utilized with the quadruple cell shown in Figure 3.8. In the first setup, the quadruple cell was oriented horizontally, such that the fourth chamber mimicked the Hex cell in the original AQuA concept, shown in Figure 5.1, with the difference that the fourth chamber was in series with the $2D^+$ MOT and MM MOT chambers, instead of in between. This setup was used to test several different MM MOT configurations, and generate the first red detuned dipole trap. The lessons learned from the horizontal setup led to the second setup, in which the quadruple cell was oriented vertically. In the vertical setup, the third chamber now mimicked the Hex cell in the first generation of fabricated AQuA cells, shown in Figure 3.19, which is quite different from the AQuA concept, and was designed concurrently with experiments in the vertical setup. This setup is currently being used for MM MOT transport guided by a red detuned, vertically oriented dipole beam, and capturing the atoms in a crossed red detuned dipole trap.

5.4.1 MM MOT and dipole trap in the horizontal UHV cell

There were two sets of experiments in the horizontal chamber setup shown in Figure 5.6. The first was generating and characterizing the MM MOT, and demonstrating transport into the third chamber. The second was testing, generating, and characterizing the dipole trap, which had not been done before in this lab. In the setup shown in Figure 5.6, two fiber launchers collimated the MM MOT beams at 1 cm diameter. The orange beam line was split equally, with 16 mW of cooling light per beam, and sent into the cell in the horizontal plane at 45° relative to the optical face of the MM MOT chamber. The red beam line was split into three, with 16 mW of cooling light per beam, with one beam sent vertically into the cell and

retroreflected, and the other two beams sent into the cell so they are counter-propagating the orange beam lines. The Andor iXon camera, which is shown on the left, was set up for fluorescence imaging (pink beam), which was used for imaging the dipole trap. For the MM MOT experiments, which demonstrated atom cloud transfer to the third chamber, the Basler A631f was used in the absorption imaging configuration, shown in Figure 4.16.

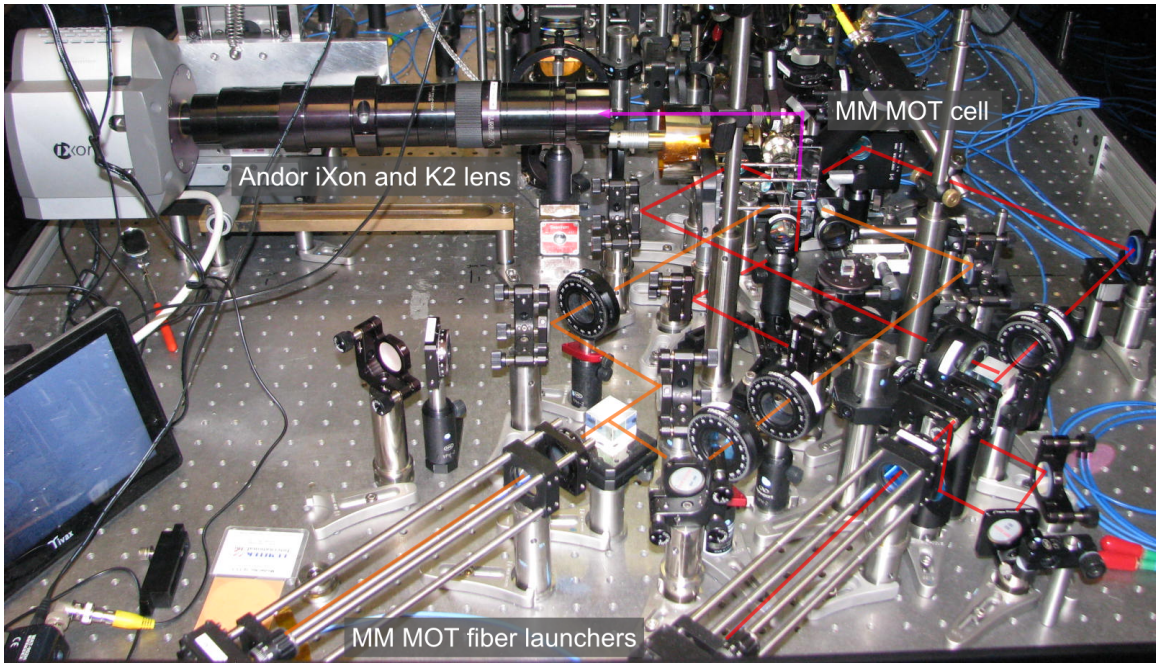

Figure 5.6: (Color) Horizontal double MOT setup. The double MOT cell is in the center. The red and orange lines indicate the two frequencies used in the moving molasses MOT. The Andor camera and K2 lens system is shown on the left.

Magnetic field coils, shown in Figure 5.7, were used to make the MM MOT. The coils have an inner dimension of 110 mm × 26 mm, cross-sectional dimension of 4.7 mm × 5.2 mm (width × thickness), and 72 turns in an 8×9 pattern. The coils were driven with four independent, bipolar drivers, which are described in Section 4.6. The symmetry of the coils is such that they generate a zero of magnetic field along their axis, similar to the permanent magnets shown in Figure 2.6. A view down the axis of the quadrupole coils is shown in Figure 5.8. On the left, equal currents are run through the four coils (orange), and the equivalent permanent magnets are shown in the corners, where red and blue represent the

north and south poles, respectively.

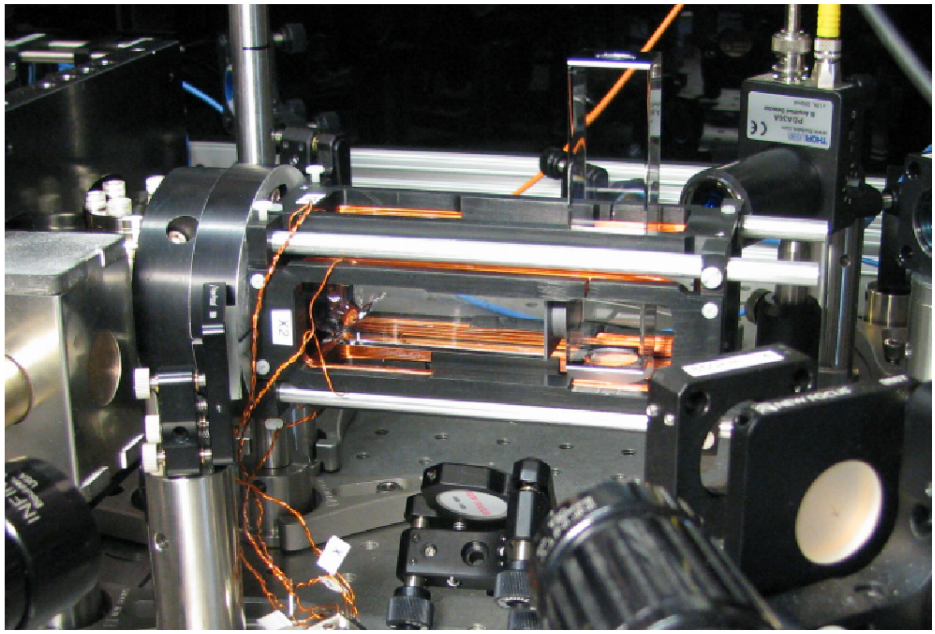

Figure 5.7: (Color) MM MOT coils in the horizontal UHV cell setup.

By driving the coils independently, quadrupole and bias fields can be generated without the need for separate pairs, simply by running the coils at different currents. A quadrupole field plus a bias field is the same as a quadrupole field with its minimum offset from the center. Shown on the right of Figure 5.8, equal currents are run through three of the coils (orange), and 1.5× the current is run through the last coil (yellow). The quadrupole field has approximately maintained its shape, but is now offset from the center. The radial gradient generated with equal currents in each coil in the anti-Helmholtz configuration was approximately 9 G/cm/A. The radial bias field generated with equal currents in each coil in the Helmholtz configuration was approximately 15 G/A.

5.4.1.1 MM MOT experiments

The MM MOT was loaded for 1-2 s at a field gradient of 8 G/cm from the $2D^+$ MOT. Small bias fields were used to optimize the MM MOT, which amounted to a current difference

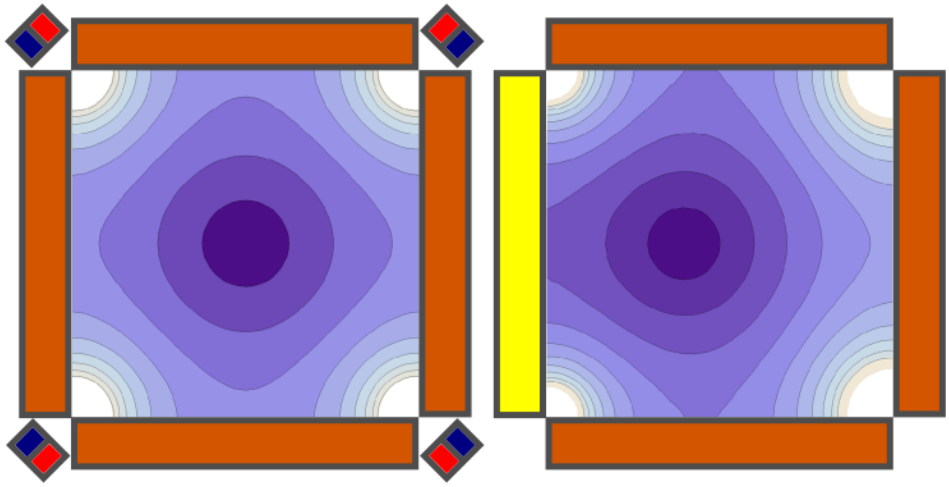

Figure 5.8: (Color) Quadrupole field generated by four independent coils. Left: Equal currents are run through the four coils (orange), and the equivalent permanent magnets are shown in the corners, where red and blue represent the north and south poles, respectively. Right: Equal currents are run through three of the coils (orange), and 1.5× the current is run through the last coil (yellow). The quadrupole field has approximately maintained its shape, but is now offset from the center.

in the coils on the order of a few percent. A photo of the MM MOT fluorescence in steady state at zero relative detuning ($\delta = 0\,\mathrm{MHz}$) during the loading stage is shown in Figure 5.9, which shows its elongated shape. After the MM MOT loading stage was a combined CMOT and MM MOT stage. Over 5 ms to 10 ms, the quadrupole coils were ramped up to 30 G/cm, the cooling light was red detuned an additional $4\,\Gamma$, and the relative detuning δ between the MM MOT beams was ramped to its final value. At the end of the CMOT and MM MOT stage, the resonant light was shuttered, and the coils were held at 30 G/cm, which formed a magnetic waveguide for the atoms that was strong enough to hold against gravity, as discussed in Section 2.1.

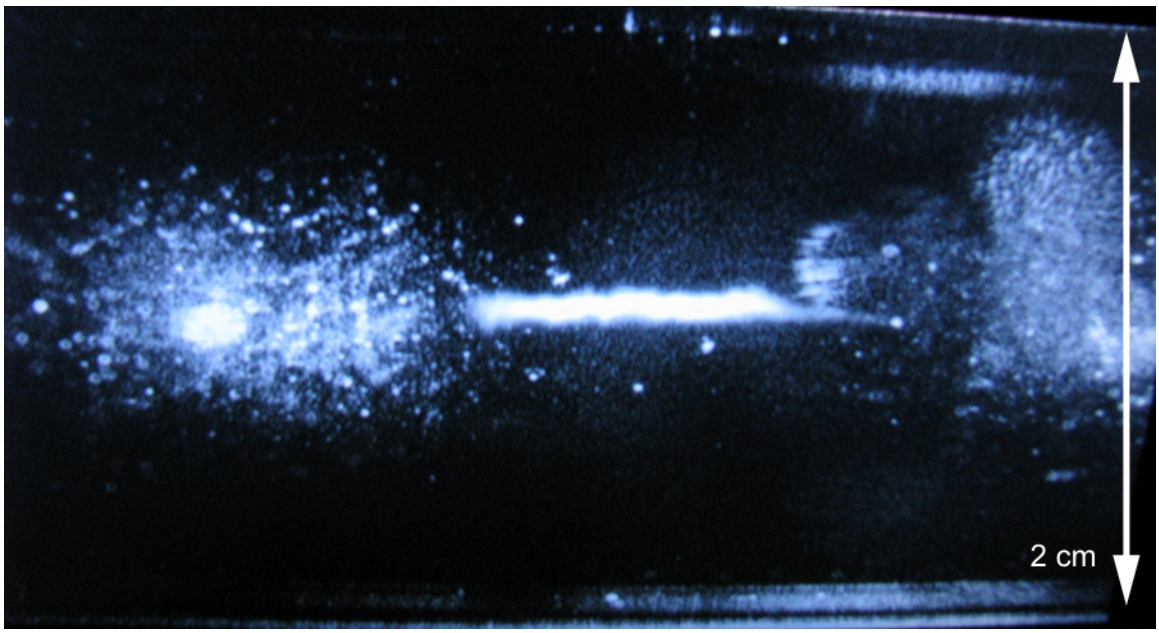

Figure 5.9: Photo of the MM MOT fluorescence in the horizontal cell. The 2 cm cell can be seen on the right. The MM MOT can be seen as the elongated, horizontal cloud in the center of the photo. Scattered cooling light off of the cell can be seen to the left and right of the MM MOT.

Shown in Figure 5.10 are absorption images of the MM MOT in the magnetic trap. Figure 5.10(a) shows the MM MOT in the second chamber after a TOF of 15 ms. In the first frame in Figure 5.10(a), part of the MM MOT can be seen on the left side of the probe beam, for zero relative detuning. Each successive frame is at the same TOF, but with

the detuning increased by increments of 100 kHz. In the final frame in Figure 5.10(a), the relative detuning is δ =0.8 MHz, and the MM MOT has traversed the probe beam. The peak OD (red) in these OD images is 0.8. Shown in Figure 5.10(b) is the MM MOT in the magnetic trap as it enters the third chamber of the cell. Here, the images were taken at a fixed detuning of δ = 1.2 MHz, and the TOF was varied. The first frame in Figure 5.10(b) is at a TOF of 15 ms. In each successive frame the TOF is increased by 1 ms, and the atom cloud can be seen traversing the probe beam. Because there is no optical pumping, these images have a large background of un-trapped atoms.

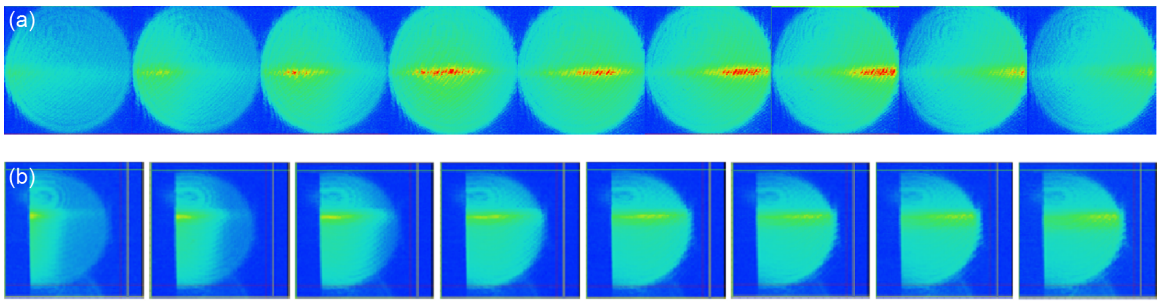

Figure 5.10: (Color) MM MOT in the horizontal second and third chamber. (a) MM MOT OD images in the second chamber at 15 ms TOF for detuning δ =0 MHz on the left, and goes up in increments of 100 kHz. The peak OD (red) is 0.8. (b) MM MOT OD images in the third chamber at a detuning δ = 1.2 MHz. The TOF is 15 ms on the left, and goes up in increments of 1 ms. The boundary of the third chamber can be seen cutting off the left section of the probe beam.

5.4.1.2 Dipole trapping experiments

Two of the limiting factors when utilizing coils to generate magnetic fields are the optical access and cell geometry. Four permanent rare-earth magnets, 40 mm in length with cross sectional dimensions of 1 mm $\times$ 1 mm, can create the same gradients in the second chamber as the magnetic field coils shown in Figure 5.7. Additionally, for the coils shown in Figure 5.7, orienting the coils such that they were rotated 90° in the horizontal plane would be impossible to implement because of the fourth chamber. A coil design that is compact

and able to fit over a complex cell geometry such as this is not straightforward.

In order to demonstrate a dipole trap in the horizontal cell, the magnetic field coils shown in Figure 5.7 were replaced with permanent magnets. The permanent magnets were rotated 90° in the horizontal plane, such that their magnetic field zero was perpendicular to the $2D^+$ MOT atom flux. The was done for two reasons: the first was to demonstrate that the perpendicular geometry maintained a sufficient capture velocity to create an MM MOT from the $2D^+$ MOT atom flux. This was a simple test, but one that was necessary to demonstrate for different possible implementations of AQuA cell geometries. Second, to implement a tightly focused dipole trapping beam, it needed to enter the MM MOT chamber from the side, so that fairly fast input and output optics could be used *ex vacuo*. The magnets were rotated to spatially mode match the elongated MM MOT cloud, shown in Figure 5.9, with the dipole trapping beam.

A more detailed photo of the dipole trapping setup is shown in Figure 5.11. The MM MOT permanent magnets can be seen in the upper left, oriented normal to the axis of the MM MOT chamber. The dipole beam was vertically linearly polarized and sent through the input PBS. Two turning mirrors and a lens were mounted to an XYZ translation stage to give fine control of the dipole trap location. Given a 1 mm input beam radius, an achromatic lens with focal length f = 100 mm focused the beam to a calculated waist of approximately $w_0 = 30\,\mu$m with a Rayleigh range of $z_R = 2.7$ mm. The power in the beam was 6 W, which produced a trap with a calculated trap depth of 2 mK at the focus. The maximum scattering rate, from Equation 2.24, was 21 photons/s, which gives a heating rate, from Equation 2.45, of $0.84\,\mu$K/s for a $100\,\mu$K cloud.

Retroreflecting the dipole trapping beam, rather than dumping it, is a more efficient use of laser power. An f = 100 mm achromat was mounted to a z-translation stage after the MM MOT chamber. The rough collimation and alignment was set by hand using a right-angle tool, which assures that the z-translation does not affect the x-y position of the output beam. Fine collimation was set with the z-translation stage. The beam was passed

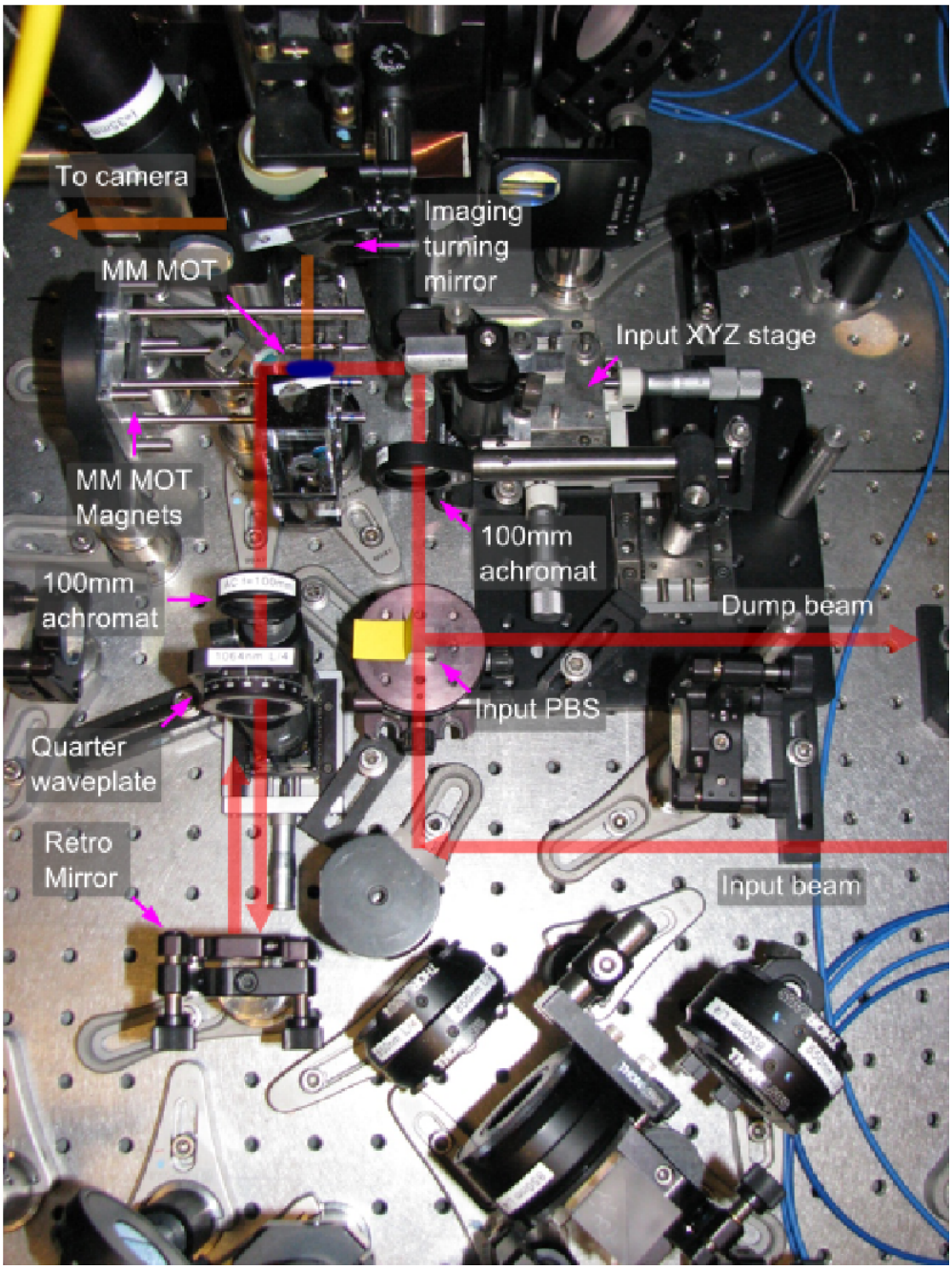

Figure 5.11: (Color) Horizontal dipole trapping setup. The MM MOT magnets are perpendicular to the $2D^+$ MOT flux, which is pointing down. The MM MOT is represented by the blue oval in the center. Fluorescence from the MM MOT was detected on a PD. The dipole trapping beam was linearly polarized and input by an XYZ-stage that contains two mirrors and an f = 100 mm plano-convex lens. The output was collimated by an f = 100 mm plano-convex lens. The output dipole beam was retroreflected where it was sent through a quarter waveplate twice to rotate its polarization 90°. The perpendicularly linearly polarized beam was then dumped at the input by a PBS. Fluorescence imaging of the dipole trap was performed by the Andor camera and K2 lens shown in Figure 5.6.

twice through a quarter waveplate oriented at 45°, which rotates its polarization 90°, from vertical linear to horizontal linear. Because the polarization in the input and retroreflected beam were orthogonal, the dipole trapping intensities added to create a single trap, rather than forming a standing wave pattern. Because the retroreflected beam had horizontal linear polarization, the input PBS served to dump the power into a beam block. The fluorescence light was reflected off of a mirror that was mounted above the MM MOT chamber and to the side of the vertical MM MOT retroreflecting mirror, where it was sent horizontally into the Andor iXon for imaging.

Fluorescence imaging of the dipole trap in three configurations is shown in Figure 5.12. A single dipole trap with no retroreflecting beam is shown in Figure 5.12(a). The radial (longitudinal) size of the trap is 8 pix to 10 pix (400 pix to 450 pix). A measured camera resolution of 6.35 μm/pix gives trap dimensions of 50 μm to 63 μm radially, and 2.5 mm to 2.9 mm longitudinally, which agree very well with the calculated values. The trap is at a slight angle due to the turning mirror on the imaging beam path, which had to be out of the way of the vertical MM MOT beam. The probe beam was co-propagating with the input dipole beam, was spatially mode matched, and had a power of 700 μW. Atoms in the dipole trap have a spatially induced light shift of their resonant line, which is proportional to dipole potential. At the trap center, the calculated light shift induced was around 4 Γ to 8 Γ.

An atom's rate of absorption is given by

$$I(\Delta) = \frac{\hbar\omega\Gamma}{2}\frac{\Omega^2}{\Omega^2 + \Gamma^2/2 + 2\Delta^2}, \tag{5.1}$$

where Γ is the natural linewidth, Ω is the Rabi frequency, ω is the resonant laser frequency, and Δ is the detuning [89, 90]. The absorption spectrum is a Lorentzian with a full width at half maximum (FWHM) of

$$\text{FWHM} = \Gamma\left(1 + 2\frac{\Omega^2}{\Gamma^2}\right)^{1/2}. \tag{5.2}$$

At low powers, the FWHM is just the natural linewidth Γ. As the power is increased, the spectrum is power broadened. At a 30 μm waist, the intensity of the probe beam was such

that it power broadened the D2 transition of Cesium to about 100 Γ, which was significantly higher than the calculated light shift induced by the dipole trap, so all of the atoms fluoresced equally. The dipole trap lifetime was measured to be around 12 s.

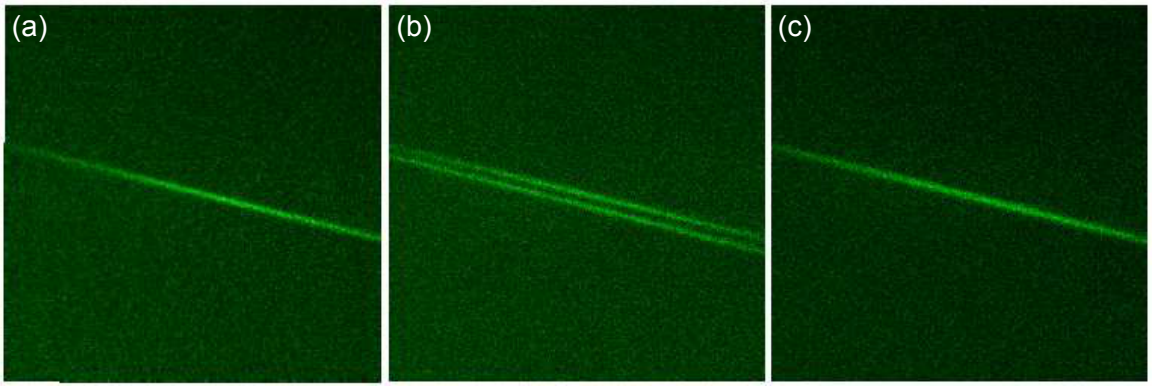

Figure 5.12: (Color) Fluorescence imaging of the dipole trap overlapped with the MOT. (a) Single focused beam creating a dipole trap. (b) The input dipole beam retroreflected and intentionally misaligned, creating two dipole traps. (c) Retroreflected dipole beam trap.

The retroreflecting beam passed through four un-coated glass faces, eight coated glass faces, and three mirror reflections, which meant approximately 82% of the input light was retroreflected onto the atoms. Two dipole traps can be seen in Figure 5.12(b). The input dipole beam trap is on the bottom, and the retroreflected dipole beam trap is on the top. The two beams were intentionally misaligned to show the two traps. Shown in Figure 5.12(c), the two dipole traps were overlapped, with a calculated trap depth of 3.6 mK.

The original objective of the horizontal cell was to implement the transport scheme diagrammed in Figure 5.1, in which the MM MOT would transport atoms from the second to the third chamber, and a moving standing wave trap, shown in Figure 2.10, would transport the atoms vertically. The magnetic trap used initially to demonstrate transport into the third chamber did not use static fields, one of the requirements from Section 1.3. Allowing the MM MOT cloud to propagate ballistically, the horizontal orientation of the cell with respect to gravity put a lower limit on the velocity that can be imparted. The cloud must reach the third chamber before it hits the side of the cell.

Because the cell is so long, a dipole guide beam along the MM MOT to hold against gravity requires high power, i.e., the beam waist cannot be made tight ($\leq$75 μm) because it needs a Rayleigh range long enough to allow it to pass through the pinhole and exit the cell. The moving standing wave trap from Section 2.4.4 also requires significant power because of the inefficiency of the double-pass AOM setup and a required Rayleigh range of $\geq$4 cm. Additionally, to create a reservoir of atoms in the third chamber, i.e., trap them, another dipole beam for creating a crossed dipole trap is required. When combined with the power required for dipole guiding and transport, this exceeded the power of the dipole laser ($\geq$30 W).

5.4.2 MM MOT and dipole trap in the vertical UHV cell

In the end it was decided that the double chamber should be oriented vertically to take advantage of gravity, which is reflected in the first generation of constructed AQuA cell, shown in Figure 3.19. In the vertical chamber, the MM MOT is tossed upwards with gravity acting against the motion, which causes the atoms to apex, similar to a ball being tossed up in the air. The magnetic field coils, shown in Figure 5.7, were replaced by four 1 mm $\times$ 1 mm $\times$ 40 mm rare-earth magnets, which were oriented as shown in Figure 5.8, with their line of zero magnetic field along the axis of the MM MOT chamber.

Figure 5.13 diagrams tier 1 of the vertical MM MOT cell setup, the 2D$^+$ MOT level. The cooling fiber was collimated to a 1 cm diameter beam by an f = 50 mm achromat. Around 5% to 10% was picked off for the push beam, which was shrunk by an approximately 3:1 telescope. The push beam diameter versus flux has been explored experimentally, with an iris used to vary the diameter. A 3 mm diameter beam was robust to small alignment errors and did not decrease the flux compared to a 1 cm diameter beam. Using a telescope rather than an iris increased the intensity of the push beam, which required less power and was more efficient. The push beam was sent upward into the cell via a PBS and a right angle mirror, which allowed imaging of the 2D$^+$ MOT.

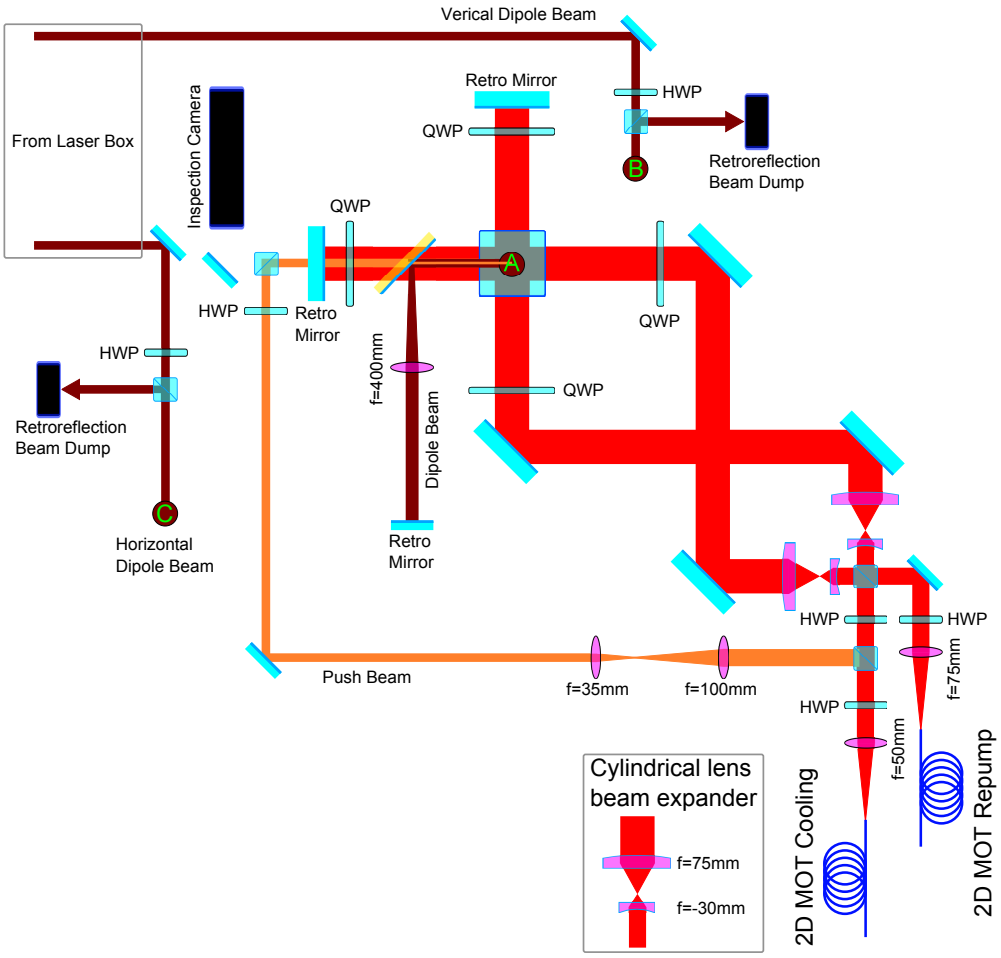

Figure 5.13: (Color) Tier 1 diagram of the vertical chamber setup, the 2D$^+$ MOT. The cooling fiber was collimated by an f = 50 mm achromat, with some light picked off for the push beam. The light was split and sent through a 2.5:1 cylindrical beam expander. A quarter waveplate made the light circularly polarized when it was sent into the cell and retroreflected. The push beam was shrunk in a 3:1 telescope and sent into the cell vertically. The dipole beams came from the laser box via free space on the left, where they were directed to tier 3 of the optical setup. The vertical dipole beam was sent upward at point B. The vertical dipole beam was sent downward from tier 3 through the cell, where it exited the cell at point A. The horizontal dipole beam was sent upward at point C.

The repump was collimated to a 1.5 cm diameter by an f = 75 mm achromat. This assured that the entire $2D^+$ MOT is exposed to repumping light, even without precise alignment. The repump light was combined with the cooling light, and split into the two 2D MOT beams with the same PBS. The combined light was sent through a 2.5:1 cylindrical beam expander, which gives the beam an elliptical profile of 1 cm × 2.5 cm with the major axis oriented vertically. The dipole beams exited the laser box on the left (from Figure 5.3) and were coupled into the system via free space. The dipole beams were directed to tier 3 of the optical setup. The vertical dipole beam was sent upward at point B. The vertical dipole beam was sent downward from tier 3 through the cell, where it exited the cell at point A. After exiting the cell, it was reflected off of a dichroic mirror, collimated with an $f = 400$ mm plano-convex lens, and retroreflected. The horizontal dipole beam was sent upward at point C.

Figure 5.14 diagrams tiers 2 and 3, which contain most of the MM MOT optics. Tier 2 contains the MM MOT cooling fiber launcher with overlapped repump which collimated 32 mW of cooling and 5 mW of repump to 1 cm in diameter. The beam was split into two with equal cooling power via a PBS, where it was passed through a half and quarter waveplate pair for full polarization control. Two mirrors send the beams into the cell at an upward angle of 45°. The probe fiber launcher is collimated with an f = 75 mm achromat to 1.5 cm in diameter. Two mirrors provided alignment into the camera, which was not mounted to tier 2, but to its own vertical translation stage adjacent to the setup. The final probe mirror is a 40 mm × 40 mm square gold mirror that allowed significant vertical translation of the probe beam without physically moving the mirrors. Because of the adjacent optics, however, the gold mirror was not able to be made large enough to cover the full distance from the MM MOT to the crossed dipole trap region. Thus, the gold mirror had to be raised and lowered approximately 1 cm to accommodate imaging at the MM MOT and crossed dipole trap region. The retroreflected horizontal MM MOT beam was split from tier 3, and was sent to tier 2 at point D, where it passed through the cell and is retroreflected. A photodiode

monitored the MM MOT fluorescence signal.

Tier 3 contains an identical MM MOT cooling fiber launcher with 48 mW of cooling light and no repump light. A PBS split off 16 mW of cooling light into the horizontal MM MOT beam at point D. The remaining 32 mW was split into two with equal power via a PBS, sent through a half and quarter waveplate pair for full polarization control, and overlapped counter-propagating to the MM MOT beams from tier 2. The vertical dipole beam enters tier 3 from point B, where it was focused by an f = 250 mm plano-convex lens. Two mirrors aligned the vertical dipole beam along the axis of the MM MOT chamber. The focal point was aligned to be half way between the MM MOT location and the crossed dipole beam location. The vertical dipole beam was passed through the $2D^+$ MOT pinhole and exited out the cell, shown in Figure 5.13. The collimation lens at the output of the vertical dipole beam is an f = 400 mm plano-convex lens. The horizontal dipole beam enters tier 3 from C, where it was input into an XYZ-stage, similar to that shown in Figure 5.11, and focused by an f = 100 mm plano-convex lens. The XYZ-stage has an accuracy of $\leq 10\,\mu$m, which allows for fine alignment of the two dipole beams, where the waists of the beams are $\leq 100\,\mu$m. The horizontal beam passed through both the third and fourth chambers of the UHV cell, where it was collimated with an f = 100 mm plano-convex lens and retroreflected, similar to that shown in Figure 5.11.

A vertical slice through the center of the vertical MM MOT setup is shown in Figure 5.15. Tier 1 is shown below the spherical cube and tier 2 breadboard, where the $2D^+$ MOT was created. The push beam was passed through a dichroic mirror and sent upward through the cell. The vertical dipole beam was sent up to tier 3 at B, as shown in Figure 5.13, where it was focused and sent downward through the cell at A. The vertical dipole beam exits through the $2D^+$ MOT pinhole where it was reflected off of a dichroic mirror. The horizontal dipole beam was sent up to tier 3 at C, as shown in Figure 5.13, where it was focused and sent horizontally through the third and fourth chamber. The MM MOT optics were mounted on both tier 2 and 3, and intersected in the middle of the UHV cell at 90°,

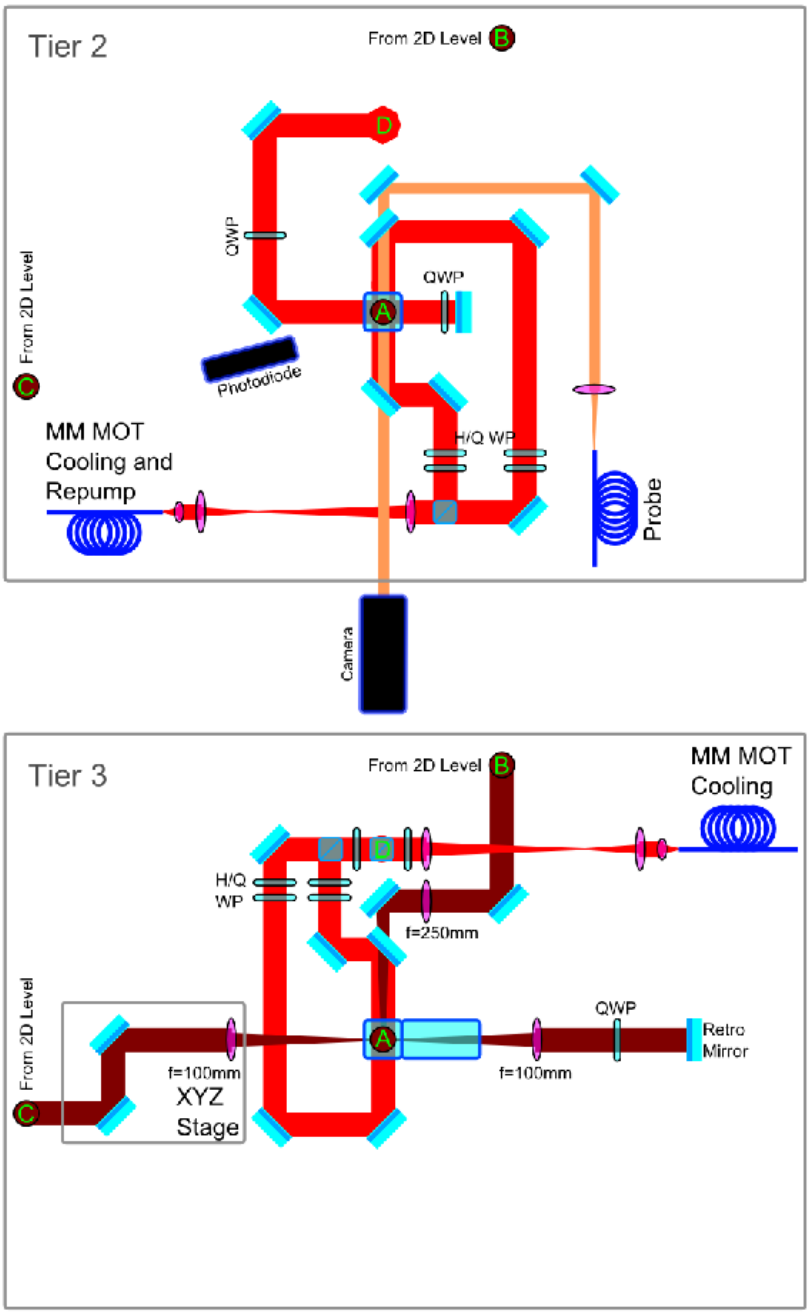

Figure 5.14: (Color) Tier 2 and 3 diagram of the vertical chamber setup. Tier 2 contains one MM MOT fiber launcher, the probe fiber launcher, and the MM MOT fluorescence PD. The camera was separate from tier 2 and was on its own vertical translation stage adjacent to the setup. Tier 3 contains an identical MM MOT fiber launcher as that on tier 2. The horizontal MM MOT beam was split from tier 3 and was sent to tier 2 at point D. The vertical and horizontal dipole beams were sent upward from tier 1 at points B and C, respectively. The vertical dipole beam was focused and sent downward through the cell at point A. The horizontal dipole beam was sent through an XYZ-stage and focused to intersect the vertical dipole beam in the cell at point A.

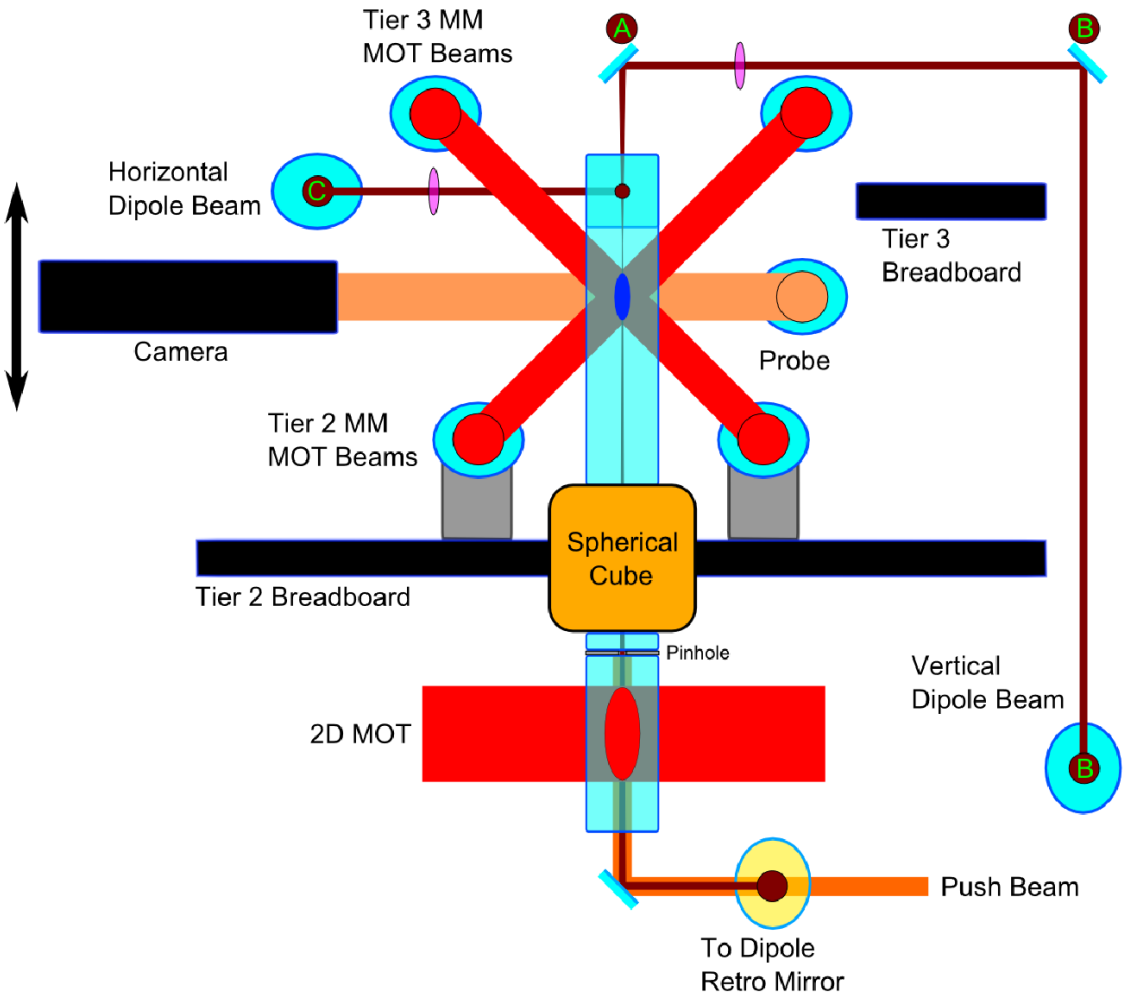

Figure 5.15: (Color) Vertical slice diagram of the vertical chamber setup. The $2D^+$ MOT is created in the lower chamber where it feeds the MM MOT in the upper chamber. The MM MOT optics are on a monolithic breadboard that is above the optical table. The dipole beam enters the cell vertically and horizontally. The points A, B and C are the same as in Figures 5.13 and 5.14

.

4 in. above the tier 2 breadboard. The probe beam and camera can translate up and down so that probing is orthogonal to the vertical dipole trap and cell optical faces.

A photo of the current setup is shown in Figure 5.16. The quadruple cell is highlighted by the red oval. Tier 1, 2 and 3 are labelled in green. The dipole beam exits the laser box and enters the cell system on the right. The $2D^+$ MOT fiber launcher and camera are labelled on the left.

Originally the camera was mounted on an XYZ-translation stage for fine control and repeatibility of the focus and centering. However, in practice, the XYZ-translation stage proved to be unstable, and led to a more than 2x increase in the imaging noise. In general, the field of view of the camera lens was large enough such that fine control of the focal plane's lateral position was unnecessary. Additionally, the focus ring on the lens provided enough control over the focal plane working distance that a translation stage was not strictly necessary. The camera was aligned using mechanical stops for repeatability. The camera was mounted to a platform that slid up and down, and clamped to, a 1.5 in. diameter, lead-filled post.

The MM MOT loading stage collected atoms from the $2D^+$ MOT for 2-3 s. Approximately 25 ms before the end of the MM MOT loading stage, the $2D^+$ MOT light was shuttered. At 250 ms before the end of the MM MOT loading stage, the vertical dipole beam was turned on at a power of 19 W, and kept on through the following stages. For an input dipole beam diameter of 2.0 mm, an f = 250 mm lens produced a calculated focal waist of $w_0 = 85\,\mu$m, which had a Rayleigh range $z_R = 2.1$ cm. The trap depth at the focus was $790\,\mu$K, with a peak scattering rate of 8.5 photons/s. The trap depth and peak scattering rate at a distance z_R from the focus was $390\,\mu$K and 4.2 photons/s, respectively.

After the MM MOT loading stage was the CMOT stage. In the CMOT, the cooling detuning was increased to around -20Γ. Because of the permanent magnets, the fields could not be ramped up, as in the CMOT stage in Section 5.4.1. The repump light power and detuning were not changed, because it did not seem to improve the efficiency of the CMOT,

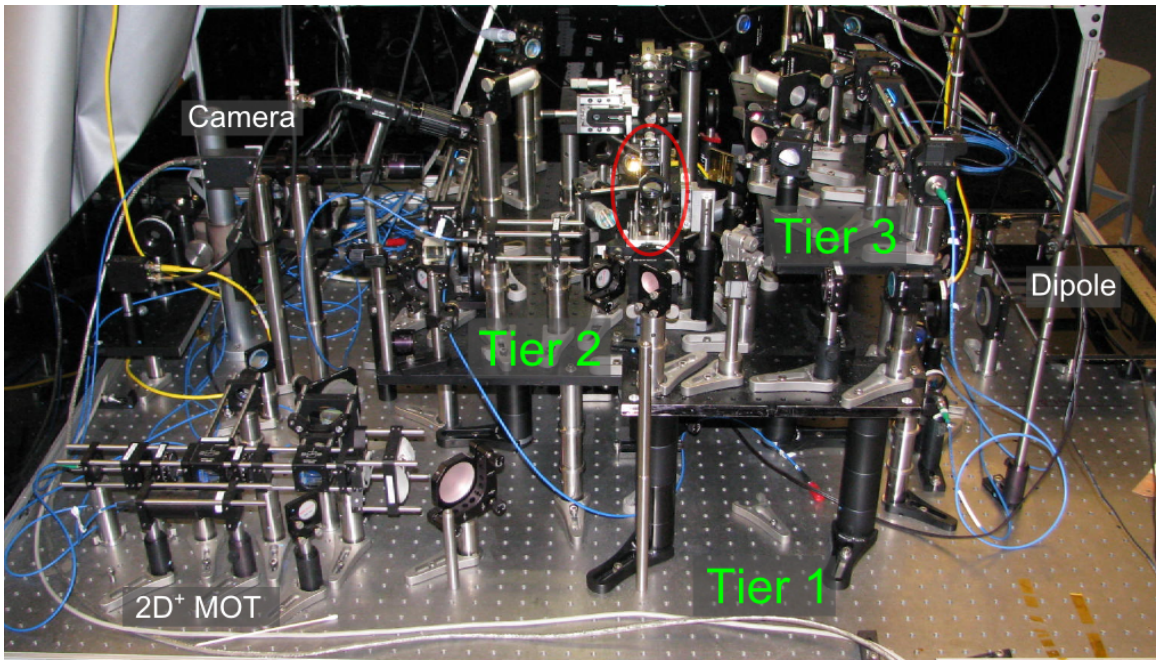

Figure 5.16: (Color) Photo of the vertical MM MOT and dipole trap setup. The quadruple cell is highlighted by the red oval. Tiers 1, 2 and 3 are labelled in green. The dipole beam exits the laser box and enters the cell system on the right. The $2D^+$ MOT fiber launcher and beam shaping, and the camera, are labelled on the left.

but instead led only to atom loss. Because of the permanent magnets, additional sub-doppler cooling was not possible. The measured temperature of the atoms after the CMOT stage was between 70 μK and 100 μK.

After the CMOT stage was the MM MOT stage. The absolute cooling frequency was held at -20 Γ, and the relative detuning δ was ramped from zero to between 0.1 MHz and 0.9 MHz over 2-3 ms. At the end of the MM MOT stage, all resonant light was shuttered. An absorption image of the dipole beam overlapped with the MM MOT at zero detuning and a 10 ms TOF is shown in Figure 5.17(a). The peak OD (white) is approximately 1.5. After receiving a kick from the MM MOT stage, the atoms, both trapped in the dipole beam and un-trapped background, co-propagate upward from the kick given by the moving molasses. An absorption image of the MM MOT cloud and dipole guide, with a detuning $\delta = 0.5$ MHz and a TOF of 35 ms, is shown in Figure 5.17(b). Here, the cloud can be seen exiting the top of the second chamber, which is the line at the top cutting off part of the probe beam. An absorption image of atoms in the dipole guide in the third chamber, with a detuning $\delta = 0.85$ MHz and a TOF of 80 ms, surrounded by a very weak background of un-trapped atoms, is shown in Figure 5.17(c). The lower edge of the third chamber, which is 6 mm above the top edge of the second chamber, forms the bottom edge of this image. The center of the guided atom cloud is approximately 5 cm above the level of the MM MOT. The peak OD in this image is approximately 0.1.

A classical model of ballistic motion was used to estimate the detuning and TOF necessary to have the atoms apex 5 cm above the level of the MM MOT. From Equation 2.16, the initial velocity of the atom cloud is $\bar{v} = \sqrt{2}\,\delta\,\lambda$, where δ is the relative detuning and λ is the cooling laser wavelength. The initial velocity required to have the atom cloud apex a distance $d = 5$ cm is given by

$$v_0 = \sqrt{2gd}, \tag{5.3}$$

where g is the acceleration of gravity. For $d = 5$ cm, the initial velocity is approximately

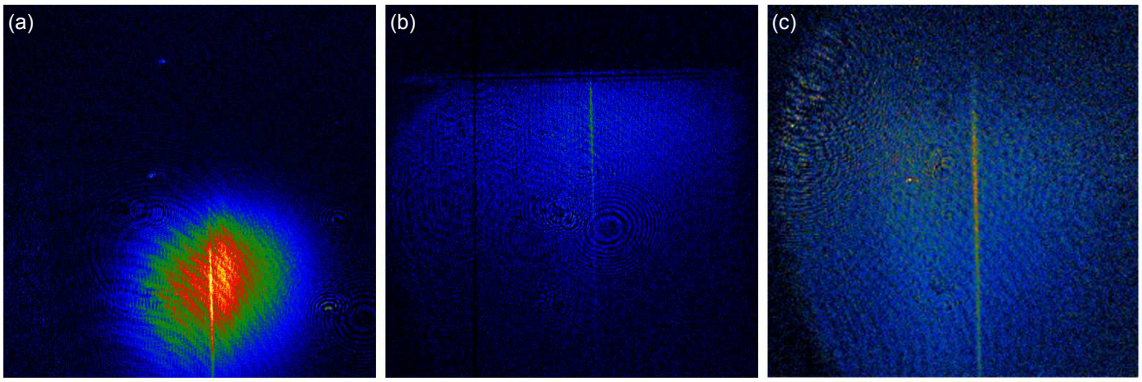

Figure 5.17: (Color) (a) The dipole beam overlapped with the MM MOT at zero detuning and a 10 ms TOF. The peak OD (white) is approximately 1.5. (b) The MM MOT cloud and dipole guide, with a detuning $\delta = 0.5$ MHz and a TOF of 35 ms. The cloud can be seen exiting the top of the second chamber. (c) The dipole guide in the third chamber, with a detuning $\delta = 0.85$ MHz and a TOF of 80 ms, surrounded by a very weak background of un-trapped atoms. The lower edge of the third chamber forms the bottom edge of this image.

$v_0 = 1\,\mathrm{m/s}$. The TOF required for the atom cloud to apex is given by

$$d = v_0 t + \frac{1}{2} g t^2. \tag{5.4}$$

For $d = 5\,\mathrm{cm}$ and $v_0 = 1\,\mathrm{m/s}$, the TOF to apex is approximately $t = 83\,\mathrm{ms}$. In ballistic expansion, the cloud size as a function of time $\sigma_i(t)$ is given by

$$\sigma_i(t) = \sqrt{\sigma_{i0}^2 + \frac{k_B T}{m} t^2}, \tag{5.5}$$

where σ_{i0} is the Gaussian width of the initial atom cloud in the i^{th} direction. Equation 5.5 was fitted to ballistic expansion images of the MM MOT at various TOF using the Levenberg-Marquardt algorithm, with T and σ_{i0} as the free parameter. The initial atom cloud size and temperature was measured to be $(T_h, T_v) = (69.8 \pm 20.0, 75.3 \pm 13.4)\,\mu\mathrm{K}$ and $(\sigma_h, \sigma_v) = (1.59 \pm 0.073, 0.792 \pm 0.093)\,\mathrm{mm}$ in the horizontal and vertical directions, respectively.

Using the initial atom number (which is measured directly from the OD) and cloud size, the initial density and atom number in the volume overlapped with the dipole beam was calculated. Using Equation 5.5 along with the measured initial cloud size, temperature, and atom number, the trap size and density at the apex of the MM MOT after $t = 83\,\mathrm{ms}$ TOF for both dipole guided and unguided background atoms was calculated. Because the dipole guided atoms were allowed to expand in only one direction, their peak OD remained higher than the background atoms, which expanded isotropically. The expected OD of the dipole guided atoms is around 0.078, and the expected OD of the background atoms is around 0.024, which is what is seen in Figure 5.17.

5.4.3 Crossed dipole trap in the third chamber

As shown in Figure 5.3, the dipole trapping beams were overlapped with resonant beams for alignment purposes. The alignment of the vertical dipole beam in this system was constrained, at best, to a 1 mm radius around the vertical axis of the MM MOT chamber. Shown in Figure 5.18(a) and (b) are ten-shot averages of absorption images of the dipole

trap in the third chamber. Figure 5.18(a) shows the dipole trap in the third chamber. Figure 5.18(b) shows the dipole trap in the third chamber, with the resonant beam that is overlapped with the horizontal dipole beam intersecting the vertical dipole trap just above the midpoint. Figure 5.18(c) shows a subtracted image of (a) and (b), showing the region where the crossed dipole trap is expected to occur.

The crossed dipole beam has up to 8 W of available power. An f = 100 mm lens produces a calculated focal waist $w_0 = 34\,\mu$m, which has a Rayleigh range $z_R = 3.4$ mm. The trap depth at the focus is $260\,\mu$K/W, with a peak scattering rate of 2.8 photons/s/W. Assuming equal trap depths from the two beams, a $100\,\mu$K atom reservoir would have a heating rate of approximately $0.3\,\mu$K/s in the crossed dipole trap.

5.5 AQuA cell optomechanics package

Shown in Figure 5.19 is the integrated optomechanics package that was developed for the AQuA cell, along the lines of the optomechanics package shown in Section 4.9. The AQuA optomechanics package has three tiers. Shown in Figure 5.19(a), the bottom tier forms the base plate of the package. Four linear roller bearing sleeves are press-fit into the corners. These guide 5/8 in. OD-ground steel posts vertically, which can be secured to the bottom tier with split-ring clamps. This allows steel rails of different lengths to be easily swapped in and out. Mounted to the bottom tier are the push beam optics for the $2D^+$ MOT, and the input dipole beam optics.

Shown in Figure 5.19(b), the second tier has matching roller bearings press-fit into it, which align it to the bottom tier, and allow it to sit above the bottom tier at a variable height. The second tier has the $2D^+$ MOT optics on the bottom side, and the MM MOT optics on the top side. The second tier was designed to be centered on the cylindrical spacer shown in Figure 3.19, which provides a gap between the $2D^+$ MOT and MM MOT chambers in the AQuA cell. The roller bearings allow for precise alignment around the overall dimension variability in cell production.

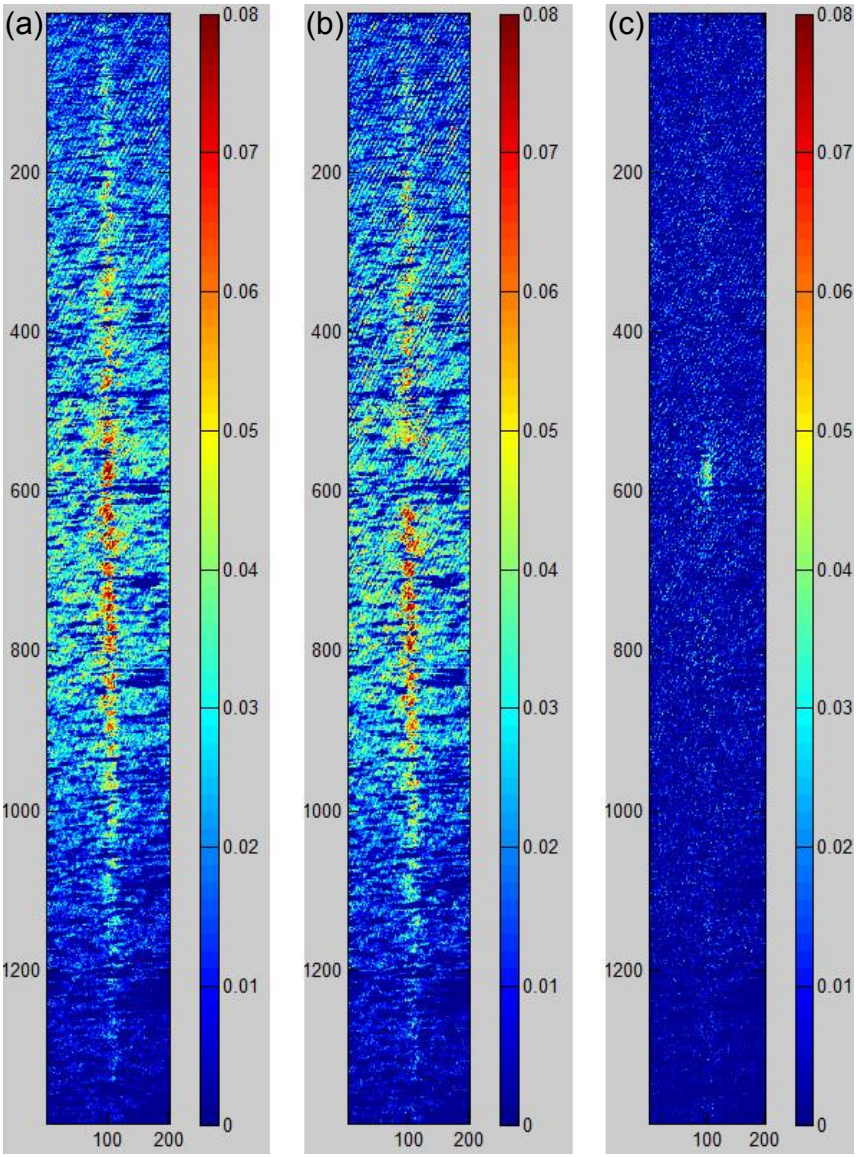

Figure 5.18: (Color) Average of ten images of the dipole trap in the third chamber. (a) Dipole trap in the third chamber with no resonant beam. (b) Dipole trap in the third chamber with the resonant beam intersecting it. (b) Subtraction of images (a) and (b) showing the region where the crossed dipole trap should occur. The OD scale is from 0 to 0.08.

Figure 5.19: (Color) Photo of the AQuA cell optomechanics package, view from the side showing the tiers. (a) Bottom tier with push beam optics, and the input dipole beam optics. The four steel rails are mounted to roller bearing sleeves that are press-fit into the base plate. (b) Second tier has the $2D^+$ MOT optics on the bottom side, and the MM MOT optics on the top side. The second tier also has roller bearings press-fit into it to allow it to be positioned vertically. The second tier is held in place against gravity temporarily by a split-ring clamp attached to the steel rods. (c) The third tier holds the AQuA cell. Alignment in all three axes is done with ball bearing grooves in the plate and clamps. The top of the third tier is left empty to incorporate the quantum computing optics around the Hex cell.

Shown in Figure 5.19(c), the third tier holds the AQuA cell via the ground plane manifold. Precise alignment of the AQuA cell in all three dimensions is achieved by ball bearing contacts. V-grooves in the third tier, and cell clamps that mount to the third tier, which also have machined v-grooves, constrain the ball bearings. The ball bearing makes a point contact to sapphire windows mounted to the AQuA cell. Sapphire windows are mounted to the AQuA cell for protective purposes by reducing the pressure applied directly to the AQuA cell from the ball bearings. The top of the third tier was intentionally left empty to allow for incorporation of the quantum computing optics around the Hex cell, shown in part in Figure 5.2, which are being designed at the University of Wisconsin.

Split-ring clamps on the steel rails allow the height of the second and third tier to be set temporarily by providing stops. This also provides protection for the optics and, most importantly, the AQuA cell. Because the steel rails aren't permanently attached to the bottom tier, they can be swapped out for longer rails. This was done specifically for the protection of the AQuA cell. Longer steel rails allow the third tier to be inserted into the optomechanics setup and be constrained in the horizontal plane, with the AQuA cell well clear of the second tier. The AQuA cell can then be safely lowered to its operating height and aligned to the first and second tiers and locked into place. Then, the shorter steel rails can be reinserted, leaving the region above the third tier accessible. The roller bearings do not constrain the tiers with the same precision as the brass bushings from Section 4.9. Once the proper tier spacing is set, the levels are rigidly attached together using custom length posts.

The optics setup of the AQuA cell package is shown in Figure 5.20. Shown in Figure 5.20(a) is the bottom tier. The push beam comes in from the second tier, is reflected off a PBS, passes through a short-pass dichroic mirror, and is sent into the cell, which is not shown in the center of the setup. The PBS is also used for imaging the $2D^+$ MOT. The dipole trapping beam comes in from the bottom side, passes through a focusing lens on a z-translation stage, is reflected off of the short-pass dichroic mirror, and is sent into the cell.

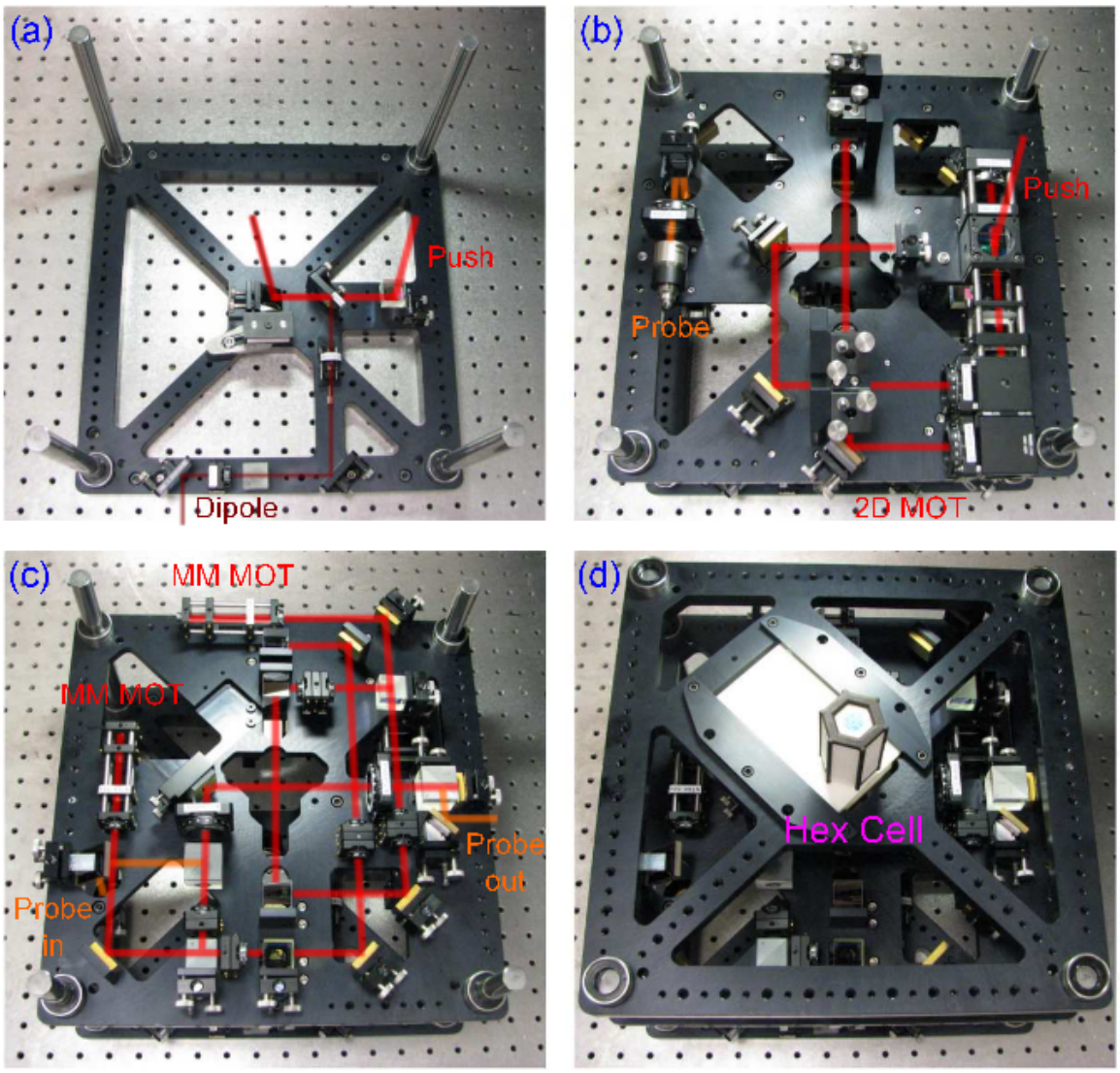

Figure 5.20: (Color) Photo of the AQuA cell optomechanics package, view from the top showing the optics layout and beam paths. (a) Bottom tier: the push beam comes in from the 2D$^+$ MOT, is reflected off a PBS, passes through a short-pass dichroic mirror, and sent into the cell. The PBS is also used for imaging the 2D$^+$ MOT. The dipole trapping beam comes in from the bottom, passes through a focusing lens, is reflected off of the short-pass dichroic mirror, and sent into the cell. (b) 2D$^+$ MOT side of the second tier: the 2D$^+$ MOT fiber comes in from the top-right, where there is beam shaping and splitting. The probe beam comes in on the left and is sent to the MM MOT side. (c) MM MOT side of the second tier: two fiber launchers bring in the two MM MOT cooling frequencies. The probe beam is combined with the horizontal MM MOT beam with opposite polarization, and is coupled out to the camera before the retroreflecting mirror. (d) Third tier showing the 3D printed model of the AQuA cell and a clean upper breadboard. The upper AQuA cell clamps can be seen on either side of the Hex cell.

Shown in Figure 5.20(b) is the bottom side of the second tier, which contains the $2D^+$ MOT optics. The $2D^+$ MOT fiber comes in from the top-right, where there is beam shaping and splitting built around the Thorlabs 30 mm cage system. The probe beam comes in on the left, where it is collimated to a 7 mm diameter with a fixed-distance aspheric fiber collimator, and is sent to the top side of the second tier.

Shown in Figure 5.20(c) is the MM MOT side of the second tier (top side). Two fiber launchers, built on the Thorlabs 16 mm cage system, bring in the two MM MOT cooling frequencies and collimate them to a 1 cm diameter with an f = 50 mm molded plastic aspheric lens (Edmund Optics NT64-582). The probe beam is combined with the horizontal MM MOT beam with perpendicular polarization via a PBS. The PBS before the retroreflecting mirror passes the horizontal MM MOT beam, which is retroreflected, and reflects the probe beam, which is coupled out to the camera.

Shown in Figure 5.20(d) is the third tier showing the AQuA cell and a clean upper breadboard. The upper AQuA cell clamps can be seen on either side of the Hex cell. On all three tiers, and especially the third tier, a grid of interspersed tapped #8-32 and #1/4-20 holes were added for flexibility.

Chapter 6

Outlook

This dissertation has so far discussed the last six years of miniature UHV cell and component development, and two main projects: the portable BEC system, which as a whole was brought to completion, and the ongoing quantum computing effort up to this point. This chapter will briefly discuss the future of improving these miniature vacuum cells and of the quantum computing project.

6.1 Cell technology outlook

There are several current technologies that can be improved upon for miniaturization of UHV cells. Anodic bonding and optical contacting are powerful methods for miniaturization and customization, but in the end, the best achievable atom lifetimes are limited by several different factors.

6.1.1 Improved vacuum from bakeout

The science chamber and the atom collection region are held at two different vacuum pressures because they perform two different functions. In some fashion, the atom collection region's efficiency is dependent on the background pressure and, to a point, is more efficient at worse vacuum. In the science chamber, having the lowest possible background pressure is paramount. In order to maintain the atom collection region at a higher pressure during operation of the UHV cell, differential pumping is employed via geometric constriction of

the conductance, as detailed in Section 3.3.

However, during the pump down and bakeout process, the limited conductance has a negative impact on ultimate performance. The same mechanism that keeps the pressure higher during operation keeps it higher during bakeout, and thus limits the ability of the bakeout process to effectively clean the cell. *In vacuo* anodic bonding was used to partially solve this problem in the AQuA cell, discussed in Section 3.5. However, poor conductance to the $2D^+$ MOT chamber and source tube is not easily solved in this way. A proposed solution is to use *in vacuo* valves, shown in Figure 6.1. These valves would be open during bakeout, so that the conductance is high, and the cell gets as clean as possible. Then, after bakeout, the valves would be closed, effectively blocking the high conductance path, and the effective conductance would be set by the designed differential pumping geometry.

Shown in Figure 6.1 are some examples of *in vacuo* valves. In Figure 6.1(a), a low pressure region (e.g., the 3D MOT chamber) is connected to the bakeout station with high conductance. A high conductance channel and a low conductance channel connect the high pressure region (e.g., the $2D^+$ MOT chamber) to the low pressure region. After bakeout, a ball bearing is moved in place to block the high conductance channel. This could be accomplished magnetically or with gravity. The high and low pressure chambers are now differentially pumped by the pinhole during operation. Shown in Figure 6.1(b) is a top down view of the $2D^+$ MOT silicon pinhole, with large cutouts for improved conductance. After bakeout, plates are rotated to block the cutouts, reducing the conductance to that of the pinhole. The plates could be spring-loaded from the back of the silicon, and their position defined by frictional forces or notches. Shown in Figure 6.1(c), a bimetallic strip is used to actuate a plate. The bimetallic strip is designed such that, during bakeout when the system is hot, the valve is open. Once bakeout is complete and the system has cooled, the bimetallic strip has relaxed, lowering the plate, which blocks the conductance.

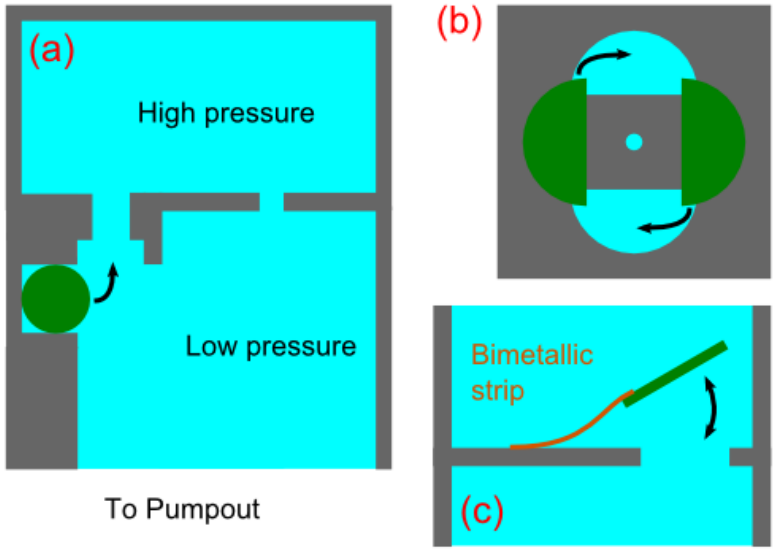

Figure 6.1: (Color) *In vacuo* valve ideas for improving cell conductance. (a) A low pressure region is connected to the pumpout station with high conductance. A high conductance channel and a low conductance channel connect the high pressure region to the low pressure region. After bakeout, a ball bearing is moved in to block the high conductance channel. The high and low pressure chambers are differentially pumped by the pinhole during operation. (b) A top down view of the $2D^+$ MOT silicon pinhole with large cutouts for improved conductance. After bakeout, spring-loaded plates are rotated to block the cutouts, reducing the conductance back to that of the pinhole. (c) A bimetallic strip is used to actuate the *in vacuo* valve. The bimetallic strip is designed such that, during bakeout when the system is hot, the valve is open. Once bakeout is complete and the system has cooled, the bimetallic strip has closed and blocked the conductance.

6.1.2 Improved vacuum during operation

As described above, the vacuum quality achievable during bakeout can be improved by temporarily increasing the conductance of the system. However, during operation of the UHV cell, it must be intentionally dirtied again. There are two ways of maintaining the best vacuum during operation: better dispensers and better pumping efficiency. As described in Section 3.4, under normal operation the current alkali metal dispensers generate a significant amount of unwanted vacuum contaminants, especially hydrogen, in addition to the alkali metal of choice. Utilizing a metal ampoule, as opposed to the alkali metal salt in the dispensers, would provide a pure source, eliminating unwanted background gasses. Developing the technology to miniaturize and integrate these ampoules with the current cell technology is an ongoing effort. The alkali metal can be loaded, under vacuum, into an array of small tubes cored into Pyrex and capped on the back side by silicon. *In vacuo* anodic bonding can be used to cap the other end of the Pyrex with thin silicon, or silicon with integrated silicon nitride windows. The hermetically sealed ampoule can now be incorporated into the source tube via anodic bonding, where it could be processed in atmosphere and at high temperatures without contamination. Once the UHV cell has finished processing, the ampoules can be opened up under vacuum through laser ablation, and the temperature modulated with a thermoelectric cooler [91].

Ion pumps are not particularly good at pumping hydrogen, thus the inclusion of NEGs into the UHV cells. However, neither ion pumps nor NEGs are good at pumping alkali metals. The gold getters described in Section 3.3 are an ongoing development and one solution to this issue. Another option is to incorporate carbon getters into these small systems. Carbon getters are used in atomic clocks to getter alkali metals. However, these systems are large and do not have as stringent vacuum requirements. There remain several challenges to incorporating carbon getters. Cleaning the carbon to the level required to maintain sub-nanotorr vacuum levels is quite challenging. It requires the carbon to be

heated to very high temperature, well above the melting point of Pyrex; thus, mounting the carbon becomes a challenge. Activation through RF induction allows maximal thermal isolation of the carbon and the surrounding cell. While promising, carbon getters remain an ongoing area of research.

It is hoped that the combined improvement of the starting vacuum quality and the operating vacuum quality of the UHV cell will eventually allow the removal of the ion pump, and for vacuum to be maintained with only passive pumping. The end goal of these technologies is to make a UHV cell that is as small, simple, and robust as possible for performing its designed function. Removing the ion pump would reduce the size and complexity of the UHV cell itself, as well as eliminate the need for high voltages and strong magnetic fields, along with the accompanying shielding.

6.1.3 Integrated tungsten feedthroughs

One of the more complicated pieces of the UHV cells are the source feedthroughs. An interesting technology that could be used to simplify this is a Pyrex wafer with integrated miniature electrical feedthroughs. Shown on the left side in Figure 6.2 is a machined piece of SCHOTT HermeS glass. The HermeS wafer is $370\pm30\,\mu$m thick with integrated feedthroughs in Borofloat glass, which has a similar molecular composition to Pyrex and is anodically bondable to silicon. Shown on the right side in Figure 6.2 is a depiction of the integrated feedthroughs, which are coplanar, hermetic (to a leak rate of $\leq 1 \times 10^{-11}$ torr·l/s), $100\,\mu$m diameter, 0.5 A tungsten pins. The standard HermeS wafer has an array of these $100\,\mu$m diameter tungsten pins, with groups of ten pins in two rows, which form a $1.00\,\text{mm} \times 1.60\,\text{mm}$ rectangle, shown in Figure 6.2. Each ten pin rectangular group is on a square grid with a pitch of 6.00 mm that covers the wafer. A standard 4 in. wafer would provide parts for about thirty source tubes, such as the one shown in Figure 6.3, with a current handling capacity of 5 A per feedthrough.

A model of a possible implementation of the SCHOTT HermeS glass source feedthrough

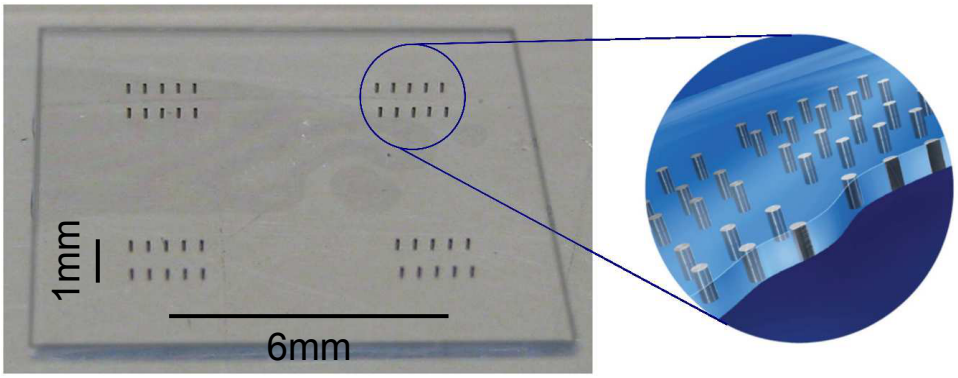

Figure 6.2: (Color) SCHOTT HermeS glass for source tube electrical feedthroughs. Left is a 12 mm × 12 mm square of the HermeS glass cut on a wafer dicing saw. Right is a diagram of the coplanar tungsten pins.

is shown in Figure 6.3. A machined silicon square provides an anodic bonding surface to the $2D^+$ MOT chamber, as in Figure 3.2(c). The silicon is machined in the center so that it both retains the pin, as before, and also provides the relief cutout for the pin head and spring. This reduces the number of required bonds and decreases the stack height. The metallized silicon and the cored, machined piece of Pyrex to which it was bonded are both replaced with the HermeS glass. The pins and spring washers can be slipped in post anodic bonding of the two pieces, which will increase the bonding yield, and allow for post bonding electrical connections to be made and repaired. Part of the challenge of implementing the HermeS glass is making intimate electrical connection to the tungsten pins. Welding to tungsten, as in Section 3.1.1, provides robust connection. However, welding to 100 μm diameter pins is very difficult. Currently being investigated is nickel plating and metallization via deposition methods.

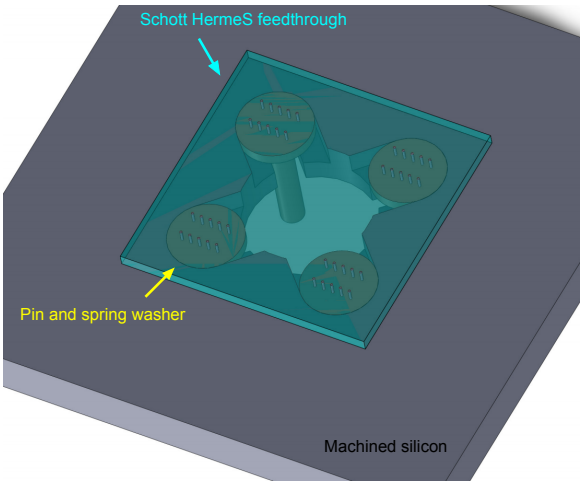

Figure 6.3: (Color) Solidworks model of an implementation of the SCHOTT HermeS glass source feedthrough. A machined silicon square provides connection to the $2D^+$ MOT chamber, as in Figure 3.2(c). The silicon is machined in the center so that it both retains the pin, as before, and also provides the relief for the pin head. The metallized silicon bonded to a cored, machined piece of Pyrex is replaced with the HermeS glass. The pins and spring washers can be slipped in post anodic bonding of the two pieces.

6.2 Quantum computing outlook

Much of the UHV technology described above will be developed under IARPA, and is planned to be incorporated in future generations of AQuA cells. The goal is that these, and future technologies, will provide the best vacuum yet seen in such small and complicated systems. Longer atom lifetimes will allow sufficient time for detection and reloading of single atoms to individual qubit array sites. Concurrent with developments improving vacuum are developments of AQuA cell geometries, which maintain excellent vacuum but improve the atom source and the optical isolation.

One way to improve the atom source is to make the atoms colder before delivering them to the qubit array. One promising technique that is currently being investigated is degenerate Raman sideband cooling, in which atoms are put into a very tight off-resonant optical lattice, where they can be cooled to the ground vibrational state [92]. Particularly interesting are Raman cooling schemes that utilize a 2D optical lattice [93], moving 3D optical lattice [94], or a tightly focused, blue detuned doughnut-mode waveguide [45], because their geometries complement the MM MOT atom transport scheme. These schemes are difficult to implement in small systems because of the high degree of control required over stray fields, but hold promise because of their incredible cooling power, non-resonant nature, and field-free requirements.

6.2.1 *In vacuo* optical isolation

In vacuo optical isolation that is both compact and provides high levels of isolation is critical for many applications, discussed in part in Section 3.3 and in [52]. Magnetic fields can guide atoms over long distances [95, 96] and nicely around curves [16] with proper placement of field generators and bias fields. Optical fields in free space, such as a laser beam in a vacuum, can only guide atoms in a straight line. Optical fibers can be used to guide light around a bend, and specialized optical fibers with a hollow core can guide both light

and atoms. Guiding of atoms through hollow fibers can be achieved with both red detuned optical dipole forces, where the light and the atoms both propagate in the hollow core [97], and blue detuned optical dipole forces, where the light propagates in the cladding, and the evanescent wave guides the atoms in the core [98–100].

In the seminal works of guiding atoms in fibers, the hollow core optical fibers could more accurately be described as hollow core capillary tubes that guide light through total internal reflection, with core diameters from under $20\,\mu$m to over $100\,\mu$m. The highly multimode light in the capillary tubes caused dark spots and irregularities in the guiding field, which put a lower limit on the transit time allowable for the atoms in the fiber, and led to a high heating rate. Additionally, the minimum bending radius of the capillary tubes, before there is any change in optical transmission, is very large.

It turns out that a hollow core capillary tube that is metallized on the inside has a doughnut mode, similar to that in Section 2.4.3, as a fundamental propagation mode [101]. Recent advances in metallization of these fibers has led to a renewed interest in capillary tubes [102,103]. The capillary tubes are intriguing for use in small vacuum systems for several reasons, including relatively large core diameters, which allow for more efficient pumping down during bakeout, and blue detuned dipole guiding, which is always advantageous when low heating and scattering rates are important.

Another fairly recent technology, that is now commercially available, is hollow core photonic crystal fiber (HC PCF). In HC PCF, a microstructured cladding region with air holes guides light in the hollow core, which supports a quasi-Gaussian single mode. The HC PCF guides light using a photonic bandgap guiding mechanism, which is fundamentally different from the total internal reflection guiding of the hollow core capillary tubes. This allows the fiber to handle high power, in a tight single mode, for generating deep red detuned traps. Several groups have demonstrated guiding of laser cooled atoms in straight sections of HC PCF, up to several centimeters [104–106]. There has also been work with BECs around the end of an HC PCF [107].

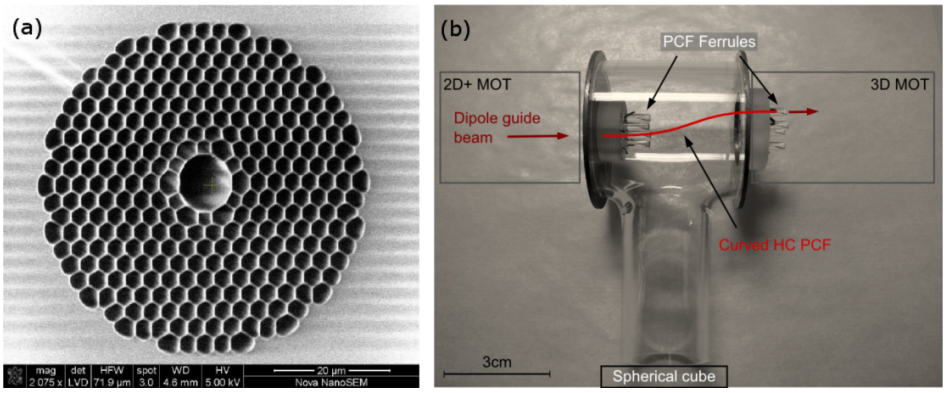

Figure 6.4: (Color) (a) Cleaved facet of the NKT HC-1060-02 hollow core photonic crystal fiber for 1060 nm. At the center is the 10 μm hollow core where a red detuned 1064 nm dipole beam would guide atoms with a mode field diameter of 7.5 μm. (b) Photo of the partially assembled PCF atom transport test cell. The $2D^+$ MOT cell is on the left, where the atom source is located. The dipole guide beam is coupled through the $2D^+$ MOT cell, and guides atoms through the connecting T-shaped chamber where they can be captured in a 3D MOT, a dipole trap, or detected, on the right.

HC PCF is the most interesting candidate for compact *in vacuo* optical isolation because it confines light as tightly as normal fiber, which allows a small minimum bend radius. A small minimum bend radius is required to guide atoms around corners, e.g., optical baffling, in a compact way. Calculations of the optical potential seen by the atoms and simulations of the efficiency of atom guiding have been done in [108]. Shown in Figure 6.4(a) is the face of the NKT HC-1060-02 HC PFC cleaved in-house. At the center is the 10 μm hollow core, through which a red detuned 1064 nm dipole beam would guide atoms. The mode field diameter of the NKT fiber is 7.5 μm. For Cesium, the dipole confinement of a 1064 nm red detuned beam confined to the core is approximately 20 mK/W. The NKT fiber has a quoted bend radius of 0.5 cm before there is any change in optical transmission.

Shown in Figure 6.4(b) is the partially constructed cell for testing the NKT HC PCF. The $2D^+$ MOT chamber is on the left, where the atom source is located. The dipole guide beam is coupled through the end of the $2D^+$ MOT chamber. The HC PCF is held at both ends by Pyrex ferrules. The ferrules are held in place by a cored Pyrex disc bonded to the silicon caps of the T-shaped chamber in the center, which connects the $2D^+$ MOT chamber and the 3D MOT chamber. There are four sets of ferrules, which hold two fibers that are curved and two fibers that are straight. This allows for redundancy and repeatability of previous results from other groups. Atoms will be guided through the connecting T-shaped chamber to the 3D MOT chamber on the right, where they can be captured in a 3D MOT, a dipole trap, or simply detected. The T-shaped chamber will be anodically bonded to a G2M that is attached to a spherical cube. One of the major concerns with utilizing HC PCF in small vacuum systems is the ability to effectively clean them during bakeout. The ferrules are offset from the center of the double MOT chamber so that a standard double MOT can be made to test the vacuum properties. Methods for cleaning the HC PCF before integration into the UHV cell, such as high pressure, hot helium are also being investigated.

Bibliography

[1] M. H. Anderson, J. R. Ensher, M. R. Mattews, C. E. Wieman, and E. A. Cornell, "Observation of Bose-Einstein condensation in a dilute atomic vapor," Science, vol. 269, p. 198, 1995.

[2] K. B. Davis, M. O. Mewes, M. R. Andrews, N. J. van Druten, D. S. Durfee, D. M. Kurn, and W. Ketterle, "Bose-Einstein condensation in a gas of sodium atoms," Phys. Rev. Lett., vol. 75, p. 3969, 1995.

[3] T. Könemann, W. Brinkmann, E. Göklü, C. Lämmerzahl, H. Dittus, T. van Zoest, E. Rasel, W. Ertmer, W. Lewoczko-Adamczyk, and M. Schiemangk, "A freely falling magneto-optical trap drop tower experiment," Appl. Phys. B: Lasers Opt., vol. 89, pp. 431–438, 2007.

[4] S. Wildermuth, S. Hofferberth, I. Lesanovsky, S. Groth, P. Krüger, J. Schmiedmayer1, and I. Bar-Joseph, "Sensing electric and magnetic fields with Bose-Einstein condensates," Appl. Phys. Lett., vol. 88, p. 264103, 2006.

[5] G. Stern, B. Battelier, R. Geiger, G. Varoquaux, A. Villing, F. Moron, O. Carraz, N. Zahzam, Y. Bidel, W. Chaibi, F. P. D. Santos, A. Bresson, A. Landragin, and P. Bouyer, "Light-pulse atom interferometry in microgravity," Eur. Phys. J. D, vol. 53, pp. 353–357, 2009.

[6] P. Treutlein, P. Hommelhoff, T. Steinmetz, T. W. Hänsch, and J. Reichel, "Coherence in microchip traps," Phys. Rev. Lett., vol. 92, p. 203005, 2004.

[7] N. Yu, J. Kohel, J. Kellogg, and L. Maleki, "Development of an atom-interferometer gravity gradiometer for gravity measurement from space," Appl. Phys. B: Lasers Opt., vol. 84, pp. 647–652, 2006.

[8] J. M. McGuirk, G. T. Foster, J. B. Fixler, M. J. Snadden, and M. A. Kasevich, "Sensitive absolute-gravity gradiometry using atom interferometry," Phys. Rev. A, vol. 65, p. 033608, 2002.

[9] W. Hänsel, P. Hommelhoff, T. W. Hänsch, and J. Reichel, "Bose-Einstein condensation on a microelectronic chip," Nature, vol. 413, p. 498, 2001.

[10] C. Monroe, D. M. Meekhof, B. E. King, W. M. Itano, and D. J. Wineland, "Demonstration of a fundamental quantum logic gate," Phys. Rev. Lett., vol. 75, p. 4714, 1995.

[11] R. Blatt and D. Wineland, "Entangled states of trapped atomic ions," Nature, vol. 453, p. 1008, 2008.

[12] L. DiCarlo, J. M. Chow, J. M. Gambetta, L. S. Bishop, B. R. Johnson, D. I. Schuster, J. Majer, A. Blais, L. Frunzio, S. M. Girvin, and R. J. Schoelkopf, "Demonstration of two-qubit algorithms with a superconducting quantum processor," Nature (London, U. K.), vol. 460, p. 240, 2009.

[13] A. Politi, J. C. F. Matthews, and J. L. OBrien, "Shors quantum factoring algorithm on a photonic chip," Science, vol. 325, p. 1221, 2009.

[14] M. Saffman, T. G. Walker, and K. Mölmer, "Quantum information with Rydberg atoms," Reviews of Modern Physics, vol. 82, p. 2313, 2010.

[15] L. Isenhower, E. Urban, X. L. Zhang, A. T. Gill, T. Henage, T. A. Johnson, T. G. Walker, and M. Saffman, "Demonstration of a neutral atom controlled-not quantum gate," Phys. Rev. Lett., vol. 104, p. 010503, 2010.

[16] W. Hänsel, J. Reichel, P. Hommelhoff, and T. W. Hänsch, "Magnetic conveyor belt for transporting and merging trapped atom clouds," Phys. Rev. Lett., vol. 86, p. 608, 2001.

[17] A. Aghajani-Talesh, M. Falkenau, A. Griesmaier, and T. Pfau, "A proposal for continuous loading of an optical dipole trap with magnetically guided ultra-cold atoms," J. Phys. B: At., Mol. Opt. Phys., vol. 42, p. 245302, 2009.

[18] A. P. Chikkatur, A. E. L. Y. Shin, D. Kielpinski, E. Tsikata, T. L. Gustavson, D. E. Pritchard, and W. Ketterle, "A continuous source of Bose-Einstein condensed atoms," Science, vol. 296, pp. 2193–2195, 2002.

[19] D. Schrader, S. Kuhr, W. Alt, M. Müller, V. Gomer, and D. Meschede, "An optical conveyor belt for single neutral atoms," Appl. Phys. B: Lasers Opt., vol. 73, p. 819, 2001.

[20] K. Afrousheh, P. Bohlouli-Zanjani, D. Vagale, A. Mugford, M. Fedorov, and J. D. D. Martin, "Spectroscopic observation of resonant electric dipole-dipole interactions between cold rydberg atoms," Phys. Rev. Lett., vol. 93, p. 233001, 2004.

[21] D. E. Pritchard, K. Helmerson, and A. G. Martin, "Atom traps," in Atomic Physics 11 (S. Haroche, J. C. Gay, and G. Grynberg, eds.), World Scientific, Singapore, 1989.

[22] J. Reichel, "Microchip traps and Bose-Einstein condensation," Appl. Phys. B: Lasers Opt., vol. 75, pp. 469–487, 2002.

[23] A. E. Leanhardt, Microtraps and Waveguides for Bose-Einstein Condensates. PhD thesis, Massachusetts Institute of Technology, 2003.

[24] R. Grimm, M. Weidemüller, and Y. B. Ovchinnikov, "Optical dipole traps for neutral atoms," Adv. At., Mol., Opt. Phys., vol. 42, pp. 95–170, 2008.

[25] C. Cohen-Tannoudji, "Manipulating atoms with photons," in Nobel Lecture, 1997.

[26] S. Chu, "The manipulation of neutral particles," in Nobel Lecture, 1997.

[27] M. Schulz, Tightly confined atoms in optical dipole traps. PhD thesis, University of Innsbruck, 2002.

[28] M. B. Squires, High repetition rate Bose-Einstein condensate production in a compact, transportable vacuum system. PhD thesis, University of Colorado, 2008.

[29] P. Berthoud, E. Fretel, and P. Thomann, "Bright, slow, and continuous beam of laser-cooled cesium atoms," Phys. Rev. A: At., Mol., Opt. Phys., vol. 60, p. R4241, 1999.

[30] K. Szymaniec, H. J. Davies, and C. S. Adams, "An atomic fountain guided by a far-off resonance laser beam," Europhys. Lett., vol. 45, pp. 450–455, 1999.

[31] P. Cren, C. Roos, A. Aclan, J. Dalibard, and D. Guéry-Odelin, "Loading of a cold atomic beam into a magnetic guide," Eur. Phys. J. D, vol. 20, pp. 107–116, 2002.

[32] L. Cacciapuoti, A. Castrillo, M. de Angelis, and G. Tino, "A continuous cold atomic beam from a magneto-optical trap," Eur. Phys. J. D, vol. 15, pp. 245–249, 2001.

[33] S. Weyers, E. Aucouturier, C. Valentin, and N. Dimarcq, "A continuous beam of cold cesium atoms extracted from a two-dimensional magneto-optical trap," Opt. Commun., vol. 143, pp. 30–34, 1997.

[34] E. Riis, D. S. Weiss, K. A. Moler, and S. Chu, "Atom funnel for the production of a slow, high-density atomic beam," Phys. Rev. Lett., vol. 64, p. 1658, 1990.

[35] Z. T. Lu, K. L. Corwin, M. J. Renn, M. H. Anderson, E. A. Cornell, and C. E. Wieman, "Low-velocity intense source of atoms from a magneto-optical trap," Phys. Rev. Lett., vol. 77, p. 3331, 1996.

[36] K. Dieckmann, R. J. C. Spreeuw, M. Weidemüller, and J. T. M. Walraven, "Two-dimensional magneto-optical trap as a source of slow atoms," Phys. Rev. A: At., Mol., Opt. Phys., vol. 58, p. 3891, 1998.

[37] P. D. Lett, W. D. Phillips, S. L. R. nad C. E. Tanner, R. N. Watts, and C. I. Westbrook, "Optical molasses," J. Opt. Soc. Am. B, vol. 6, p. 2084, 1989.

[38] M. A. Kasevich, Atom Interferometry in an Atomic Fountain. PhD thesis, Stanford University, 1992.

[39] K. Takase, Precision Rotation Rate Measurements with a Mobile Atom Interferometer. PhD thesis, Stanford University, 2008.

[40] C. F. Roos, P. Cren, J. Dalibard, and D. Guéry-Odelin, "A source of cold atoms for a continuously loaded magnetic guide," Phys. Scr., vol. T105, pp. 19–22, 2003.

[41] D. M. Stamper-Kurn, M. R. Andrews, A. P. Chikkatur, S. Inouye, H.-J. Miesner, J. Stenger, and W. Ketterle, "Optical confinement of a Bose-Einstein condensate," Phys. Rev. Lett., vol. 80, p. 2027, 1998.

[42] J. D. Jackson, Classical Electrodynamics. Wiley, 1998.

[43] L. Allen and J. H, Optical resonance and two-level atoms. Wiley, New York, 1975.

[44] S.-C. Chu, T. Ohtomo, and K. Otsuka, "Generation of doughnutlike vortex beam with tunable orbital angular momentum from lasers with controlled hermitegaussian modes," Appl. Opt., vol. 47, p. 2583, 2008.

[45] M. Schiffer, M. Rauner, S. Kuppens, M. Zinner, K. Sengstock, and W. Ertmer, "Guiding, focusing, and cooling of atoms in a strong dipole potential," Appl. Phys. B: Lasers Opt., vol. 67, pp. 705–708, 1998.

[46] G. Li, S. Zhang, L. Isenhower, K. Maller, and M. Saffman, "A crossed vortex bottle beam trap for single-atom qubits," Opt. Lett., vol. 37, p. 851, 2012.

[47] W. Ketterle, K. B. Davis, M. A. Joffe, A. Martin, and D. E. Pritchard, "High densities of cold atoms in a *dark* spontaneous-force optical trap," Phys. Rev. Lett., vol. 70, pp. 2253–2256, 1993.

[48] L. Isenhower, W. Williams, A. Dally, and M. Saffman, "Atom trapping in an interferometrically generated bottle beam trap," Opt. Lett., vol. 34, p. 1159, 2009.

[49] S. E. Olson, M. L. Terraciano, M. Bashkansky, and F. K. Fatemi, "Cold atom confinement in an all-optical dark ring trap," arXiv.org, vol. arXiv:0802.1213v1, p. 5, 2008.

[50] E. A. Donley, T. P. Heavner, F. Levi, M. O. Tataw, and S. R. Jefferts, "Double-pass acousto-optic modulator system," Rev. Sci. Instrum., vol. 76, p. 063112, 2005.

[51] W. Alt, D. Schrader, S. Kuhr, M. Müller, V. Gomer, and D. Meschede, "Single atoms in a standing-wave dipole trap," Phys. Rev. A, vol. 67, p. 033403, 2003.

[52] E. A. Salim, Ultracold matter systems and atomtronics instrumentation. PhD thesis, University of Colorado, 2011.

[53] S. R. Segal, Progress towards an ultracold atomic Sagnac gyroscope. PhD thesis, University of Colorado, 2010.

[54] R. Folman, P. Krüger, D. Cassettari, B. Hessmo, T. Maier, and J. Schmiedmayer, "Controlling cold atoms using nanofabricated surfaces: Atom chips," Phys. Rev. Lett., vol. 84, p. 4749, 2000.

[55] C. J. Vale, B. Upcroft, M. J. Davis, N. R. Heckenberg, and H. Rubinsztein-Dunlop, "Foil-based atom chip for Bose-Einstein condensates," J. Phys. B: At., Mol. Opt. Phys., vol. 37, pp. 2959–2967, 2004.

[56] B. V. Hall, S. Whitlock, F. Scharnberg, P. Hannaford, and A. Sidorov, "A permanent magnetic film atom chip for Bose-Einstein condensation," J. Phys. B: At., Mol. Opt. Phys., vol. 39, pp. 27–36, 2006.

[57] P. Treutlein, Coherent manipulation of ultracold atoms on atom chips. PhD thesis, LudwigMaximiliansUniversität München, 2008.

[58] E. A. Salim, S. C. Caliga, J. B. Pfeiffer, and D. Z. Anderson, "High resolution imaging and optical control of Bose-Einstein condensates in an atom chip magnetic trap," Appl. Phys. Lett., vol. , pp. , *In Progress*.

[59] M. Talukdar and E. Baker, "Conductivity studies on silver oxide," Solid State Commun., vol. 7, pp. 309–310, 1969.

[60] E. A. Salim, J. DeNatale, D. M. Farkas, K. M. Hudek, S. E. McBride, J. Michalchuk, R. Mihailovich, and D. Z. Anderson, "Compact, microchip-based systems for practical applications of ultracold atoms," Quantum Inf Process, vol. 10, pp. 975–994, 2011.

[61] J. Reichel and V. Vuletic, eds., Atom Chips. Wiley-VCH, 2011.

[62] T. Pfau, "Continuous progress on atom lasers," Science, vol. 296, pp. 2155–2156, 2002.

[63] E. P. Power, G. Raithel, L. George, B. Vanderelzen, P. Herrera-Fierro, R. Murphy, and S. M. Yalisove, "Design and fabrication of a chip-based continuous-wave atom laser," arXiv.org, vol. arXiv:1202.0479v1, p. 10, 2012.

[64] C. Monroe, W. Swann., H. Robinson, and C. Wieman, "Very cold trapped atoms in a vapor cell," Phys. Rev. Lett., vol. 65, p. 1571, 1990.

[65] K. E. Gibble, S. Kasapi, and S. Chu, "Improved magneto-optic trapping in a vapor cell," Opt. Lett., vol. 17, p. 526, 1992.

[66] G. Tinelli and D. Holcomb, "NMR and structural properties of CsAu and RbAu," J. Solid State Chem., vol. 25, pp. 157–168, 1978.

[67] H. Hirano, Y. Kondo, and N. Yoshimura, "Matrix calculation of pressures in highvacuum systems," J. Vac. Sci. Technol., A, vol. 6, p. 2865, 1988.

[68] S. Dushman, Scientific Foundations of Vacuum Technique. John Wiley & Sons Inc, 1962.

[69] K. B. Wear, "Electrical characteristics of sputter-ion pumps," J. Appl. Phys., vol. 48, p. 1936, 1967.

[70] G. L. Saksaganskii, Getter and Getter-Ion Vacuum Pumps. Routledge, 1994.

[71] D. M. Farkas, K. M. Hudek, E. A. Salim, S. R. Segal, M. B. Squires, and D. Z. Anderson, "A compact, transportable, microchip-based system for high repetition rate production of Bose-Einstein condensates," Appl. Phys. Lett., vol. 96, p. 093102, 2010.

[72] M. E. Gehm, K. M. OHara, T. A. Savard, and J. E. Thomas, "Dynamics of noise-induced heating in atom traps," Phys. Rev. A: At., Mol., Opt. Phys., vol. 58, p. 3914, 1998.

[73] H. J. Lewandowski, D. M. Harber, D. L. Whitaker, and E. A. Cornell, "Simplified system for creating a Bose-Einstein condensate," J. Low Temp. Phys., vol. 132, p. 309, 2003.

[74] W. Petrich, M. H. Anderson, J. R. Ensher, and E. A. Cornell, "Behavior of atoms in a compressed magneto-optical trap," J. Opt. Soc. Am. B, vol. 11, pp. 1332–1335, 1994.

[75] H. H. Metcalf and P. van der Straten, Laser Cooling and Trapping. Springer, 1999.

[76] W. Happer, "Optical pumping," Rev. Mod. Phys., vol. 44, pp. 169–249, 1972.

[77] S. Du, Atom-chip Bose-Einstein condensation in a portable vacuum cell. PhD thesis, University of Colorado, 2005.

[78] W. Ketterle and N. J. van Druten, "Evaporative cooling of trapped atoms," Advances in Atomic, Molecular, and Optical Physics, vol. 37, pp. 181–236, 1996.

[79] W. Ketterle, D. Durfee, and D. Stamper-Kurn, "Making, probing and understanding Bose-Einstein condensates," in Proceedings of the International School of Physics Enrico Fermi, Course CXL (M. Inguscio, S. Stringari, and C. Wieman, eds.), pp. 67–176, IOS, Amsterdam, The Netherlands, 1999.

[80] M. Horikoshi and K. Nakagawa, "Atom chip based fast production of Bose-Einstein condensate," Appl. Phys. B: Lasers Opt., vol. 82, p. 262, 2006.

[81] S. Du and E. Oh, "Three-wire magnetic trap for direct forced evaporative cooling," Phys. Rev. A, vol. 79, p. 013407, 2009.

[82] K. M. Hudek, D. M. Farkas, S. Du, and D. Z. Anderson, "Efficient direct forced evaporative cooling on an atom chip magnetic trap," Phys. Rev. A: At., Mol., Opt. Phys., vol. , pp. , *In Progress.*

[83] D. M. Harber, J. M. McGuirk, J. M. Obrecht, and E. A. Cornell, "Thermally induced losses in ultra-cold atoms magnetically trapped near room-temperature surfaces," J. Low Temp. Phys., vol. 133, p. 229, 2003.

[84] Y. Lin, I. Teper, C. Chin, and V. Vuletić, "Impact of the Casimir-Polder potential and Johnson noise on Bose-Einstein condensate stability near surfaces," Phys. Rev. Lett., vol. 92, p. 050404, 2004.

[85] T. van Zoest, N. Gaaloul, Y. Singh, H. Ahlers, W. Herr, S. T. Seidel, W. Ertmer, E. Rasel, M. Eckart, E. Kajari, S. Arnold, G. Nandi, W. P. Schleich, R. Walser, A. Vogel, K. Sengstock, K. Bongs, W. Lewoczko-Adamczyk, M. Schiemangk, T. Schuldt, A. Peters, T. Könemann, H. Müntinga, C. Lämmerzahl, H. Dittus, T. Steinmetz, T. W. Hänsch, and J. Reichel, "Bose-Einstein condensation in microgravity," Science, vol. 328, pp. 1540–1543, June 2010.

[86] D. DiVincenzo, "The physical implementation of quantum computers," Fort. der Physik, vol. 48, p. 771, 1998.

[87] C. Benvenuti, "Extreme high vacuum technology for particle accelerators," in IEEE Proceedings 2001 Particle Accelerator Conference, 2001.

[88] E. Urban, T. A. Johnson, T. Henage, L. Isenhower, D. D. Yabus, T. G. Walker, and M. Saffman, "Observation of Rydberg blockade between two atoms," Nature, vol. 5, p. 110, 2009.

[89] M. L. Citron, H. R. Gray, C. W. Gabel, and J. C. R. Stroud, "Experimental study of power broadening in a two-level atom," Phys. Rev. A, vol. 16, p. 1507, 1977.

[90] B. H. Bransden and C. J. Joachain, Physics of Atoms and Molecules. Addison-Wesley, 2003.

[91] E. W. Streed, A. P. Chikkatur, T. L. Gustavson, M. Boyd, Y. Torii, D. Schneble, G. K. Campbell, D. E. Pritchard, and W. Ketterle, "Large atom number Bose-Einstein condensate machines," Rev. Sci. Instrum., vol. 77, p. 023106, 2006.

[92] D. L. Haycock, S. E. Hamann, G. Klose, and P. S. Jessen, "Atom-trapping in the lamb-dicke regime in a far-off-resonance optical lattice," in Society of Photo-Optical Instrumentation Engineers (SPIE) Conference Series (M. G. Prentiss and W. D. Phillips, eds.), pp. 163–172, 1997.

[93] G. D. Domenico, N. Castagna, G. Mileti, and P. Thomann, "Laser collimation of a continuous beam of cold atoms using zeeman-shift degenerate-raman-sideband cooling," Phys. Rev. A, vol. 69, p. 063403, 2004.

[94] P. Treutlein, K. Y. Chung, and S. Chu, "High-brightness atom source for atomic fountains," Phys. Rev. A, vol. 63, p. 051401(R), 2001.

[95] A. Greiner, J. Sebastian, P. Rehme, A. Aghajani-Talesh, A. Griesmaier, and T. Pfau, "Loading chromium atoms in a magnetic guide," J. Phys. B: At., Mol. Opt. Phys., vol. 40, pp. F7–F84, 2007.

[96] A. Griesmaier, A. Aghajani-Talesh, M. Falkenau, J. Sebastian, A. Greiner, and T. Pfau, "A high flux of ultra-cold chromium atoms in a magnetic guide," J. Phys. B: At., Mol. Opt. Phys., vol. 42, p. 145306, 2009.

[97] M. J. Renn, D. Montgomery, O. Vdovin, D. Z. Anderson, C. E. Wieman, and E. A. Cornell, "Laser-guided atoms in hollow-core optical fibers," Phys. Rev. Lett., vol. 75, p. 3253, 1995.

[98] H. Ito, K. Sakaki, W. Jhe, and M. Ohtsu, "Evanescent-light induced atom-guidance using a hollow optical fiber with light coupled sideways," Opt. Commun., vol. 141, pp. 43–47, 1997.

[99] R. G. Dall, M. D. Hoogerland, K. G. H. Baldwin, and S. J. Buckman, "Guiding of metastable helium atoms through hollow optical fibres," J. Opt. B: Quantum Semiclass. Opt., vol. 1, pp. 396–401, 1999.

[100] D. Mu̇ller, E. A. Cornell, D. Z. Anderson, and E. R. I. Abraham, "Guiding laser-cooled atoms in hollow-core fibers," Phys. Rev. A: At., Mol., Opt. Phys., vol. 61, p. 033411, 2000.

[101] J. P. Crenn, "Optical study of the eh_{11} mode in a hollow circular oversized waveguide and gaussian approximation of the far-field pattern," Appl. Opt., vol. 23, p. 3428, 1984.

[102] Z. Wang and J. Yin, "Atomic quantum motion and single-mode waveguiding in a hollow metallic waveguide," J. Opt. Soc. Am. B, vol. 25, p. 1051, 2008.

[103] F. K. Fatemi, M. Bashkansky, E. Oh, and D. Park, "Efficient excitation of the te_{01} hollow metal waveguide mode for atom guiding," Opt. Express, vol. 18, p. 323, 2010.

[104] T. Takekoshi and R. J. Knize, "Optical guiding of atoms through a hollow-core photonic band-gap fiber," Phys. Rev. Lett., vol. 98, p. 210404, 2007.

[105] S. Vorrath, S. A. M̈ller, P. Windpassinger, K. Bongs, and K. Sengstock, "Efficient guiding of cold atoms through a photonic band gap fiber," New Journal of Physics, vol. 12, p. 123015, 2010.

[106] M. Bajcsy, S. Hofferberth, T. Peyronel, V. Balic, Q. Liang, A. S. Zibrov, V. Vuletic, and M. D. Lukin, "Laser-cooled atoms inside a hollow-core photonic-crystal fiber," Phys. Rev. A, vol. 83, p. 063830, 2011.

[107] C. A. Christensen, S. Will, M. Saba, G.-B. Jo, Y.-I. Shin, W. Ketterle, and D. Pritchard, "Trapping of ultracold atoms in a hollow-core photonic crystal fiber," Phys. Rev. A: At., Mol., Opt. Phys., vol. 78, p. 033429, 2008.

[108] R. Liu, Q. Zhou, Y. Yin, and J. Yin, "Laser guiding of cold molecules in a hollow photonic bandgap fiber," J. Opt. Soc. Am. B, vol. 26, p. 1076, 2009.

[109] E. L. Raab, M. Prentiss, A. Cable, S. Chu, and D. E. Pritchard, "Trapping of neutral sodium atoms with radiation pressure," Phys. Rev. Lett., vol. 59, p. 2631, 1987.

[110] J. Reichel, W. Hänsel, and T. W. Hänsch, "Atomic micromanipulation with magnetic surface traps," Phys. Rev. Lett., vol. 83, p. 3398, 1999.

[111] I. Sivan, "Magneto-optical trap based multi-directional cold atomic fountain IARPA," Master's thesis, University of Oxford, 2010.

Appendix A

Electronics

The unipolar coil driver is shown in Figure A.1 and is based around a high-power MOSFET (IRFP2907) for current control. The AD797 is an ultra-low noise op-amp that is controlled by a 0 V to +10 V signal from the computer-controlled DAC. The input voltage divider changes the gain of the output current to the input voltage, and values were chosen such that the input gain is 1 A/V. A tunable inductance-compensating Zobel network (R3, C3, and R4) stabilizes the circuit and allows driving of the various coils, which can vary in inductance from below 1 mH to over 4 mH, with typical values of 1-2 mH. A non-inverting amplifier with an inductive load as the main feedback element is unstable due to the phase shifts introduced by the inductance. The Zobel network provides an alternative high-frequency path around the load.

Current is sensed with a low-resistance (for efficiency), very low temperature coefficient (0.5 ppm/°C for stability) resistor R_{sense}. Due to feedback, the amplifier will output the necessary current to force the voltage drop across the sense resistor to equal the voltage on the amplifier's positive input. Current is monitored with the OP27 non-inverting unity-gain buffer circuit.

The bipolar coil driver shown in Figure A.2 is based on an MP108 power op-amp from Apex Precision Power. The MP108 can output currents up to 12 A at voltages up to 200 V and is configured as a non-inverting voltage-to-current converter. Here, by placing the load inside the amplifier's feedback path, accuracy and linearity are greatly improved.

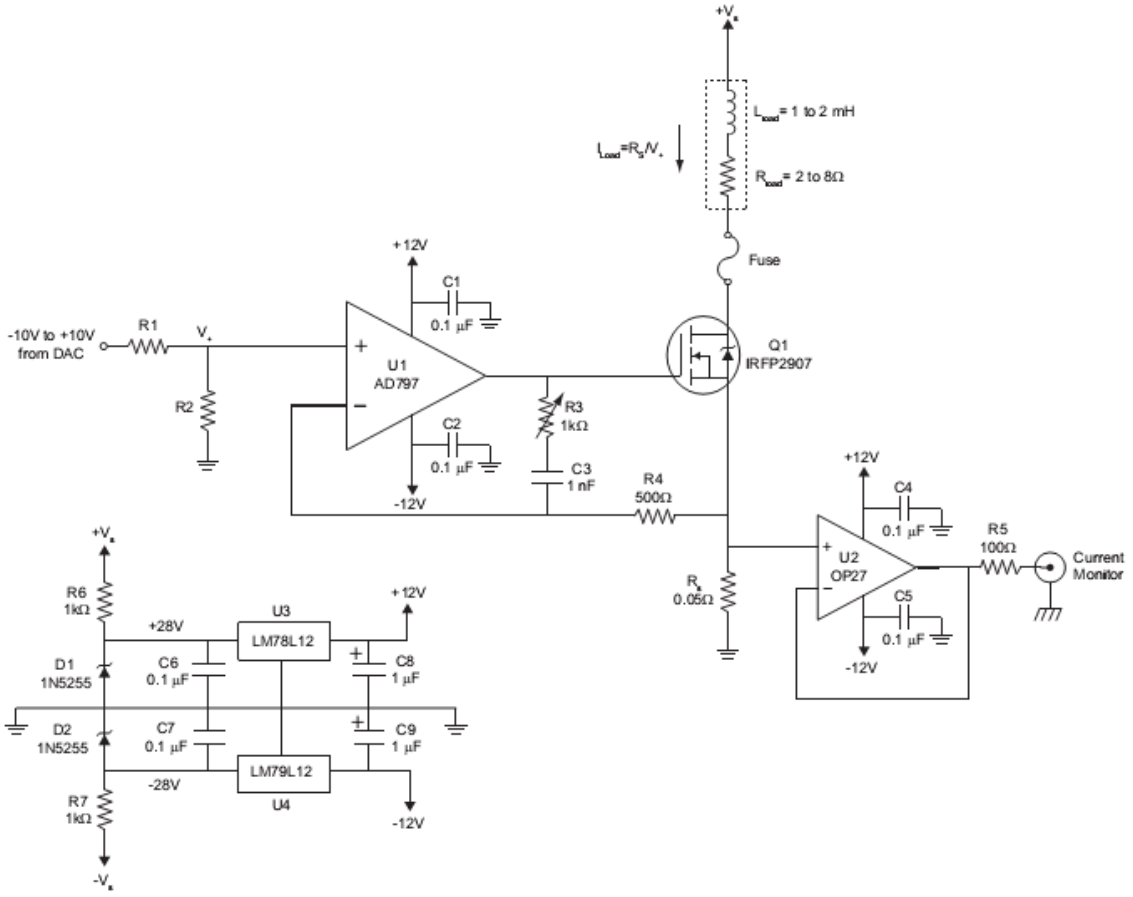

Figure A.1: Unipolar coil driver circuit diagram.

However, current flowing through the load cannot be returned directly to ground. This is not a problem when driving coils that are isolated from other circuits, as is the case here.

The amplifier is controlled by a -10 V to +10 V DAC signal. A pair of signal diodes (1N4148) across the inputs ensures that the amplifier's common-mode input voltage range of 25 V is never exceeded. Current is monitored across the sense resistor using an instrumentation amplifier (AD620).

One of the benefits of the MP108 is that the output MOSFETs can be powered from different supplies than the small signal stages of the amplifier. The output stage is powered by supply voltages V_S while the small signal stages are powered by "boost" voltages V_B. When V_B is 10 V higher than V_S, the output MOSFETs are driven into the triode region, thereby allowing the amplifier output voltage to reach its rail V_S. This configuration greatly improves efficiency by reducing the voltage drop across the output MOSFETs.

A different bipolar circuit design was used to drive the chip wires because they are a non-inductive load and is shown in Figure A.3. The computer-controlled signal comes in through the AD797 and drives the PA07 5 A power op-amp. The PA07 was chosen because it provides optimum linearity, especially at low levels, as the output stage is internally biased for class A/B operation using a thermistor-compensated base-emitter voltage-multiplier circuit. Signal diodes are again used to clamp the op-amp's common-mode input, and current is monitored across the sense resistor with an AD620. A Bussmann GMC-2.5A fuse is placed in-line with the output to protect the chip traces from an output of 5 A for greater than 500 ms or 4 A for greater than 1 s, while allowing the standard operational current of the z-wire trace of 3.25 A for up to 5 s, which is longer than an experimental cycle.

Because the chip wires are patterned onto silicon substrate, which is an imperfect thermal conductor, we designed a chip-protection circuit that did not just limit current (e.g., via a fuse) but also took into account heat buildup of the system. This "power"-protection circuit is shown in Figure A.4. An instrumentation amp (AD620) monitors the current output across R_S, which provides the input to an analog multiplier (AD633). The

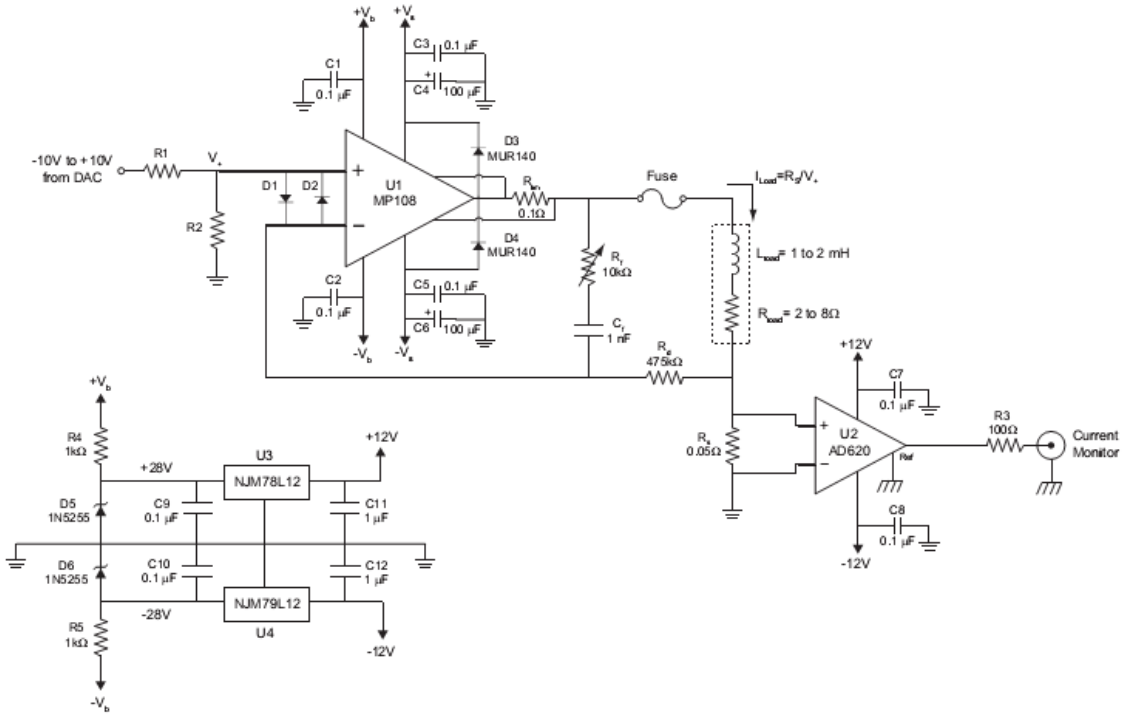

Figure A.2: Bipolar coil driver circuit diagram.

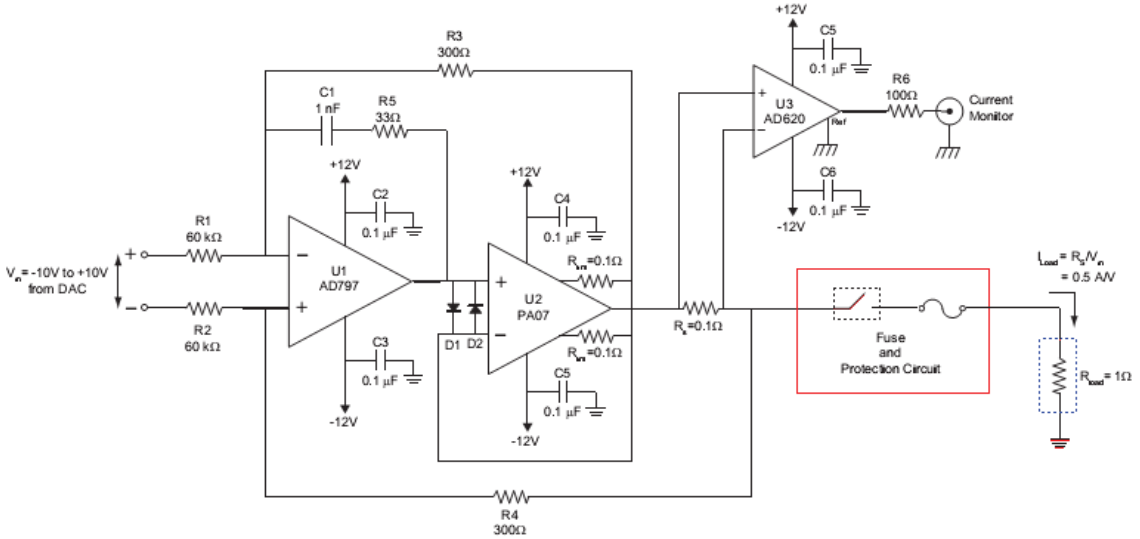

Figure A.3: Bipolar chip driver circuit diagram.

analog multiplier transfer function is given by

$$V_{out} = \frac{(x_1 - x_2)(y_1 - y_2)}{10\,\mathrm{V}}. \tag{A.1}$$

By applying the input to x_1 and y_1 and grounding x_2 and y_2, analog multiplier acts as a squaring circuit. Because power $\propto$ current^2 the AD633 effectively turns the current monitor into a power monitor. The output of the AD633 is the input into a "leaky" integrator op-amp circuit using an OP27, which acts as the "heat" dissipation mechanism. R_1 and R_2 control the time constants associated with heating and cooling of the chip. This is then input to a comparator with a latching mechanism (AD790) that opens a reed relay when the voltage exceeds that set by R_3, disconnecting the output until the latch has been reset. The trip voltage is monitored with another AD620.

The switching-mode power supplies used to power the coil and chip driver circuits are shown in Figure A.5. The Excelsys XQB, shown in pink, is a low-noise, 900 W chassis that has six floating output channels each capable of up to 240 W of output power, with output voltage and current determined by the plug-and-play modules, which are labeled Xg3, Xg4, and Xg5. For the coil driver power supply, three Xg3s are run in series to provide a positive rail of +30 V at 20 A. An Xg4 provides a negative rail of -30 V at 10 A. Two Xg5s provide the $\pm$40 V "boost" voltages. The asymmetric nature of the modules in the coil driver in Figure A.5(a) takes advantage of the fact that once an orientation for both the MOT and transport (quadrupole or big-Z) coils has been chosen, the power supply can be wired to apply most of the current in the forward direction.

The chip driver Excelsys power supply configuration has two Xg3s to provide the $\pm$12 V rails and ground, which are floating with respect to earth ground. A second set of Xg3s in the same configuration provides a second chip wire channel. For both the coil and chip drivers, each rail is filtered in the same fashion. Both are filtered with 0.1 μF ceramic bypass capacitors. In addition, 100 μF electrolytic bypass capacitors are used to filter the supply voltages. A Trisil (SMTPA62) is a bidirectional thyristor device that a symmetric breakdown

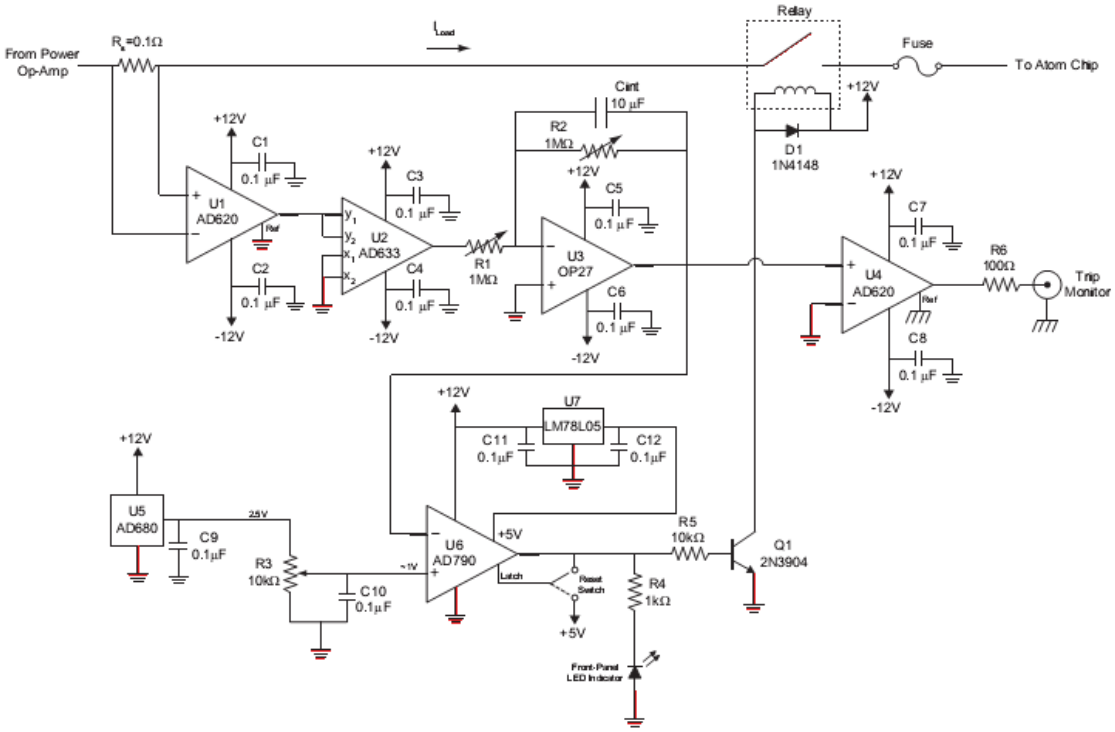

Figure A.4: Bipolar chip driver protection circuit diagram.

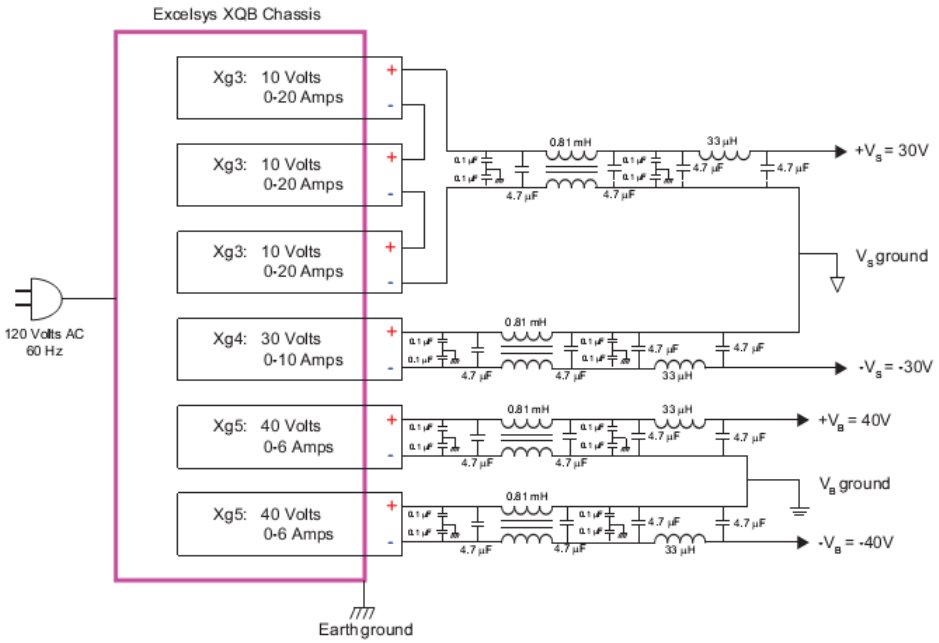

(a) Coil driver Excelsys power supply configuration.

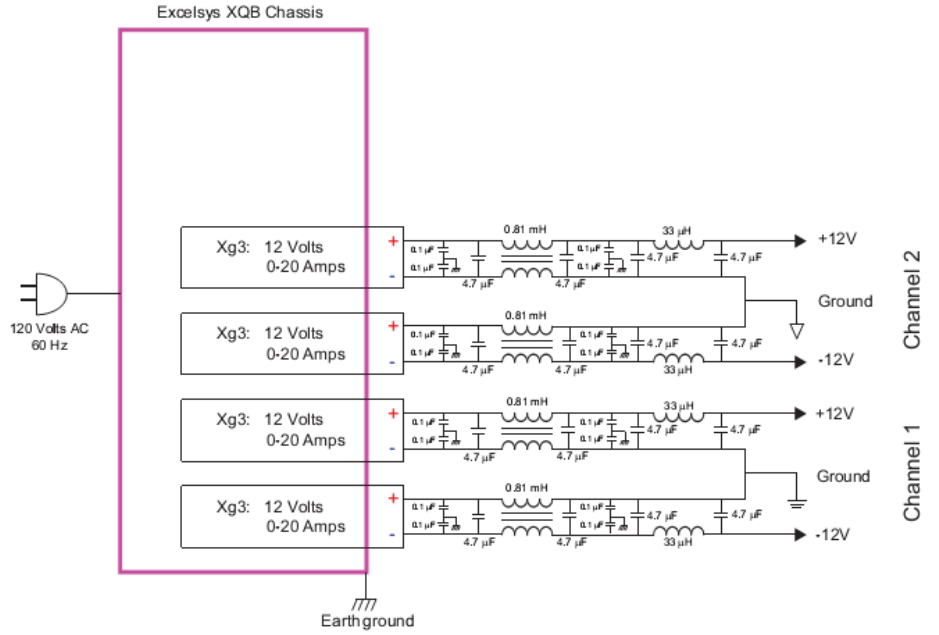

(b) Chip driver Excelsys power supply configuration.

Figure A.5: (a) Three Xg3s are run in series to provide a positive rail of +30 V at 20 A. An Xg4 provides a negative rail of -30 V at 10 A. Two Xg5s provide the ±40 V "boost" voltages. (b) Two Xg3s provide the ±12 V rails and ground, and are floating with respect to earth ground. A second set of Xg3s in the same configuration provides a second chip wire channel. Two empty slots provide space for an additional driver pair. For both the coil and chip drivers, each rail is filtered in the same fashion.

voltage of $\pm 62\,\mathrm{V}$, which is used on all four supply pins to protect against overvoltage.

Appendix B

Effect of finite trace width on atom chips

In this chapter we will extend the analytic evaluation of the magnetic field generated by infinitely thin atom chip wires to having a finite width for the purpose of non-numerically evaluating a chip trap over a larger range of approximations. If we assume that the atom chip traces are infinitely thin, we can calculate the magnetic field above the chip in a straight forward manner from the Biot-Savart law. Consider a line of current running along the y-direction from y_i to y_f at position x_c and $z_c = 0$. The magnetic field at point (x_0, y_0, z_0) is

$$B_x^{\text{ywire}} = -\frac{\Delta_{yi} z_0}{(\Delta_x^2 + z_0^2)\sqrt{\Delta_x^2 + z_0^2 + \Delta_{yi}^2}} + \frac{\Delta_{yf} z_0}{(\Delta_x^2 + z_0^2)\sqrt{\Delta_x^2 + z_0^2 + \Delta_{yf}^2}}, \tag{B.1}$$

$$B_y^{\text{ywire}} = 0, \tag{B.2}$$

$$B_z^{\text{ywire}} = \frac{\Delta_{yi} \Delta_x}{(\Delta_x^2 + z_0^2)\sqrt{\Delta_x^2 + z_0^2 + \Delta_{yi}^2}} - \frac{\Delta_{yf} \Delta_x}{(\Delta_x^2 + z_0^2)\sqrt{\Delta_x^2 + z_0^2 + \Delta_{yf}^2}}, \tag{B.3}$$

where

$$\Delta_{yi} = y_i - y_0; \qquad \Delta_{yf} = y_f - y_0; \qquad \Delta_x = x_c - x_0. \tag{B.4}$$

The magnetic field of a line of current running along the x-direction from x_i to x_f at position y_c and $z_c = 0$ at point (x_0, y_0, z_0) can similarly be written

$$B_x^{\text{ywire}} = 0, \tag{B.5}$$

$$B_y^{\text{ywire}} = -\frac{\Delta_{xi} z_0}{(\Delta_y^2 + z_0^2)\sqrt{\Delta_y^2 + z_0^2 + \Delta_{xi}^2}} + \frac{\Delta_{xf} z_0}{(\Delta_y^2 + z_0^2)\sqrt{\Delta_y^2 + z_0^2 + \Delta_{xf}^2}}, \tag{B.6}$$

$$B_z^{\text{ywire}} = \frac{\Delta_{xi}\Delta_y}{(\Delta_y^2 + z_0^2)\sqrt{\Delta_y^2 + z_0^2 + \Delta_{xi}^2}} - \frac{\Delta_{xf}\Delta_y}{(\Delta_y^2 + z_0^2)\sqrt{\Delta_y^2 + z_0^2 + \Delta_{xf}^2}}, \tag{B.7}$$

where

$$\Delta_{xi} = x_i - x_0; \qquad \Delta_{xf} = x_f - x_0; \qquad \Delta_y = y_c - y_0. \tag{B.8}$$

We can now consider a wire of current with finite width w running along the x-direction from x_i to x_f at position y_c and $z_c = 0$. Ignoring the height of the wire, the magnetic field at point (x_0, y_0, z_0) calculated in Equation B.5 is modified to become

$$B_x^{\text{xwire}} = 0 \tag{B.9}$$

$$B_y^{\text{xwire}} = \tan^{-1}\left(\frac{\Delta_{xi}\Delta_{y+}}{z_0\sqrt{\Delta_{xi}^2 + \Delta_{y+}^2 + z_0^2}}\right) - \tan^{-1}\left(\frac{\Delta_{xf}\Delta_{y+}}{z_0\sqrt{\Delta_{xf}^2 + \Delta_{y+}^2 + z_0^2}}\right)$$
$$+ \tan^{-1}\left(\frac{\Delta_{xi}\Delta_{y-}}{z_0\sqrt{\Delta_{xi}^2 + \Delta_{y-}^2 + z_0^2}}\right) - \tan^{-1}\left(\frac{\Delta_{xf}\Delta_{y-}}{z_0\sqrt{\Delta_{xf}^2 + \Delta_{y-}^2 + z_0^2}}\right) \tag{B.10}$$

$$B_y^{\text{xwire}} = \log\left(\frac{\Delta_{xi} + \sqrt{\Delta_{xi}^2 + \Delta_{y+}^2 + z_0^2}}{\Delta_{xf} + \sqrt{\Delta_{xf}^2 + \Delta_{y+}^2 + z_0^2}} \frac{\Delta_{xf} + \sqrt{\Delta_{xf}^2 + \Delta_{y-}^2 + z_0^2}}{\Delta_{xi} + \sqrt{\Delta_{xi}^2 + \Delta_{y-}^2 + z_0^2}}\right), \tag{B.11}$$

and similarly for a wire running along the y-direction from y_i to y_f at position x_c and $z_c = 0$ is modified to

$$B_x^{\text{ywire}} = \tan^{-1}\left(\frac{\Delta_{x+}\Delta_{yi}}{z_0\sqrt{\Delta_{x+}^2 + \Delta_{yi}^2 + z_0^2}}\right) - \tan^{-1}\left(\frac{\Delta_{x-}\Delta_{yi}}{z_0\sqrt{\Delta_{x-}^2 + \Delta_{yi}^2 + z_0^2}}\right)$$
$$+ \tan^{-1}\left(\frac{\Delta_{x+}\Delta_{yf}}{z_0\sqrt{\Delta_{x+}^2 + \Delta_{yf}^2 + z_0^2}}\right) - \tan^{-1}\left(\frac{\Delta_{x-}\Delta_{yf}}{z_0\sqrt{\Delta_{x-}^2 + \Delta_{yf}^2 + z_0^2}}\right) \tag{B.12}$$

$$B_y^{\text{ywire}} = 0 \tag{B.13}$$

$$B_y^{\text{ywire}} = \log\left(\frac{\Delta_{x+} + \sqrt{\Delta_{x+}^2 + \Delta_{yi}^2 + z_0^2}}{\Delta_{x-} + \sqrt{\Delta_{x-}^2 + \Delta_{yi}^2 + z_0^2}} \frac{\Delta_{x-} + \sqrt{\Delta_{x-}^2 + \Delta_{yf}^2 + z_0^2}}{\Delta_{x+} + \sqrt{\Delta_{x+}^2 + \Delta_{yf}^2 + z_0^2}}\right), \tag{B.14}$$

where

$$\Delta_{x+} = w/2 + (x_0 - x_c) \qquad \Delta_{x-} = w/2 - (x_0 - x_c) \tag{B.15}$$

$$\Delta_{y+} = w/2 + (y_0 - y_c) \qquad \Delta_{y-} = w/2 - (y_0 - y_c). \tag{B.16}$$

From Equations B.1 and B.5 or Equations B.9 and B.12, any chip pattern with linear wires can be patterned and modeled through a superposition of the vector magnetic fields from each trace segment.

In order to find the position of the trap minimum (x_m, y_m, z_m) for a specified geometry, we numerically minimize $B = \|B(x, y, z)\|$. To find the eigenfrequencies of the trap we first take the Hessian of B given by

$$dB_{xyz} = \begin{pmatrix} \frac{\partial^2 B}{\partial x^2} & \frac{\partial^2 B}{\partial x \partial y} & \frac{\partial^2 B}{\partial x \partial z} \\ \frac{\partial^2 B}{\partial x \partial y} & \frac{\partial^2 B}{\partial y^2} & \frac{\partial^2 B}{\partial y \partial z} \\ \frac{\partial^2 B}{\partial x \partial z} & \frac{\partial^2 B}{\partial y \partial z} & \frac{\partial^2 B}{\partial z^2} \end{pmatrix}. \tag{B.17}$$

Evaluating the eigenvectors of dB_{xyz} at the trap minimum (x_m, y_m, z_m) gives us the eigenaxes of the trap and the eigenfrequencies are given by

$$(\omega_i, \omega_j, \omega_k) = \sqrt{\frac{\mu_B}{4\pi^2 m_{Rb}} \text{eigenvalue}(dB_{xyz})|_{(x_m, y_m, z_m)}}, \tag{B.18}$$

where (i, j, k) label the three eigenaxes.